Istanbul Technical University - Department of Meteorological Engineering has been organizing the International Symposium on Atmospheric Sciences - ATMOS every two years, since 2000. This book consists of scientific papers that were presented at the 10th ATMOS event in 2022 and were selected by the scientific committee after being refereed again. This book, which consists of papers under the theme of EARTH, AIR QUALITY and CLIMATE, will provide valuable contributions to related research and researchers.

Dr. Ceyhan Kahya
After graduating from Kültür College and Istanbul Technical University - Department of Meteorological Engineering, Dr. Kahya has completed M.Sc. and Ph.D. studies. Dr. Kahya's main research areas are air pollution, indoor-outdoor air quality, human health, atmospheric chemistry, atmospheric boundary layer, disaster management and engineering ethics.

Dr. Ahmet Öztopal
After graduating from Balıkesir High School and Istanbul Technical University - Department of Meteorological Engineering, Dr. Öztopal has completed M.Sc. and Ph.D. studies. Dr. Öztopal's main research areas are climate, climate change, satellite meteorology and radar meteorology.

İTÜ YAYINEVİ 250

9 789755 616414

Dr. Ceyhan KAHYA
Dr. Ahmet ÖZTOPAL

Earth, Air Quality and Climate

EARTH, AIR QUALITY and CLIMATE

Editors: Dr. Ceyhan KAHYA
Dr. Ahmet ÖZTOPAL

İTÜ YAYINEVİ 250

EARTH, AIR QUALITY AND CLIMATE

Editors:
Dr. Ceyhan KAHYA
Dr. Ahmet ÖZTOPAL

Istanbul Technical University
Faculty of Aeronautics and Astronautics
Department of Meteorological Engineering

EARTH, AIR QUALITY AND CLIMATE
Editors, Dr. Ceyhan KAHYA, Dr. Ahmet ÖZTOPAL

İstanbul, 2024

Cover Design: Sıla Burcu BAŞARIR
Layout: Akın ÖZARSLANTÜRK

e-ISBN 978-975-561-641-4

İTÜ Yayınevi. No: 2024.1/3

Earth, air quality and climate/ editors, Ceyhan Kahya, Ahmet Öztopal –
Istanbul: ITU Press, 2024.
231 pages. -- (İTÜ Yayınevi. No: 2024.1/3)
ISBN 978-975-561-641-4
1. Air Pollution 2. Atmosphere 3.Climatology 4. Earth (Planet)
TL556.E278 2024 CIP

İTÜ YAYINEVİ
Sertifika No: 70051
İTÜ Ayazağa Kampüsü
Mustafa İnan Kütüphanesi
34469 Maslak İSTANBUL
0212 285 75 05
www.ituyayinevi.itu.edu.tr / ituyayinevi@itu.edu.tr

CONTENTS

FOREWORD

As a result of intensive industrialization and urbanization that has continued uninterruptedly since the Industrial Revolution in the 18th century, our Earth is facing major environmental problems. Even today, when there is more environmental awareness than in the past, the continued intensive use of fossil fuels leads to deterioration in air quality, which in turn leads to global warming. Climate change caused by global warming disrupts the balance of the atmosphere and subsequently increases the severity and frequency of extreme weather events. This increases the loss of life and property and negatively affects the habitability of our planet. Efforts in atmospheric science are underway to obtain longer-term reliable estimates and involved in multi-disciplinary and collaborative studies.

This book contains 14 valuable scientific papers on the theme of Earth, Air Quality and Climate selected from the 10th International Symposium on Atmospheric Sciences - ATMOS'22.

We sincerely would like to thank all the authors for their valuable contribution.

Ceyhan Kahya and Ahmet Öztopal
Editors

CHAPTER 1

THE INFLUENCE OF THE HORIZONTAL COMPONENT OF THE ATMOSPHERIC CIRCULATION ON THE CONVECTION OVER POLAND

Kamil LEZIAK

University of Warsaw, Poland
Faculty of Geography and Regional Studies
Chair of Physical Geography
Department of Climatology

Abstract

The goal of this research was to determine the influence of the horizontal component of the atmospheric circulation on the convection over Poland. The following hypothesis has been formulated: the horizontal component of the atmospheric circulation significantly influences the convection over Poland during situation with advective thermals; that influence appears due to changes in strength and potential of convective processes. The character and strength of the convection were determined on the basis of atmospheric soundings performed at eleven sounding stations. Convective indices were used, representing information about different aspects of convection. The analysis of convection characteristics in various circulation conditions was performed using authorial algorithms. Statistically significant changes in convection properties in relation to circulation parameters were established. The biggest potential of the convection development and the strength of the convection are related to the cyclonic circulation. Advection from the southern sectors results in increased potential and strength of convection. Regional differences have been noticed, i.e. the delay in the annual maximum of convective indices at the shore of the Baltic Sea in comparison to the inland areas. The research hypothesis has been confirmed, proving that both the potential and strength of the convection were modified by the horizontal component of the atmospheric circulation.

Keywords: *Convection, atmospheric circulation, convective indices, Poland.*

1.1. INTRODUCTION

Convection is one of the most important processes in the atmosphere. In the broadest term it can be described as the motion of fluid caused by the action of a gravitational field due to density variations (Markowski, 2007), although in atmospheric sciences convection is often defined as predominantly vertical motions of air caused by deviations from hydrostatic equilibrium ("free convection") or driven by external forces ("forced convection"). Convection contributes to the transport of energy, momentum and mass between different air layers (Miyamoto et al., 2013). It can be a source of gravity waves as well as a mechanism responsible for development of various weather systems (Lane, 2015). The latter can produce many severe weather phenomena like storms, heavy rainfall, hailstorms, tornadoes, etc. which cause significant property damage and pose a threat to human life (Kłysik and Fortuniak, 1993).

The aim of this study is to determine the influence of the horizontal component of the atmospheric circulation on the convection over Poland. For the purpose of this study horizontal component of the atmospheric circulation has been defined as the movement of air masses predominantly in a horizontal plane relative to the Earth's surface. It includes advection of air masses caused by heterogenous field of the atmospheric pressure (i.e. the presence of mid-latitude cyclones and anticyclones).

Convection in the atmosphere has been the subject of many studies (e.g., Atkinson and Zhang, 1996, Moncrieff, 2010, Kirshbaum et al., 2018, Moustakis et al., 2020, Lin et al., 2022). However, studies on the dependence of convection on the atmospheric circulation have been rarely undertaken in Poland. They were generally limited to the assessment of the variability of one to three convective indices at three Polish aerological stations over a period of several years (Malinowska, 2011, 2012, Poręba, 2016, Palarz and Cieliński-Mysław, 2017a, b). This study is an attempt to comprehensively determine the influence of the horizontal component of the atmospheric circulation on various aspects of convection, utilising data from Polish and foreign sounding stations.

1.2. MATERIALS AND METHODS

The main data used to describe convection over Poland, its characteristics and development, were the results of atmospheric soundings acquired from the repository of University of Wyoming. Atmospheric soundings are performed at sounding stations twice a day (at 00 and 12 UTC), in specific cases more often (four to eight times a day). They provide an insight into the state and thermodynamic properties of the atmosphere in the vertical profile. In order to better understand spatial diversity of conditions favourable for the development of convection, it is preferable to use data from multiple locations. Due to a small number of sounding stations in Poland and their large distance from each other, sounding data from the neighbouring countries were used, from sounding stations closest to the Polish border (Figure 1.1). In total, the results of atmospheric soundings conducted at eleven stations (three Polish and eight foreign ones) were used in the research, while the main analysis has been carried out on the basis of data from nine stations that conducted regular soundings at 12 UTC. The data represent time period 2000-2020.

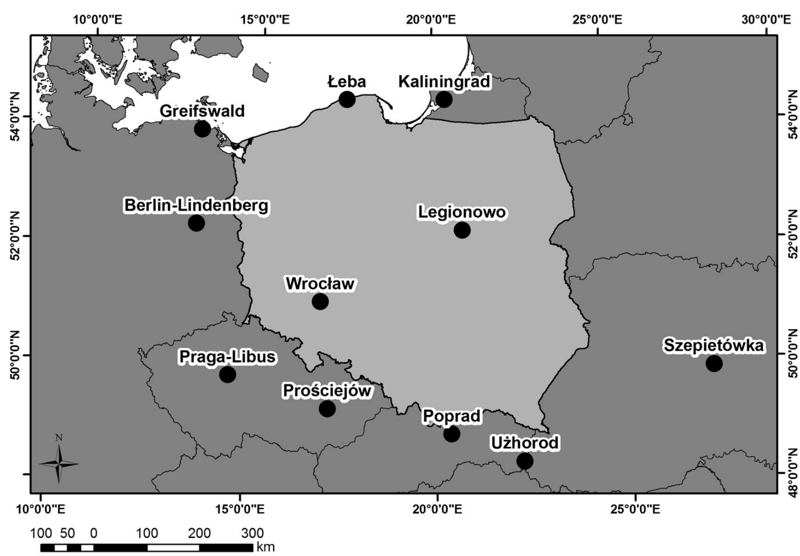

Figure 1.1. Location of sounding stations from which data were obtained for the research.

The results of atmospheric soundings included two types of data: Skew-T thermodynamic diagrams illustrating the change in air temperature and dew point with height, and the values of convective indices calculated for the entire vertical profile of the sounding. Those indices play crucial role in determining characteristics of convection, allowing for the assessment of the potential and strength of convective processes (Table 1.1). It is assumed that specific characteristics of the weather situation that affect the development of convection and the formation of dangerous weather phenomena (e.g., tornadoes) can be reflected by physical indices (Vescio, Thompson, 2001).

Table 1.1. Convective indices used in the study and their application. Indices with acronyms ending in V are variants calculated using virtual temperature.

Acronym	Name	Application
CAPE, CAPV	Convective Available Potential Energy	assessing the potential for the development of convection, assessing potential strength of convective processes
CINS, CINV	Convective Inhibition	assessing the stability of the atmosphere and determining the presence of a layer inhibiting convective processes
SHOW	Showalter Index	assessing the stability of the atmosphere and the potential for the development of thunderstorms, assessing the stability of Planetary Boundary Layer (in pair with LIFT)
LIFT	Lifted Index	assessing the stability of the atmosphere and the potential for the development of thunderstorms, assessing the stability of Planetary Boundary Layer (in pair with SHOW)
BRCH, BRCV	Bulk Richardson Number	assessing the character of the convection and the organisation of convection cells, determining the probability of development of certain convective systems
TOTL	Total Totals Index	assessing the severity of thunderstorms and their organisation
SWET	Severe Weather Threat Index	assessing the danger of severe weather phenomena related to deep convection

To describe characteristics of the atmospheric circulation over Poland atmospheric pressure data from NCEP/NCAR reanalysis were acquired (Kalnay et al., 1996). Daily sea level pressure values from 12 UTC were used, from 425 grid points located between latitudes 30°N & 70°N and longitudes 10°W & 50°E, at the latitudinal and longitudinal interval of 2.5°. Those data were used to calculate zonal and meridional circulation indices, as well as a pressure distribution index, according to modified Lityński method (Lityński 1969), in which indices were calculated individually for each sounding station. On their basis, using Lityński's method of determining the type of atmospheric circulation, three synthetic parameters were defined, and their values calculated for each sounding station:

- circulation mode parameter (LCMD),
- advection parameter (LADV),
- circulation type parameter (LCTP).

Circulation mode parameter determines the character of the atmospheric circulation above the sounding station - whether it is cyclonic (LCMD = "C"), anticyclonic (LCMD = "A") or transitional (LCMD = "0"). Advection parameter reflects the general direction of the flow of air masses (i.e. LADV = "NE" means that air masses come from the north-east; LADV = "0" is used in a situation when there is no discernible advection). Circulation type parameter combines circulation mode followed by the direction of advection, in a form of a single parameter. There are 27 possible types of atmospheric circulation, resulting from the combination of all circulation modes and values of advection parameter. For example, LCTP = "SEC" means there is a cyclonic circulation with advection from south-east, while LCTP = "NW0" means there is a transitional situation with advection from north-west.

In order to determine the influence of the horizontal component of the atmospheric circulation on the convection over Poland, an analysis of the spatial distribution and the variability of the convection during various circulation conditions (represented by LCMD, LADV and LCTP parameters) was performed. A following hypothesis has been formulated: the horizontal component of the atmospheric circulation significantly influences convection over Poland during the situation with advective thermals and that influence appears due to changes in the strength and potential of convective processes.

Sounding data from all stations were imported into a SQL database. Then, using the INNER JOIN method, they were merged with the above-mentioned atmospheric circulation data. To each database record, representing a single atmospheric sounding, corresponding values of LCMD, LADV and LCTP were assigned. As a result, a Cartesian product of convection indices and circulation parameters was created. That dataset was then divided into subsets using an original VBA script. Each of the subsets included a data series related to a single convection index, in one time category (yearly, half-yearly, seasonal or monthly values), with a single value of one of the circulation parameters, attributed to a single sounding station. Warm half-year has been defined as months from April to September, and cold half-year has been defined as months from October to March. Seasons have been defined as following three-month periods: spring - from March to May, summer - from June to August, autumn - from September to November, winter - from December to February.

In order to determine differences in characteristics of the convection in various atmospheric circulation conditions an original script was written in R. The R script allowed for a comparison of subsets relating to the same sounding station, time category and convection index, with different circulation mode, direction of the advection or type of the atmospheric circulation. The comparison was made using the extended five-number summary method (Hoaglin et al. 2000), additionally presenting the mean value. The comparison of five-number summary of various datasets allows to determine their mutual relations, e.g., whether the mean values in one set are greater than in the other, one set is more dispersed than the others, the extreme values in a given set are greater than in the others, etc. The results of the comparison were presented in the form of box plots using a modified Tukey's method (Chambers et al. 1983), showing the position of the mean value as a "+" symbol, and the indentation in the sides of the boxes, corresponding to the confidence interval of the median. The width of each box is directly proportional to the square root of the number of observations in the given subset.

To verify the hypothesis the statistical significance of differences between values of convection indices at sounding stations was checked, for different values of each of the atmospheric circulation parameters. For this purpose, an original VBA script was used, with which the two-sample Kolmogorov–Smirnov test was carried out. This test was performed in an each-to-each relation, in arrays containing data subsets that differed only in the value of the associated atmospheric circulation parameter (LCMD, LADV or LCTP). This method of examining statistical significance allowed for more detailed and more accurate results than if each subset was compared with the sum of the other subsets (for example, if the BRCH values for advection from the north were compared with the set of BRCH values for all other advection directions). Based on the results of the two-sample Kolmogorov-Smirnov test, it was determined which pairs of compared samples (subsets of values of convection indices under different circulation characteristics) have significantly different distributions, therefore belonging to two different populations. In all tests an alpha level of 0.05 was assumed. In the following chapters, only statistically significant relations have been described. To not exceed spale alotted, few boxplots have been presented to assist with visual comparison of the data.

1.3. RESULTS

1.3.1. The Influence of Circulation Mode (LCMD) on Convection

Differences were observed in the potential for convective development, depending on the character of atmospheric circulation represented by the value of circulation mode parameter. They were visible, among other things, in mean and maximum values, as well as in interquartile range. Convective available potential energy, in both CAPE and CAPV variants, was higher in cyclonic circulation than in anticyclonic circulation. Those relations were present on both Polish and foreign sounding stations, in yearly data series and during the warm half-year. It allows one to assume that increased potential for the development of convection in cyclonic circulation mode is prevalent on the territory of Poland during warm months. Considering seasonal differences, CAPE values in summer were the highest in respective convection modes, in comparison to other seasons (Figure 1.2). The highest amount of convection available potential energy in summer can be attributed to reduced cloud cover and increased insolation, leading to higher air and surface temperature and increased positive buoyancy of the atmosphere.

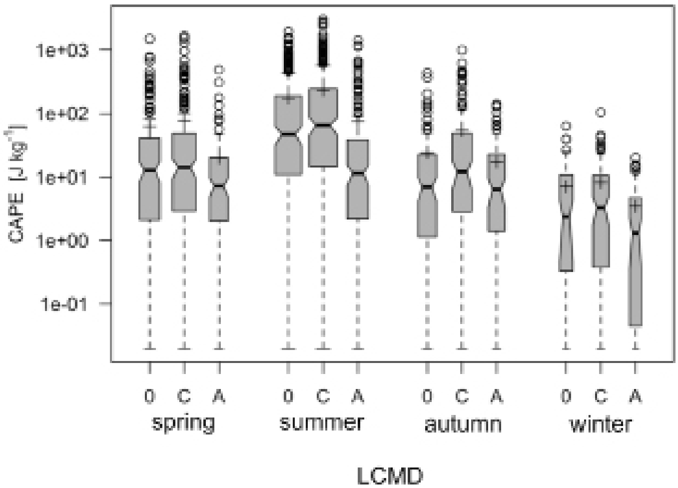

Figure 1.2. Seasonal changes of CAPE values depending on LCMD parameter in Wrocław (2000-2020).

It should be noted that high CAPE or CAPV value does not necessary mean that strong convection will occur in certain atmospheric circulation mode. As these indices reflect the amount of potential energy available for convection, there may be other factors that will prevent that potential energy to be transformed into kinetic energy of a convective process. One of them is convective inhibition (CINS, CINV) representing the negative buoyancy of the atmosphere.

Unlike convective available potential energy, convective inhibition dependence on circulation mode varies with location. At the Baltic Sea shore convective inhibition did not change depending on circulation mode, with an exception of Łeba, where, annually, in transitional circulation CINS modulus was higher than in cyclonic one. At inland sounding stations CINS modulus differed depending on circulation mode. In Legionowo, Wrocław and Berlin cyclonic circulation resulted in decreased convective inhibition, while in Prague - in increased. The large diversity of relations observed at different stations suggests that convection mode does not have the same effect on the inhibition of the convection process in each place. Local factors, including terrain features and dynamics of the air flow may affect convective inhibition.

It has been determined that the stability of the atmosphere changes significantly with the atmospheric circulation mode, which is reflected by values of the Showalter Index and Lifted Index. On all stations lower values of SHOW (representing higher instability and higher risk of storms) occur in cyclonic circulation, while higher values occur in anticyclonic circulation. The difference between SHOW values in transitional and cyclonic circulation were the smallest in summer, although both LCMD = “C” and LCMD = “0” represented significantly higher instability than anticyclonic circulation in the same season. It should be noted, however, that even in summer values of Showalter Index were mostly positive, which indicates weak instability. Lifted Index, in general, followed the same pattern. On all stations value of LIFT was decreased in cyclonic and increased in anticyclonic circulation. While Lifted Index was lower in the warm half-year (indicating increased instability of the atmosphere), differences between values in various circulation modes were more prominent in the cold half-year.

Atmospheric circulation mode may also influence the risk of the development of dangerous convective systems (e.g., supercells, quasi-linear convective systems, etc.) and severe weather phenomena (e.g. tornadoes, hailstorms, thunderstorms). A relation between convection mode and values of certain convective indices used for risk assessment for severe weather events was discovered. In annual series Bulk Richardson Number (in both BRCH and BRCV variants) showed clear differentiation, depending on atmospheric circulation mode. Decreased values of Bulk Richardson Number were observed in anticyclonic circulation and increased in cyclonic circulation. Only in Wrocław no significant difference was found between values of BRCH in cyclonic and transitional circulation, but anticyclonic circulation was still characterised by decreased values. Similar relations were observed in Prague and Prosciejov, which allows to assume that they might be representative for the southern part of Poland. In the whole country, according to yearly data series, cyclonic circulation was found to be more favourable for development of supercells or discrete cells, due to the higher ratio of free to forced convection (represented by higher values of BRCH). Seasonally, the differences were not as distinctive, although they followed a similar pattern. Autumn was an exception, when the only significant change was the increase of Bulk Richardson Number in cyclonic circulation in Łeba and Legionowo, but only in relation to BRCH value in anticyclonic circulation.

Values of Total Totals Index on all sounding stations in yearly data series were higher in cyclonic circulation than in anticyclonic circulation. The same relation occurred in half-yearly data, but differences between TOTL values in different circulation modes were greater in the cold half-year than in the warm half-year. Seasonal data showed that in summer the differentiation of TOTL values in cyclonic, transitional and anticyclonic circulation was the smallest and values in cyclonic circulation were higher in winter than in summer. Although it could suggest bigger possibility of severe thunderstorms in winter, it should be noted that due to increased inhibition of convective processes, thunderstorms are less likely during the cold period of the year.

While Bulk Richardson Number presents information about possible organisation of the convection and proportions between free and forced convection, and Total Totals Index informs about the possibility of thunderstorms and their severity, Severe Weather Threat Index is a complex parameter assessing the risk of severe weather phenomena caused by deep convection, including tornadoes and tornado outbreaks. In a similar way to BRCH, BRCV and TOTL, SWET values were increased in cyclonic circulation mode and decreased in anticyclonic circulation mode. This relation was confirmed in all data series, regardless of their time categories (yearly, half-yearly, seasonal). Additionally, values of Severe Weather Threat Index in transitional circulation mode in summer were higher than in the same circulation mode in other seasons. Maximum values of SWET exceeded 300, which can indicate moderate risk of severe weather phenomena.

1.3.2. The Influence of Advection (LADV) on Convection

The direction of the advection of air masses was determined by the value of the advection parameter (LADV). LADV can take one of nine values - 8 basic compass directions or the value “0”, representing a situation in which there is no significant advection (i.e. horizontal pressure gradient is omittable). Therefore it is possible to determine whether convection occurs with advective thermals or not. Advective thermals are present only when air masses transfer certain thermodynamic properties over a given area (i.e. LADV ≠ “0”). However, it should be emphasised that even when advection occurs, properties of the Earth surface below influence thermodynamic properties of the air, to some degree. When

LADV = “0” thermodynamic properties of the atmosphere result from energy exchange between the surface of the Earth and the lower troposphere, within the planetary boundary layer.

Differences were observed in the amount of convective available potential energy depending on the direction of advection. It has been noticed in yearly data series that on inland stations decreased values of CAPE occurred during north-eastern advection while increased - during advection from south and south-west. In the northern Poland increased values of CAPE occurred during advection from south (against advection from east, north-east and north-west) and from north (against advection from the eastern sector). However, there were no differences in convective available potential energy during circulation with advective thermals and when there was no discernible advection.

The analysis of half-yearly data series showed that there is a big contrast between the warm and cold half-year. On all stations convective available potential energy was on average higher in the warm half-year than in the cool half-year, but its differentiation depending on the direction of advection was much greater in the cold half-year. That means that the direction of the flow of air masses is of a greater importance in shaping the potential for convection development in the cold half-year than in the warm half-year. This regularity was most clearly visible in the central part of Poland.

Convective inhibition was also differentiated depending on the value of LADV parameter. At the whole territory of Poland CINS modulus was increased during advection from the southern sector and decreased during advection from north and north-east, in both yearly and half-yearly data series. Convective inhibition was decreased in the cold half-year in comparison to the warm half-year.

In regard to the stability of atmosphere, yearly data series of Showalter Index showed little differentiation depending on the direction of advection. Semi-annual data showed small variations: values of SHOW were decreased in the warm half-year, which corresponds to the decreased stability of the warmer atmosphere. In the warm half-year on most sounding stations advection from south-eastern sector contributed to a slight, but significant, decrease in the value of Showalter Index, while advection from the north-western sector was responsible for its increase. In the cold half-year advection from east and south-east caused an increase, and advection from north-west - decrease in SHOW values. Those regularities occurred both at the shore of the Baltic Sea and inland.

Lifted Index followed a similar pattern. On all Polish stations LIFT value was slightly increased during advection from south-east and east, but no other relations in yearly data series were found. In the warm half-year LIFT was decreased during advection from south and south-east, and increased during advection from west. In the cold half-year at the Baltic Sea shore advection from north or north-west caused Lifted Index to decrease. On the inland stations Lifted Index increased with advection from the eastern sector.

Both BRCH and BRCV parameters were differentiated depending on the direction of advection. Bulk Richardson Number varied between coastal and inland stations, as well as within the coastal stations themselves. In yearly data series in Łeba advection from north-west resulted in an increase of BRCH, while in Greifswald and Kaliningrad advection from the south-eastern sector had the same effect. In Legionowo and Wrocław during advection from southern and eastern sectors Bulk Richardson Number was increased, while advection from west and north-west decreased it. Similar regularities occurred at neighbouring foreign sounding stations, with an exception of Prosciejov. Half-yearly data series revealed that on all stations BRCH values were increased in the warm half-year (favouring the development of certain convective systems like supercells, quasi-linear convective systems, etc.).

Total Totals Index showed little to no differentiation depending on the direction of advection in yearly data series. Only in Łeba and Greifswald TOTL values were slightly increased during advection from north and north-east, and decreased during advection from east and south-east. In the warm half-year Total Total Index was less differentiated, depending on the direction of advection, than in the cold half-year. At the Baltic Sea shore there were no significant changes in its value, although the interquartile range was slightly increased during advection from the western sector; this could indicate a greater variability of thermodynamic properties of air masses coming from this sector. In the cold half-year on all Polish stations TOTL values were increased during advection from the northern sector (Figure 1.3).

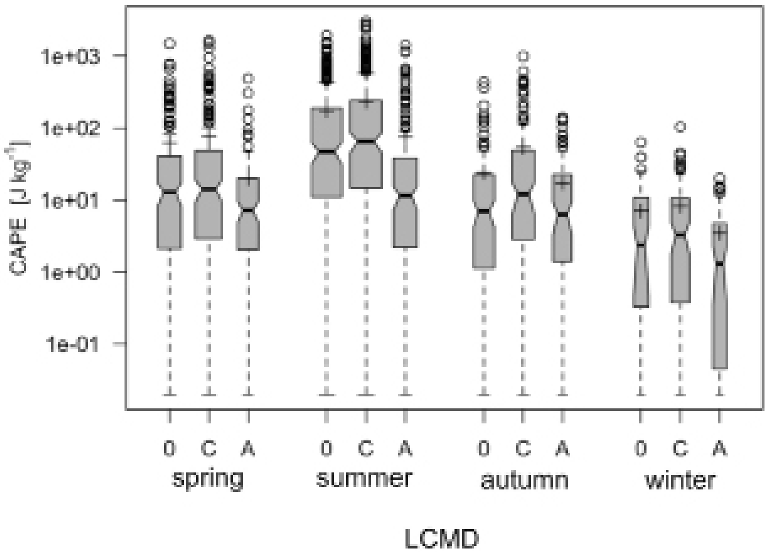

Figure 1.3. Half-yearly changes of TOTL values depending on LADV parameter in Łeba (2000-2020).

It has been observed that Severe Weather Threat Index varied, depending on the direction of advection. In yearly data series relations on all the coastal stations were similar: SWET values increased during advection from the western sector and decreased during advection from the eastern sector. On inland stations there were some differences. In Legionowo SWET values were increased during advection from south-west and north-west only, and decreased during advection from east. In Wrocław advection from south and from the western sector resulted in an increase, and advection from north and north-east - in a decrease of SWET value. Similar regularities were noticed on the neighbouring foreign stations. In the warm half-year Severe Weather Threat Index was increased during advection from the south-western sector and decreased during advection from the south-eastern sector. In the cold half-year on all stations advection from the western sector and from the north resulted in increased SWET values, while advection from the eastern sector - in decreased values.

1.3.3. The Influence of Circulation Type (LCTP) on Convection

Circulation type parameter (LCTP) provides a combined information about the circulation mode and the direction of advection of air masses. While LCMD and LADV parameters on their own present important data regarding the properties of the atmospheric circulation, it is necessary to take into account their combined influence in order to determine specifics of the circulation in a comprehensive way. Due to coexistence of various circulation modes and advection properties, LCTP may not reflect regularities and relations of convective indices that have been noticed for one or both of its components. It should also be noted that only certain differences between values of convective indices in different circulation types represented by LCTP parameter have been proven to be statistically significant. Especially, when analysing monthly data series, it has been observed that there were very few pairs of circulation types that represented small, statistically significant differences. Therefore, it may be assumed that when examining relation between atmospheric circulation and convection, data that are too detailed temporally will not yield applicable results.

In yearly data series convective available potential energy at the shore of the Baltic Sea was decreased in SEA, WA and 0A circulation types, and increased in EC and SEC (Figure 1.4). The difference in the amount of convective available potential energy in various circulation types was smaller on the inland stations, although the maximum values of CAPE were higher. In Legionowo and Wrocław CAPE was increased in 0C, SC, SEC and SE0 circulation and decreased in SEA and NEA. Seasonal data showed many regional differences, which made it impossible to draw conclusions applicable to all sounding stations. In summer convective available potential energy was increased in circulation types with advection from east or south-east (EC, EA in Łeba, E0, EC, SEC, SE0 and SC in Legionowo, EC, SE0, SEC in Wrocław) and decreased in circulation types with advection from the northern sector (e.g. N0 and NEA in Legionowo, NA in Wrocław). In autumn cyclonic types were responsible for increased CAPE values, but associated direction of advection was different in different locations (NC, NWC in Łeba, SWC and NWC in Legionowo, EC in Wrocław). In winter both the frequency of circulation types and their respective CAPE values varied greatly.

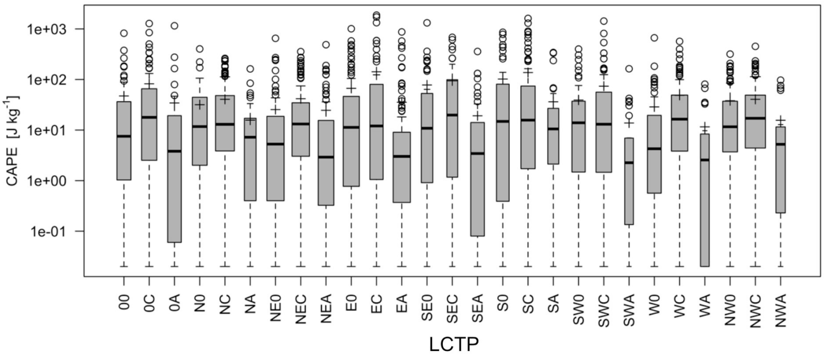

Figure 1.4. Yearly changes of CAPE values depending on LCTP parameter in Łeba (2000-2020).

Convective inhibition on all stations was decreased in NEC and increased in SE0 circulation type, in both yearly and half-yearly data series. Seasonal differences were noticeable between regions. In spring at coastal areas convective inhibition was increased in transitional circulation types (e.g. E0 and S0 in Łeba), in the central Poland CINS was decreased in NC and NWC circulation types and increased in SWC, S0 and WA. In summer in Łeba convective inhibition was decreased in certain cyclonic and transitional types with advection from the northern sector (e.g. NEC, NWC, N0, NW0) and increased in types SE0, SEA and SA. It should be noted that in Legionowo and Wrocław transitional types E0, SE0, S0 were responsible for increased values of CINS, along with SWC type.

It has been determined that at all sounding stations Showalter Index was differentiated in circulation types with the same direction of advection, but different circulation modes. This means that, when determining the stability of the atmosphere using SHOW, the mode of the circulation is more important than the direction from which air masses flow. There were no statistically significant differences between values of Showalter Index in circulation types that shared the same circulation mode.

Lifted Index, yearly, was higher in anticyclonic circulation types than in cyclonic circulation types. Those relations were present at all stations. Decreased values of Lifted Index (indicating lower stability of the atmosphere) occurred in summer and spring. In spring certain anticyclonic circulation types resulted in increased LIFT values: NA, NWA and SA on all stations, additionally

EA, NEA and 0A in Legionowo and Wrocław. Decreased values were associated with SWC and SC types. In summer Lifted Index was higher in anticyclonic circulation types than in cyclonic or transitional ones: WA (on all stations), SWA and NA (in Łeba), SA and NEA (in Legionowo and Wrocław) and NA (in Wrocław).

Bulk Richardson Number was found to be increased in yearly data series, at the coastal stations in circulation types SEC, EC and E0 and decreased in types NEA, NWA and SWA. At the inland stations Bulk Richardson Number was increased in SE0, SEC and 0C circulation types, which favoured stronger convection development. In summer at all stations BRCH values were increased in SEC and E0 types, and additionally in NC and NEC in Łeba, SE0 and SWC in Legionowo, SE0 in Wrocław. Decreased values occurred in NWA and 0A types.

Total Totals Index on all stations was higher in cyclonic circulation types than in anticyclonic ones. Concurrently, there were no significant differences between values within groups od cyclonic, anticyclonic or transitional circulation types. This means that, similarly to the case of Showalter Index, the decisive factor for the value of Total Totals Index was circulation mode and not the direction of the flow of air masses. In addition TOTL value range was similar at all stations, both Polish and foreign ones. It may lead to an assumption that Total Total Index in the context of circulation types was not differentiated at the Polish territory and its values did not depend on mesoscale characteristics of the atmospheric circulation.

Severe Weather Threat Index was, however, differentiated within circulation types sharing the same circulation mode. In yearly data series cyclonic circulation types (i.e. SEC, SC, NEC) were characterised by higher values of SWET than types with anticyclonic or transitional circulation. Additionally, in SWC type in Legionowo, SWC and WC in Łeba, SWC and NWC in Wrocław, Severe Weather Threat Index was higher than in the rest of the cyclonic types. In spring SWET values were increased in cyclonic circulation types with advection from the western sector (in Łeba additionally in 0C, and in Wrocław - in SC) and decreased in all anticyclone types. In summer at the Baltic Sea shore Severe Weather Threat Index was increased in cyclonic circulation types with advection from the south-eastern and south-western sector, as well as in 0C type. In Legionowo increased values occurred during cyclonic types with advection from the north-eastern sector, while in Wrocław - in types SWC and SW0.

1.4. CONCLUSION

It has been shown that both the amount of convective available potential energy and the value of convective inhibition vary significantly, depending on the direction of advection and on the circulation mode, in situation with applied thermals (i.e. when LADV ≠ "0"). This means that the potential for convective development depends on the horizontal component of the atmospheric circulation. There were also significant differences in values of Bulk Richardson Number, Lifted Index, Severe Weather Threat Index and other indices, depending on the direction of advection and on circulation type. On this basis it has been concluded that the formulated hypothesis is confirmed, because both the potential and strength of convection (reflected by mentioned indices) changed significantly depending on the properties of the horizontal component of the atmospheric circulation.

It has been determined that in cyclonic circulation mode the amount of convective available potential energy was higher and the value of convective inhibition - lower than in anticyclonic circulation. This confirms that the potential for convective development is higher in cyclonic than in anticyclonic circulation. Bulk Richardson Number, Showalter Index, Lifted Index, Severe Weather Threat Index and Total Totals Index had significantly different values in cyclonic and anticyclonic circulation modes. Values of the indices in cyclonic mode pointed to increased potential or strength of the convection (i.e. SHOW and LIFT values were lower, TOTL and BRCH values - higher than in the anticyclonic mode).

In situation with advective thermals it has been observed that the potential for convection and its strength was higher during advection from the southern sector than from other directions. The amount of convective available potential energy was increased during advection from the south, (at some stations also from the south-east). Advection from the western sector has also increased values of convective indices, to a lesser degree. Additionally, the indices determining the strength of convection had their value increased (or decreased, when lower values indicated more unstable atmosphere, e.g. SHOW or LIFT) during advection from the southern sector.

The highest potential for convective development occurs in in summer in cyclonic circulation types, which is consistent with other studies (e.g. Poręba, 2016). This is also the situation with the highest strength of convection, as represented by a set of convective indices. However, the direction of advection is a much more differentiating factor in the cold half-year than in the warm one. In the warm half-year at most of the stations potential for convective development depended more on the circulation mode than on the direction of advection.

On the shore of the Baltic Sea the influence of atmospheric circulation on the convection is different than in the rest of Poland, which confirms studies by Malinowska (2012) and Palarz & Cieliński-Mysław (2017). Differences are visible, among other things, in directions of advection associated with increased values of convective indices and in the shift of the time of the year when convective indices reach their maximum values. In the warm half-year at the coastal stations the strength of convective processes is greater during advection from the southern sector, and in the cold half-year during advection from the northern sector. This can be seen, for example, in reduced values of Lifted Index in the cold half-year with advection from the north and in the warm half-year with advection from the south.

It should be emphasised that the size of differences and their statistical significance change, depending on temporal resolution and time range of data series. Therefore, it is possible that a certain regularity does not occur, or is insignificant, in yearly or half-yearly data series, but is important in certain season or a month, or vice versa. While the most prominent or significant regularities have been discussed in this study, a full description of all possible relations between convective indices and atmospheric circulation parameters would greatly exceed the space allotted to this paper. A topic worth further investigation is the long-term stability of regularities and relations presented in this study.

REFERENCES

Atkinson B. W. and J. Wu Zhang (1996), Mesoscale shallow convection in the atmosphere, Reviews of Geophysics, 34, 4, 403-431.

Chambers J. M., W. S. Cleveland, B. Kleiner and P.A. Tukey (1983), Comparing data distributions: notched box plots. Graphical methods for data analysis, Wadsworth International Group, Belmont, 60–63.

Hoaglin D. C., F. Mosteller and J. W. Tukey (2000), Understanding robust and exploratory data analysis, Wiley, New Jersey.

Kalnay E., M. Kanamitsu, R. Kistler, W. Collins, D. Deaven, L. Gandin, M. Iredell, S. Saha, G. White, J. Woollen, Y. Zhu, M. Chelliah, W. Ebisuzaki, W. Higgins, J. Janowiak, K. C. Mo, C. Ropelewski, J. Wang, A. Leetmaa, R. Reynolds, R. Jenne, and D. Joseph (1996), The NCEP/NCAR 40-Year Reanalysis Project, Bulletin of the American Meteorological Society, 77, 3, 437-472.

Kirshbaum D. J., B. Adler, N. Kalhoff, C. Barthlott and S. Seraffin (2018), Moist Orographic Convection: Physical Mechanisms and Links to Surface-Exchange Processes, Atmosphere, 9, 80, 1-26

Kłysik K. and K. Fortuniak (1993), Maksymalne opady dobowe w środkowej Polsce, Przegląd Geograficzny, 64, 1–2, 97–110.

Lane T. P. (2015), GRAVITY WAVES | Convectively Generated Gravity Waves in: North G. R., Pyle J., Zhang F. (eds.), Encyclopedia of Atmospheric Sciences (Second Edition), Academic Press, Melbourne (pp. 171-179) (ISBN 9780123822253).

Lin J., T. Qian, P. Bechtold, G. Grell, G. J. Zhang, P. Zhu, S. R. Freitas, H. Barnes and J. Han (2022), Atmospheric Convection, Atmosphere-Ocean (ahead of print), 1-55.

Lityński J. (1969), Liczbowa klasyfikacja typów cyrkulacji i typów pogody dla Polski, Prace Państwowego Instytutu Hydrologiczno-Meteorologicznego, 97, 3-14.

Malinowska M. (2011), Variability of chosen instability indices in Poland in XXI century, Prace i Studia Geograficzne, 47, 97–107.

Malinowska M. (2012), Związki między chwiejnością powietrza nad Polską a cyrkulacją atmosferyczną in: Bielec-Bąkowska Z., Łupikasza E., Widawski A. (eds.), Rola cyrkulacji atmosfery w kształtowaniu klimatu, Wydział Nauk o Ziemi Uniwersytetu Śląskiego, Sosnowiec, 67–74.

Markowski P. (2007), An Overview of Atmospheric Convection in: Giaiotti D. B., Steinacker R., Stel F. (eds.), Atmospheric Convection: Research and Operational Forecasting Aspects, SpringerWienNewYork [sic], Udine (pp. 1-6) (ISBN 9783211489635).

Miyamoto Y., Y. Kajikawa, R. Yoshida, T. Yamaura, H. Yashiro and H. Tomita (2013), Deep moist atmospheric convection in a subkilometer global simulation, Geophysical Research Letters, 40, 4922-4926.

Moncrieff M. W. (2010), The Multiscale Organization of Moist Convection and the Intersection of Weather and Climate, Geophysical Monograph Series, 189, 3-26.

Moustakis Y., C.J. Onof and A. Paschalis (2020), Atmospheric convection, dynamics and topography shape the scaling pattern of hourly rainfall extremes with temperature globally, Communications Earth & Environment, 1, 11, 1-9.

Palarz A. and D. Cieliński-Mysław (2017a), Factors inhibiting convection under conditions of extreme atmospheric instability, Geographia Polonica, 90, 1, 39-51.

Palarz A. and D. Cieliński-Mysław (2017b), Ekstremalne wartości wskaźników chwiejności atmosfery w Polsce i ich związek z mechanizmami ograniczającymi rozwój konwekcji, Prace Geograficzne, 148, 11-32.

Poręba S. (2016), Uwarunkowania cyrkulacyjne konwekcji w południowej Polsce, Badania Fizjograficzne Seria A, 67, 179-193.

Vescio M. D., and R. L. Thompson (2001), Subjective Tornado Probability Forecasts in Severe Weather Watches, Weather and Forecasting, 16, 2, 192–195.

CHAPTER 2

AIRBORNE NANO PARTICULATE MATTER SIZE DISTRIBUTION AND SOURCES: A REVIEW

Ülkü ALVER ŞAHİN

Istanbul University-Cerrahpaşa, Türkiye
Engineering Faculty
Environmental Engineering Department

Abstract

Inhalable particulate matter in the atmosphere is an important environmental, health and climate issue in the present. It has been reported by scientists that the mass concentrations of coarse particles show significant decreases over time, but fine and ultra fine particles do not decrease at this level. It is seen that nano-sized particles continue to increase, and it is determined that they contribute up to 90 % in the number concentration of fine particles. The particle size distribution of airborne particles is hugely diverse, ranging from newly formed particles of a few nanometres in diameter through to particles of tens of micrometres in diameter. Although particle number size distribution data have been used widely in source analysis of air pollution in Europe and America, limited studies have been conducted in East Asia and no studies in Latin America, Africa and West Asia including Türkiye. All these studies have shown that size distribution differs between regions, while the nucleation and Aitken modes are dominant in America and Europe, however the coarser modes (accumulation) are effective in Asia. This clearly represents that the regional air pollution sources should be evaluated, and control strategies should be planned differ.

Keywords: *Nanoparticles, particle counts, ultra fine particles, size distribution, sources.*

2.1. INTRODUCTION

Airborne particulate matter (PM) is an air pollutant of concern due to its adverse effects on human health and its effects on climate change. Atmospheric PM covers a very wide range of particle sizes and can be considered an important pollutant because of its diverse chemical composition. In the past years, most of the PM was releasing into the atmosphere due to the coal combustion. In the present, with the decrease in coal use, although sulphur emissions and coal-derived particles have been significantly reduced, traffic, secondary aerosol formation, ammonium, organic carbon have been continuing to dominate on PM, especially in developed countries. Most studies have reported that the mass concentrations of PM_{10} show significant decreases over time, but $PM_{2.5}$ does not decrease at this level. In particular, it is seen that nano-sized particles named as ultrafine particles (UFP) continue to increase and it is determined that they contribute up to 80-90% in the number concentration of $PM_{2.5}$ (Harrison, 2020). In addition, recent study reported that UFP especially <30 nm particles from traffic highly correlated to the mortality related to the respiratory and circular systems (Rivas et al., 2019).

The particle size distribution of airborne PM is hugely diverse, ranging from newly formed particles (NPF) of a few nanometres in diameter through to particles of tens of micrometres in diameter (Harrison et al., 2000). Particle reduction strategies should be focused on the number of the particle rather than its mass and that the sources should be identified. Recently particle number size distribution (PNSD) data from nanometres to 10 micrometres measured every one-minute intervals have been using widely in source analysis in the world, especially in Europe and United State (Beddows et al., 2008; Harrison et al., 2018; Zeraati-Rezaei et al., 2020). Limited studies have been conducted in East Asia and no studies in Latin America, Africa and West Asia including Türkiye (Wu and Boor, 2021). All these studies have shown that PNSD differs be-tween regions, while the nucleation and Aitken modes are dominant in America and Europe, however the coarser modes (accumulation) are effective in Asia. This clearly represents that the regional air pollution control strategies should be planned differ. Air pollution problem in urban areas is an important public health, climate problem and it is necessary to focus on determining the size distribution and sources of nanoparticle counts and particle mass together and create reduction plans for both number and mass of PM (de Jesus et al., 2020). The aim of this study is to review and discuss the studies on the number and sources of nano particulate matter in the literature.

2.2. PARTICLE NUMBER SIZE DISTRIBUTION

PNSD is generally characterized by a multi-lognormal structure, usually based on four main modes: the nucleation mode (Dp < 30 nm), the Aitken mode (30 nm < Dp < 100 nm), the accumulation mode (100 nm < Dp < 1 μm) and the coarse mode (Dp > 1 μm) (Vu et al. 2015). In the latest study, wide range PNSD has been described as 5 modes through adding to large fine (1 μm < Dp < 2.5 μm) and coarse (Dp > 2.5 μm) fractions (Şahin et al. 2022). In the literature, PN concentrations and size distribution changes have been studied widely in background sites (Dall'Osto et al., 2019), urban areas (Harrison et al. 2019), near airports (Stacey et al., 2020), traffic sites (Knibbs et al., 2009) and arctic regions (Tatzelt et al., 2022). Table 2.1 shows the number concentrations of each particle fractions and Figure 2.1 represents the contribution to total PN measured in the urban background of different cities around the world.

The highest particle number count (PN) has been observed in Delhi, India (20-50 $x10^3$ $\#/cm^3$), followed by Wuhan, Hong Kong and Beijing, all cities in the Asia. Both European cities and United Kingdom (UK) cities have relatively similar PN values varied between 5 and $10x10^3$ $\#/cm^3$. The lowest PN has been detected in Antarctica with approximately 300 $\#/cm^3$. All these counts have been observed in the urban background sites. However, in near traffic, urban, industrial area PN can be more. Kumar et al. (2014) reported the PN levels at the roadside in 42 different cities and determined average total PN 11.7 $x10^4$ $\#/cm^3$ in Asia, 3.15 $x10^4$ $\#/cm^3$ in Europe cities. It is clearly shown that the PN from traffic are at least 10 times more than in the urban background. Another study conducted by Presto et al. (2021) reported that PN in urban areas and near highway sites are 3 and 5 times higher than suburban sites in North America, respectively. The highest UFP ratio (85 %) in the total PN has been found in Helsinki and the lowest (43 %) in Beijing (Figure 2.1).

Several studies investigated the correlation between PN and $PM_{2.5}$ in various cities, considering different factors contributing to their spatial and temporal variations. de Jesus et al. (2020) investigated all these studies and summarized some key findings. The general results indicate that the correlation between $PM_{2.5}$ and PN varies temporally, spatially and depending on the particle size. The minimum and maximum correlations using hourly data were determined as 0.07 in Los Angeles and 0.53 in Shanghai, respectively. In addition, the correlations were found 0.31 for summer, 0.84 for autumn and 0.69 for winter at the urban background site in Delhi (Şahin et al., 2022). More-over, Wu and Boor (2021) reported that the $PM_{2.5}$ derived from PNSD shows a good agreement with the measurement at local stations, especially for four stations in Pittsburgh. Consequently, the correlation increases as the particle size increases, from Europe to Asia, from warm season to cold season and on weekdays. The studies show some discrepancies of these relations for some locations. These situations have been associated to the difference in measurement locations of PNSD and $PM_{2.5}$. The studies concluded that there is a minimum PN associated with $PM_{2.5}$ loading for the clean and rural sites and the increase in PN is no longer proportional to $PM_{2.5}$ for more polluted sites (urban and traffic sites) (de Jesus et al., 2019). This indicates that the traffic and photo-chemically generated UFP contribution to particle mass are lower.

Table 2.1. Comparison of PNC in different areas reported around the world

Regions	Cities	Season/Time	PN Size Range (nm-μm)	PN Concentrations (#/cm³)				Reference
				Nucleation	Aitken	Accumulation	Total	
America	Rochester	14 years	10 - 6	-	-	-	4450	Presto et al., 2021
	Redwood	6 years	10 -6	-	-	-	6782	Presto et al., 2021
UK	Leicester	Spring	10 -1	2002 1455	3258 2407	1576 874	6837 4737	Hama et al., 2017
	London	A year	19-0.6	1632	3825	1437	6680	von Bismarck-Osten et al., 2013
Europe	Barcelona	winter	7-0.8	2839	3677	1233	7749	
	Madrid	Winter summer	7-0.8	991 1222	4682 3707	2218 960	7890 5889	Alonso-Blanco et al., 2018
	Copenhagen	year	6-0.7	1294	2994	984	5287	von Bismarck-Osten et al., 2013
	Leipzig	year	5-0.8	4495	3287	1632	9398	von Bismarck-Osten et al., 2013
	Helsinki	year	3 -1	3080	3099	1053	7231	von Bismarck-Osten et al., 2013
Asia	Delhi	Autumn Summer Winter	15-10	1296 821 1489	12828 9965 1761	15186 8107 17599	29355 18906 36730	Şahin et al., 2022
	Delhi	Autumn Summer Winter Spring	12-0.5	4950 1060[0 6300 12550	19000 21900 26350 23400	12800 9650 18100 11600	38000 43400 52500 49000	Gani et al., 2020
	Beijing	winter	3-0.8	5100	1300	8400	26600	Chen et al., 2017
	Wuhan	All year	15-0.6	4923	12193	4801	21917	Zhang et al., 2016
	Hong Kong	Autumn	6-0.4	5900	6700	2400	15000	Lyu et al., 2018
Antartica	Circum	summer	11-0.4	-		--	300	Tatzelt et al., 2022

Figure 2.2a shows the mean PNSD of around the world as geographical regions (included 43 country and 114 cities) from Wu and Boor (2021). Figure 2.2b and c show the average PNSD derived from hourly mean particle number and volume data measured in London, Beijing and Delhi at the urban background sites adopted from Harrison (2020) and Şahin et al. (2022). All the PNSDs were generated from particles below 1 μm. Figure 2.2a indicates that there is essential regional variability for the shape and particle count concentrations. The PNSD around America and Europe show modes at approximately 20-50 nm indicated nucleation and Aitken mode particles. However, the PNSD modes tend to skew to the right and are often dominated by Aitken at approximately 70-80 nm in east and by accumulation at above 100 nm in central, south, and southeast of Asia. Figure 2.2b and c show that the lowest concentrations are in London. The particles from Beijing are greater in both number and size while those in Delhi are far greater both in number and in volume with a much larger modal diameter close to100 nm. Compared to the particle number size distribution, the volume distribution clearly shows higher amount in Delhi. The trend in diameter may reflect different predominant emission sources or may be the result of particle growth in the atmosphere. In more polluted atmospheres, particles grow more rapidly by coagulation which de-pends upon particle number concentrations and by condensational growth largely due to atmospheric oxidation processes creating species of low volatility which condense onto existing particles causing them to grow (Harrison, 2020). The wide-range PNSD is essential for the description of inhalable particles (< 10 μm) and coarse mode of particle account and sources. Although, there are a few studies of wide-range particle characterization in Beijing (Jing et al., 2013) in Venice, Italy (Maisol et al., 2016) and in Delhi (Şahin et al., 2022), the results from Asia show that the number size distributions have one mode while the volume distributions have two peaks centred below and above 1 μm size. These indicated that the two main sources can be dominate which might be secondary aerosol depends on the sulphate, nitrate, and organics at high relative humidity in the fine mode and road dust, soil, construction activity in the coarse mode. When the data of two different studies conducted by Thamban et al. (2021) and Şahin et al. (2022) are compared, the modes in the mass size distributions of organic aerosols are very consistent with the modes in the particle volume size distribution of Delhi.

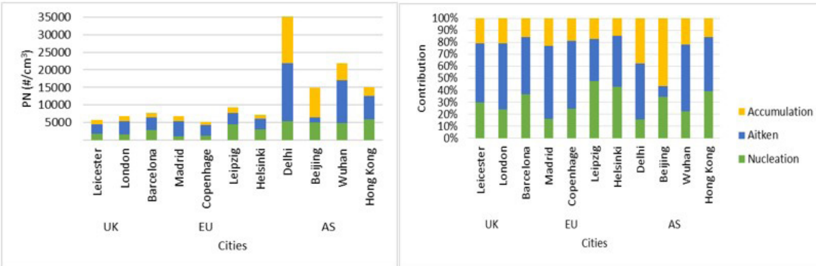

Figure 2.1. PN counts and the modes contribution to total PN measured in the cities of world.

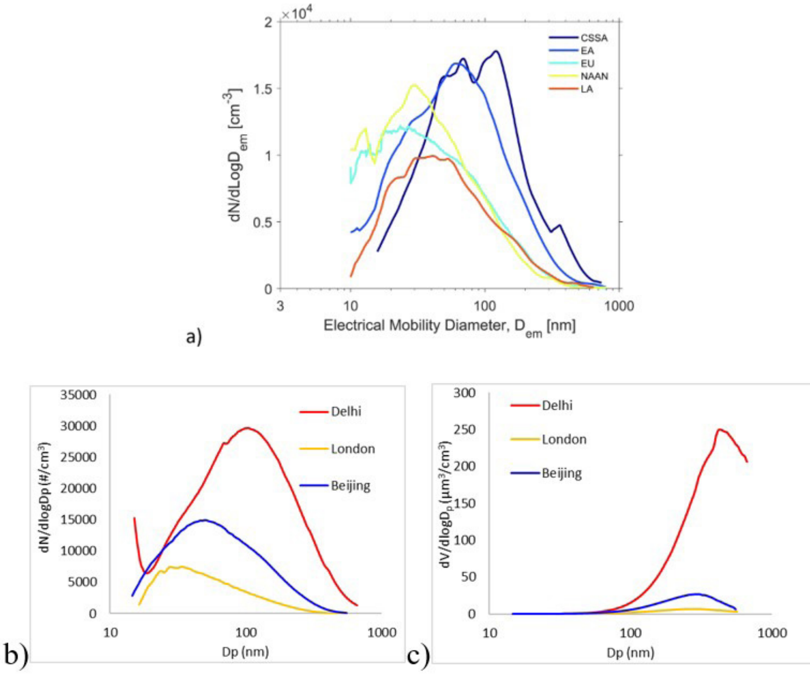

Figure 2.2. a) The average particle number size distribution around the world as geographical regions. The geographical regions include North America, Australia, and New Zealand (NAAN), Europe (EU), East Asia (EA), Central, South, and Southeast Asia (CSSA), Latin America (LA). b) and c) The average particle number and volume size distribution in London, Delhi and Beijing. (Harrison, 2020; Wu and Boor, 2021).

2.3. PARTICLE NUMBER SOURCES

PNSDs represent the source of particle counts though the peak modes of distribution (Vu et al., 2015). Nucleation mode particles can occur from the condensation of exhaust gases to sulphate and nitrate aerosols (Harrison et al., 2019). Aitken mode particles, on the other hand, are mostly composed of soot/ash cores containing adsorbed, volatile components such as poly-aromatic hydrocarbons (PAHs), carboxylic acids (Chow and Watson, 2007). Particles in the accumulation mode are formed because of fuel and oil combustion in road vehicles or by the growth of particles (Vu et al., 2015). Coarse particles are very few in the total number of particles (0.59-8 #/cm^3) and are indicative of mechanical dust formation (Şahin et al., 2022). These physical properties of particles reflect the sources and are widely used in source determining models such as Positive Matrix Factorization (PMF). General PNSD source profile and associated daytime and air pollutants are summarized in Table 2.2, which were adapted from Liang et al. (2020); Agudelo-Castañeda et al. (2019); Brines et al. (2015).

An inventory report of ultrafine particle emissions conducted within Europe and determined 75 % traffic contribution of total particle number (AQEG, 2018). Shipping and road traffic are the main contributors. Near the London airport, the nucleation contribution of particle count is calculated 44 %, followed by road and shipping traffic with 26 % (Maisol et al., 2016). On a very busy road in central London, 71.9 % of total particle number is related to the traffic (65.4 % from exhaust and 6.5 % from resuspension and brake) and the rest is from urban background (Harrison et al., 2011). Leoni et al. (2018) determined particle number sources in a European air pollution hot spot for air pollution, Ostrava in Czech Republic. Industrial and road traffic nanoparticles with 45 nm and 26 nm modes of PNSD are accounting 28 % and 24 %, respectively, following coal burning with 14 % contribution of sources. In Los Angeles, the major contributors of the total particle number concentration from 13 nm to 10 µm sizes were found traffic and nucleation with 60 % and 17 %, respectively (Sowlat et al., 2016). Similarly, the study conducted by Yue et al. (2008) in Erfurth, German show that ultrafine particles are mainly due to vehicle emissions and exhibit a high correlation with NOx and CO. The study by Rivas et al. (2020) in four cities in Europe found that traffic emissions are the main contributor in all stations, with a potential maximum contribution ranging from 71 to 94% of PNSD. The study also pointed out that the high level of solar radiation like in Barcelona can be separated the photo nucleation factor by PMF analyses and the contribution of nucleation is higher than other cities: London, Helsinki, Zurich. The main two contributors of particle numbers at the urban areas of Beijing have been detected as traffic with 47.9 % and 44 % and combustion with 29.7 % and 32 % by Liu et al. (2014) and Cai et al. (2020), respectively.

Zhu et al. (2022) investigated the major sources of particle counts in different cities around the world during 1997–2020. Hopke et al. (2022) searched the literature for source apportionment of PNSD. Figure 2.3 shows the contribution of traffic and nucleation at all urban background sites data from the supplementary of Hopke et al. (2022) study. According to present knowledge, there is not any source apportionment study based on PNSD around Asia and Africa. The studies mostly in Europe show that traffic is the dominant source of particle counts around the world cities at the urban background sites. In addition, although the second dominant source in Europe is the combustion and nucleation process, in Asia is biomass burning and cooking.

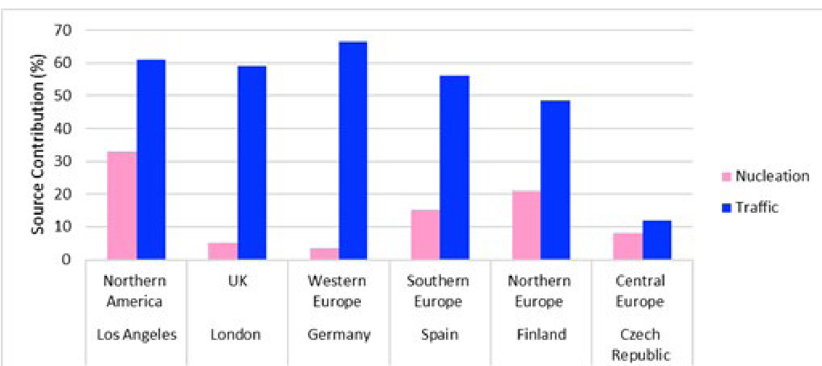

Figure 2.3. Nucleation and Traffic Source Contribution of PNSD at the urban back-ground area around the world. The data from Hopke et al. (2022).

Table 2.2. General PNSD Source profile and associated daytime and air pollutants.

Peak PN Sizes-Modes (nm)	Sources	Associated Pollutants	Daytime / Season
<20	Nucleation, NPF	O_3	-Midday, summer -Diurnal NPF and Growth -Growth of nucleated or other urban particles
30-50	Fresh Traffic	NO, BC	Rush Hours (morning and evening)
30-100	Aged Traffic	NO_2	Rush Hours (morning and evening)
50-100	Regional and Urban Background	NO_2, BC	Nighttime
100-200	Heating (coal)	SO_2	Nighttime, winter
>200 (or 300)	Regional accumulation/secondary	$PM_{2.5}$	Nighttime

2.4. CONCLUSION

According to the given knowledge of the studies published, there is poor correlation between PN and $PM_{2.5}$. Furthermore, the long-term trend of PM_{10} and $PM_{2.5}$ show the decreasing trend however the UFP especially nucleation mode particle has been in-creasing slightly. Around the world, traffic is the main source of particle number concentration. However, the contribution of traffic to the number of nanoparticles can reach up to 70 % in Europe and America, while it is around 50 % in Asia. The second most important source of atmospheric particle number is nucleation processes in Europe, whereas combustion in Asia. There appear to be some differences, such as the role of photo nucleation being more dominant in cities with high sunlight. It is observed that the most widespread PNSD and source apportionment studies have been con ducted in the America and

Europe, but not enough studies have been conducted in Asia, Australia, and Africa. The studies are clearly representing that the regional air pollution control strategies should be planned differ and necessary to focus on deter-mining the size distribution and sources of nanoparticle counts. Moreover, determining the UFP concentrations for all regions of word is essential to be used as input parameters in future epidemiological studies to adverse health effects as well as by policymakers to set targeted and more protective emissions standards.

Author Contributions: Ü.A.Ş conceived, designed, prepared the study.

Funding and Acknowledgement: We gratefully acknowledge the Scientific and Technical Re-search Council of Türkiye (TUBITAK) for financially supporting this study with project no. 122Y079 and grant no. 1059B191801445.

Data Availability Statement: The author will provide it on request.

Conflicts of Interest: The authors declare no conflict of interest.

REFERENCES

Alonso-Blanco, E., Gómez-Moreno, F.J., Artíñano, B., Iglesias-Samitier, S., Juncal-Bello, V., Piñeiro-Iglesias, M., López-Mahía, P., Pérez, N., Brines, M., Alastuey, A., García, M.I., Rodríguez, S., Sorribas, M., del Águila, A., Titos, G., Lyamani, H., Alados-Arboledas, L. (2018), Temporal and spatial variability of atmospheric particle number size distributions across Spain, Atmospheric Environment, 190, 146-160.

Agudelo-Castañeda, D.M., Teixeira, E.C., Braga, M., Rolim, S.B.A., Silva, L.F.O., Beddows, D.C.S., Harrison, R.M., Querol, X., (2019), Cluster analysis of urban ultrafine particles size distributions, Atmospheric Pollution Research, 10, 1, 45-52.

Asmi, A., Wiedensohler, A., Laj, P., Fjæraa, A. M., Sellegri, K., Birmili, W., ... & Putaud, J. P. (2011), Number size distributions and seasonality of submicron particles in Europe 2008-2009, Atmos. Chem. Phys., 11, 5505–5538.

Beddows, D. C., & Harrison, R. M. (2008), Comparison of average particle number emission factors for heavy and light duty vehicles derived from rolling chassis dynamometer and field studies. Atmospheric Environment, 42(34), 7954-7966.

Brines, M., Dall'Osto, M., Beddows, D.C.S., Harrison, R.M., Gómez-Moreno, F., Núñez, L., Artíñano, B., Costabile, F., Gobbi, G.P., Salimi, F., Morawska, L., Sioutas, C., Querol, X. (2015), Traffic and nucleation events as main sources of ultrafine particles in high insolation developed world cities. Atmos. Chem. Phys. 15, 5929–5945.

Chen, X., Wang, Z., Li, J., Chen, H., Hu, M., Yang, W., Wang, Z., Ge, B., Wang, D. (2017), Explaining the spatiotemporal variation of fine particle number concentrations over Beijing and surrounding areas in an air quality model with aerosol microphysics, Environmental Pollution, 231, 2, 1302-1313.

Chow, J. C., & Watson, J. G. (2007). Review of measurement methods and compositions for ultrafine particles. Aerosol and Air Quality Research, 7(2), 121-173.

Dall'Osto, M., Beddows, D. C., Tunved, P., Harrison, R. M., Lupi, A., Vitale, V., ... & Massling, A. (2019). Simultaneous measurements of aerosol size distributions at three sites in the European high Arctic. Atmospheric Chemistry and Physics, 19(11), 7377-7395.

de Jesus, A.L., Thompson, H., Knibbs, L.D., Kowalski, ., Cyrys, J., Niemi, J.V., Kousa, A., Timonen, H., Luoma, K., Petäjä, T., Beddows, D., Harrison, R.M., Hopke, P., Morawska, L. (2020), Long-term trends in PM2.5 mass and particle number concentrations in urban air: The impacts of mitigation measures and extreme events due to changing climates, Environmental Pollution, 263, Part A, 114500.

Gani S., Bhandari, S., Patel, K., Seraj, S., Soni, P., Arub, Z., Habib, G., Ruiz, L.H. and Apte, J.S. (2020). Particle number concentrations and size distribution in a polluted megacity: the Delhi Aerosol Supersite study, Atmos. Chem. Phys., 20, 8533–8549.

Hama, S.M.L., Cordell, R.L., Kos, G. P.A., Weijers, E.P., Monks, P.S. (2017), Sub-micron particle number size distribution characteristics at two urban locations in Leicester, Atmospheric Research, 194, 2017, 1-16.

Harrison RM. (2020), Airborne particulate matter. Phil. Trans.R. Soc.A378: 20190319. http://dx.doi.org/10.1098/rsta.2019.0319

Harrison, R. M., Shi, J. P., Xi, S., Khan, A., Mark, D., Kinnersley, R., & Yin, J. (2000). Measurement of number, mass and size distribution of particles in the atmosphere. Philosophical Transactions of the Royal Society of London. Series A: Mathematical, Physical and Engineering Sciences, 358(1775), 2567-2580.

Harrison, R. M., Rob MacKenzie, A., Xu, H., Alam, M. S., Nikolova, I., Zhong, J., ... & Liang, Z. (2018). Diesel exhaust nanoparticles and their behaviour in the atmosphere. Proceedings of the Royal Society A, 474(2220), 20180492.

Harrison, R. M., Beddows, D., Alam, M. S., Singh, A., Brean, J., Xu, R., ... & Grimmond, S. (2019). Interpretation of particle number size distributions measured across an urban area during the FASTER campaign. Atmospheric Chemistry and Physics, 19(1), 39-55.

Herenz, P., Wex, H., Mangold, A., Laffineur, Q., Gorodetskaya, I. V., Fleming, Z. L., Panagi, M., and Stratmann, F. (2019), CCN measurements at the Princess Elisabeth Antarctica research station during three austral summers, Atmos. Chem. Phys., 19, 275–294.

Knibbs, L.D., de Dear, R.J., Morawska, L., Mengersen, K.L, (2009), On-road ultrafine particle concentration in the M5 East road tunnel, Sydney, Australia, Atmospheric Environment, 43, 22–23, 2009, 3510-3519.

Kumar, P., Morawska, L., Birmili, W., Paasonen, P., Hu, M., Kulmala, M., Harrison, R.M., Norford, L., Britter, R. (2014), Ultrafine particles in cities. Environ. Int. 66, 1–10.

Liang, C.S., Wu, H., Li, H-Y., Zhang, Q., Li, Z., He, K-B. (2020), Efficient data preprocessing, episode classification, and source apportionment of particle number concentrations, Science of The Total Environment, 744, 140923.

Lyu, X.P., Guo, H., Cheng, H.R., Wang, D.W. (2018), New particle formation and growth at a suburban site and a background site in Hong Kong, Chemosphere, 193, 664-674.

Masiol, M., Vu, T. V., Beddows, D. C., & Harrison, R. M. (2016). Source apportionment of wide range particle size spectra and black carbon collected at the airport of Venice (Italy). Atmospheric Environment, 139, 56-74.

Tatzelt, C., Henning, S. Welti, A., Baccarini, A., Hartmann, M., Gysel-Beer, M., van Pinxteren, M., Modini, R.L., Schmale, J., Stratmann, F. (2022), Circum-Antarctic abundance and properties of CCN and INPs, Atmos. Chem. Phys., 22, 9721–9745.

Rivas, I., Vicens, L., Basagaña, X., Querol, X., Hüglin, C., Katsouyanni, K., ... & Kelly, F. (2019). Association between sources of ultrafine particles and mortality in four European Cities. Environmental Epidemiology, 3, 334-335.

Stacey, B., Harrison, R. M., & Pope, F. (2020). Evaluation of ultrafine particle concentrations and size distributions at London Heathrow Airport. Atmospheric Environment, 222, 117148.

Şahin, Ü. A., Harrison, R. M., Alam, M. S., Beddows, D. C. S., Bousiotis, D., Shi, Z., Crilley, L. R., Bloss, W., Brean, J., Khanna, I., and Verma, R. (2022) Measurement Report: Interpretation of Wide Range Particulate Matter Size Distributions in Delhi, Atmos. Chem. Phys., 22, 5415-5433.

Van Dingenen, R., Raes, F., Putaud, J. P., Baltensperger, U., Charron, A., Facchini, M. C., ... & Harrison, R. M. (2004). A European aerosol phenomenology—1: physical characteristics of particulate matter at kerbside, urban, rural and background sites in Europe. Atmospheric Environment, 38(16), 2561-2577.

von Bismarck-Osten, C., Birmili, W., Ketzel, M., Massling, A., Petäjä, T., Weber, S. (2013), Characterization of parameters influencing the spatio-temporal variability of urban particle number size distributions in four European cities, Atmospheric Environment, 77, 2013, 415-429,

Vu, T. V., Delgado-Saborit, J. M., & Harrison, R. M. (2015). Particle number size distributions from seven major sources and implications for source apportionment studies. Atmospheric Environment, 122, 114-132.

Wu, T. and Boor, B. E. (2021), Urban aerosol size distributions: a global perspective, Atmos. Chem. Phys., 21, 8883–8914.

Zeraati-Rezaei, S., Alam, M. S., Xu, H., Beddows, D. C., & Harrison, R. M. (2020). Size-resolved physico-chemical characterization of diesel exhaust particles and efficiency of exhaust after treatment. Atmospheric Environment, 222, 117021.

Zhang, T.; Zhu, Z.; Gong, W.; Xiang, H.; Fang, R. (2016), Characteristics of Fine Particles in an Urban Atmosphere—Relationships with Meteorological Parameters and Trace Gases. Int. J. Environ. Res. Public Health 2016, 13, 807.

Zhu,Y., Sulaymon, I.D., Xie, X., Mao, J., Guo, S., Hu, M., Hu, J. (2022), Airborne particle number concentrations in China: A critical review, Environmental Pollution, 307, 2022, 119470.

CHAPTER 3

NON-STATIONARY INVESTIGATION OF EXTREME TEMPERATURE WITH RESPECT TO SOIL MOISTURE AS A COVARIATE

Sedigheh ANVARI

Graduate University of Advanced Technology, Iran
Institute of Science and High Technology
and Environmental Science
Department of Ecology

Mahnoosh MOGHADDASI

Arak University, Iran
Faculty of Agriculture and Environment
Department of Water Science and Engineering

Abstract

An increase of extreme temperatures during the last two decades have been observed all over Iran, with recent studies detecting positive trends in extreme temperature. This study aims to analyse the stationary (S) and non-stationary (NS) behaviour of the annual maximum temperatures (AMT) in an arid province of Iran, Kerman, during the periods of 1979-2019. Trend, homogeneity and stationarity tests were applied to define the basic characterization of the AMTs. The frequency analyse of the AMTs were carried out using Generalized Extreme Value (GEV) under two assumptions of S-GEV and NS-GEV function and the distribution parameters were estimated using maximum likelihood estimator (MLE). In addition to time-varying NS-GEV investigations, the soil moisture (SM) was also employed as the covariate. Our findings revealed that in comparison with the S-GEV case, the NS-GEV frequency analyses have increasing effects on return values of the AMTs. The NS-GEV estimations of 50-year return levels were detected to be significantly higher than in the S-GEV. The NS-GEV frequency analysis of AMTs with SM as the covariate resulted in a better values of evaluation criteria than time-varying NS-GEV.

Keywords: *Extreme temperature, non-stationary, frequency analysis, time-varying, soil moisture, Iran.*

3.1. INTRODUCTION

The extreme value analysis (EVA) is generally performed using either annual maximum series (AMS), also called block maxima (BM), or the peaks-over-threshold (POT) approach. The generalized extreme value (GEV) and generalized Pareto distribution (GPD) are used as probability distributions for values selected with AMS and POT methods, respectively (Katz et al., 2002; Hawkes et al., 2008; AghaKouchak & Nasrollahi, 2010; Li et al., 2015). The EVA can be performed under both stationary (S) and non-stationary (NS) assumptions. In this regard, Maximum likelihood estimation (MLE) is the simplest and the most applicable method for EVA studies (Coles 2001; Katz et al., 2002; Katz, 2010; Vanem, 2015; Razmi et al., 2017).

Moreover, for the NS conditions of hydroclimate extremes, the trend component can be included in the GEV parameters (location, scale, and shape) as a function of time (linear, exponential, or quadratic) or other covariates. Soil moisture (SM) and near-surface temperature variations are some covariates that link the land-atmosphere interactions with extreme temperature (Miralles et al., 2014; Hao et al., 2017; Ganeshi et al., 2020).

Regarding the NS extreme temperature issues, Ganeshi et al. (2020) fitted the NS-GEV model to the extreme temperature of north-central India (NCI) to assess the impact of long-term soil moisture changes in the 1948–2014 period. Aksu (2021) estimated the return levels of absolute extreme temperatures in 50 stations in Turkey. Time, teleconnection patterns of AO, and NAO covariates were considered as the possible trend drivers.

During the last two decades, Middle Eastern countries, including Iran, have experienced a positive trend in extreme temperature (Zamani & Berndtsson, 2018; Babaeian et al., 2019). For example, Moghaddasi et al. (2022) compared EVT methods, including block maxima (BM) and peaks-over-threshold (POT), to analysis the NS behavior of maximum monthly temperature in Arak plain of Iran over the 1901–2016 years. However, such these investigations for Kerman proving, as our case of interest, have not been carried out.

Accordingly, in this study, the behavior of extreme temperature in south-eastern of Iran (having an arid climate condition) investigated using S-GEV and NS-GEV distribution functions. The NS-GEV models were applied with the covariant of time and SM. Subsequently, the return levels were estimated and the regional variation was analyzed.

3.2. STUDY AREA AND DATASETS

Iran is situated in West Asia spanning an area of 1,648,195 km^2. It is the fourth-largest country in Asia and lies between latitudes 24–40° N and longitudes 43–62° E. The change in topography is significant in short distances, with a mean elevation of 5,137 m above sea level. Different climates are dominant across the country. For example, in the central provinces like Kerman, winters are mild and the summers are very hot, with average daily temperatures in July exceeding 38°C. According to Figure 3.1, the Kerman province having an arid climatic zone along with its 12 weather stations were chosen as the case study. Based on temperature analysis in these stations, it was concluded that all stations have recorded higher increasing trends (Table 3.1). The research datasets included the following:

- Climate Research Unit (CRU): For whole 12 stations in Kerman province, the CRU monthly climate variables from 1979 to 2019 with a 0.5-degree spatial resolution were downloaded. These data were then interpolated using Inverse Distance Weighted (IDW). (New et al., 1999; Mitchell & Jones, 2005). The CRU datasets were compared with observational point-based data measured in the selected stations. The statistical indices based on normalized root mean square error (NRMSE), mean bias error (MBE), and coefficient of determination (R2) criteria revealed that the accuracy of these CRU data is reliable.

- ERA5 gridded datasets: the soil moisture gridded datasets (m^3/m^3) were extracted from ERA5 with the resolution 0.125*0.125 on a monthly time-scale during the 1979–2019 period for the selected stations. The ERA5 is the fifth generation ECMWF atmospheric reanalysis of the global climate covering the period from January 1950 to present. ERA5 is produced by the Copernicus Climate Change Service (C3S) at ECMWF (Hersbach et al., 2018; Hersbach et al., 2020).

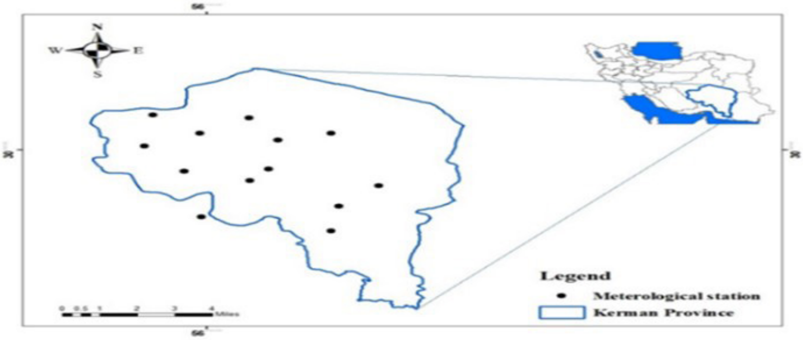

Figure 3.1. Geographic location of selected stations in Kerman province, Iran

Table 3.1. Summary statistics and quantiles of the CRU data for the selected stations

Statistics	Baft	Rafsanjan	Kerman	Sirjan	Shahrbabak	Zarand	Kahnoj	Bam	Jiroft	Shahdad	Anar
Num. data	41	41	41	41	41	41	41	41	41	41	41
Mean	38.37	37.73	35.53	36.04	35.94	36.83	38.60	38.37	34.59	38.41	37.84
St. deviation	0.82	0.95	0.91	0.84	0.88	0.96	0.76	0.82	0.91	0.93	0.93
Skewness	-0.05	-0.03	-0.10	-0.02	-0.03	-0.04	-0.08	-0.05	-0.20	-0.16	-0.15
Kurtosis	-0.67	-0.66	-0.60	-0.90	-0.90	-0.49	-0.26	-0.67	-0.78	-0.99	-0.83
10%quantile	37.5	36.4	34.4	34.9	34.7	35.6	37.5	37.5	33.3	37.2	36.5
25%quantile	37.7	36.9	34.7	35.2	35.2	36.1	38.1	37.7	34.0	37.7	37.1
50%quantile	38.3	37.9	35.7	36.1	36.1	37.0	38.6	38.3	34.8	38.6	38.0
75%quantile	39.0	38.3	36.2	36.6	36.5	37.5	39.1	39.0	35.2	39.1	38.4
90%quantile	39.4	38.9	36.6	37.0	37.0	37.9	39.5	39.4	35.7	39.6	39.0

3.3. METHODOLOGY

The adopted methodology includes the following steps: (1) the required data including station-based observations, CRU, and ERA5 were extracted for all 12 stations in the case study. In this step, the non-parametric Mann-Kendall trend, Augmented Dickey-Fuller (ADF), and Pettit's tests were respectively used for trend, stationary, and change-point detection of the AMT. (2) The S-GEV and NS-GEV extreme value analysis was performed using the MLE method. In addition to time-varying NS-GEV investigations, soil moisture (SM) was also employed as the covariate. (3) Finally, the frequency analysis was performed to calculate the temperature values in different return periods.

3.4. GENERALIZED EXTREME VALUE (GEV)

The GEV distribution is derived from the EVT and has been used to model hydroclimatic extremes (Katz, 2010). The GEV distribution (Eq.1) includes three distribution parameters (1) the location parameter (μ) specifies the center of the distribution; (2) the scale parameter (σ) determines the size of deviations around the location parameter; and (3) the shape parameter (ξ) governs the tail behavior of the GEV distribution (Coles et al., 2001; Delgado el al., 2010).

$$f(x) = p(X \le x) = H(x; \boldsymbol{\xi}, \sigma, \mu) = \begin{cases} \exp(-\left(1 - \frac{\boldsymbol{\xi}}{\sigma}(x-\mu)\right)^{1/\xi}) & \boldsymbol{\xi} \neq 0 \\ e^{\frac{x-\mu}{\sigma}} & \boldsymbol{\xi} = 0 \end{cases} \tag{3.1}$$

$$F(x) = 1 - \frac{1}{T} \tag{3.2}$$

The Maximum Likelihood Estimation (MLE): MLE is widely used for fitting conceptual models and estimating PDF (probability density function) parameters (Efron, 1982). The likelihood is expressed as follows:

$$L(\theta) = \prod_{t=1}^{n} g(Y_t|\theta)_+ \tag{3.3}$$

where g is the probability density function of variable Yt, n is the number of observations and θ indicates the set of the parameters with trend (that could be μt , σt and ξt). The plus sign (+) subscript indicates that the argument should be positive (Obeysekera and Salas 2014). The MLE of θ is the value of θ that maximizes l(θ).

3.5. TIME-VARYING NS-GEV AND NS-GEV WITH SOIL MOISTURE COVARIATE

The time-varying parameters in NS-GEV distribution could be modeled as the function of covariates such as time or other physical drivers like SM (Cheng et al., 2014; Moghaddasi et al., 2022). The time-varying GEV distribution under the NS assumption is according to Eq. 4. To investigate the relation between annual extreme temperatures (AMTs) and SM series, we derived the antecedent SM during summer (May-June-July), known as SM-MJJ, and evaluated its relationship with the AMTs in the summer season (June-July–Aguste/ JJA). The NS-GEV equation with SM as the covariate can be written as Eq.5.

$$\mu(t) = \mu_0 + \mu_1 t \tag{3.4}$$

$$\mu(SM) = \mu_0 + \mu_1 SM \tag{3.5}$$

where μ0 and μ1 are the S- and NS-location parameters, respectively. Finally, to compare the goodness of the fitted distributions, the akaike information criterion (AIC) was imployed (Akaike 1974).

3.6. RESULTS AND DISCUSSION

3.6.1. Trend, Homogeneity and Stationary Frequency Analysis of AMTs

The significance of the trend through all stations in Kerman province was investigated using the Mann–Kendall test at the 5% significance level. Since the p-value was smaller than the (5%) significance level in all stations, it is concluded that the null hypothesis (no trend) should be rejected and the alternative hypothesis was therefore accepted. The homogeneity of AMTs was also assessed using Pettit's test. The results showed that all stations were non-homogeneous. In our case, most of the breaks were detected in the middle of the extreme temperature series.

After confirmation of the trend existence in data, Augmented Dickey–Fuller (ADF) (Said and Dickey 1984) and Kwiatkowski–Phillips–Schmidt–Shin (KPSS) tests were employed to check data stationarity. The results of ADF showed the time series of AMTs were non-stationary in all selected stations. For instance, in the Kerman station, the ADF statistic was obtained at -2.075, i.e., lower than the critical value (-3.401). The p-value was greater than the (5%) significance level, and so it is concluded that the null hypothesis of the non-stationary state should be accepted.

In the following, the standard S-GEV model was fitted based on the MLE method to the AMTs for both Kerman and Bam stations, as examples (Figure 3.2 and 3.3). The first graph in these figures is Q-Q probability plot that fits the GEV distribution to AMTs. The GEV theoretical distribution with one obtained from the empirical distribution is also illustrated in these figures that they have a good agreement to each other. The last one is known as the return level plot that relates the return level of AMTs to reture period. This plot is an effective tool to graphically observe the return levels.

As shown in these figures, for the 50-year return level, the S-GEV model resulted in extreme temperature equaling 39.86°C and 37.27°C with a 95% confidence interval of [39.46–40.26] and [36.83–37.69], for Bam and Kerman stations, respectively. The AIC indice for stationary assumptions were equal to 309.09 and 317.43, respectively. The results showed that all the mentioned stations have a non-stationary trend. This issue was also confirmed by Moghaddasi et al., (2022) for another region of Iran dominated by an arid climate zone. Aksu (2021) also approved that over the fifty stations extrated from seven geographical regions of Turkey, more than half of the absolute annual maximum time series (26/50) showed a non-stationary positive trend.

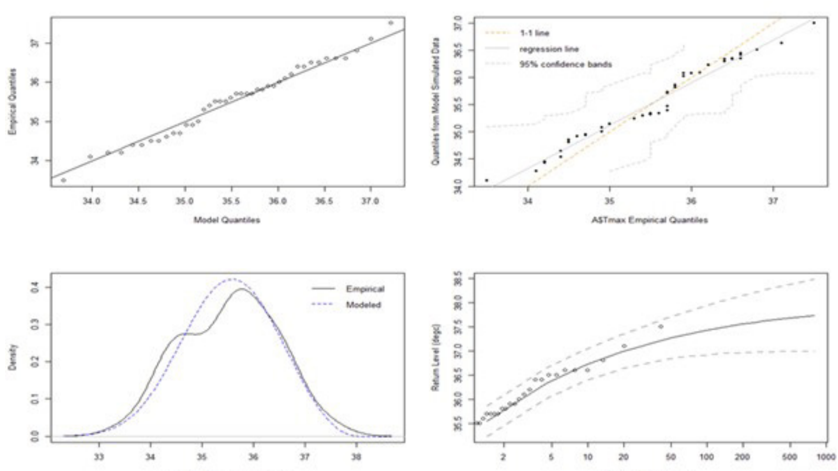

Figure 3.2. The return level against returen period for Kerman station

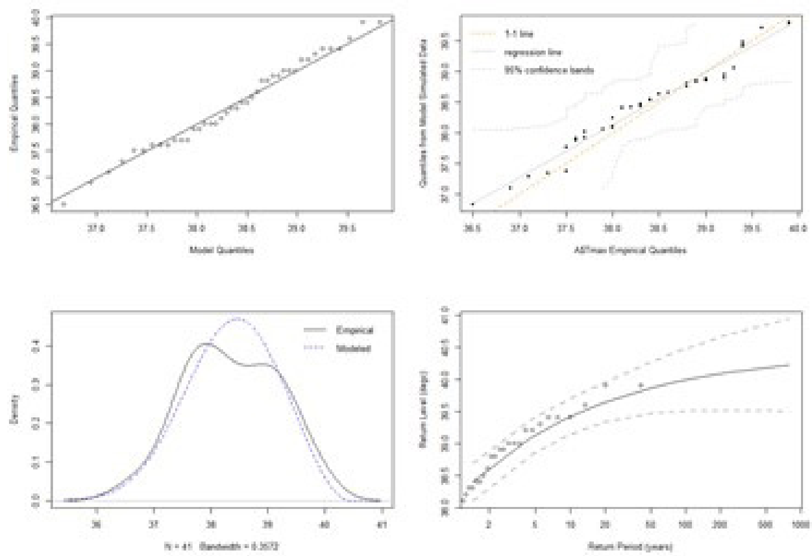

Figure 3.3. The return level against returen period for Bam station

3.6.2. Time-varying NS-GEV and NS-GEV with Soil Moisture Covariate

As mentioned earlier, in this section, a 41-year period (1979–2019) was considered for NS frequency analysis of AMT in relation to time (Time-varying NS-GEV) and soil moisture (NS-GEV with Soil Moisture) data, as a covariate. The AIC for S-GEV and NS-GEV were equal to 113.96 and 73.96 at Kerman station, showing a significant decrease in these indices, indicating that the NS behavior of AMT is acceptable. The AIC of other stations also confirmed this behaviour. As an example, the time-varying NS-GEV for the Kerman station resulted in the following equation:

$$\mu\,(\mathrm{t}) = 0.063 * t + 35.23 \tag{3.6}$$

In the following, the NS-GEV frequency analysis of AMT in relation to the SM variable as a covariate was considered during the 1979–2019 period. To this end, the relationship between AMT-JJA and SM-MJJ was investigated for all the selected stations at the mentioned period. For instance, a significant negative significant correlation coefficient was observed in Kerman station, equal to 0.81. This negative correlation also was compatible with those of Whan et al., (2015). For Southern-Central and Southeastern Europe, these researchers applied GEV distribution to investigate the influence of soil moisture (SM), as the covariate on extreme temperatures in summer (TXx). They identified a negative relationship between SM and TXx, where by a 100 mm decrease in model-based SM is associated with a 1.6oC increase in TXx in their case study.

Table 3.2 demonstrates the AIC criteria for three models of S-GEV, time varying NS-GEN and NS-GEN with SM as covariate at the selected stations. Regarding the NS-GEV with SM-MJJ as the covariate, the AIC was equal to 71.62 for the Kerman station, but according to Table 3.2, the AIC under SM-MJJ was mostly bigger than AIC under time-varying in other stations. In other words, the SM-MJJ as a covariate can be used only in Kerman station.

Table 3.2. The AIC criteria for three GEV models with SM as covariate at the selected stations

Station	S-GEV	NS-GEV _Time	NS-GEV _SM
Anar	114.66	72.84	106.22
Baft	99.18	59.72	91.38
Bam	105.17	71.35	71.33
kahnooj	100.43	77.32	94.93
Kerman	113.97	73.96	71.63
Lalehzar	105.16	69.42	98.37
Miandeh Jiroft	112.87	72.17	94.56
Rafsanjan	117.69	76.84	111.26
Shahdad	114.07	74.19	115.24
Sharebabak	110.68	66.76	89.91
Sirjan	106.87	58.94	96.83
Zarand	118.75	76.38	83.23

3.7. SUMMARY AND CONCLUSION

In the present study, the S-GEV and NS-GEV were fitted to AMTs extracted from extreme temperatures during 1979–2019 period at Kerman province, Iran. In addition to time-varying NS-GEV investigations, the analysis was also carried out with soil moisture (SM) as the covariate. The required AMTs were extracted from the CRU gridded data sets and SM data was collected from ERA5 (span from 1979–2019). The maximum likelihood estimator (MLE) was adopted to estimate the S-GEV and NS-GEV distribution parameters. Moreover, the akaike information criterion (AIC) was utilized to select the most appropriate probability distribution models.

Considering the Augmented Dickey-Fuller (ADF) results, it was concluded that the AMT time series was NS. This result was also confirmed by AIC criteria calculated for both S-GEV and NS-GEV assumptions. The time-varying NS-GEV frequency analyses was carried out for all 12 stations in Kerman province. As a result, the NS behavior of AMTs for the selected stations was found to be affected by the covariates of time. Also, a negative correlation was observed between AMTs and antecedent SM in the summer season (SM-MJJ) that were above 0.5 for all stations. Furthermore, The NS-GEV frequency analysis of AMTs with SM-MJJ as the covariate resulted only in better values of AIC at Kerman station.

Overall, taking into account the NS conditions due to the natural and/or anthropogenic activities, NS frequency analysis is recommended to be applied for estimating the hydrologic variables in different design periods. Our results quantified the impact of antecedent SM on subsequent extreme temperatures, recommending analyzing the role of antecedent drought in intensifying hot extremes.

REFERENCES

AghaKouchak A. and Nasrollahi, N. (2010) Semi-parametric and parametric inference of extreme value models for rainfall data. Water Resour Manag 24:1229–1249.

Akaike, H. (1974). A new look at the statistical model identification. IEEE transactions on automatic control, 19(6), 716-723.

Aksu, H. (2021). Nonstationary analysis of the extreme temperatures in Turkey. Dynamics of Atmospheres and Oceans, 95, 101238.

Babaeian, I., Karimian, M., Modirian, R. and Mirzaei, E. (2019) Future climate change projection over Iran using CMIP5 data during 2020–2100. NIVAR. Journal of Meteorological Organization, 43, 61–70.

Coles, S. (2001). An Introduction to Statistical Modeling of Extreme Values. Springer, London.

Delgado, J. M., Apel, H., and Merz, B. (2010). Flood trends and variability in the Mekong river. Hydrology and Earth System Sciences, 14, 407-418. https://doi.org/10.5194/hess-14-407-2010.

Efron, B. (1982). Maximum Likelihood and Decision Theory. The Annals of Statistics, 10(2), 340- 356.

Ganeshi, N. G., Mujumdar, M., Krishnan, R., & Goswami, M. (2020). Understanding the linkage between soil moisture variability and temperature extremes over the Indian region. Journal of Hydrology, 589, 125183.

Hao, Z., Hao, F., Singh, V. P., & Ouyang, W. (2017). Quantitative risk assessment of the effects of drought on extreme temperature in eastern China. Journal of Geophysical Research: Atmospheres, 122(17), 9050-9059.

Hawkes PJ, Gonzalez-Marco D, Sánchez-Arcilla A, Prinos P (2008) Best practice for the estimation of extremes: Areview. J Hydraul Res 46:324–332.

Hersbach, H., Bell, B., Berrisford, P., Hirahara, S., Horányi, A., Muñoz-Sabater, J. & Thépaut, J. N. (2020). The ERA5 global reanalysis. Quarterly Journal of the Royal Meteorological Society, 146(730), 1999-2049.

Hersbach, H., de Rosnay, P., Bell, B., et al., 2018. Operational global reanalysis: progress, future directions and synergies with NWP, ERA Report Series 27, ECMWF, Reading, UK.

Katz R (2010) Statistics of extremes in climate change. Climatic Change 100(1):71-76.

Katz, R. W., Parlange, M. B., & Naveau, P. (2002). Statistics of extremes in hydrology. Advances in water resources, 25(8-12), 1287-1304.

Li, L., Zhang, L., Xia, J., Gippel, C. J., Wang, R., & Zeng, S. (2015). Implications of modelled climate and land cover changes on runoff in the middle route of the south to north water transfer project in China. Water Resources Management, 29(8), 2563-2579.

Miralles, D. G., Teuling, A. J., Van Heerwaarden, C. C., & Vilà-Guerau de Arellano, J. (2014). Mega-heatwave temperatures due to combined soil desiccation and atmospheric heat accumulation. Nature geoscience, 7(5), 345-349.

Mitchell, T. D., & Jones, P. D. (2005). An improved method of constructing a database of monthly climate observations and associated high-resolution grids. International Journal of Climatology: A Journal of the Royal Meteorological Society, 25(6), 693-712.

Moghaddasi, M., Anvari, S., & Akhondi, N. (2022). A trade-off analysis of adaptive and non-adaptive future optimized rule curves based on simulation algorithm and hedging rules. Theoretical and Applied Climatology, 148(1), 65-78.

Moghaddasi, M., Anvari, S., & Mohammadi, T. (2022). Comparison of extreme value theory approaches in temperature frequency analysis (case study: Arak plain in Iran). Arabian Journal of Geosciences, 15(12), 1-13.

New, M., Hulme, M., & Jones, P. (1999). Representing twentieth-century space–time climate variability. Part I: Development of a 1961–90 mean monthly terrestrial climatology. Journal of climate, 12(3), 829-856.

Razmi, A., Golian, S., & Zahmatkesh, Z. (2017). Non-stationary frequency analysis of extreme water level: application of annual maximum series and peak-over threshold approaches. Water resources management, 31(7), 2065-2083.

Vanem, E. (2015). Non-stationary extreme value models to account for trends and shifts in the extreme wave climate due to climate change. Applied Ocean Research, 52, 201-211.

Zamani, R. and Berndtsson, R. (2018) Evaluation of CMIP5 models for west and southwest Iran using TOPSISI-based method. Theoretical and Applied Climatology, 137, 533–543.

CHAPTER 4

INVESTIGATION OF DISPERSION MODELS AND POSSIBLE HEALTH EFFECTS OF AIR POLLUTANTS EMITTED FROM AN INDUSTRIAL PLANT

Ömer Mert BAYRAKTAR

Kocaeli University, Türkiye
Faculty of Engineering
Department of Environmental Engineering

Atilla MUTLU

Balıkesir University, Türkiye
Faculty of Engineering
Department of Environmental Engineering

Abstract

Air pollution has emerged as a significant environmental challenge in the 21st century, exacerbated by the surge in population and industrial activities. Failure to mitigate air pollution poses a grave threat to both the environment and public health. Various nations have instituted regulations to curb emissions as a preventive measure. This research focuses on the comprehensive analysis of a cement plant in Balikesir, assessing the release of PM_{10} through diverse models and estimating the health risks associated with airborne heavy metals.

Meteorological models were constructed using local station data in conjunction with AERMET and satellite data employing the WRF model. The AERMOD, ADMS, and ISC3 air pollution dispersion models were employed to compute PM_{10} dispersion originating from the cement plant. The results of air dispersion and heavy metal data were integrated into the HARP model to evaluate the 70-year (lifetime) cancer, chronic, and acute risks. Correlation analyses were conducted using air quality monitoring station data to determine the model that provided the most accurate estimates for the study.

The correlation analyses revealed that the meteorological models using WRF, coupled with air quality models employing hourly ADMS and daily AERMOD, demonstrated the best fit for this investigation. Additionally, our findings indicated that the cancer risk ratio exceeded the limit stipulated by the Environmental Protection Agency (EPA).

Keywords: *Air pollution, WRF model, dispersion model, cancer, HARP.*

4.1. INTRODUCTION

It is a fact that many countries, associations and researchers have different definitions of air pollution, but in the simplest term is natural and anthropogenic emission resources mixing into the air or undesirable situations where pollutants in the external environment (dust, gas, smoke, odor, musk and aerosols) can harm living things and have a negative effect on vital activity can be called air pollution (Wang et al., 2004; Daly et al., 2007). Types of air pollutants are divided into two categories depending on the source. These are primary and secondary air pollutants. Primary air pollutants are defined as releasing directly from the source, such as sulphur oxides (SO_X), hydrogen sulphide (H_2S), nitrogen oxides (NO_X), carbon monoxide (CO), carbon dioxide (CO_2) and particular matter (PM) (Sonwani and Saxena, 2016). Secondary air pollutants are derived from primary pollutants as a result of reactions in the atmosphere, such as sulfuric acid (H_2SO_4), nitrogen dioxide (NO_2), sulphur trioxide (SO_3) and PAN (Peroxy Acetyl Nitrate). Also, beside of source type pollutant, there are inorganic pollutant sources such as ozone (O_3), NO_x, H_2S and finally heavy metals (Speight, 2017). In the analysis of the causes of air pollution, there are several factors, but they are mainly separated into natural and anthropogenic factors (Bai et al., 2018). Natural sources include volcanic eruptions, dust storms, forest fires, ocean, and marine activity, but anthropogenic sources are related to human activities such as residential heating, transportation, industrial and mining activity. The problem of air pollution increased with the industrial revolution as fossil fuels started to be used in factories (Ünal et al., 2019). From the past to present, increasing air pollution has become a non-negligible environmental and health problem in the world, such as the Great

London Smog and the Donora Disaster being the most prominent examples. In addition, one of the most serious problems the world has ever seen, severe acute respiratory syndrome coronavirus 2 (SARS-CoV-2), was found to cling to air pollutants (Bontempi, 2020; Srivastava, 2021). Many studies and reports show that millions of people die every year due to the health effects of air pollution (Schwartz, 2000; Prüss-Üstün, 2016; Landrigan, 2017; Landrigan et al., 2018; Khilnani et al., 2018). The effect of pollutant dose is destructive damage to human health like cancer, or there may occur acute and chronic risks that are less devastating than cancer (Kampa et al., 2008; Lelieveld et al., 2015; Turner et al., 2020). Predictive models are useful in many ways, including the ability to simulate a lot of work in a short period of time with near-real data. Air pollution dispersion and health effects depend on various factors. These factors can basically list meteorological, terrain and emission data. Thus, the requirements needed for data were prepared for different models, such as meteorological models; AERMET, CALMET and WRF, air quality dispersion models; AERMOD, ADMS, ISC3, WRF-Chem and CMAQ, health risk models; HARP, AirQ+ and BenMAP can be given examples. In this study, it was prepared of cement plant PM_{10} distribution with effect of health risk from heavy metals. Also, which model gives the best results when compared with the air quality monitoring station data calculated with the spearman correlation analysis.

4.2. STUDY AREA AND DATA

4.2.1. Study Area

Balikesir is the seventeenth most crowded region in Turkey, as well as this region also has the most preferred touristic place because Balikesir has the Aegean Sea coast, and the population increases when the weather warms up. The highest renewable energy from wind power in Turkey is generated in the Balikesir region. Also, Balikesir has various mine areas, such as Havran, Kepsut and Ayvalik, which are the most known in terms of mineral reserves: Gold, copper, lead, zinc, and iron. In terms of the geographic location of Balikesir, inversion is a big problem for our daily lives. Especially Altieylul and Karesi regions are dangerous to inversion, where the most known industrial regions are surrounded by high elevation. Northern winds, Mediterranean and continental climate are the climatic characteristics of the city. Balikesir region and the important places are shown in Figure 4.1 (Bayraktar, 2022).

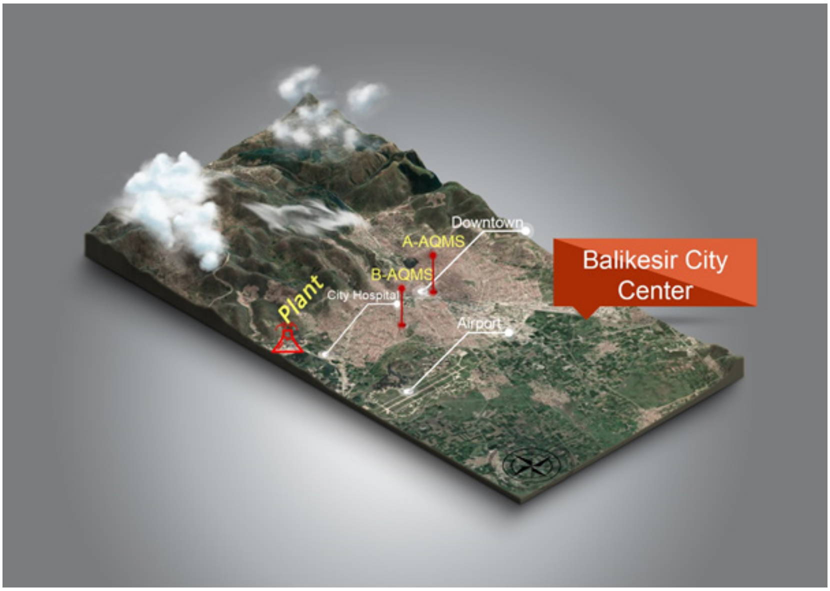

Figure 4.1. Balikesir downtown and important regions (Web-1)

4.2.2. Meteorological Data

Meteorological data, which is one of the most important data sets for air quality dispersion models, was provided by two different data sets for the used meteorological models. Firstly, the local meteorological data set was obtained from the Turkish State Meteorological Service. This data was provided from two separate stations: Surface data set from 17150 Balikesir Airport and upper air from 17064 Istanbul Region station. Surface station 4.5 km and upper air station 180 km approximately are far from the source. The other meteorological data set, GDAS data was used "0.25 Degree Global Tropospheric Analyses and Forecast Grids (ds083.3)" from NOAA. When local and NOAA data sets are compared in terms of data and property: Local data set has missing data and is far from the study area (NOAA, 2015). However, the NOAA dataset used in this study is more reliable than the local dataset because the GDAS data have a resolution of 0.25 degrees. Also, the dataset is stable and compatible with some models. In this study, all one-year 2019 data was taken from local and GDAS data. Surface station data was converted to an understandable format, and upper air station data was used in the TD6201 format for the AERMET model. GDAS data set simulation was prepared using two domains. Firstly, the purpose of the out-domain was to keep a wide study area that used much more data in the simulation, so that was convergence to real data. The inside of the second domain has a much higher grid ratio than the out-domain, so it's much closer to real data. Workspace images of the models are shown in Figure 4.2 below.

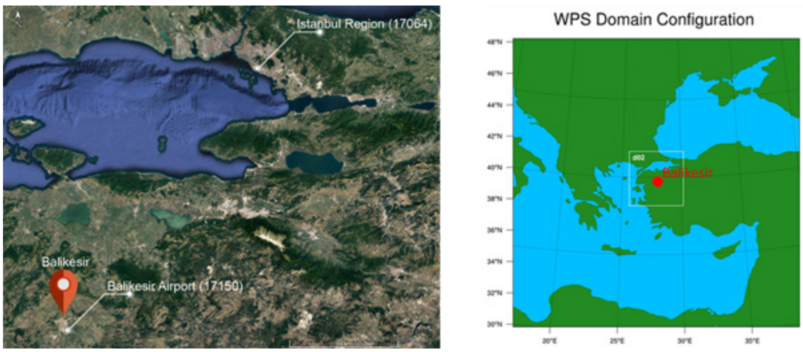

Figure 4.2. Workspace map of meteorological models (Google, 2022)

4.2.3. Pollutant Data

In this study, the pollutant PM_{10} was analysed, which was released from seven different sources. Also, these data were divided into two different pollutants, which belong to the sources of PM_{10} and heavy metal data. Firstly, air quality dispersion models were prepared with PM_{10} data, and then a health risk model was used to analysis of cancer, chronic and acute risks from the air quality dispersion models and heavy metal data. During the study period, 1-year 2019 data were used from the source. Pollutant sources of the plant are given in Table 4.1 and Table 4.2.

Table 4.1. PM_{10} Pollutants Concentration (Bayraktar, 2022)

No	Source Type	PM_{10} (kg/h)
Stack 1	Point	4.41
Stack 2	Point	0.48
Stack 3	Point	3.29
Stack 4	Point	2.21
Transporter Line	Line	1.75
Unloading Area	Area	0.56
Storage Area	Area	0.30

Table 4.2. Heavy Metal Pollutants Concentration (Bayraktar, 2022)

Heavy Metal	Stack 1 (kg/yr)	Stack 2 (kg/yr)	Stack 3 (kg/yr)	Stack 4 (kg/yr)
Antimony	14.06	-	-	1.36
Arsenic	22.23	0.91	0.45	11.79
Copper	9.98	1.81	0.45	14.97
Cadmium	-	0.91	-	0.45
Cobalt	7.71	-	0.45	2.27
Chromium	43.54	0.45	0.45	16.33
Lead	35.83	3.18	0.45	11.34
Mangan	7.71	1.81	0.91	43.09
Thallium	-	1.36	-	0.45
Vanadium	21.32	1.81	0.45	10.43

4.3. METHOD AND MODELS

In this study, the performance of the models was prepared using two different meteorological models, AERMET and WRF; air quality dispersion models, ISC3, AERMOD and ADMS; and finally, the health risk model HARP was used to calculate the dispersion of pollutants. The results from the processing of AERMET are given to surface (sfc) and profile (pfl) data that were needed for the air quality meteorological data, but WRF model outputs are more complex than AERMET. Thus, the model outputs need to be converted into an understandable format for air quality models. The Mesoscale Model Interface Program (MMIF) or WRF-Python are useful for converting these data (Web-2; Web-3). MMIF directly converts the meteorological model outputs of MM5 and WRF to AERMOD, SCICHEM and CALPUFF (EPA, 2018). All meteorological data sets were run with air quality models using PM_{10} pollutant data from the source. Also, model settings were determined at 289 (288 + Balikesir City Hospital) grid points inside the 2 km radius from the source. The model results were compared which correlation method from hourly and daily AQMS data. Hourly, daily, and yearly maps were prepared for dispersion from the source. The health risk model was used with AERMOD output and heavy metal data, but HARP model is only compatible with AERMOD so in this study, HARP model just prepared that 70 years of cancer, chronic and acute health effects were run with AERMOD results. The model flow chart for this study is given in Figure 4.3.

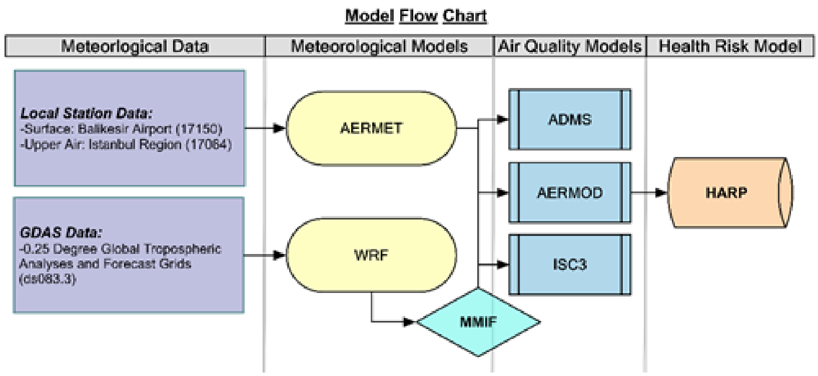

Figure 4.3. Model system flow diagram for this study

4.3.1. Meteorological Models

AERMET is part of the meteorological pre-processor of AERMOD. The main purpose of the model is to organize meteorological data for some air quality models. AERMET uses two different meteorological data sets: Surface and upper air data. As a different data set, surface data is obtained, which is the 0–2 m height from the top of the station, but upper air data is used to help with air balloons. Developed by the National Oceanic and Atmospheric Administration (NOAA), WRF is a large-scale, new-generation digital weather forecasting model that is used in many different fields, such as industrial, energy sector, hydrological, and air quality (Karadavut, 2014; Kafadar, 2015). WRF uses the compressible Euler method and can be run hydrostatically or non-hydrostatically. Thus, WRF can be separated from Advance Research WRF (ARW) and the Non-hydrostatic Mesoscale Model (NMM) (Janjic, 1997; Rogers et al., 2009). The model can also use different options, such as micro-physics, planetary boundary layer, cumulus parameterization, shortwave, and longwave options. In this study, the WRF-ARW 4.1.5 version was used with GDAS data. As shown in Figure 4.2, two domain configurations were used from the inside out: 10 km and 30 km. Also, both models were run for 1 year in 2019.

4.3.2. Air Quality Models

Three air quality models were used to analyze dispersion. ISC3 model is older than other models, and it is not used as actively as other models (Web-4). ISC3 is based on a Gaussian model that can be used for dispersion of pollutants in industrial complexes. This model can use point, area, line and volume sources with terrain features. ISC3 also uses surface and mixing height meteorological data. AERMOD has been developed by the American Meteorological Society/Environmental Protection Agency Regulatory Model (EPA, 2021). AERMOD is an enhanced version of the ISC3 short-term model. Also, AERMOD has some pre-processors, such as AERMET and AERMAP. Finally, ADMS has been developed by the Cambridge Environmental Research Consultant (CERC). ADMS is similar to the other two models, like the Gauss model, meteorological parameters and terrain features. When all models are compared to each other, they use the same model dispersion method but have different features, such as source and terrain options.

4.3.3. Health Risk Model

The HARP model is an air toxicity analysis program (CalEPA, 2015). The model has been in development since 2015 by the California Air Resources Board. Model system tools have been separated into the Emissions Inventory Module (EIM), Air Dispersion Modelling and Risk Assessment Tool (ADMRT), and Risk Assessment Standalone Tool (RAST). In this study, output of model results was prepared with ADMRT module. The ADMRT module is used to calculate AERMOD outputs, which calculate potential health effects. The module uses AERMOD model outputs to calculate potential health effects, which are cancer and non-cancer (acute and chronic) health problems (ATSDR, 2021).

Carcinogenic (CR) Eqs. (4.1) and noncarcinogenic (HQ) Eqs. (4.2) risk factors:

$$CR = IUR \ x \ EPC \ x \ EF \tag{4.1}$$

$$HQ = \frac{EPC \ x \ EF}{MRL} \tag{4.2}$$

4.4. RESULTS

In this study, results were prepared for the highest PM_{10} concentration of polar grids shown in Figure 4.4 and Figure 4.5.

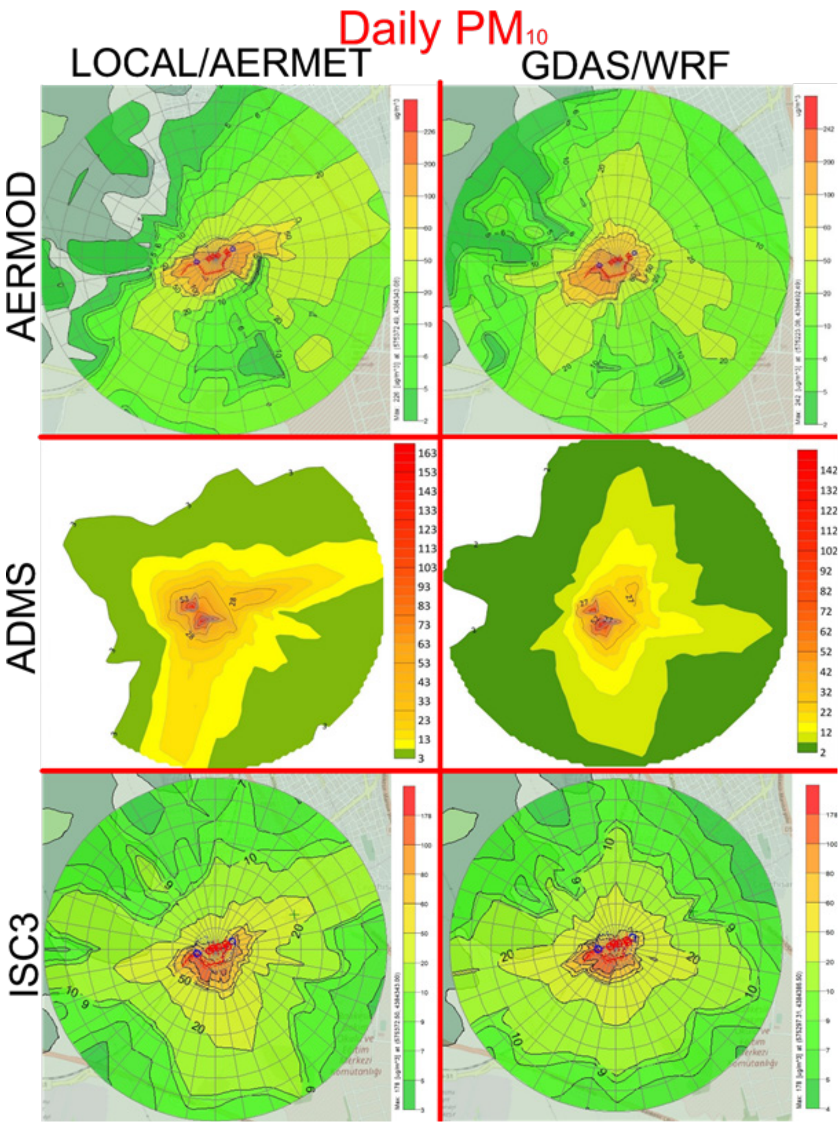

Figure 4.4. Daily PM_{10} pollutant dispersion maps

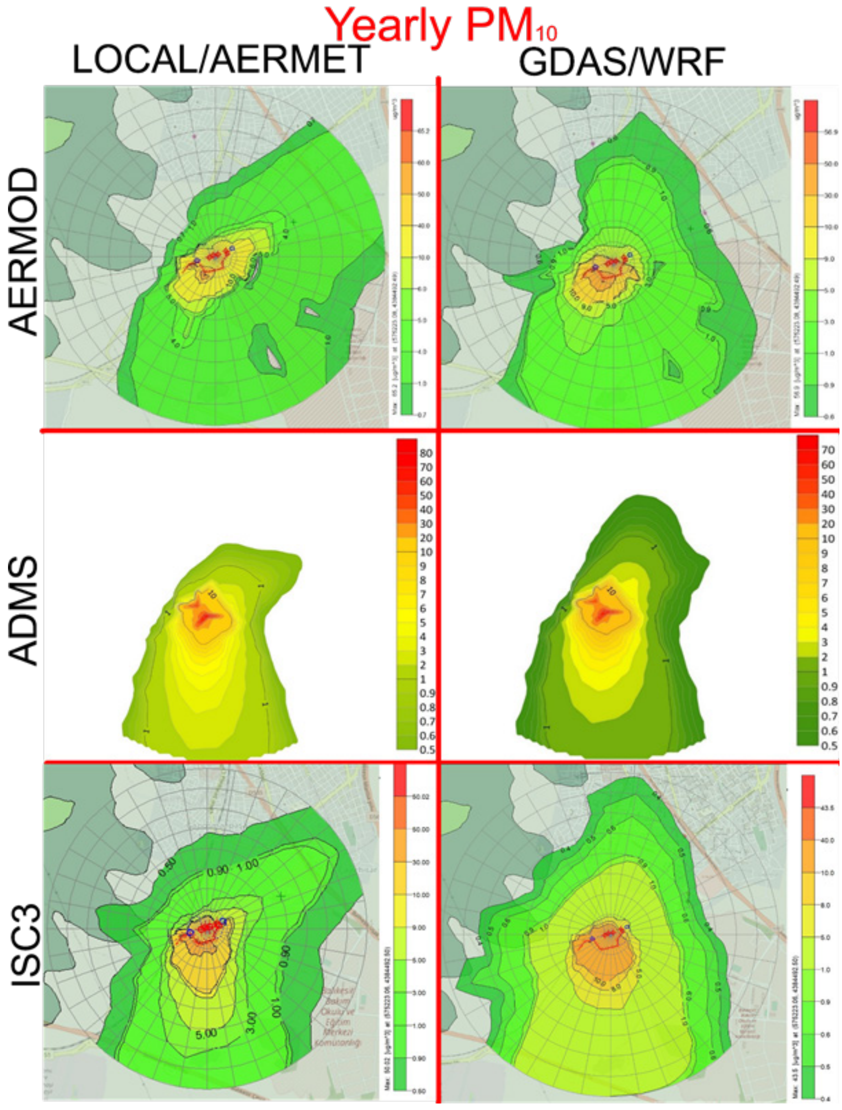

Figure 4.5. Yearly PM_{10} pollutant dispersion maps

When Figure 4.4 and Figure 4.5 are compared, the highest PM_{10} levels of grids are shown with two time periods in Table 4.3.

Table 4.3. Day and year PM_{10} pollutant values

Highest Value (**μg/m³ / time**)	**AERMET AERMOD**	**AERMET ADMS**	**AERMET ISC3**	**WRF AERMOD**	**WRF ADMS**	**WRF ISC3**
24 Hour (Day)	225.7 24.01.19	163.4 27.08.19	178.5 24.01.19	242.5 12.12.19	148.3 06.10.19	177.8 18.03.19
1 Year	65.2	80.4	50.1	56.9	70.6	43.5

Before the model performance test of this study, models were re-run just AQMS locations; the other main parameters were used with the same. Because the size of the impact area is limited to a two-kilometer radius, AQMS locations are excluded from this area. In this study, spearman correlation analysis was used with PM_{10} data from AQMS from points in locations that are shown in Figure 4.1. Correlation results are shown in Table 4.4.

Table 4.4. Hour and day correlation analysis of results

Correlation Rates	**AERMET AERMOD**	**AERMET ADMS**	**AERMET ISC3**	**WRF AERMOD**	**WRF ADMS**	**WRF ISC3**
A-AQMS (Hour)	-0.16	0.09	0.06	0.04	0.22	0.14
B-AQMS (Hour)	-0.15	0.06	0.05	-0.01	0.1	0.01
A-AQMS (Day)	0.33	-0.13	0.27	0.63	0.44	0.39
B-AQMS (Day)	0.15	0.2	0.16	0.5	0.33	0.3

The results of the HARP model outputs were compared according to the "*de minimis*" limit risk values determined by representative of the United States Environmental Protection Agency (EPA). The negligible limit risk rate by the EPA is determined as if cancer risk is one person for a million (1×10^{-6}). Non-cancer (chronic and acute) risks need to be below the rate of one value set by the EPA (EPA, 2001; Fiori and Meyerhoff, 2002; EPA, 2009). Distribution maps of health risk are given in Figure 4.6.

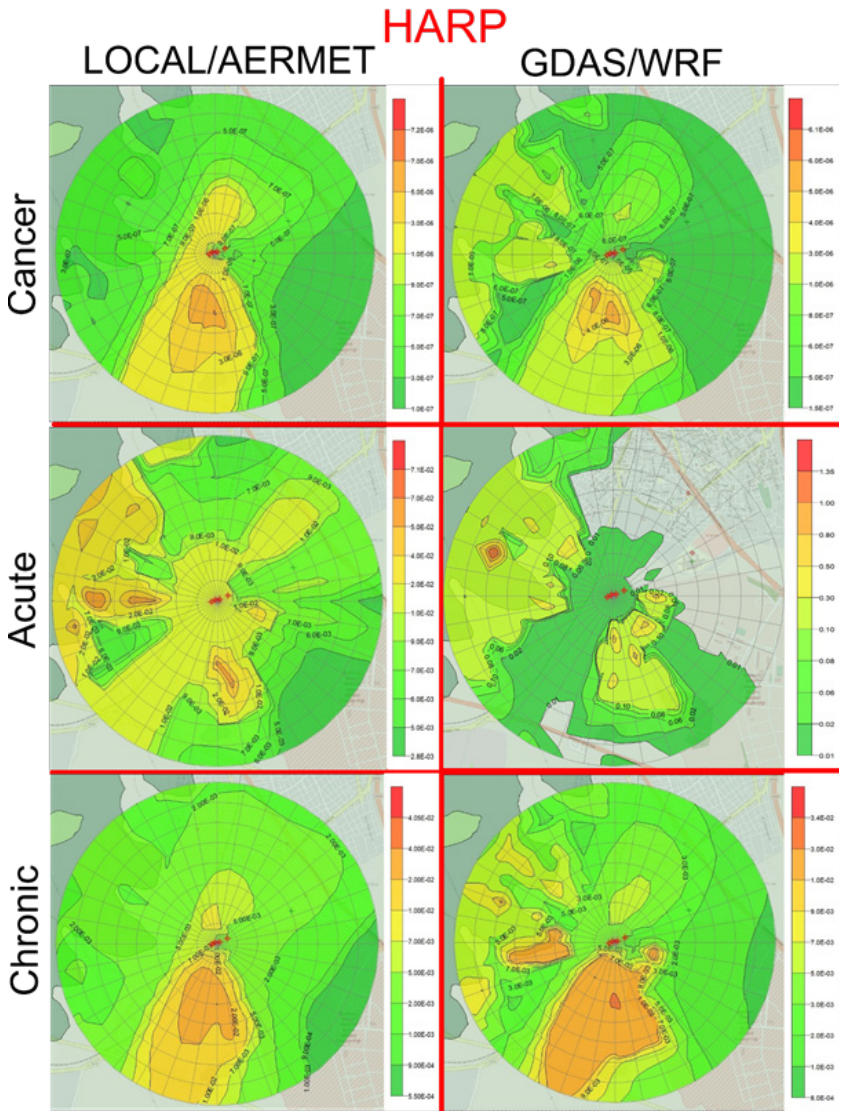

Figure 4.6. Dispersion of health risk models

Finally, Table 4.5 shows the health risk rate of cancer, acute and chronic, from 289 grid points. Also, Balikesir City Hospital is under the limit of risk. The highest cancer rates in the hospital are AERMET-AERMOD 0.59 x 10^{-6} and WRF-AERMOD 0.42 x 10^{-6}.

Table 4.5. Health risk results of HARP models

Type	Classification	AERMET AERMOD	WRF AERMOD
Cancer	Highest	7.20×10^{-6}	6.05×10^{-6}
	Mean	0.99×10^{-6}	1.07×10^{-6}
	Lowest	0.11×10^{-6}	0.15×10^{-6}
Acute	Highest	0.0707	1.3468
	Mean	0.0034	0.0698
	Lowest	0.0004	0.0054
Chronic	Highest	0.0405	0.0345
	Mean	0.0055	0.0060
	Lowest	0.0006	0.0008

4.5. CONCLUSION

It is obvious that air pollution is a non-negligible problem for all living creatures. Therefore, many different studies for preventing air pollution have been conducted from the past to present. Nowadays, improvements in technology have reached a higher level, so we could use simulation models and different methodologies. In this study, especially yearly results show that the effect of wind data is the dispersion of PM_{10} pollutant from the north to south region because Balikesir predominant wind direction is north (Mutlu and Bayraktar, 2021). The highest daily concentration was determined with the WRF-AERMOD model result, but the highest yearly concentration was determined using the AERMET-ADMS model result, and the peak date of concentration is mostly inside winter seasons. The results show that most of the local AERMET models have a higher concentration rate than the WRF model results. The main reason for this, local station data set has restricted meteorological parameters, which also show that the rate of calm conditions and missing data are higher. Therefore, air pollution dispersion has been spread close to the source location, but GDAS data is more reliable than local station data, so WRF model results are lower. When correlation analyses were performed with two AQMS, the highest correlation of the hourly timeline was found in the WRF-ADMS model, but the highest daily correlation rate was found in the WRF-AERMOD model. In general, AERMOD and ADMS have better performance than ISC3. Also, various studies have been executed that relate to these models. Hanna et al. (2001) studied the same models and found that ISC3 has poor performance than the other models. Neshuku, (2012) emphasized that mine open pit PM_{10} dispersion using two models, AERMOD and ADMS, and also that model comparison shows ADMS is better than AERMOD. Kumar (2006) studied SO_2 pollutant dispersion model with AERMOD for Ohio. When the model prediction time-line period increased, 24-hour predictions were better than 1-hour predictions. Also, the same conditions from this study are valid for the AQMS correlation. The model created from previous research was used to assess the health risks associated with both carcinogenic and noncarcinogenic sources. HARP user guide emphasized the use of diesel particulate matter measurements, which are inhalation effects from cancer and noncancer risks. Also, Donoghue and Coffey (2014) studied the inhalation of cancer, chronic and acute risks using PM_{10} pollutants from effects of heavy metals in alumina refineries. When the refinery results are examined from the EPA limit value, cancer and non-cancer health effects are negligible. In this study, both meteorological results of the cancer health risk model showed that some grids exceeded the limit risk value from the EPA, but acute and chronic limit risk rates were under the limit except for one WRF acute value. Also, air quality models yearly and health risk models are determined similarity relations between the two models.

REFERENCES

ATSDR. (2021). Guidance for Inhalation Exposure, V5. Agency for Toxic Substances and Disease Registry. https://www.atsdr.cdc.gov/pha-guidance/resources/ATSDR-EDG-Inhalation-508.pdf 08.09.2021.

Bai, Lu, et al. "Air pollution forecasts: An overview. *International journal of environmental research and public health, 15*.4 (2018): 780.

Bayraktar, Ö. M. (2022). Bir Sanayi İşletmesinden Salınan Hava Kirleticilerine Ait Dağılım Modellerinin ve Olası Halk Sağlığı Etkilerinin İncelenmesi. M.Sc. Thesis, Balikesir University, Institute of Science and Technology.

Bontempi, E. (2020). First data analysis about possible COVID-19 virus airborne diffusion due to air particulate matter (PM): the case of Lombardy (Italy). *Environmental research, 186*, 109639.

CalEPA. (2015). User manual for The Hotspots Analysis and Reporting Program Air Dispersion Modeling and Risk Assessment Tool Version 2. California Environmental Protection Agency.

Daly, A., & Zannetti, P. (2007). An introduction to air pollution–definitions, classifications, and history. *Ambient air pollution. P. Zannetti, D. Al-Ajmi and S. Al-Rashied, The Arab School for Science and Technology and The EnviroComp Institute*, 1-14.

Donoghue, A. M., & Coffey, P. S. (2014). Health risk assessments for alumina refineries. *Journal of Occupational and Environmental Medicine, 56*(5 Suppl), S18.

EPA. (2001). Risk Assessment Guidance for Superfund: Volume I Human Health Evaluation Manual (Part D, Standardized Planning, Reporting, and Review of Superfund Risk Assessments). https://www.epa.gov/sites/default/files/2018-03/documents/175137.pdf. Date of access: 25.03.2022

EPA. (2009). Risk Assessment Guidance for Superfund Volume I: Human Health Evaluation Manual (Part F, Supplemental Guidance for Inhalation Risk Assessment). https://www.epa.gov/sites/default/files/2015-09/documents/partf_200901_final.pdf. Date of access: 24.03.2022.

EPA. (2018). Guidance on the use of the Mesoscale Interface Program (MMIF) for AERMOD applications. U.S. Environmental Protection Agency. 5182-5235.

EPA. (2021). User's guide for the AMS/EPA regulatory model (AERMOD). U.S. https://gaftp.epa.gov/Air/aqmg/SCRAM/models/preferred/aermod/aermod_userguide.pdf. Date of access: 24.01.2022.

Fiori, J. M., & Meyerhoff, R. D. (2002). Extending the threshold of regulation concept: de minimis limits for carcinogens and mutagens. *Regulatory Toxicology and Pharmacology, 35*(2), 209-216.

Google (2022). Retrieved August 09, 2022, from https://www.google.com/maps/@39.6793894,27.882914,11.21z

Hanna, S. R., Egan, B. A., Purdum, J., & Wagler, J. (2001). Evaluation of the ADMS, AERMOD, and ISC 3 dispersion models with the OPTEX, Duke Forest, Kincaid, Indianapolis and Lovett field datasets. *International Journal of Environment and Pollution, 16*(1), 301-314.

Janjic, Z.I. (1997). Advection scheme for passive substances in the NCEP Eta Model. *Research Activities in Atmospheric and Oceanic Modeling, 3*, 14.

Kafadar, M. (2015). COPERT4 modeliyle hesaplanan karayolları emisyonlarının duyarlılığının İstanbul hava kalitesine etkisinin WRF/CMAQ model sistemiyle belirlenmesi. M.Sc. Thesis, Istanbul Technical University, Institute of Science and Technology.

Kampa, M., & Castanas, E. (2008). Human health effects of air pollution. *Environmental pollution, 151*(2), 362-367.

Karadavut, C. (2014). WRF ve ALARO sayısal hava tahmin modelleri için verifikasyon sonuçlarının karşılaştırılması. M.Sc. Thesis, Istanbul Technical University, Institute of Science and Technology.

Khilnani, G. C., & Tiwari, P. (2018). Air pollution in India and related adverse respiratory health effects: past, present, and future directions. *Current opinion in pulmonary medicine, 24*(2), 108-116.

Kumar, A., Dixit, S., Varadarajan, C., Vijayan, A., & Masuraha, A. (2006). Evaluation of the AERMOD dispersion model as a function of atmospheric stability for an urban area. *Environmental Progress, 25*(2), 141-151.

Landrigan, P. J. (2017). Air pollution and health. *The Lancet Public Health, 2*(1), e4-e5.

Landrigan, P. J., Fuller, R., Acosta, N. J., Adeyi, O., Arnold, R., Baldé, A. B., ... & Zhong, M. (2018). The Lancet Commission on pollution and health. *The lancet, 391*(10119), 462-512.

Lelieveld, J., Evans, J. S., Fnais, M., Giannadaki, D., & Pozzer, A. (2015). The contribution of outdoor air pollution sources to premature mortality on a global scale. *Nature, 525*(7569), 367-371.

Mutlu, A., & Bayraktar, O. M. (2021). Urban scale air quality analysis due to coal-based residential heating. *Air Quality, Atmosphere & Health, 14*(9), 1487-1503. https://doi.org/10.1007/s11869-021-01063-1.

Neshuku, M. N. (2012). C*omparison of the performance of two atmospheric dispersion models (AERMOD and ADMS) for open pit mining sources of air pollution* (Doctoral dissertation, University of Pretoria). https://doi.org/10.5065/D65Q4T4Z.

Prüss-Üstün, A., Wolf, J., Corvalán, C., Bos, R., & Neira, M. (2016). *Preventing disease through healthy environments: a global assessment of the burden of disease from environmental risks*. World Health Organization.

Rogers, E., DiMego, G., Black, T., Ek, M., Ferrier, B., Gayno, G., ... & Carley, J. (2009). The NCEP North American mesoscale modeling system: Recent changes and future plans. In Preprints, *23rd Conference on weather analysis and forecasting/19th conference on numerical weather prediction* (Vol. 2). Omaha, USA.

Schwartz, J. (2000). The distributed lag between air pollution and daily deaths. *Epidemiology*, 11(3), 320-326.

Sonwani, S., & Saxena, P. (2016). Identifying the sources of primary air pollutants and their impact on environmental health: a review. *IJETR, 6*(2), 111-130.

Speight, J. G. (2017). *Removal of Inorganic Compounds from the Environment.* Butterworth-Heinemann, (pp. 427-478). https://doi.org/10.1016/B978-0-12-849891-0.00009-6.

Srivastava, A. (2021). COVID-19 and air pollution and meteorology-an intricate relationship: A review. *Chemosphere*, 263, 128297.

Turner, M. C., Andersen, Z. J., Baccarelli, A., Diver, W. R., Gapstur, S. M., Pope III, C. A., ... & Cohen, A. (2020). Outdoor air pollution and cancer: An overview of the current evidence and public health recommendations. *CA: a cancer journal for clinicians, 70*(6), 460-479.

Ünal, Z., Dinç, U., Özen, C., & Toros, H. (2019). Air Pollution Forecasting for Ankara with Machine Learning Method. *Journal of Research in Atmospheric Science, 1*(1).

Wang, L. K., Pereira, N. C., & Hung, Y. T. (Eds.). (2004). Air pollution control engineering (Vol. 1, pp. 157-165). Totowa, NJ: Humana press, doi.org/10.1007/978-1-59259-778-9.

Web-1: https://www.3d-map-generator.com/3d-map-generator-terrain, accessed 7 August 2022.

Web-2: https://wrf-python.readthedocs.io/en/latest, accessed 30 September 2022.

Web-3: https://www.epa.gov/scram/air-quality-dispersion-modeling-related-model-support-programs#mmif, accessed 30 September 2022.

Web-4: https://www.epa.gov/scram/air-quality-dispersion-modeling-alternative-models#isc3, accessed 30 September 2022.

CHAPTER 5

DETERMINATION OF MICROPLASTICS IN RAINDROPS IN THE URBAN AREA OF ANKARA, TURKEY

Afsoun NIKRAVAN, Parisa BABAEI, Arzu MERAL, Batuhan KİBAR, Gülen GÜLLÜ

Hacettepe University, Türkiye
Faculty of Engineering
Department of Environmental Engineering

Abstract

Atmospheric transmission is one of the most prevalent ways for MPs to enter the environment. Among environmental compartments, the atmosphere is characterized as a pollution receptor and transporter. The purpose of this work is to identify microplastics in the raindrops collected in three different regions of Ankara, Turkey, as well as probable sources of supply. MPs were extracted from digested samples by floating them with saline solutions above the settled solid phase. A scanning electron microscope (SEM) was used to examine and describe the morphologies and compositions of MPs. An optical microscope and ImageJ software were used to find and count microplastics. NOAA online software and HYSPLIT v4' were used to estimate the possible source range of MPs associated with the rain sampling period. Microscopically, 274 particles were identified as MPs among the 4 rain samples. MPs concentrations varied from 57 to 86 MPs Ml^{-1}. All rain samples contained fibres, fragments, films, and spherule forms. The rain samples had the most fragments (45.62 percent of MPs), followed by films (25.18%), fibres (22.62%), and spheres (6.56%). Smaller MP particles in the rain had more variety, suggesting that the microplastics in the raindrop's samples have been broken down by long-term deposition.

Keywords: *Microplastics, raindrops, atmosphere, Ankara.*

5.1. INTRODUCTION

Plastic products are incredibly adaptable in various environments because of their low thermal and electrical conductivity, low density, and high resistance to corrosion. Plastics are produced easily and widely because of their low cost and are utilized in many important industries, including agriculture, food packing, transportation, medical uses, and technical applications (Xia et al., 2020). On the other hand, it is known that only a little fraction of these plastics gets recycles when they are disposed of, most of them are released into the environment, where they may stay for a number of years before totally disintegrating. Plastics pose a global danger to aquatic environments due to their widespread use, inappropriate disposal, and persistence. A variety of environmental factors, including solar radiation, abrasion, and interactions with various organisms, lead plastic to break down and fragment into tiny pieces known as microplastics (MPs). Microplastics, which are thought to pose a risk to human health, can be released into the environment and have previously been discovered in almost every ecosystem (Pellini et al.,2018). MPs are defined as fragments, fibres, granules, flakes, and spheres and their diameters are less than 5 mm (Jiang, 2018). Due to the limited degradability of most plastics, MPs may collect in the natural environment; thus, it is crucial to analyze and determine their presence.

In many different areas across the planet, including the atmosphere, seas, rivers, soil, freshwater, and even food, microplastics have been discovered (Bergmann et al., 2019; Materić et al., 2020; Scheurer et al., 2018; Van Cauwenberghe et al., 2015). Among environmental compartments, the atmosphere is recognized as a pollution receptor and transporter (Zhang D et al., 2020). On the other side, atmospheric winds can operate as microplastic transporters, causing long-range, in fact even global, dispersion of microplastic floating in the atmosphere. The dust storm is another mechanism for the transmission of microplastics (Abbasi and Turner, 2021). Furthermore, rain and snow enhance the accumulation of MPs on the underlying surface. In general, oceans, lakes, atmospheric winds, raindrops, snow, and dust storms are mechanisms to transport microplastics in the hydrosphere and atmosphere.

It is known that raindrops as one of the mechanisms to accumulate microplastics in the atmosphere received much less attention. This paper focuses on the identification of microplastics in raindrops in Ankara, Turkey. In addition, the shape and size of rain samples were determined. It should be noted that only a small number of studies have discovered microplastics in the atmospheric raindrops of metropolitan areas.

5.2. MATERIALS AND METHODS

5.2.1. Raindrop's Sampling

Rain samples were collected from two different points of Hacettepe University (Beytepe Campus) in 12 January and 24 February 2022 (Table 5.1). At the sampling stations, rain samples were collected during the rain scattering period (60 minutes) in customized glass deposition collectors.

Table 5.1. Descriptions and locations of rain samples

Samples Codes	Collection Date (DD/MM/YYYY)	Sampling region
SR1	12.01.2022	Close to parking and main street
SR2	12.01.2022	Less populated and sheltered area
SR3	24.02.2022	Close to parking and main street
SR4	24.02.2022	Less populated and sheltered area

To catch enough material and reduce sample loss while sampling, used a wide neck collecting bottle. The volume of water collected in the collector was then measured and transferred to a pre-sterilized amber glass container, which was kept dark and frozen until chemical analysis.

5.2.2. Trajectory Calculations

In order to identify the origin of air masses, 48-hour backward trajectories calculated by the NOAA online software and HYSPLIT v4' were used. Transparency was achieved by integrating frequency distributions of the computed trajectories at six- hour intervals at a height of 500 m above the ground.

For 48-hour periods and six-hour intervals, Ankara's HYSPLIT-derived trajectory frequencies are displayed in Figure 5.1. BSC Daily Dust Forecast, BSC-DREAM8b v2.0 model was used to generate dust Load map. According to the maps obtained, the strong wind from the southwest, along with the dust from the Saharan desert, reached the sampling point, it caused rain on January 12 and February 24, 2022.

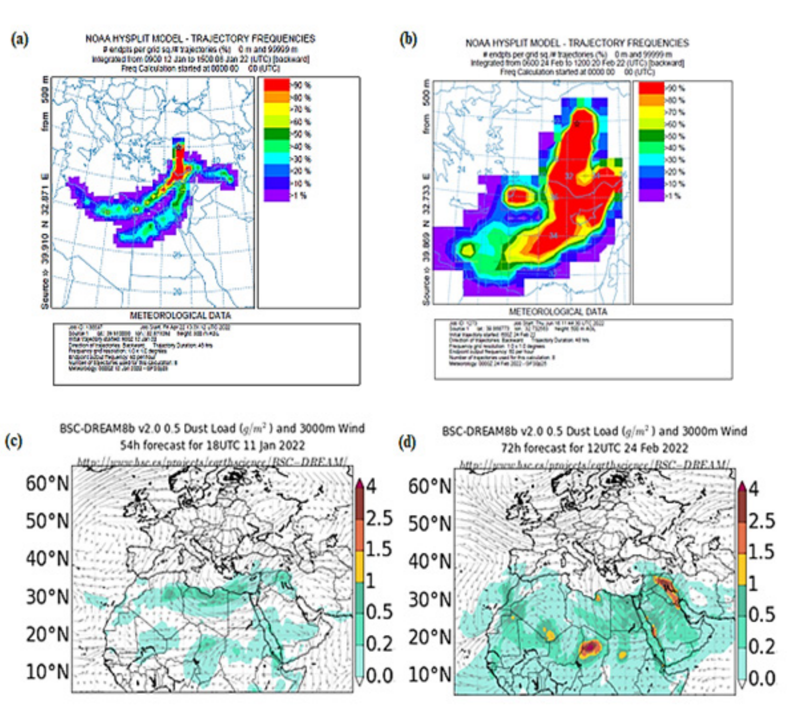

Figure 5.1. 48 hours backward trajectory frequencies estimated for Ankara using HYSPLIT for heights of 500 m (a) 12 January 2022 (b) 24 February 2022 and BSC-DREAM8b v2.0 0.5 Dust Load maps (c) Dust Load map on 12 January 2022 (d) Dust Load map on 24 February 2022

5.2.3. Microplastic Identification

Materials were processed in a clean facility using clean techniques, and microplastics were extracted using methods as in previous studies (Abbasi et al, 2022, Abbasi and Turner., 2021). MPs were isolated from digested samples by floating them in saline solutions above the settled solid phase. Before drying at room temperature in a cleanroom, rainwater samples were passed through Whatman filter paper of 45 mm diameter.

We used scanning electron microscopy plus energy-dispersive X-ray spectroscopy (SEM/EDS) analysis for screening MPs surface morphology and elemental composition. High-resolution imaging of particle surface features and indications of elemental composition were both made possible by SEM/EDS. EDS was therefore employed to screen for potential microplastics and exclude non-plastics. In this study, an optical microscope was used to determine the physical shapes of microplastics and counted by ImageJ software.

Four categories were used to categorize each microplastic particle: fibers, films, fragments, and spherule. Microplastics were evaluated in size as five groups: $L < 100$ µm, $100 \leq L < 250$ µm, $250 \leq L < 500$ µm, $500 \leq L < 1000$ µm, $1000 \leq L < 5000$ µm.

5.3. RESULTS AND DISCUSSION

5.3.1. Microplastic Distribution and Abundance

Microplastics were found in all the raindrops samples. The rain samples considered contained 274 particles in total that were microscopically recognized as MPs. When the data were normalized to precipitation volume, the MP abundance in the individual samples ranged from 0.57 (MPs mL^{-1}) on the university campus, where the quieter and sheltered area (student residences), to over 0.86 (MPs mL^{-1}) at the more populated parts of the campus close to the car parking and main street. According to previous studies, in the first 10 minutes of rain events, many air MPs particles were deposited (Abbasi, S., 2021; Abbasi and

Turner,2021). This is most likely caused by rain fallout sweeping MPs out of the atmosphere. Abbasi has discovered and measured the amount of MP particles in an Iranian city (Shiraz) during a monsoon rain event. According to Abbasi and Turner (2021), precipitation provides an average of 5% and 7% of annual MPs deposition in Shiraz and Mount Derak, respectively, and at most 30% of total monthly deposition in a semi-arid area. Typhoon Sinlaku (2020) affected the passage of atmospheric MPs in the South China Sea during the East Asian Summer Monsoon, according to Li et al. (2021).

5.3.2. Shape and Size Distribution of the Microplastic

The size and shape distribution of MPs in precipitation was shown in Figure 5.2. All varieties and sizes of microplastic were discovered in every examined sample. The most common shape of microplastics observed in all rain samples were fragments (45.62%), films (25.18%), fibers (22.62%) and spherule (6.56%), respectively. The distribution is thought to be linked to many human activities such as: textiles, tire wear, industrial and similar non-natural sources. Recent investigations have noted the presence of microplastics in rain samples, with a larger abundance of films and fragments than fibers, which is consistent with the findings of this study (Abbasi, S., 2022).

Figure 5.2.b depicts the MPs' size distribution in the rain samples. For all samples, the percentage distribution for dimensions are L<100 μm (55.84%), 100 μm < L<250 μm (28.66%), 250 μm < L<500 μm (7.66%), 500 μm < L<1000 μm (5.11%), and 1000 μm <L<5000 (2.55%). According to the results, the maximum number of MPs was found in the L<100 μm fraction, while the minimum number was observed in the 1000 μm <L<5000 μm. It is estimated that this is due to the fact that plastics from regional sources can be exposed to rain after breaking down. Microplastics are exposed to various weather conditions during transport in the atmosphere, which can cause them to become smaller particles.

Our results are in line with other research, including that from Shiraz, Iran, and the precipitation (Abbasi and Turner., 2021).

Unfortunately, we are unable to quantitatively compare our findings with values in the area since no other study has examined the presence of microplastics in the raindrops in Turkey.

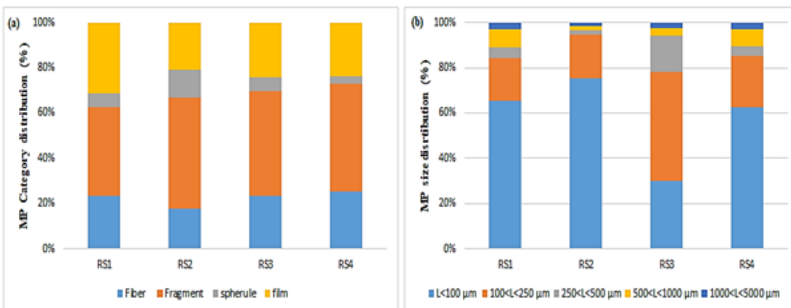

Figure 5.2. (a) Microplastics shape distribution (%),
(b) Microplastics size distribution (%)

Using the SEM-EDS analytical technique, the form and composition of the microplastic surface were reported. Figure 5.3 displays the SEM-EDS spectra of representative samples with varied MP shapes. The reported MPs were composed of clean and straight fibres and broken, sharply angled fragments and films of various sizes and shapes. Curved or spiral microplastics were seen in some samples. The results obtained by the EDS analysis revealed that all particles are plastic, since the basic structures of MPs are largely carbon and oxygen.

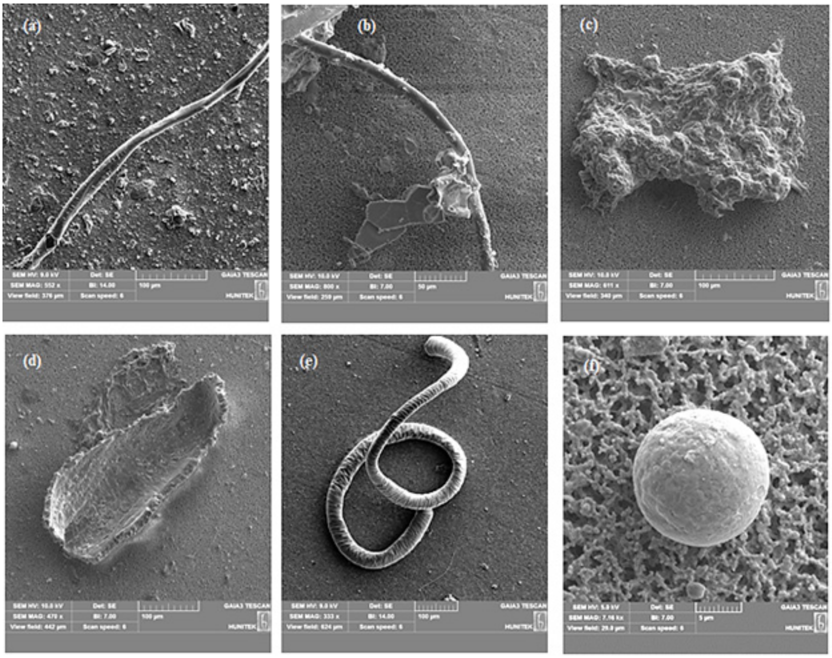

Figure 5.3. SEM images of the microplastic in rain samples: (a) a smooth fiber, (b) less damaged fiber, (c) damaged film, (d) fragment, (e) damaged fiber, (f) fresh circular

5.4. CONCLUSION

This study is the first to establish MP contamination of rain in Turkey. In this study, concentrations of MPs ranged between 57 and 86 MPs ml^{-1}. MPs observed in rain samples have different sizes and structures, and there is a statistical difference between their physical properties. Respectively, Fragments, films, fibres and spherule were observed as microplastic types. Smaller particles of microplastics were found more. The results of the HYSPLIT modeling suggest that the MPs are obtained from both nearby and remote sources.

There is no doubt that microplastics in wet deposition is a great concern for the study of atmospheric microplastics as it relates to the vertical transport of atmospheric microplastics to the ground surface, so This study and similar studies are very important to reveal the transportability of microplastics in the atmosphere. The limited number of studies on this subject is a cause for concern, and it is important to conduct more and better studies with more examples.

Acknowledgements

We would like to thank Hünitek - Hacettepe University Advanced Technologies Application and Research Center- for their great contribution for the analysis of samples under SEM and optic microscope.

REFERENCES

Abbasi, S. (2021). Microplastics washout from the atmosphere during a monsoon rain event. Journal of Hazardous Materials Advances, 4, 100035. https://doi.org/10.1016/j.hazadv.2021.100035

Abbasi, S., & Turner, A. (2021). Dry and wet deposition of microplastics in a semi-arid region (Shiraz, Iran). *Science of the Total Environment*, *786*. https://doi.org/10.1016/j.scitotenv.2021.147358.

Abbasi, S., Alirezazadeh, M., Razeghi, N., Rezaei, M., Pourmahmood, H., Dehbandi, R., Mehr, M. R., Ashayeri, S. Y., Oleszczuk, P., & Turner, A. (2022). Microplastics captured by snowfall: A study in Northern Iran. Science of the Total Environment, 822. https://doi.org/10.1016/j.scitotenv.2022.153451

Bergmann, M., Mützel, S., Primpke, S., Tekman, M. B., Trachsel, J., & Gerdts, G. (2019). White and wonderful? Microplastics prevail in snow from the Alps to the Arctic. In *Sci. Adv* (Vol. 5).

Cauwenberghe, L. Van, Claessens, M., Vandegehuchte, M. B., & Janssen, C. R. (2015). Microplastics are taken up by mussels (Mytilus edulis) and lugworms (Arenicola marina) living in natural habitats. *Environmental Pollution*, *199*, 10–17.

J.Q. Jiang (2018). Occurrence of microplastics and its pollution in the environment: a review. Sustainable *Production and Consumption, 13,* 16-23. https://doi.org/10.1016/j.spc.2017.11.003.

Li, C. , Wang, X. , Zhu, L. , Liu, K. , Zong, C. , Wei, N. , Li, D. , 2021. Enhanced impacts eval- uation of Typhoon Sinlaku (2021) on atmospheric microplastics in South China Sea during the East Asian Summer Monsoon. Sci. Total Environ., 150767

Materić, D., Kasper-Giebl, A., Kau, D., Anten, M., Greilinger, M., Ludewig, E., van Sebille, E., Röckmann, T., & Holzinger, R. (2020). Micro- and Nanoplastics in Alpine Snow: A New Method for Chemical Identification and (Semi) Quantification in the Nanogram Range. *Environmental Science & Technology, 54*(4), 2353–2359.

Pellini, G., Gomiero, A., Fortibuoni, T., Ferrà, C., Grati, F., Tassetti, A. N., Polidori, P., Fabi, G., & Scarcella, G. (2018). Characterization of microplastic litter in the gastrointestinal tract of Solea solea from the Adriatic Sea. *Environmental Pollution, 234*, 943–952.

Scheurer, M., & Bigalke, M. (2018). Microplastics in Swiss Floodplain Soils. *Environmental Science & Technology, 52*(6), 3591–3598.

Xia, W., Rao, Q., Deng, X., Chen, J., & Xie, P. (2020). Rainfall is a significant environmental factor of microplastic pollution in inland waters. *Science of The Total Environment, 732*, 139065.

Zhang, D., Liu, X., Huang, W., Li, J., Wang, C., Zhang, D., & Zhang, C. (2020). Microplastic pollution in deep-sea sediments and organisms of the Western Pacific Ocean. *Environmental Pollution, 259*, 113948.

CHAPTER 6

HCHO/NO_2 COLUMN RATIOS DERIVED FROM TROPOMI FOR UNDERSTANDING OZONE FORMATION REGIME

Merve EKE[1,2], Fulya ÇİNGİROĞLU[3], Burçak KAYNAK[1]

[1]Istanbul Technical University, Türkiye
School of Civil Engineering
Department of Environmental Engineering

[2]Gebze Technical University, Türkiye
School of Engineering
Department of Environmental Engineering

[3]Istanbul Technical University, Türkiye
Eurasia Institute of Earth Sciences

Abstract

Ozone (O_3) is an important secondary air pollutant that has serious negative health impacts. O_3 formation depends on nitrogen oxides (NO_x) and volatile organic compounds (VOCs) in the troposphere. Thus, O_3 formation sensitivity changes according to the ratio of VOCs and NO_x. Formaldehyde (HCHO) is a commonly found non-methane VOC and a good indicator of VOC levels in a region. Hence, HCHO and NO_2 ratio (FNR) can be used to understand the O_3 sensitivity, similar to VOC and NO_x ratio. Both HCHO and NO_2 can be monitored by satellite retrievals, and the spatial and temporal resolution of column concentrations were increased with the instrument TROPOMI launched in 2018. Thus, in this study, FNR derived from TROPOMI HCHO and NO_2 retrievals was used for understanding the O_3 formation regimes over Marmara Region. Six air quality monitoring stations (AQMS) exceeded the European Union (EU) O_3 standard (maximum daily 8-hr O_3>120 μg/m^3) for more than 100 days between 2019-2021. In 2020, Çan exceed the limit of more than 100 days. FNR was selected as <1.5 VOC limited, >2.3 NO_x limited, and intermediate values are

transition regimes. Çan and Limanköy were mostly NO_x limited during the period and Kültürpark changed with NO_x limited, VOC limited, and transition. O_3 and NO_2 concentrations were higher in Çan and Kültürpark, respectively.

Keywords: *Formaldehyde, nitrogen dioxide, ozone, FNR, remote sensing.*

6.1. INTRODUCTION

Ozone is an important component that impacts radiative forcing (Mickley et al., 2001). Tropospheric ozone is a secondary pollutant that is considered one of the major air pollutants with impacts on health and crop production. Studies showed that menace of food supply is an issue in USA mid-West, Europe, South Asia, and China because of O_3. Moreover, projections indicated that between 3 and 16% of yield was lost of essential crops in 2000 (Emberson, 2020). Environmental Protection Agency (EPA) states that ozone pollution health impacts are observed with cough, breathing harder and throat irritation. Moreover, it is related to mortality, especially in older ages, and the relation increases in summer seasons (US EPA, 2022). Jyoti (2019) found that 67.2% of people in an urban environment in China are exposed to >100 µg/m^3 O_3 concentration which is above World Health Organization (WHO) recommendation, and according to the study, total O_3 related mortality was 69.6×103 in China in 2016. Moreover, it was demonstrated by Hung (2019) that the rise in O_3 because of urbanization resulted in 1100 premature mortality in China. Zhang (2019) showed that 10 µg/m^3 increase in O_3 concentration caused a rise in mortality of cardiovascular illness up to 0.983% using 2015-2017 daily cardiovascular illness mortality data.

Volatile organic compounds (VOCs) are one of the main precursors of O^3 by forming radicals (HOx) (Logan et. al., 1990). Ozone formation depends on the amount of NO_x and VOCs and their ratios in the atmosphere. In urban areas, NO_x concentration is higher; thus, the environment becomes VOC-limited. On the contrary, if the VOCs concentrations are higher as in forestry and agricultural areas, biogenic volatile organic compounds (BVOCs) concentration increases, thus environment becomes NO_x limited (Logan et. al., 1990; Ryan et al., 2020). Natural sources of NO_x

and VOCs can be listed as soil, lighting for NO_x, vegetation for VOCs and wildfires for both of these pollutants (Lu and Zhang, 2019). It is important to determine the impacts of NO_x and VOC concentrations on O_3 production to control O_3 pollution. Sillman (1997) proposed to examine O_3/NO_y, O3/NO_z, H_2O_2/HNO_3 ratios to understand O_3-NO_x-VOC sensitivity. It was suggested by Tonnesen and Dennis (2000) that formaldehyde (HCHO) which is one of the rare VOCs species that can be used in remote sensing monitoring, and NO_2 ratio (FNR) can be used in O_3 formation sensitivity studies to determine whether the atmosphere is VOC limited, NO_x limited or in between.

Jin (2017) determined that the range of FNR changes seasonally from 0.6 to 1.8 in August to January, 0.9 to 2.7 in July to December as VOC limited respectively, and above 1.0 as a transition in Europe using GEOS-Chem chemical transport model and comparing with satellite retrievals of Ozone Monitoring Instrument (OMI). Besides, recent studies state that FNR ratio can be higher than 2 for NO_x limited and lower than 1 for VOC limited regimes (Jin et al., 2017). Vazquez (2021) compared FNR values from 2006-2016 April months which is usually the warmest month in the Mexico City and found that VOC limited area increased from 2006 to 2016 utilizing from Jin (2017) study due to a decrease in HCHO concentration. Ryan (2020) indicated that O_3 concentration exceeded 35 ppb when the FNR was above 2, especially on the days when the temperature was higher than 35°C in Melbourne Australia.

There are some studies that investigated O_3 in Turkey. Im (2013) stated that O_3 mixing ratios were increasing 28% on weekends which might be because of O_3-NO_x-VOC sensitivity in Istanbul September 2007-December 2009. Moreover, a study showed that O_3 mixing ratio was increasing in March, and maximum values were observed in August with 25 ppb and 30 ppb in urban and semi-urban regions respectively. Bozkurt (2018) measured NO_2, VOCs, SO_2, and O_3 in Düzce and found that NO_2 and VOCs reached the highest concentration in winter with 10.88-71.44 and 7.81-112.03 $\mu g/m^3$ ranges respectively. The highest O^3 concentration range was observed in summer period with 23.40-93.79 $\mu g/m^3$. Sari (2020) investigated the impacts of meteorological conditions which are relative humidity, temperature, and wind speed on ozone episodes in Biga and found that decrease in wind speed is related to ozone episodes.

This study aims to understand the conditions of the regions where O_3 pollution is problematic by determining the VOC limited and NO_x limited regimes. High resolution TROPOspheric Monitoring Instrument (TROPOMI) retrievals of HCHO and NO_2 were used to calculate FNR and compared ground-based O_3 measurements. Results can provide suggestions for policy makers to control O_3 pollution in these regions. Even though impacts of meteorological conditions and NO_x concentration on O_3 were previously examined in Turkey, there was not any comprehensive study that includes FNR.

6.2. METHODOLOGY

6.2.1. Study Area

Marmara Region comprises 8% of Turkey and it is considered as the most developed region in Turkey with its geographical formations and location (MoEUCC MTHMM, 2022). It includes more than half of the industrial activities in Turkey with significant number of organized industrial zones and air pollution can be a major issue in the region. Metropolitan city Istanbul is located in this region and covers 19% of Turkey population (TUIK, 2021). Trade, agriculture, and tourism are other sources of the region. Currently, there are approximately 90 air quality monitoring stations in Marmara Region and 41 of these stations are measuring O_3.

6.2.2. Observations

Hourly ground observations of O_3 and NO_2 were obtained from Ministry of Environment, Urbanization and Climate Change (MoEUCC) for three years between 2019-2021 (MoEUCC SIM, 2022). 8-hour (hr) average of O_3 was calculated to investigate the exceedances (max daily 8-hr O_3) and determine the polluted regions. Hourly and daily NO_2 concentration were processed and investigated.

TROPOMI satellite retrievals of HCHO and NO_2 were obtained from GES DISC between 2019- 2021, and spatial and temporal processing were made. Retrievals within 6 km radius was selected for each ground station location to calculate the average concentrations over the ground stations. The ratio of HCHO and NO_2 was calculated daily and then averaged. The ozone season of May-September months were specifically investigated. Meteorological data were taken from the Turkish State Meteorological Service (TSMS). Wind speed and wind direction were used to create pollution roses of ground-based O_3 and NO_2 measurements to understand the impact of transportation on O_3 pollution.

To understand the impact of FNR (HCHO/NO_2) ratio, time series analysis of FNR and O_3 was performed using satellite retrievals and ground station measurements.

6.3. RESULTS AND DISCUSSION

According to EU standards, Maximum daily 8-hr average O_3 concentration should not exceed 120 µg/m^3. Total number of days that exceed this limit in May-September (Northern Hemisphere O_3 season, 153 days) for three years were investigated (Table 6.1). Calculated maximum 8-hr O_3 concentrations showed that exceeded threshold days were 232 in Keşan district in 3 years. It was found that Erdek, Kültürpark, Uludağ University, Çan, Keşan, and Yalova districts were exposed O_3 concentration above the limit for more than 100 days in 3 years. The most polluted year was 2019 with 947 days followed by 721 and 707 days in 2020 and 2021, respectively. Erdek (98 days) and Keşan (99 days) had the highest O_3 polluted days in 2019. In addition, Çan exceeded limit with 106 days in 2020 which is 70% days of May-September period that exceeded the EU standard. Edirne, Çanakkale, Bursa, Balıkesir, and Yalova provinces were found as major cities that were over the ozone limit on most of the days of May-September period. Limanköy, Şile, Lapseki, and Silivri AQMS were also O_3 polluted regions, although they are distant coastal areas.

Table 6.1. Total days of Daily maximum 8 hr-O_3 >120 µg/m³ in AQMS in Marmara Region.

	O_3 exceedance days			NO_2 (10^{16} molec/cm²)			HCHO (10^{16} molec/cm²)		
Region	**2019**	**2020**	**2021**	**2019**	**2020**	**2021**	**2019**	**2020**	**2021**
Keşan	99	79	54	0.13	0.13	0.13	0.76	0.75	0.76
Çan	***65***	***106***	***46***	***0.14***	***0.14***	***0.16***	***0.85***	***0.84***	***0.75***
Uludağ University	76	51	58	0.25	0.23	0.27	1.01	0.99	0.83
Erdek	98	9	39	0.17	0.16	0.18	0.89	0.93	0.74
Kültürpark	***42***	***46***	***40***	***0.32***	***0.30***	***0.35***	***0.97***	***0.95***	***0.90***
Yalova	53	20	40	0.32	0.29	0.36	1.05	1.00	0.97
Yalova Altınova	36	24	38	0.34	0.33	0.40	0.97	0.91	0.84
Balıkesir	71	9	5	0.17	0.18	0.18	0.98	0.93	0.87
Kağıthane MTHM	1	78	1	0.40	0.31	0.38	0.85	0.77	0.79
Bilecik Bozüyük	24	49	6	0.14	0.14	0.15	0.83	0.87	0.70
Lapseki	12	33	34	0.15	0.15	0.15	0.96	0.82	0.72
Silivri	16	16	44	0.17	0.14	0.18	0.86	0.82	0.76
Bilecik	47	14	7	0.15	0.17	0.18	0.93	0.89	0.78
Kestel	28	15	23	0.27	0.26	0.29	1.00	0.94	0.84
Başakşehir	2	21	42	0.36	0.29	0.35	0.82	0.73	0.75
Gölcük	22	12	28	0.30	0.27	0.34	0.89	0.98	0.96
Armutlu	37	0	23	0.20	0.18	0.20	0.94	1.00	0.89
Bandırma	16	13	25	0.18	0.17	0.17	0.92	0.86	0.71
Limanköy	***11***	***25***	***11***	***0.13***	***0.12***	***0.11***	***0.83***	***0.73***	***0.81***
Şile	12	16	5	0.17	0.15	0.17	0.87	0.80	0.75

Season variations of measurements of high-O_3 AQMSs were investigated and three cases were selected which had NO_2 levels low (Limanköy), moderate (Çan), and relatively high (Kültürpark). Seasonal changes showed that O_3 concentration increases from winter to summer as expected (Figure 6.1). In hourly variation, it was observed that O_3 concentration increases for a while after 6:00 p.m. which is not the peak hours of O_3 production. The reason for the increase can be explained by moving 8-hr O_3 average. Kültürpark NO_2 concentration is higher compared with the Çan and Limanköy stations in all seasons. In addition, it exceeded the 40 µg/m³ EU NO_2 annual standard for all seasons. However, O_3 concentration in Kültürpark is lower than the Çan AQMS. Another case is Limanköy, where the NO_2 concentrations did not exceed 20 µg/m^3, but O$_3$ concentration was consistently high in all seasons and showed very small decrease in winter and very little variation in diurnal profiles.

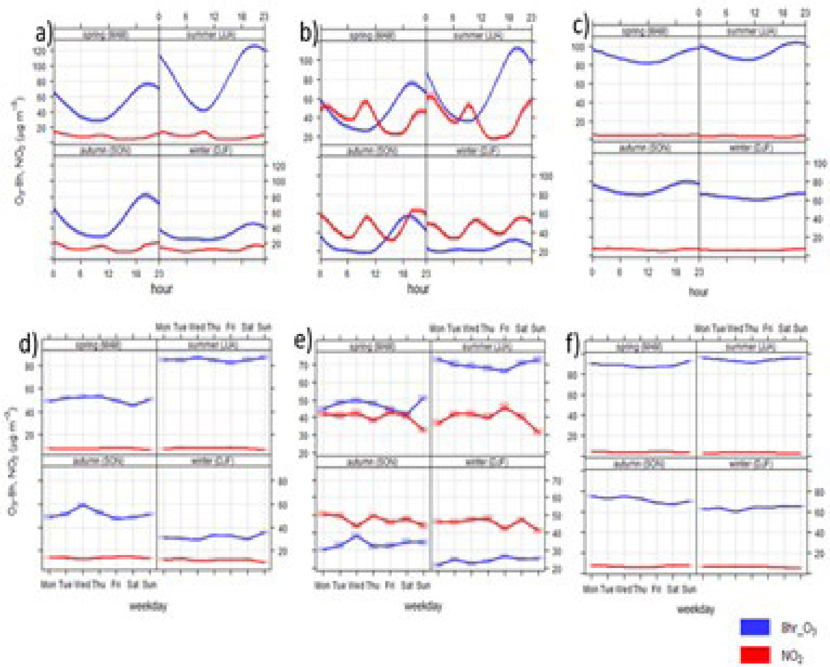

Figure 6.1. Diurnal (upper) and weekly (lower) profiles with respect to seasons of Çan (a, c), Kültürpark (b, e) and Limanköy (c, f) AQMSs for three years.

In order to understand the relationship between meteorological parameters and O$_3$ pollution, pollution roses for NO$_2$ and O$_3$ were prepared for May-Sep season for each year to understand the transportation of pollutants (Figure 6.2). In addition, change of HCHO and NO$_2$ concentrations and O$_3$ concentration levels for the same period was added. Çan AQMS is surrounded by urban and industrial areas and O$_3$ was transported from northeast to the measurement location. FNR was generally higher than two, so it was indicating NO$_x$ limited region for most of the days. On the other hand, NO$_2$ transportation was not observed. Hence, O$_3$ can be transported to region after it is formed.

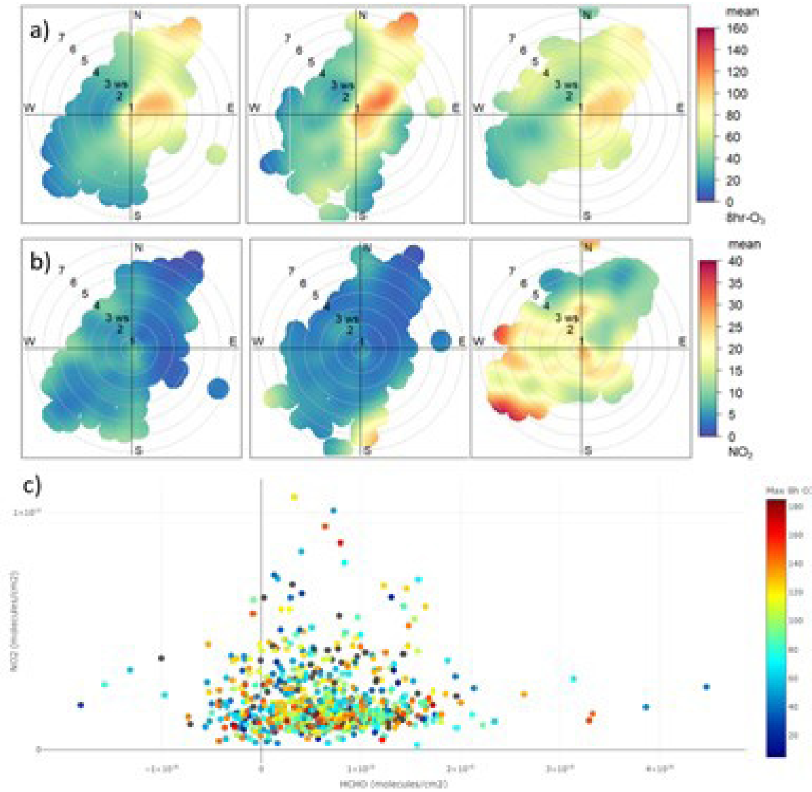

Figure 6.2. Pollution rose of O_3 (a) and NO_2 (b) in 2019-2021 (left to right), change of ground O_3 with satellite retrievals of HCHO and NO_2 for Çan.

Kültürpark NO_2 pollution rose showed that NO_2 was emitted locally in the AQMS region with highest levels observed in calm days (Figure 6.3). A significant increase is observed from 2019 to 2021 for NO_2 concentrations, although O_3 concentrations were similar. Number of NO_x limited days were higher than transition and followed by VOC limited days. In addition, O_3 concentration was observed higher from south-west to the measurement location. O_3 might be formed in the AQMS region enhanced by transport of VOCs to the region.

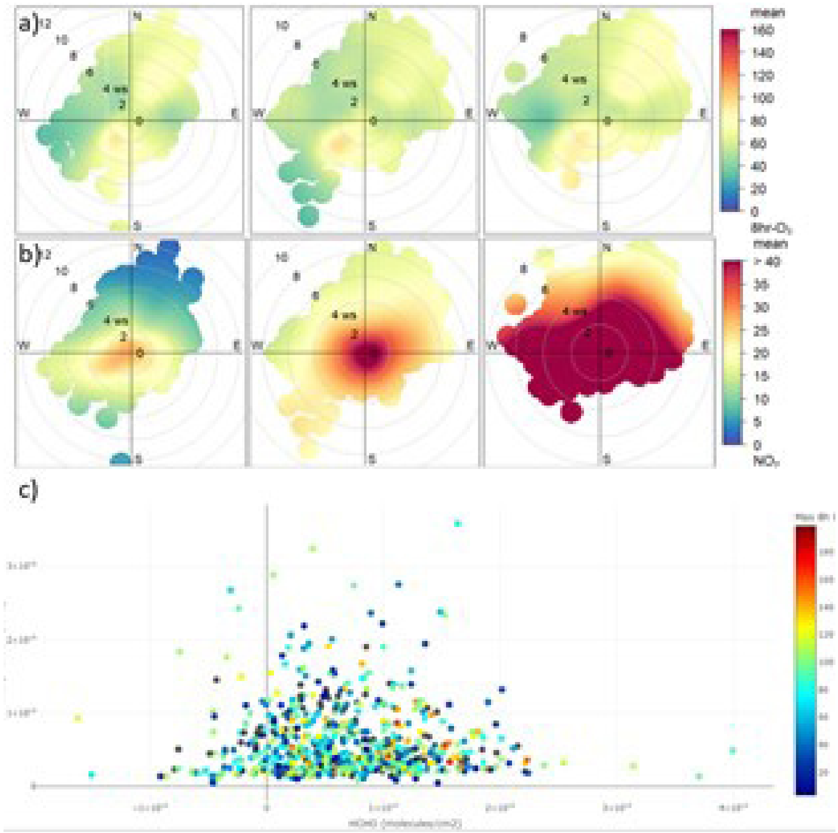

Figure 6.3. Pollution rose of O_3 (a) and NO_2 (b) in 2019-2021 (left to right), change of ground O_3 with satellite retrievals of HCHO and NO_2 for Kültürpark.

Even though Limanköy is at distant rural area, O_3 levels were found high compared with other stations close to industrial areas and urban centers (Figure 6.4). Pollution rose of Limanköy showed that NO_2 is transported from south which is the sea. Hence, Limanköy might be affected by shipping NO_x and VOC emissions instead of other anthropogenic sources emissions. When the scatter plots are examined, an increase in HCHO concentration causes increase in O_3 concentration in Çan. Kültürpark showed more variety between NO_2 and HCHO compared with the Çan. In Limanköy, on days when O_3 concentration is lower 60 µg/m^3 is more than Çan and Kültürpark. Moreover, NO_2 is more consistent than HCHO. FNR profile was similar with Çan station with higher than 2 in most of the season.

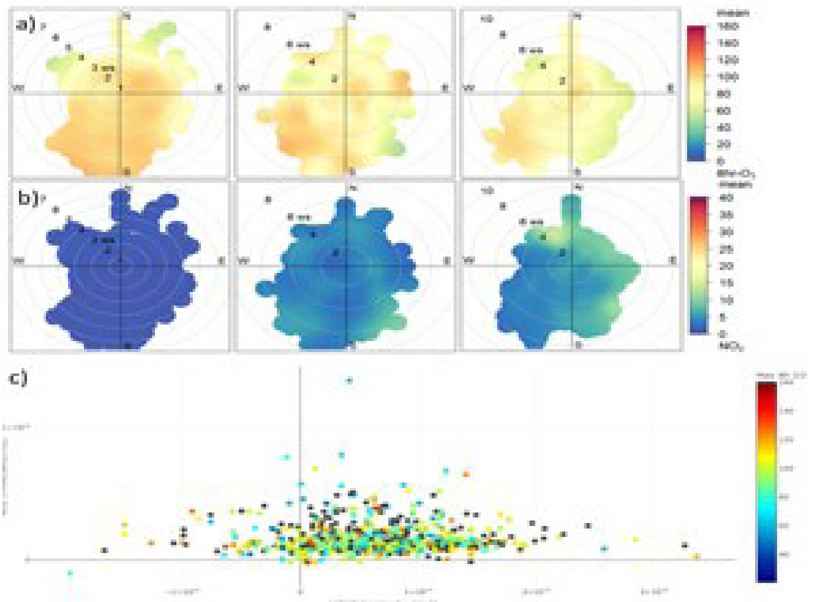

Figure 6.4. Pollution rose of O3 (a) and NO2 (b) in 2019-2021 (left to right), change of ground O3 with satellite retrievals of HCHO and NO2 for Limanköy.

Daily changes in daily maximum 8-hr O_3 concentration with FNR was examined with time series for the selected three stations (Figure 6.5). FNR was selected as <1.5 VOC limited, >2.3 NO_x limited, and intermediate values are transition regimes according to literature studies (Jin et al., 2017). Although there were few days with transition regime, Çan was mostly NO_x limited during the May-September periods. NO_x limited regime was dominant especially in 2020 when the O_3 pollution level peaks. Furthermore, O_3 concentration exceeded EU limits for almost whole period. O_3 concentration significantly decreased during winter period due to radiation and temperature. Kültürpark and Çan O_3 concentration varied between 0-50 µg/m^3, and almost decreased to zero. The difference between these stations for winter period was the FNR ratio. Kültürpark showed great variability between NO_x limited, transition, and VOC limited regime including winter season. Variability can be one of the reasons for higher O_3 concentration compared with Çan, since Çan showed a VOC limited profile in the winter season. The reason for Kültürpark variability can be transportation of VOCs or green areas, gas stations, and traffic next to AQMS. In addition, some of the days when O_3 concentration peaks were VOC limited. Hence, O_3 production regime was variable during the period. In Limanköy, region was mostly NO_x limited similar with Çan, and O_3 concentration was lower compared with other two stations. However, unlike the Kültürpark and Çan, concentration did not decrease in winter season, and was mostly higher than 50 µg/m³. High levels of ozone might be indicating transport.

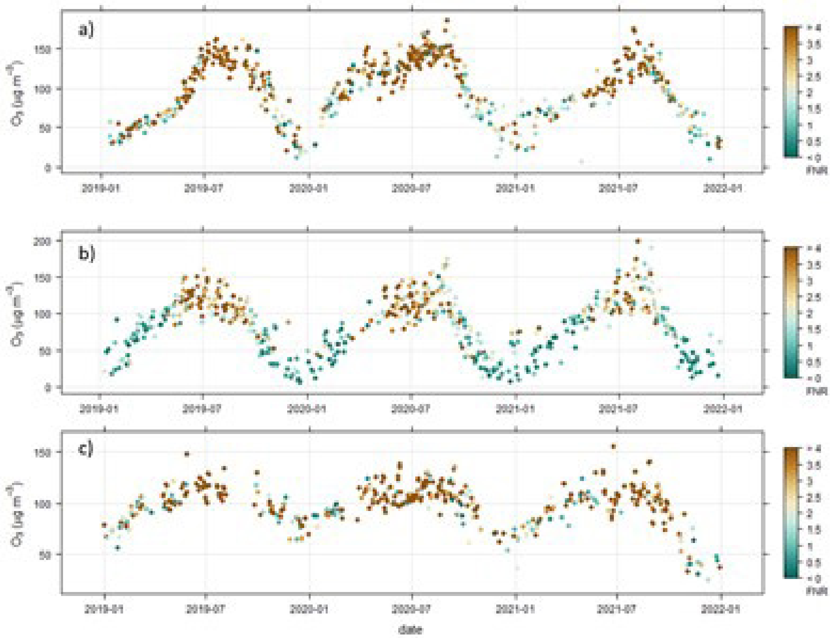

Figure 6.5. Time series of O_3 and HCHO/NO_2 in study period for Çan (a), Kültürpark (b) and Limanköy (c).

6.4. CONCLUSIONS

In this study, O_3 pollution in Marmara Region was investigated considering the O_3 formation regimes; NO_x limited, VOC limited, and transition. Çan, Kültürpark, and Limanköy AQMS were selected to represent high NO_2, low NO_2, and a distant coastal area that O_3 pollution might cause by transportation. Seven AQMS measurements were indicated high O_3 exposure above the limit of more than 100 days in May-September period. These AQMSs were Keşan, Çan, Uludağ University, Erdek, Yalova, Kültürpark and Yalova. O_3 concentration increased during spring and summer because of the increase in photochemical reactions that form O_3. Kültürpark NO_2 concentration was higher than Çan and Limanköy, but O_3 concentration was higher in Çan. Limanköy O_3 level was found higher in winter season compared with Kültürpark and Çan. Pollution rose of O_3 showed that it is transported from urban and industrial regions. When O_3 concentration was higher satellite retrievals of HCHO and NO_2 varied in Kültürpark, but there was an increase in HCHO in Çan and Limanköy regions. Similar results were observed between O_3 and FNR time series. Thus, O_3 formation may cause by both VOCs and NO_x. It is important to understand the regime for O_3 formation.

Clean Air Action Plans for ozone control must be prepared considering NO_x limited and VOC limited regimes instead of policies focusing on reduction of NO_x directly. Otherwise, decreasing NO_x to control O_3 formation cannot be effective, also it might even increase O_3 concentrations depending on VOC/NO_x ratios.

REFERENCES

Bozkurt, Z., Özden, Ö., Dö, T., Artun, G., Gaga, E.O., 2018. Atmospheric concentrations of SO_2 , NO_2, ozone and VOCs in Düzce, Turkey using passive air samplers: Sources, spatial and seasonal variations and health risk estimation 9, 1146–1156. https://doi.org/10.1016/j.apr.2018.05.001

Emberson, L., 2020. Effects of ozone on agriculture , forests and grasslands. Philosophical Transactions of the Royal Society A, 378(2183), 20190327. https://doi.org/10.1098/rsta.2019.0327

Hung, S., Yim, L., Wang, M., Gu, Y., 2019. Effect of Urbanization on Ozone and Resultant Health Effects in the Pearl River Delta Region of China Journal of Geophysical Research: Atmospheres 568–579. https://doi.org/10.1029/2019JD030562

Im, U., Incecik, S., Guler, M., Tek, A., Topcu, S., Unal, Y. S., ... & Tayanc, M., 2013. Analysis of surface ozone and nitrogen oxides at urban, semi-rural and rural sites in Istanbul, Turkey. Science of the Total Environment, 443, 920-931. https://doi.org/10.1016/j.scitotenv.2012.11.048

Jin, X., Fiore, A.M., Murray, L.T., Valin, L.C., Lamsal, L.N., Duncan, B., Boersma, K.F., Smedt, I. De, Abad, G.G., Chance, K., Tonnesen, G.S., 2017. Evaluating a Space-Based Indicator of Surface Ozone-NO_x-VOC Sensitivity Over Midlatitude Source Regions and Application to Decadal Trends. Journal of Geophysical Research: Atmospheres 439–461. https://doi.org/10.1002/2017JD026720

Jyoti, K., Ye, W., Arora, M., Nagendra, S.M.S., 2019. Ozone pollution in Chinese cities : Assessment of seasonal variation , health effects and economic burden*. Environ. Pollut. 247, 792–801. https://doi.org/10.1016/j.envpol.2019.01.049

Logan, A., Wofsy, C., 1990. The Sensitivity of Ozone to Nitrogen Oxides and Hydrocarbons in Regional Ozone Episodes 1 Now at of Atmospheric, Oceanic, and Space Sciences, al ., to explore the factors that influence ozone in Michigan, al areas during stagnation periods, again focusing on precursor the American Geophysical NO_x and 95, 1837–1851.

Lu, X., Zhang, L., 2019. Meteorology and Climate Influences on Tropospheric Ozone: a Review of Natural Sources, Chemistry, and Transport Patterns 238–260. https://doi.org/10.1007/s40726-019-00118-3

Mickley, L.J., Jacob, D.J., Rind, D., 2001. Uncertainty in preindustrial abundance of tropospheric ozone: Implications for radiative forcing calculations. J. Geophys. Res. 106, 3389–3399. https://doi.org/10.1029/2000JD900594

Ren, B., Xie, P., Xu, J., Li, A., Qin, M., Hu, R., Zhang, T., Fan, G., 2022. Vertical characteristics of NO_2 and HCHO , and the ozone formation regimes in Hefei, China. Sci. Total Environ. 823, 153425. https://doi.org/10.1016/j.scitotenv.2022.153425

Ryan, R.G., Rhodes, S., Tully, M., Scho, R., 2020. Surface ozone exceedances in Melbourne , Australia are shown to be under NO_x control , as demonstrated using formaldehyde: NO_2 and glyoxal: formaldehyde ratios. Science of the Total Environment, 749, 141460. https://doi.org/10.1016/j.scitotenv.2020.141460

Sari, D., Incecik, S., Ozkurt, N., 2020. Analysis of surface ozone episodes using WRF-HYSPLIT model at Biga Peninsula in the Marmara region of Turkey. Atmos. Pollut. Res. 11, 2361–2378. https://doi.org/10.1016/j.apr.2020.09.018

Sillman, S., Logan, J. A., & Wofsy, S. C., 1990. The sensitivity of ozone to nitrogen oxides and hydrocarbons in regional ozone episodes. Journal of Geophysical Research: Atmospheres, 95(D2), 1837-1851. https://doi.org/10.1029/JD095iD02p01837

Vazquez, J., Inoue, K., Tonokura, K., 2021. Diagnosis of ozone formation sensitivity in the Mexico City Metropolitan Area using $HCHO/NO_2$ column ratios from the ozone monitoring instrument. Environ. Adv. 6, 100138. https://doi.org/10.1016/j.envadv.2021.100138

Zhang, J., Chen, Q., Wang, Q., Ding, Z., Sun, H., Xu, Y., 2019. The acute health effects of ozone and $PM_{2.5}$ on daily cardiovascular disease mortality: A multi-center time series study in China. Ecotoxicol. Environ. Saf. 174, 218–223. https://doi.org/10.1016/j.ecoenv.2019.02.085

Web 1: (EPA, 2022), https://www.epa.gov/ozone-pollution-and-your-patients-health/health-effects-ozone-general-population, accessed 15 August 2022.

Web 2: (TUIK, 2021), https://data.tuik.gov.tr/Bulten/Index?p=Adrese-Dayali-Nufus-Kayit-Sistemi-Sonuclari-2021-45500, accessed 15 August 2022.

Web 3: (MTHMM MoEUCC, 2022), https://mthmm.csb.gov.tr/bolgemiz-i-85694, accessed 15 August 2022.

Web 4: (MTHMM SIM, 2022), https://sim.csb.gov.tr/STN/STN_Report/StationDataDownloadNew, accessed 15 August 2022.

Web 5: (GES DISC, 2022), https://disc.gsfc.nasa.gov/datasets?keywords=TROPOMI%20HCHO&page=1, accessed 15 August 2022.

Web 6: (GES DISC, 2022), https://disc.gsfc.nasa.gov/datasets?keywords=TROPOMI%20NO2&page=1, accessed 15 August 2022.

CHAPTER 7

CHARACTERIZING INHALABLE MAJOR ELEMENTAL COMPONENTS OF $PM_{2.5}$ IN ISTANBUL (TURKEY) AND THEIR IMPACT ON PATHOGENS: A CASE STUDY DURING COVID-19 CONSECUTIVE LOCK-DOWN AND UNLOCK-DOWN DAYS

Aslı BAYSAL[1, 2], Hasan SAYGIN[3], Sevilay ZORA[1], Burcu ONAT[4]

[1]Istanbul Aydın University, Türkiye
Health Services Vocational School of Higher Education

[2]Istanbul Technical University, Türkiye
Science and Letters Faculty
Chemistry Department

[3]Istanbul Aydın University, Türkiye
Application and Research Center for Advanced Studies

[4]Istanbul University-Cerrahpasa, Türkiye
Engineering Faculty
Environmental Engineering Department

Abstract

Fine particulate matter with an aerodynamic diameter of ≤2.5 µm ($PM_{2.5}$) is known to be associated with a variety of adverse health effects. $PM_{2.5}$ is known to have interactions with some bacterial infection in the respiratory system, like lung disease. Many studies examined the potentially toxic elements in $PM_{2.5}$ using their total composition; however, their occurrence under various inhalable conditions were limitedly examined. Moreover, previous studies relating the human health mainly focused the cytotoxicity of $PM_{2.5}$ through various human cell lines however pathogen related impact of $PM_{2.5}$ were limitedly examined. Therefore, this study reports the identification of total and inhalable major elemental components in $PM_{2.5}$ filters collected from Istanbul-Turkey during Covid lock-down weekends and non-lockdown weekdays and their relationship with some main pathogenic bacteria. For this purpose, $PM_{2.5}$ air samples were collected during COVID-19 consecutive lock-down and unlock-down days in the campus of Istanbul Aydin University, Istanbul-Turkey. The $PM_{2.5}$ samples were extracted using two types of simulated biological lung fluids (Gamble solution and Artificial Lung Fluids) to mimic inhalable conditions. Moreover, we investigated the impact of inhalable $PM_{2.5}$ on model pathogen species; like Staphylococcus aureus and Bacillus subtilis. Their viability and ability to form biofilm under inhalable conditions were evaluated. Our data show that exposure to $PM_{2.5}$ affected viability and biofilm formation of all pathogens according to inhalation conditions.

Keywords: *Pathogens, COVID, airborne particulates, biofilm, in vitro.*

7.1. INTRODUCTION

Particulate matter with an aerodynamic diameter of ≤2.5 µm ($PM_{2.5}$) is a complex and dynamic mixture of components with physical, chemical, and biological origins and their different chemical, biological and physical properties is known to be associated with a variety of adverse health effects (Deng et al., 2016; Woo et al., 2018).

In the last decades, many studies have investigated the risks that $PM_{2.5}$ poses to human health and to ecosystems. However, many of these studies focused the cytotoxicity and determination the hazardous substances. On the other hand, biological origins of the $PM_{2.5}$ consist various bacteria species. Moreover, bacterial respiratory infections are a major cause of mortality and morbidity for humans, as well as many studies have indicated that inhalation of PM causes inflammation, oxidative stress, and tissue damage (Li et al., 2018; Liu et al., 2018; Pompilio and Di Bonaventura, 2020; White et al., 2020). Besides, there has been great concern about the potential health hazards of biological origins in PM, especially allergenic or toxigenic bacteria (Deng et al., 2016). The bacteria in the air can originate from naturally in the outdoor environment or from anthropogenic sources such as traffic, industrial emissions and human activities. Although several microorganism-related studies (e. g. allergens and pathogens) have been examined mainly their occurances, specie type and concentration, it is not clear about the interaction with elemental composition and bacteria and their behaviour under human related conditions (Li et al., 2018; Liu et al., 2018; Liu et al., 2020; Pompilio and Di Bonaventura, 2020; Suraju et al., 2015). To mimic the human related conditions, in vitro solution mostly good model system, for instance, artificial lysosomal fluid (ALF) and Gamble's solution (GS). The ALF reflects the intracellular environment and inflammatory conditions, and a GS mimics the normal conditions of interstitial fluid within the lungs (Saygin and Baysal, 2022a).

Therefore, this study aims to obtain knowledge on the impact of $PM_{2.5}$ in regards to the culturability of Staphylococcus aureus (S. aureus) and Bacillus subtilis (B. subtilis) by determination viability and biofilm production under inhalable conditions (e. g. ALF and GS). Moreover, major elemental composition under these inhalable conditions and their impact on bacterial responses during COVID-19 consecutive lock-down and unlock-down days.

7.2. MATERIALS AND METHODS

7.2.1. Sampling

$PM_{2.5}$ samples were collected in the campus of Istanbul Aydin University in Istanbul-Turkey (40° 59' 29"N, 28° 47' 50"E) from December 2020 to March 2021 (Figure 7.1). Istanbul is a megacity with 13–17 million inhabitants and responsible for 40% of Turkey's industrial activities (Baysal et al., 2017; Baysal et al., 2020; Ozbek and Baysal, 2016; Baysal and Saygin, 2022). The sampling location is highly populated residential areas, having high industrial organizations and high-traffic density and located between main roads and near Istanbul Ataturk Airport which had one of the highest densities as an international airport in the world at the sampling time.

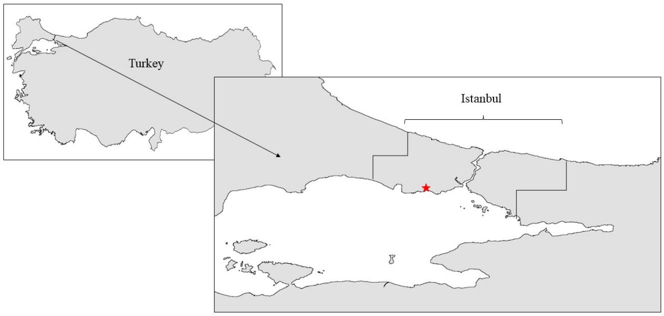

Figure 7.1. The location of $PM_{2.5}$ sampler in Istanbul Aydin University Florya campus, Istanbul, Turkey.

The $PM_{2.5}$ samples were collected using low volume air sampler device for collecting the outdoor air samples on the quartz filter during 48-h. The samples were classified as weekend and weekdays since COVID-19 restrictions were applied in Turkey and the lock-down occurred between Friday night to Monday early morning during these periods. The samples collected during 48 h intervals in unlock-down weekdays and lock-down weekends. The $PM_{2.5}$ samples were collected as 5 unlock-down weekdays and 5 lock-down weekend during the COVID pandemic.

7.2.2. Simulated Biological Fluids and Analytical Methods for $PM_{2.5}$ Extractions

The $PM_{2.5}$ collected filters were divided to equal portions for the extraction of inhalable composition (ALF and GS). The chemical compositions of the lung fluids were shown in Table 7.1. A quarter of each $PM_{2.5}$ filters were extracted in 10 mL ALF and GS. Then the samples agitated during 24-h under 37°C, centrifuged and filtrated with a 0.45 µm syringe filter successively (Kastury et al., 2018).

Table 7.1. Chemical composition of artificial lung fluids (Kastury et al. 2018)

Chemical (g/L)	**ALF**	**GS**
Sodium chloride	3.21	8.0
Sodium hydroxide	6.00	-
Citric acid	20.8	-
Calcium chloride (dihydrate)	0.128	0.185
Sodium phosphate	-	0.0479
Sodium hydrogen phosphate dibasic (anhydrous)	0.071	-
Sodium sulphate	0.039	-
Sodium hydrogen carbonate	-	0.35
Magnesium chloride (anhydrous)	0.05	-
Magnesium sulfate (anhydrous)	-	0.0977
Glycine	0.059	-
Sodium citrate (dihydrate)	0.077	-
Sodium tartrate (dihydrate)	0.09	-
Sodium lactate	0.085	-
Sodium pyruvate	0.086	-
Potassium chloride	-	0.4
Potassium dihydrogen phosphate	-	0.06
Benzalkonium chloride	0.05	
pH	4.5	7.4

7.2.3. Determination of Major Elements

All the extracting solutions were stored at 4°C before instrumental analysis with Inductively Coupled Plasma Optical Emision Spectrometer (ICP-OES, Spectro Blue- Spectro, Kleve-Germany). To ensure the quality and accuracy, blank measurements, triplicate measurements, a external calibration were performed.

7.2.4. Viability, Biofilm, Protein and Oxidative Stress Responses of Bacteria

S. *aureus* (ATCC 25923) and B. *subtilis* (ATCC 11774) were selected as a bacteria model approach and used during the experiments. The bacteria were cultivated and incubated at 37°C for 24 hours. Tryptic Soy Broth (TSB) medium was prepared and autoclaved at 121°C for 15 min, then cultivated bacterium were collected in TSB and incubated at 37°C for 4 hours. End of this period, the liquid phase of bacteria suspension removed, and precipitation of the bacteria mixed in TSB medium. Bacteria suspension in TSB and extracted $PM_{2.5}$ samples in each inhalable-relevant conditions were mixed at same amount and incubated at 37°C for 20 hours. The bacteria including the extracted $PM_{2.5}$ samples in each inhalable-relevant conditions were taken and the optical density (OD) of the samples were measured at 600 nm 96 well plates for the pathogen viability. The biochemical pathways of the activity were examined through protein and oxidative responses (antioxidant content) according to our previous studies (Saygin and Baysal, 2022a, b). The crystal violet method was applied for the biofilm formation using microtiter methods (O'Toole, 2011; Suraju et al., 2015).

7.3. RESULTS AND DISCUSSION

According to the gravimetric measurements, the mean $PM_{2.5}$ mass concentrations were 25.0 μg/m^3 and 22.7 μg/m^3 in weekdays and weekends in Istanbul, respectively, the weekdays being equal with the target value of 25 μg/m^3 set by the European Commission for the annual mean value for $PM_{2.5}$ mass concentration (directive 2008/50/EC). On the other hand, there was no significant difference between the weekdays and weekends mass concentrations while higher averadge mass concentration obtained in weekdays. This result may expect since the sampling area located highly industrial area and air and car traffic area in Istanbul, Turkey (Figure 7.2).

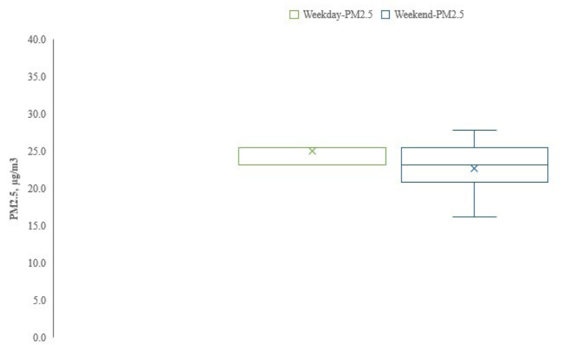

Figure 7.2. Box and whisker chart of the $PM_{2.5}$ levels of collected from outdoor during COVID-19 consecutive lock-down (weekend) and unlock-down days (weekdays)

Major elements are found in nature and serve either a structural or functional role in the cells. Moreover, these elements also find in naturally and some of them (e.g., P, K, Fe) originated mostly from anthropogenic activities or traffic emissions (Onat et al., 2013). Thus, major elemental composition under ALF and GS conditions were determined by ICP-OES. As indicated in Table 7.2, Na and Mg levels were decreased whereas K, P, and Fe levels increased under ALF conditions in weekends compared to weekdays. Moreover, different responses were obtained under GS conditions, and Na, K and Fe levels were increased however Mg and P decreased. Different response of major elements under different conditions may be originated pH of the artificial fluids and different solubility between weekdays and weekends can be influence the anthropogenic sources.

Table 7.2. Major elemental characteristic of outdoor $PM_{2.5}$ collected during COVID-19 consecutive lockdown and unlockdown days.

Element, ppm	ALF		GS	
	Weekdays	Weekends	Weekdays	Weekends
Na	16.3	ND	9.6	59.1
Mg	9.1	1.3	3.3	2.2
K	2.1	2.6	ND	2.6
P	4.9	7.4	1.8	1.1
Fe	24.9	60.7	0.1	2.5

The changes on the bacterial viability are a good indicator to observe the environmental changes under various conditions (White et al., 2020). Therefore, to understand the impact of lock-down on the ambient air quality, the activity of S. *aureus* and B. *subtilis* was examined and the results presented in Figure 7.3. The results indicated that S. *aureus* and B. *subtilis* levels under inflammatory condition (ALF) were not affected from the lock-down or unlock-down, as well as their controls. On the other hand, under interstitial fluid within the lung conditions (GS) were increased the bacterial viability in weekends compared to weekdays and control. These results indicated that inflammatory conditions repressed the anthropogenic impact on the tested bacteria, contrarily; interstitial fluid within the lung conditions influenced from the anthropogenic sources and declined the viabilities.

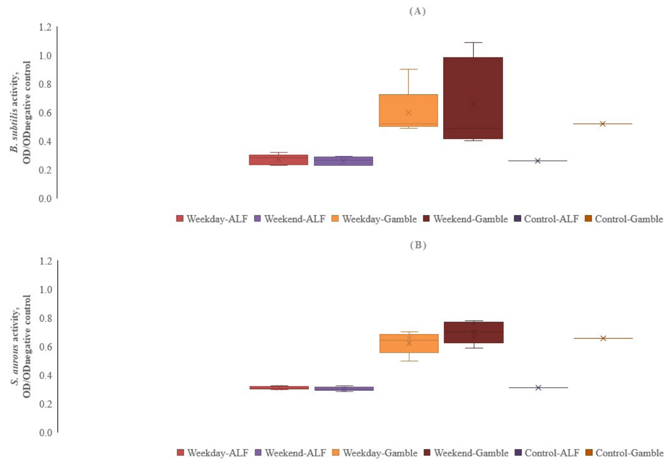

Figure 7.3. Box and whisker chart of the viability in the presence of various inhalable forms of $PM_{2.5}$ collected from outdoor during COVID-19 consecutive lock-down and unlock-down days

Biofilm formation is a way by which microorganisms survive and adjust to the involving environment, specifically adverse conditions (Malheiro and Simões, 2017; Hussey et al., 2017). Therefore, we also examined the biofilm formation of the tested bacteria under two different respiratory conditions which is ALF and GS. As illustrated in Figure 7.4, similar responses were obtained under GS condition and the biofilm production increased at lock-down weekends compared to unlock-down weekdays, however, both biofilm responses were lower when the presence of outdoor $PM_{2.5}$ rather than control groups. This result can be originated higher major elemental composition in weekends under GS conditions. However, under ALF conditions, biofilm formation behavior of S. *aureus* and B. *subtilis* was varied. Unsignificant and wide amount of B. *subtilis* biofilms formed in weekdays, whereas, restricted and lower amount of biofilms produced at weekends compared to control group. On the other hand, the S. *aureus* biofilms were similarly varied and higher at weekends. This result might be explained by the nutrient elements under ALF conditions, for instance, declining the Na and Mg, and increasing P and Fe in weekends under ALF conditions. This result can be linked with study of Suraju et al., (2015) since chemical transformation of PM component affected the pathogen behavior and oxidative characteristics.

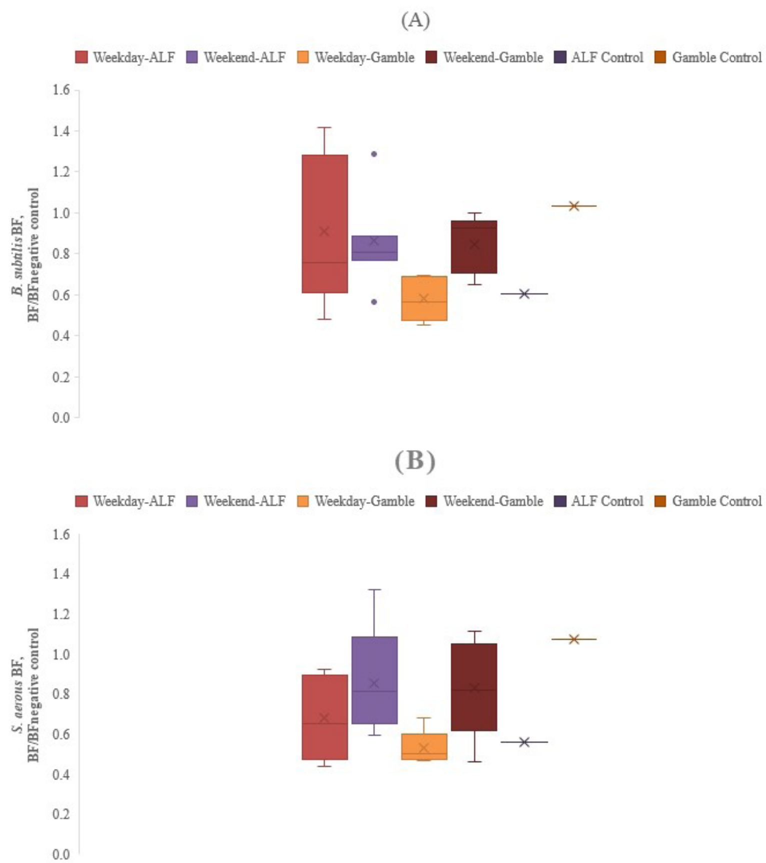

Figure 7.4. Box and whisker chart of the biofilm formation of the bacteria in the presence of various inhalable forms of $PM_{2.5}$ collected from outdoor during COVID-19 consecutive lock-down and unlock-down days

To observe the role of cell protein and oxidative sources on the viability and biofilm formation of bacteria in the presence of outdoor $PM_{2.5}$ under ALF and GS conditions, the protein and antioxidant levels were characterised (Figure 7.5 and 7.6). Since main cell responses to the different substances can be occurred by the change on the antioxidance balance due to the oxidative species (Robinson, 2017). These results indicated that both protein antioxidant behavior have a role on the bacteria viability under ALF condition. However, the activity and biofilm formation of S. aureus was influenced by the proteins, not antioxidant mechanism in the presence of outdoor $PM_{2.5}$ under GS conditions.

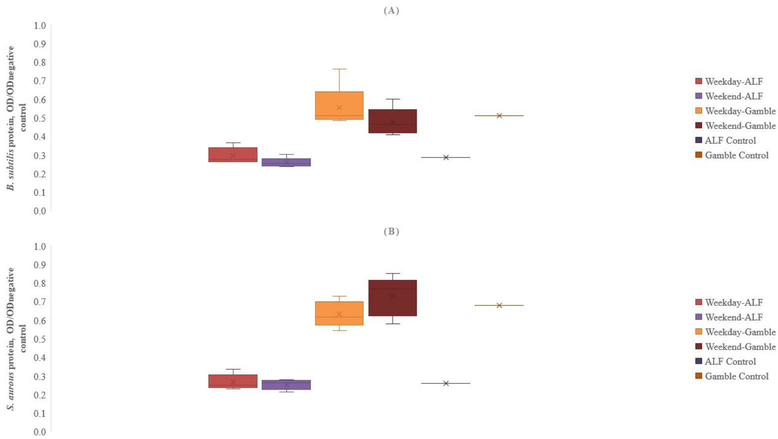

Figure 7.5. Box and whisker chart of the protein levels of bacteria in the presence of various inhalable forms of $PM_{2.5}$ collected from outdoor during COVID-19 consecutive lock-down and unlock-down days

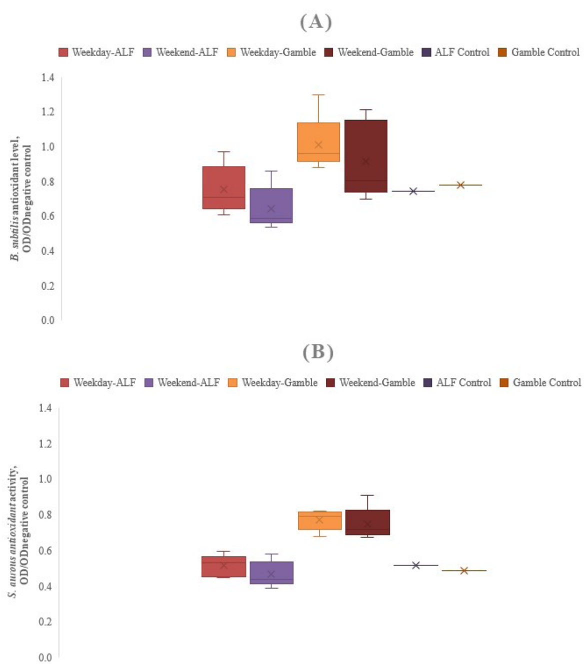

Figure 7.6. Box and whisker chart of the antioxidant levels of the bacteria in the presence of various inhalable forms of $PM_{2.5}$ collected from outdoor during COVID-19 consecutive lock-down and unlock-down days

7.4. CONCLUSION

The preliminary results of this study provide strong evidence that outdoor $PM_{2.5}$ make a substantial contribution on specific microorganisms, especially their biofilm formation, metabolic response such as protein and antioxidant activity under lung-related conditions. Moreover, solubility of major nutrients can affect from $PM_{2.5}$ collected at different anthropogenic sources and lung-related conditions. All these results indicated the importance of airborne characteristics on the bacterial response and human health.

REFERENCES

Baysal A., H. Baltaci, N. Ozbek, O. Destanoglu, G.S. Ustabasi, G. Gumus (2017), *Chemical characterization of surface snow in Istanbul (NW Turkey) and their association with atmospheric circulations.* Environental Monitoring and Assessessment. 189, 275

Baysal A., H. Saygin, G.S. Ustabasi (2020), *Microplastic Occurrences in Sediments Collected from Marmara Sea-Istanbul, Turkey.* Bulletin of Environmental Contamination and Toxicology. 105, 522–529.

Baysal A. and H. Saygin (2022), *An assessment of ecological and possible human health risks from Cr and Ni in sediments affected by the industrial marine area in Tuzla Aydinli Bay, Istanbul, Turkey between 2016–2020.* Stochastic Environmental Research and Risk Assessment. https://doi.org/10.1007/s00477-022-02289-w

Deng W.J., Y.M. Chai, H.Y. Lin, W.W.M. So, K.W.K. Ho, A.K.Y. Tsui, R.K.S. Wong (2016), *Distribution of bacteria in inhalable particles and its implications for health risks in kindergarten children in Hong Kong*. Atmospheric Environment, 128, 268-275.

Hussey S.J.K, J. Purves, N. Allcock, V.E. Fernandes, P.S. Monks, J.M. Ketley, P.W. Andrew, J.A. Morrissey (2017), *Air pollution alters Staphylococcus aureus and Streptococcus pneumoniae biofilms, antibiotic tolerance and colonisation.* Environmental Microbiology. 19(5), 1868-1880.

Kastury F., E. Smith, R.R. Karna, K.G. Scheckel, A.L. Juhasz (2018), *Methodological factors influencing inhalation bioaccessibility of metal(loid)s in PM2.5 using simulated lung fluid.* Environmental Pollution. 241, 930–937.

Li Q., F. Dong, Q. Dai, C. Zhang and L. Yu (2018), *Surface properties of $PM_{2.5}$ calcite fine particulate matter in the presence of same size bacterial cells and exocellular polymeric substances (EPS) of Bacillus mucitaginosus.* Environmental Science and Pollution Research. 25, 22429–22436.

Liu H., X. Zhang, H. Zhang, X. Yao, M. Zhou, J. Wang, Z. He, H. Zhang, L. Lou, W. Mao, P. Zheng, B. Hu (2018), *Effect of air pollution on the total bacteria and pathogenic bacteria in different sizes of particulate matter.* Environmental Pollution. 233, 483-493.

Liu M., M.K. Nobu, J. Ren, X. Jin, G. Hong, H. Yao (2020), *Bacterial compositions in inhalable particulate matters from indoor and outdoor wastewater treatment processes.* Journal of Hazardous Materials, 385, Article 121515

Pompilio A. and G. Di Bonaventura (2020), *Ambient air pollution and respiratory bacterial infections, a troubling association: epidemiology, underlying mechanisms, and future challenges.* Critical Reviews in Microbiology, 46:5, 600-630.

Robinson D.L. (2017), *Composition and oxidative potential of PM2.5 pollution and health.* Journal of Thoracic Disease. 9(3), 444-447

Malheiro J., M. Simões, Antimicrobial resistance of biofilms in medical devices. in Biofilms and Implantable Medical Devices, 2017. ISBN. 978-0-08-100382-4. Woodhead Publishing

Onat B., U.A. Sahin, T. Akyuz (2013), *Elemental characterization of PM2.5 and PM1 in dense traffic area in Istanbul, Turkey.* Atmospheric Pollution Research. 4 (1), 101-105.

O'Toole G.A. (2011), *Microtiter dish biofilm formation assay.* Journal of Visualized Experiments: JoVE. 30(47), 2437.

Ozbek N., H. Baltaci, A. Baysal (2016), *Investigation of fluorine content in PM2.5 airborne particles of Istanbul, Turkey.* Environmental Science and Pollution Research. 23, 13169–13177.

Saygin H. and A. Baysal (2022a), *Interaction of nanoplastics with simulated biological fluids and their effect on the biofilm formation.* Environmental Science and Pollution Research. https://doi.org/10.1007/s11356-022-21468-4

Saygin H. and A. Baysal (2022b), *Single and combined effects of antibiotics and nanoplastics from surgical masks and plastic bottles on pathogens.* Comparative Biochemistry and Physiology Part C: Toxicology & Pharmacology. 257, 109340.

Suraju M.O., S. Lalinde-Barnes, S. Sanamvenkata, M. Esmaeili, S. Shishodia, J.A. Rosenzweig (2015), *The effects of indoor and outdoor dust exposure on the growth, sensitivity to oxidative-stress, and biofilm production of three opportunistic bacterial pathogens.* Science of the Total Environment. 15, 538, 949-958.

White J.K., J.L. Nielsen, C.M. Larsen, A.M. Madsen (2020), *Impact of dust on airborne Staphylococcus aureus' viability, culturability, inflammogenicity, and biofilm forming capacity.* International Journal of Hygiene and Environmental Health, 230, 113608.

Woo S.H., S.M. Lee, K.C. Park, G.N. Park, B. Cho, I. Kim, J. Kim, S. Hong (2018), *Effects of fine particulate matter on pseudomonas aeruginosa adhesion and biofilm formation in vitro.* BioMed Research International. 4, 2018, 6287932

CHAPTER 8

ESTIMATING THE COOLING DEGREE DAYS EVOLUTION UNDER CLIMATE CHANGE

Dimitrios MELAS[1], Stavros KEPPAS[1], Serafim KONTOS[1], Daphne PARLIARI[1], Francesca de'DONATO[2], Stefania ARGENTINI[3], Giampietro CASASANTA[3]

[1]Aristotle University of Thessaloniki, Greece
Laboratory of Atmospheric Physics
School of Physics

[2]Regional Health Authority, Italy
Department of Epidemiology

[3]CNR-ISAC - Italian National Research Council, Italy
Institute of Atmospheric Science and Climate

Abstract

This study describes the implementation and operation of an integrated modelling system for the monitoring of the heat waves and of the urban heat island effect in the Mediterranean region. The analysis focuses on the current and future evolution of the Cooling Degree Days (CDD) under climate change during summertime. High-resolution regional climate simulations for Rome and Thessaloniki were conducted, with three 5-year time-slice periods (2006–2010, 2046–2050, 2096–2100) under the Representative Concentration Pathway (RCP) 8.5 emission scenario. The analysis revealed a considerable increase of CDD at the distant future, indicating a significant impact on the expected air conditioning energy consumption. This research was funded by National Network on Climate Change and its Impacts - CLIMPACT funded by the Public Investment Program of Greece and the LIFE Programme of the European Union in the framework of the project "Implementation of a forecasting system for urban heat island effect for the development of adaptation strategies - LIFE ASTI".

Keywords: *Urban heat island, modelling, climate change.*

8.1. INTRODUCTION

Global warming is one of the effects of the climate change. Although temperature increase is expected in most areas of the planet even under a moderate scenario (e.g., RCP4.5) of greenhouse gas emissions and concentrations in the atmosphere (Nazarenko et al., 2015), it may°Ccur with different intensities at different parts of the world (Legg, 2021).

Mediterranean Sea is frequently affected by the atmospheric conditions°Ccurring over the warm and semi-arid/arid area of north Africa, which is the main origin of heat wave episodes during summer (e.g., García-Herrera et al., 2005; Harpaz et al., 2014). In particular Eastern Mediterranean is expected to experience an average temperature increase by up to 4-6°C during summertime with an increasing number of heat waves within a longer period (e.g., Tolika et al., 2009; Michelozzi et al., 2010; Lionello et al., 2014; Zittis et al., 2016; Keppas et al., 2021). Although this warming effect due to greenhouse gasses does not seem to significantly affect the Urban Heat Island (UHI) effect in the cities (Rosenweig et al., 2005; Lauwaet et al., 2016; Roberge et al., 2018; Van der Schriek et al., 2020; Keppas et al., 2021), it will be added on the already increased urban temperatures around the world (especially during nighttime) (e.g., Christen and Vogt, 2004; Parker et al., 2010; Ciardini et al., 2019).

The increasing average annual temperature drags both winter and summer temperature to higher levels, triggering more frequent and intense heat wave episodes but less in number and intensity cold outbreaks in mid-latitude areas (McMichael et al., 2006; Rousi et al., 2022). As a result, energy demands for preserving comfortable temperature within buildings decreases during winter and presents an increasing trend in summer (Jiang et al., 2009; Lebassi et al., 2010; Petri and Caldeira, 2015; Spinoni et al., 2018), and this is enhanced in cities due to UHI effect (Santamouris et al., 2001). Energy demands for such purpose can be estimated indirectly through Cooling Degree Days (CDD) and Heating Degree Days (HDD), which are indirectly indicators of how warm or cold a day is (CIBSE, 2006).

Recent studies have shown that CDDs demonstrated an increasing trend during the last three decades in Europe (Spinoni et al., 2015; Spinoni et al., 2018). As an extreme case, Milan's CDDs boomed by 171% from 1980 to 2010, while in general, across Italian cities, there was a pronounced trend in medium season months (such as June and September) and over zones of moderate or colder climate (rather than warmer areas) (De Rosa et al., 2015). Papakostas et al. (2010) showed that CDDs increased in Athens and Thessaloniki during the period 1993-2002 by up to 69% and 21% respectively. Central and northern Europe present significant changes in CDD both in present and future. A significant CDD increase was found in Switzerland by up to 50-170% between 1901 and 2003, which is expected to further raise by up to 2100% until 2085 in Zurich (Christenson et al., 2006), while in Belgium there has been a trend of +1.4°d/year for the period 1974-2018, which is estimated at ~+2.6°d/year for the next 7 decades (Ramon et al., 2020). Finally, in the already warm climate of Indian cities, a 1-4.6°C has been ass°Ciated with 11.9-83% CDD increase by 2080 (Ukey and Rai, 2021).

In the present study, CDD projection under the business-as-usual greenhouse gas emissions scenario is investigated for the middle and the end of 21st century. The study f°Cuses on two cities (Rome and Thessaloniki), which are typically affected by heat waves during summer, and no previous works have conducted on this energy-related parameter, while both cities are estimated to be strongly affected by the climate change in the next decades (Ulbrich et al., 2006; Lelieveld et al., 2012).

8.2. METHODOLOGY AND DATA

For the simulations of the present and future climate of the cities of Rome and Thessaloniki, the Weather Research and Forecasting (WRF-ARW) numerical prediction model was used as regional climate model. The WRF future projections were produced under the National Network on Climate Change and its Impacts (CLIMPACT) project (https://climpact.gr/). Four two-way nested domains were set for simulating the climate over Europe (d01), eastern Mediterranean (d02), Thessaloniki/Rome (d03/d04, Figure 8.1) with horizontal spatial resolution of 50 km, 10 km and 2 km respectively and 35 vertical sigma layers from the surface of the Earth to the top of the model (100mb). The single-layer urban canopy model (SLUCM) was used for the better representation of physical pr°Cesses over urban areas distinguishing them into high density residential, low density and residential and industrial-commercial areas (Kusaka et al., 2001; Kusaka and Kimura, 2001). The model was run for three periods: a. 2006-2010 (referred to as the reference period), b. 2046-2050, and c. 2096-2100 producing 3-hour time interval outputs. A more detailed description of the model, its physics schemes and evaluation with observational data can be found in Keppas et al. (2021).

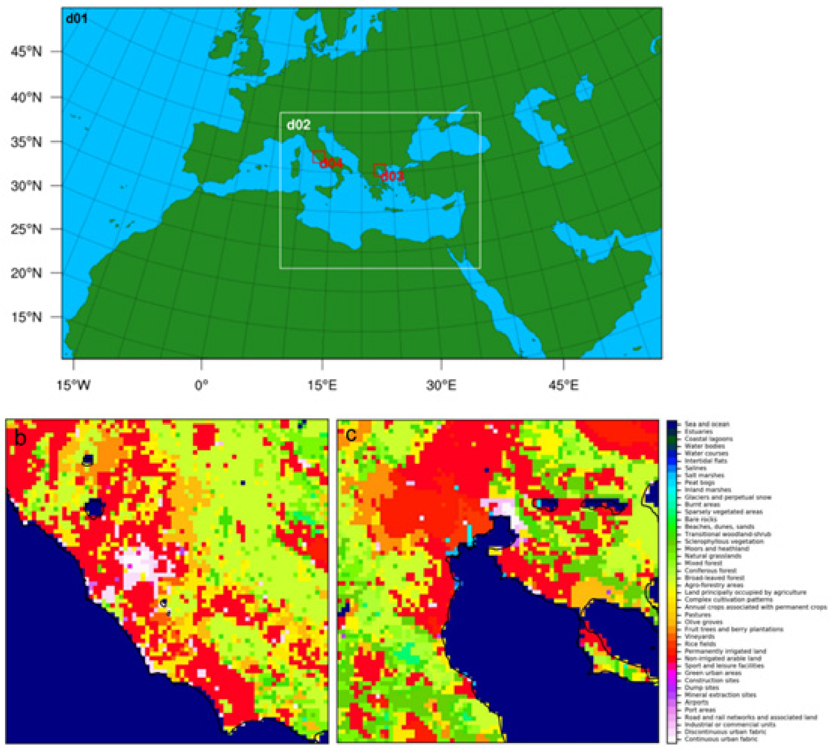

Figure 8.1. (a) Modeling domains of the study. Land use classes according to CLC for d03(b) and d04 (c).

For the land use representation, Global Land Cover by National Mapping Organizations version 1 (GLCNMO v1) was used for d01 and d02 (30arcsecs resolution) (Tateishi et al., 2011), while high resolution (~250m) Corine Land Cover (CLC) was used for d03 and d04 (Büttner, 2014). Finally, the boundary conditions, for the three periods previously mentioned, were obtained from the National Centre for Atmospheric Research (NCAR) and the Community Earth System Model (CESM), which participated in phase 5 of the Coupled Model Intercomparison Experiment (CMIP5). The data, which refer to the business-as-usual greenhouse gas emission scenario RCP8.5 (Meinshausen et al., 2011), come with a spatial resolution of 1° and a 6-hour temporal resolution. A similar set up of schemes was applied also in the operational regional WRF model, which have been applied to three large urban agglomerations of Greece in order to provide warnings about extreme weather conditions (https://urbanheat.physics.auth.gr/) in the framework of CLIMPACT.

In order to estimate the weather-related impacts on the energy demands for cooling purposes of the buildings in the two cities of interest, the index Cooling Degree-Days (CDD) was calculated using the approach in Table 8.1 (Spinoni et al., 2018). It should be noted that for the purposes of this study, T_{avg}, T_{min} and T_{max} were calculated for the areas characterized by urban land use in both cities.

Table 8.1. CDD equations with base temperature (T_{base}) =22°C depending on 4 criteria based on the comparison of daily average (T_{avg}), minimum (T_{min}) and maximum (T_{max}) temperature.

Condition	CDD Equation
$T_{max} \leq T_{base}$ (i.e., uniformly cold day)	No cooling is required so CDD = 0
$T_{avg} \leq T_{base} < T_{max}$ (i.e., mostly cold day)	$CDD = (T_{max} - T_{base})/4$
$T_{min} < T_{base} < T_{avg}$ (i.e., mostly warm day)	$CDD = ((T_{max} - T_{base})/2) - ((T_{base} - T_{min})/4)$
$T_{min} \geq T_{base}$ (i.e., uniformly warm day)	$CDD = T_{avg} - T_{base}$

The modeling system is evaluated for Thessaloniki and Rome for the year 2015, where measurements exist over urban areas. The evaluation is performed on the daily mean temperature during summertime (i.e., May-September), the parameter relevant with the CDD, utilizing common statistics (e.g., bias, correlation etc). For each city five urban stations have been selected, based on the characterization of CORINE land use database, namely for continuous urban fabric, discontinuous urban fabric and industrial or commercial units. The l°Cations of the stations for each city are depicted in Figure 8.2.

Figure 8.2. Meteorological stations in the urban areas of (a) Thessaloniki and (b) Rome used in this study.

8.3. RESULTS

8.3.1. Model Evaluation

Table 8.2 and 8.3 summarize the statistical metrics of each station for Thessaloniki and Rome, as well the overall performance of each area respectively. Concerning Thessaloniki, most of the stations underestimate by 0.15-0.99°C, with Paparrigopoulou slightly underestimating the daily mean temperatures. The RMSE on the other hand is slightly increased, relative to MB, by ~0.5°C, indicating a small tendency of the model to overestimate the variations of the daily temperatures. The cause of the latter can be seen on the scatterplot in Figure 8.3.a, where there are few days where the modelling system overestimates by ~3-4°C in the ranges of 15-17°C, 20-23°C and 27-29°C. The Pearson correlation and the IOA for all stations range between 0.93-0.95 and 0.94-0.97 respectively, showing an excellent performance of the modelling system. Overall, for Thessaloniki, the modelling performance on the daily mean temperatures for the selected period is considered as excellent (IOA~0.96).

For Rome the evaluation is showing even better performance of the modelling system, relative to Thessaloniki. Here, the MB shows a slight underestimation for all stations, but of small magnitude relative to Thessaloniki (0.1-0.77°C), with an overall bias of -0.36°C (Table 8.3). RMSE is also lower for Rome's stations, with a maximum of 1.31°C at E.U.R. station, and the most significant deviations appearing in the range of 21-25°C (Figure 8.3.b). The general performance of the modelling system in Rome's greater area is also found excellent (IOA~0.98). Summarizing for both cities, the representation of the daily mean temperatures by the modelling system is found excellent, ensuring thus the validity of the CDD analysis.

Table 8.2. Statistical metrics of the modelling system with the daily measured temperature for Thessaloniki stations for the period May-September 2015. The metrics used are the Mean Bias (MB), Pearson correlation coefficient (R), Root Mean Square Error (RMSE) and the Index of Agreement (IOA).

Stations	MB	RMSE	R	IOA
Eptapurgio	0.99	1.52	0.95	0.95
Malakopi	1.07	1.73	0.93	0.94
Martiou	0.15	1.20	0.94	0.97
Paparrigopoulou	-0.20	1.20	0.95	0.97
Pedio Areos	0.67	1.37	0.94	0.96
Overall	0.61	1.44	0.93	0.96

Table 8.3. Same as in Table 8.2, for Rome.

Stations	MB	RMSE	R	IOA
Boncompagni	-0.22	0.97	0.97	0.98
E.U.R.	-0.77	1.31	0.96	0.97
Spinaceto	-0.41	0.96	0.97	0.98
Ottavia	-0.31	1.03	0.96	0.98
Batteria	-0.10	0.95	0.97	0.98
Overall	-0.36	1.05	0.97	0.98

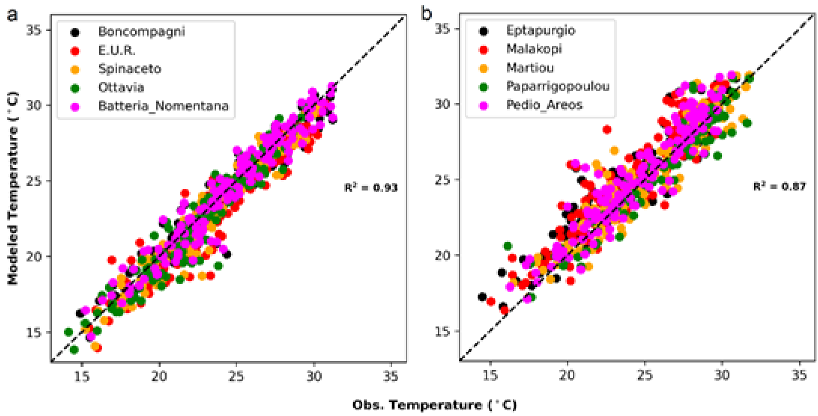

Figure 8.3. Scatterplots of the modeled versus observed daily mean temperatures for five stations in Thessaloniki (a) and Rome (b) for the period May-September 2015.

8.3.1.1. CDD Analysis

Summertime in the Mediterranean is characterized by warm and dry weather, and this is the reason that in both cities there are energy needs for cooling purposes. In the present climate, Rome exhibits a minimum average daily CDD of 1°C days in May peaking at ~4°C days in August (Figure 8.4.a), while the accumulated CDD increases from 33°C days/month in May to 132°C days/month in August (Figure 8.4.b). September presents larger, relative to May, average daily CDD by 1°C days and average accumulated CDD by 27°C days/month. Meanwhile, Thessaloniki presents higher CDD values than Rome through the entire summertime. Average daily CDD ranges from ~2°C days in May to ~7°C days in July, while the monthly accumulated CDD is 73°C/month and 206°C days in May and August respectively (Figure 8.4.d, e). In contrast το Rome, May and September are characterized by similar CDD values in Thessaloniki.

Regarding the future CDDs, a slight decrease in both cities during May by 2050 is expected (Figure 8.4.a, b, d, e). This CDD drop is larger in Rome by almost 50% (Figure 8.4.c) with daily and monthly accumulated values being <1°C days and <15°C/month. In Thessaloniki the decrease is not significant (by 12%; Figure 8.4.f). However, for the rest of summer months CDD seems to increase by 20-40% against present climate values in both cities (Figure 8.4.c, f). The largest increase for the period 2046-2050 is estimated in September (+30%) for Rome and August (+50%) for Thessaloniki.

By the end of the current century, CDD increase is dramatic in both cities, as May approaches the levels of June in present climate, while the energy needs for cooling purposes for September are estimated to be around the current warmest month's levels. In both cities, CDD will increase by more than 120% in September, reaching ~5°C days in average and accumulated monthly CDD of 140 to 164°C days per month (Rome/Thessaloniki). However, the warmest month, which is August, is far more intensive reaching ~7 and 10°C days with an accumulated CDD of 230 and 324°C days for Rome and Thessaloniki respectively (Figure 8.4.a, b, d, e). In general, CDD is expected to increase by 50-130%, and consequently the energy demand for air conditioning at the end of the century in both cities.

Under the present climate, the majority of summertime days with CDD>0 are attributed to 0-3 and 3-6°C days classes, with only 7 days per year being within 6-9°C days (Figure 8.5.a). May, June and September exhibit 18, 15 and 16 days of 0-3°C days, while July and August demonstrate 22 and 23 days in 3-6°C days class respectively. Untill 2050, days in 3-6°C days drop by 4 and, thus, days in May are characterized by 0-3°C days (Figure 8.5.b). All the other months are characterized by 17-22 days of 3-6°C days, while some days July and August (10, 7 days) appear within the area of 6-12°C days. Finally, by 2100, there will be 28 days in May with CDD between up to 6°C days (Figure 8.5.c). Meanwhile, the majority of July, August and September days (26, 23 and 25 days) will be characterized by 3-9°C days. In addition, it is expected that each of months June-September will present a small number of days (<7) with 9-12°C days.

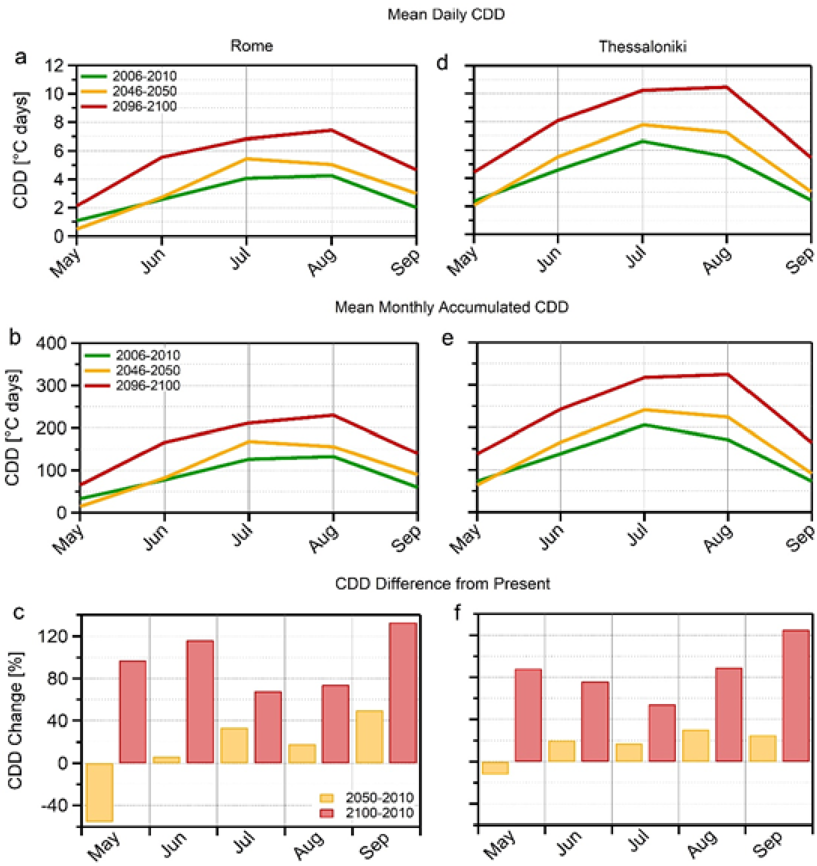

Figure 8.4. Mean daily and mean accumulated CDD per month for periods 2005-2006, 2046-2050 and 2096-2100 (depictd by green, orange and red solid lines respectively) in the cities of Rome (a, b) and Thessaloniki (d, e). The difference in the average monthly accumulated CDD between the averages of 2046-2050/2096-2100 (orange/red) and 2006-2010 are depicted for Rome (c) and Thessaloniki (f).

Thessaloniki, as already shown from CDD analysis, larger energy demands should be expected, relative to Rome, under the current climate. A possible explanation would be the fact that Rome's climate is strongly affected by a significant sea body at the west, while Thessaloniki is a city l°Cated along the coastaline of a small gulf. Almost half of May and September days are attributed to 0-3°C days bin, while ~12 days per year for each month are characterized by CDD 3-6°C days under the current climate (Figure 8.5.d).

The rest of the months are mostly distributed between 3-6 and 6-9°C days bins. In particular, June and August demonstrate 18 days with 3-6°C days each, while July is characterized by 16 days with 6-9°C days, which is slightly higher than the condition expected for July in Rome by 2100. In general, the distribution of CDD in Rome in the period 2096-2100 presents similarities with CDD distribution in Thessaloniki's present climate (Figure 8.5.c, d). By 2050, no significant changes are expected in May, June and September. However, ~25 days in July and ~22 days in August will demonstrate 6-12°C days (Figure 8.5.e). Finally, a fairly broad range of CDD is expected from 1 to 18°C days by 2100. May will include ~7 days per year with 6-12°C days, and September will be characterized by 12 days of 6-9°C days (which is <1 days for the present climate). The most energy intensive (for cooling purposes) months, July and August will demonstrate ~23 and ~22 days respectivey with 9-18°C days with >5 days to be attributed to values >12°C days (Figure 8.5.f).

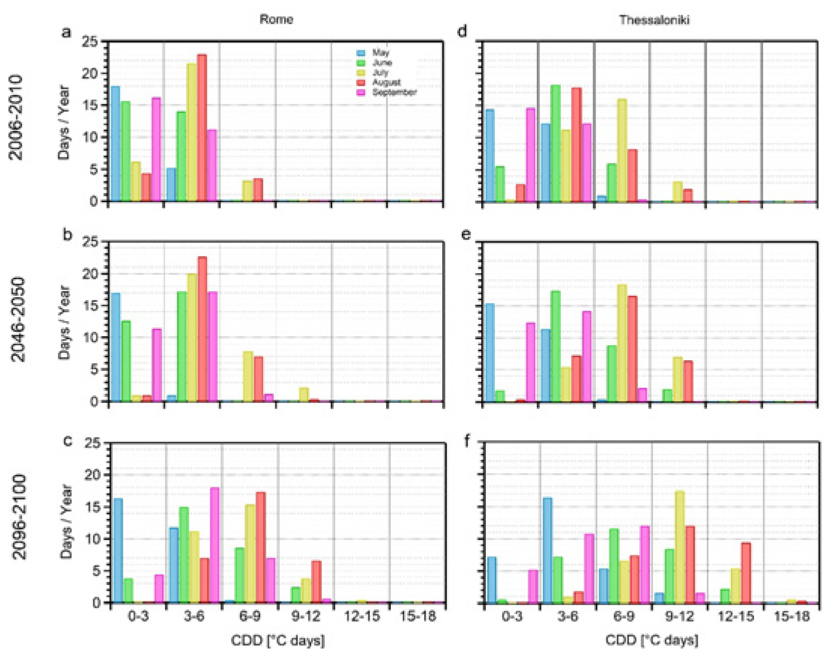

Figure 8.5. Average number of days per year for 6 different CDD classes with margins (0-3), (3-6), (6-9), (9-12), (12-15), (15-18) for periods 2006-2010, 2046-2050 and 2096-2100 for Rome (a-c) and Thessaloniki (d-f). Each month's bars appear in a certain colour defined in (a).

8.4. CONCLUSION

The present study f°Cuses on the evolution of the variable Cooling Degree Days (CDD) during the summertime in two cities of central and east Mediterranean respectively, Rome and Thessaloniki. For such purposes, the results of high spatial resolution (2km) climate simulations were utilized, that were produced for the periods 2006-2010, 2046-2050 and 2096-2100 under the RCP8.5 emission scenario. The data analysis was conducted taking into account only the urban areas enclosed by the cities of interest.

As Mediterranean already experiences hot and dry summer with increased demands for cooling purposes, energy demand future projections are of great importance to be justified. CDD is an indicator providing insights in the sector of energy and it is comprehensively analysed for both cities, which are characterized by different topography and slightly different climate.

The WRF model set up was evaluated for the summer period of 2015, utilizing five urban meteorological stations for each city. In general, the modelling system shown good performance for both Thessaloniki and Rome, with IOA above 0.9 and low biases.

The results of this study are summarized in the following key points:

- Rome exhibits lower CDD in average compared to Thessaloniki. The average daily CDD per month for Rome ranges between 1-4°C days with the minimum°Ccurring in May and the maximum in August. CDD in Thessaloniki ranges between 2-7°C days with the minimum in May/September and maximum in July.

- Average monthly accumulated CDD is maximized in August in Rome (132°C days) and in July in Thessaloniki (206°C days) in the present climate.

- In the present climate, the majority of summertime days in Rome are characterized by 0-6°C days, while in Thessaloniki May and September days are attributed to 0-6°C days bins. All the other months include days with 3-9°C days, with some days of 9-12°C days in July and August.

- In the future, CDD is expected to increase by up to ~50% by 2050 with maximum increase in September (+50%) for

Rome and August for Thessaloniki (+30%). A decrease is expected in May in Rome (-50%) and Thessaloniki (-12%). All months demonstrate increase by 2100 by 98% and 87% in Rome and Thessaloniki respectively, with the maximum percentage increase°Ccurring in September for both cities.

- By 2100, the most energy intensive month will be August with average monthly accumulated CDD of 230°C days and 324°C days in Rome and Thessaloniki.
- CDD distribution for Rome in 2100 demonstrates similar traits to CDD distribution for Thessaloniki under the current climate.
- By 2100, July and August will be characterized by 6-12°C days and 6-15°C days instead of 0-6°C days and 3-9°C days for Rome and Thessaloniki, which refer to the current climate. September will also be a month ass°Ciated with relatively high CDD especially for Thessaloniki.

Future work will benefit from the high resolution of the model, discriminating urban areas with different topographical characteristics in order to investigate the distribution of energy needs at different parts of the cities.

Acknowledgements

The participation of Dimitrios Melas, Stavros Keppas, Serafim Kontos, Daphne Parliari in this research work was supported by National Network on Climate Change and its Impacts—CLIMPACT, code number 98807, funded by the Public Investment Program of Greece, General Secretary of Research and Technology—Ministry of Development and Investments. The participation of Francesca de'Donato, Stefania Argentini, Giampietro Casasanta was supported by the LIFE Programme of the European Union in the framework of the project "Implementation of a forecasting system for urban heat island effect for the development of adaptation strategies—LIFE ASTI", grant number LIFE 17 CCA/GR/000108. Results presented in this work have been produced using the Aristotle University of Thessaloniki (AUTh) High Performance Computing Infrastructure and Resources.

REFERENCES

Büttner, G. CORINE land cover and land cover change products. In Land Use and Land Cover Mapping in Europe; Springer: Dordrecht, The Netherlands, 2014; pp. 55–74.

De Rosa, M., Bianco, V., Scarpa, F., & Tagliafico, L. A. (2015). Historical trends and current state of heating and cooling degree days in Italy. *Energy conversion and management, 90,* 323-335.

García-Herrera, R., Díaz, J., Trigo, R. M., & Hernández, E. (2005, February). Extreme summer temperatures in Iberia: health impacts and ass°Ciated synoptic conditions. In *Annales Geophysicae* (Vol. 23, No. 2, pp. 239-251). Copernicus GmbH.

Christen, A.; Vogt, R. Energy and radiation balance of a central European city. Int. J. Clim. 2004, 24, 1395–1421.

Christenson, M., Manz, H., & Gyalistras, D. (2006). Climate warming impact on degree-days and building energy demand in Switzerland. *Energy conversion and management, 47*(6), 671-686.

Ciardini, V.; Caporaso, L.; Sozzi, R.; Petenko, I.; Bolignano, A.; Morelli, M.; Melas, D.; Argentini, S. Interconnections of the urban heat island with the spatial and temporal micrometeorological variability in Rome. Urban Clim. **2019**, 29, 100493.

CIBSE, T. (2006). Degree-days: theory and application. *London: The Chartered Institution of Building Services Engineers*, 16.

Harpaz, T., Ziv, B., Saaroni, H., & Beja, E. (2014). Extreme summer temperatures in the East Mediterranean—dynamical analysis. *International Journal of Climatology, 34*(3), 849-862.

Jiang, F., Li, X., Wei, B., Hu, R., & Li, Z. (2009). Observed trends of heating and cooling degree-days in Xinjiang Province, China. *Theoretical and applied climatology, 97*(3), 349-360.

Keppas, S. C., Papadogiannaki, S., Parliari, D., Kontos, S., Poupkou, A., Tzoumaka, P., ... & Melas, D. (2021). Future climate change impact on urban heat island in two mediterranean cities based on high-resolution regional climate simulations. *Atmosphere, 12*(7), 884.

Kusaka, H., Kondo, H., Kikegawa, Y., & Kimura, F. (2001). A simple single-layer urban canopy 962 model for atmospheric models: Comparison with multi-layer and slab models. Boundary-layer 963 meteorology, 101(3), 329-358. 964

Kusaka, H., & Kimura, F. (2004). Coupling a single-layer urban canopy model with a simple 965 atmospheric model: Impact on urban heat island simulation for an idealized case. Journal of the 966 Meteorological S°Ciety of Japan. Ser. II, 82(1), 67-80.

Lauwaet, D.; De Ridder, K.; Saeed, S.; Brisson, E.; Chatterjee, F.; van Lipzig, N.; Maiheu, B.; Hooyberghs, H. Assessing the current and future urban heat island of Brussels. Urban Clim. 2016, 15, 1–15.

Legg, S. (2021). IPCC, 2021: Climate Change 2021-the Physical Science basis. *Interaction, 49*(4), 44-45.

Lebassi, B., Gonzalez, J. E., Fabris, D., & Bornstein, R. (2010). Impacts of climate change in degree days and energy demand in coastal California.

Lelieveld, J., Hadjinicolaou, P., Kostopoulou, E., Chenoweth, J., El Maayar, M., Giannakopoulos, C., ... & Xoplaki, E. (2012). Climate change and impacts in the Eastern Mediterranean and the Middle East. *Climatic change, 114*(3), 667-687.

Lionello, P., Abrantes, F., Gacic, M., Planton, S., Trigo, R., & Ulbrich, U. (2014). The climate of the Mediterranean region: research progress and climate change impacts. *Regional Environmental Change, 14*(5), 1679-1684.

McMichael, A. J., Woodruff, R. E., & Hales, S. (2006). Climate change and human health: present and future risks. *The Lancet, 367*(9513), 859-869.

Meinshausen, M.; Smith, S.J.; Calvin, K.; Daniel, J.S.; Kainuma, M.L.T.; Lamarque, J.F.; Matsumoto, K.; Montzka, S.; Raper, S.C.B.; Riahi, K.; et al. The RCP greenhouse gas concentrations and their extensions from 1765 to 2300. Clim. Chang. 2011, 109, 213–241.

Michelozzi, P., De'Donato, F. K., Bargagli, A. M., D'Ippoliti, D., De Sario, M., Marino, C., ... & Perucci, C. A. (2010). Surveillance of summer mortality and preparedness to reduce the health impact of heat waves in Italy. *International journal of environmental research and public health, 7*(5), 2256-2273.

Nazarenko, L., Schmidt, G. A., Miller, R. L., Tausnev, N., Kelley, M., Ruedy, R., ... & Zhang, J. (2015). Future climate change under RCP emission scenarios with GISS M odelE2. *Journal of Advances in Modeling Earth Systems, 7*(1), 244-267.

OrtizBeviá, M. J., Sánchez-López, G., Alvarez-Garcìa, F. J., & RuizdeElvira, A. (2012). Evolution of heating and cooling degree-days in Spain: Trends and interannual variability. *Global and Planetary Change, 92*, 236-247.

Papakostas, K., Mavromatis, T., & Kyriakis, N. (2010). Impact of the ambient temperature rise on the energy consumption for heating and cooling in residential buildings of Greece. *Renewable Energy, 35*(7), 1376-1379.

Parker, D. E. (2010). Urban heat island effects on estimates of observed climate change. *Wiley Interdisciplinary Reviews: Climate Change, 1*(1), 123-133.

Petri, Y., & Caldeira, K. (2015). Impacts of global warming on residential heating and cooling degree-days in the United States. *Scientific reports, 5*(1), 1-14.

Ramon, D., Allacker, K., De Troyer, F., Wouters, H., & van Lipzig, N. P. (2020). Future heating and cooling degree days for Belgium under a high-end climate change scenario. *Energy and Buildings, 216*, 109935.

Roberge, F.; Sushama, L. Urban heat island in current and future climates for the island of Montreal. Sustain. Cities Soc. 2018, 40, 501–512.

Rosenzweig, C.; Solecki, W.D.; Parshall, L.; Chopping, M.; Pope, G.; Goldberg, R. Characterizing the urban heat island in current and future climates in New Jersey. Glob. Environ. Chang. Part B Environ. Hazards 2005, 6, 51–62.

Rousi, E., Kornhuber, K., Beobide-Arsuaga, G., Luo, F., & Coumou, D. (2022). Accelerated western European heatwave trends linked to more-persistent double jets over Eurasia. *Nature Communications, 13*(1), 1-11.

Santamouris, M., Papanikolaou, N., Livada, I., Koronakis, I., Georgakis, C., Argiriou, A., & Assimakopoulos, D. N. (2001). On the impact of urban climate on the energy consumption of buildings. *Solar energy, 70*(3), 201-216.

Spinoni, J., Vogt, J., & Barbosa, P. (2015). European degree-day climatologies and trends for the period 1951–2011. *International Journal of Climatology, 35*(1), 25-36.

Spinoni, J., Vogt, J. V., Barbosa, P., Dosio, A., McCormick, N., Bigano, A., & Füssel, H. M. (2018). Changes of heating and cooling degree-days in Europe from 1981 to 2100. *International Journal of Climatology, 38*, e191-e208.

Tateishi, R.; Uriyangqai, B.; Al-Bilbisi, H.; Ghar, M.A.; Tsend-Ayush, J.; Kobayashi, T.; Kasimu, A.; Hoan, N.T.; Shalaby, A.; Alsaaideh, B.; et al. Production of global land cover data–GLCNMO. *Int. J. Digital Earth 2011*, 4, 22–49.

Tolika, K., Maheras, P., & Tegoulias, I. (2009). Extreme temperatures in Greece during 2007: Could this be a "return to the future"?. *Geophysical Research Letters, 36*(10).

Ukey, R., & Rai, A. C. (2021). Impact of global warming on heating and cooling degree days in major Indian cities. *Energy and Buildings, 244*, 111050.

Ulbrich, U., May, W., Li, L., Lionello, P., Pinto, J. G., & Somot, S. (2006). The Mediterranean climate change under global warming. In *Developments in earth and environmental sciences* (Vol. 4, pp. 399-415). Elsevier.

Van der Schriek, T.; Varotsos, K.V.; Giannakopoulos, C.; Founda, D. Projected future temporal trends of two different urban heat islands in Athens (Greece) under three climate change scenarios: A statistical approach. Atmosphere 2020, 11, 637.

Zittis, G., Hadjinicolaou, P., Fnais, M., & Lelieveld, J. (2016). Projected changes in heat wave characteristics in the eastern Mediterranean and the Middle East. *Regional environmental change, 16*(7), 1863-1876.

CHAPTER 9

SYNOPTIC AND MESO-SCALE OVERVIEW OF THE 13-14 JULY 2021 FLASH-FLOODS OVER THE EASTERN BLACK SEA REGION

Meral DEMİRTAŞ

University of Samsun, Türkiye
Faculty of Aeronautics and Astronautics
Department of Meteorological Engineering

Abstract

In 13-14 July, the eastern Black Sea region of Turkey experienced severe flash-floods, which led to some casualties and damages. This study examined precipitation amounts of Rize. Analysing 48-hour total precipitations of Güneysu (245 mm), Çayeli (246 mm) and Rize centre (205 mm) highlighted that they were well above July climatological average (158 mm). Examining in detail daily and maximum hourly precipitation amounts of 14 July showed that hourly maximum precipitations were very high for Güneysu, Çayeli-Bakır and Çayeli-TEİAŞ. 24-hour precipitation was 219 mm in Güneysu, and maximum hourly was 67 mm, which was about 31% of its daily precipitation. Çayeli-Bakır recorded 200 mm daily precipitation, and maximum hourly was 69 mm, which covered 35% of its daily precipitation. 24-hour precipitation was 192 mm in Çayeli-TEİAŞ, and maximum hourly precipitation was 64 mm. It indicated that 33% of daily precipitation fell in one hour. Analyses of weather maps, satellite and weather radar images and lightning data revealed surface and upper level atmospheric conditions that paved the way for the extreme precipitation events. The quasi-stationary surface low and the upper level through were located over the flood affected region and the prevailing winds transported hot and humid air of the Black Sea towards land and led to large precipitation for 2 successive days. Examining the mean sea surface temperatures (SST) of the Black Sea for 13-14 July period showed that its south-eastern part had 26-30°C which are very close to tropical SST. The SST analysis for the period 13-14 July highlighted that an extensive area of seawater being 2–4°C warmer than July climatological averages, which might be attributed to the pronounced hourly maximum precipitations.

Keywords: *Climate change, high-impact weather, the Eastern Black Sea region, flash floods.*

9.1. INTRODUCTION

Anomalous swings from one high-impact weather event to another are informally termed as "climate whiplash" or "weather whiplash", and it is attributed to the climate change induced climate variability. The summer of 2021 displayed some examples of "weather whiplash" events; some European countries and Turkey experienced various extreme weather events such as devastating flash-floods and severe heatwaves, some led to casualties and widespread structural damages. In July, catastrophic flooding events led to casualties in Austria, Belgium, Croatia, Germany, Italy, Luxembourg, the Netherlands, and Switzerland. 243 people died in these floods; 196 in Germany, 43 in Belgium, two in Romania, one in Italy and one in Austria (Web-1). On 14 July, torrents of rain led to flash floods and landslides in Rize, which is located in the eastern Black Sea Region of northern Turkey. Several houses collapsed or had buried under heavy landslides and flood accumulated debris. More than 70 roads in the flood affected region were closed. It was reported that 6 people had died and 2 went missing (Web-2).

Its topography, physiographic characteristics and location make the eastern Black Sea region very vulnerable to extreme weather conditions, e.g. large precipitation, destructive flash-floods, which can lead to fatalities, damages and disruption (Baltaci et al., 2011). The flash-flood events of 13-14 July highly affected Giresun, Trabzon, Rize, Artvin and their provinces. This study mainly highlights precipitation amounts of Rize stations to bring attention on precipitation amounts and precipitation intensity. According to Turkish State Meteorological Service's (TSMS) 1961-2020 observational records; average precipitation of July is 158.1 mm (Web-3). Examining the 48-hour total precipitations of Güneysu (245 mm), Çayeli (246 mm) and Rize centre (205 mm) showed that they received high amounts of precipitations, which were well above the July climatological average (158 mm) (Figure 9.1).

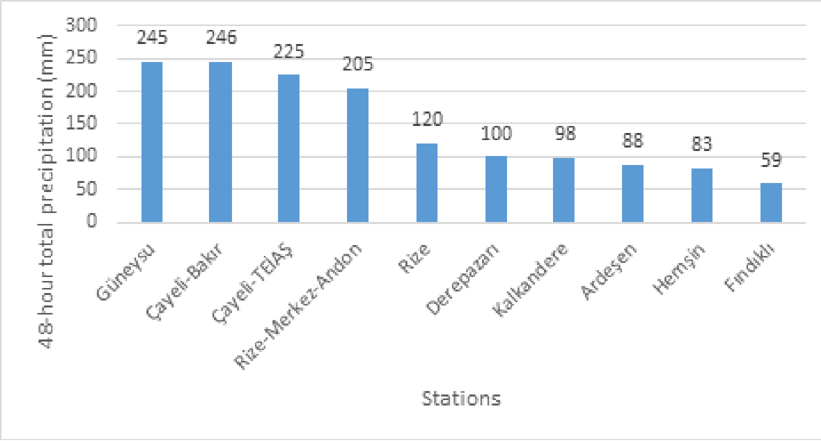

Figure 9.1. 48-hour total precipitation (in mm) for Rize and its provinces.

Analysing daily total precipitation amounts for 13-14 August shows that Rize received most of its precipitation on 14 July (Figure 9.2). Examining in detail daily and hourly maximum precipitation amounts of 14 July for Rize revealed that hourly maximum precipitation amounts were very high for Güneysu, Çayeli-Bakır and Çayeli-TEİAŞ stations. For example, on 14 July, the observed 24-hour total precipitation was 219 mm in Güneysu station, and its hourly maximum precipitation was 67 mm, which was approximately 31% percent of its daily total precipitation. Similarly, Çayeli-Bakır station recorded 200 mm daily total precipitation, and its maximum hourly precipitation was 69 mm, which covered approximately 35% percent of its daily total precipitation. The total 24-hour precipitation was 192 mm in Çayeli-TEİAŞ station, and hourly maximum precipitation was 64 mm. It indicated that 33% percent of daily precipitation fell in one hour.

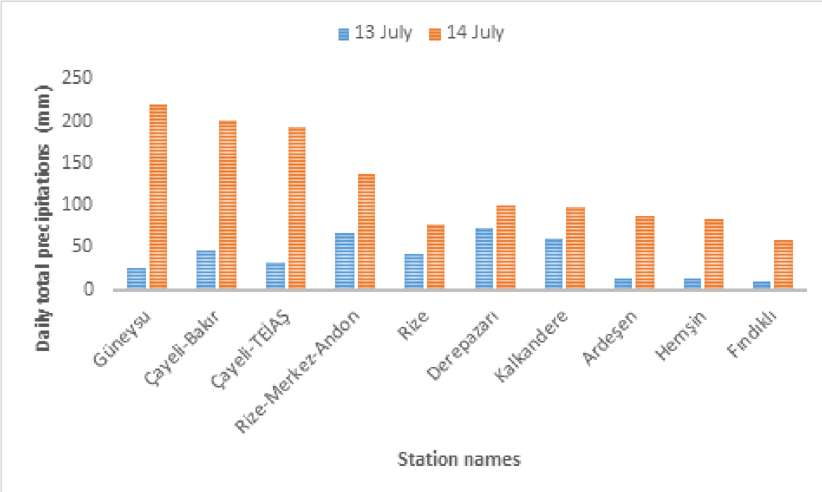

Figure 9.2. 13-14 July recorded 24-hour total precipitation (in mm) for Rize and its provinces.

9.2. MATERIAL AND METHODS

The National Oceanic and Atmospheric Administration (NOAA) - National Center for Environmental Predictions (NCEP)'s Global Forecasting System (GFS) Model simulations, which has a 0.25°x0.25° longitude-latitude grid horizontal resolution, is used to examine surface and upper-level synoptic atmospheric conditions. The Moderate Resolution Imaging Spectroradiometer (MODIS) instrument of the National Aeronautics and Space Administration (NASA) Terra satellite images are provided from the NASA's Worldview Snapshots application, part of the Earth Observing System Data and Information System (EOSDIS), which has 250 m horizontal resolution, was used for satellite based observational analysis. Lightning data are obtained from Blitzortung, and it is used for observational analysis of convective cloud activities. The reflectivity scanning of Trabzon dual polarized C-Band Doppler radar, which has a volume-scanning of 1-km horizontal resolution and 6-minute interval in a maximum radar range of 250 km, is provided by TSMS, and utilized for examining precipitation observations. Sea surface temperature (SST) data is taken from the NOAA OI SST V2 High Resolution Dataset, which is provided by the NOAA Physical Sciences Laboratory (PSL). The SST data are employed for analysing horizontal distribution of SST and its relation to climatological anomalies.

9.3. RESULTS AND DISCUSSIONS

9.3.1. A Brief Synoptic Overview

At the surface, on 13 July, while large-scale high-pressure systems were over the eastern Atlantic the north-western Europe, there were one low pressure system over the western Europe – which caused heavy rainfall and floods in Germany- and another low centre over the Black Sea (Figure 9.3.a). The low centre over the Black Sea was located from the central part of the Black Sea to its east, and accompanying precipitation was noted over the eastern Black Sea coastal regions of Turkey (Figure 9.3.a).

On 14 July day, the surface low over the Black Sea was quasi-stationary but further deepened over the same location and precipitation area extended towards the west and the east (Figure 9.3.b). This low-pressure system did not move much due to the quasi-stationary high-pressure systems on its west and its east, which helped to maintain this surface low's position and hence enabled the continuation of the related weather conditions (Demirtaş, 2016; Demirtaş, 2017).

At the 500 hPa level, on 13 July, a low centre was located over the western Europe –which played a key role in orchestrating the heavy rain and flooding in Germany and nearby countries- and there was a diffluent system to its east. On the east, a north-south elongated trough was over the northern Turkey with accompanying westerly and north westerly strong winds (Figure 9.3.c).

On the following day, the upper-level low centre on the west became further deepened, and a southwest-northeast oriented ridge formed on its east (Figure 9.3.d). The upper-level trough over the Black Sea region was almost zonal and covered the most of the Black Sea and the northern Turkey, and the strong westerly winds continued to transport hot and humid air from the Black Sea to over the flash-flood ridden Rize and its provinces (Figure 9.3.d).

The GFS model's performance in simulating precipitation was good in terms of placing it on flood affected region, but predicted precipitation amounts were very poor, this can be attributed to global model's low horizontal and vertical resolutions and associated generalized model physics. A meso-scale event of this type may be simulated better with a regional numerical weather prediction model which may have finer horizontal and vertical resolutions, and equipped well with high resolution model physics to employ explicit cumulus formation and accompanying large precipitations. Predictability of severe weather events like this one well in advance can be better handled with ensemble forecasting techniques, which contains several sets of initial and boundary conditions to address uncertainty in atmospheric flow and model physics (Demirtaş, 2016).

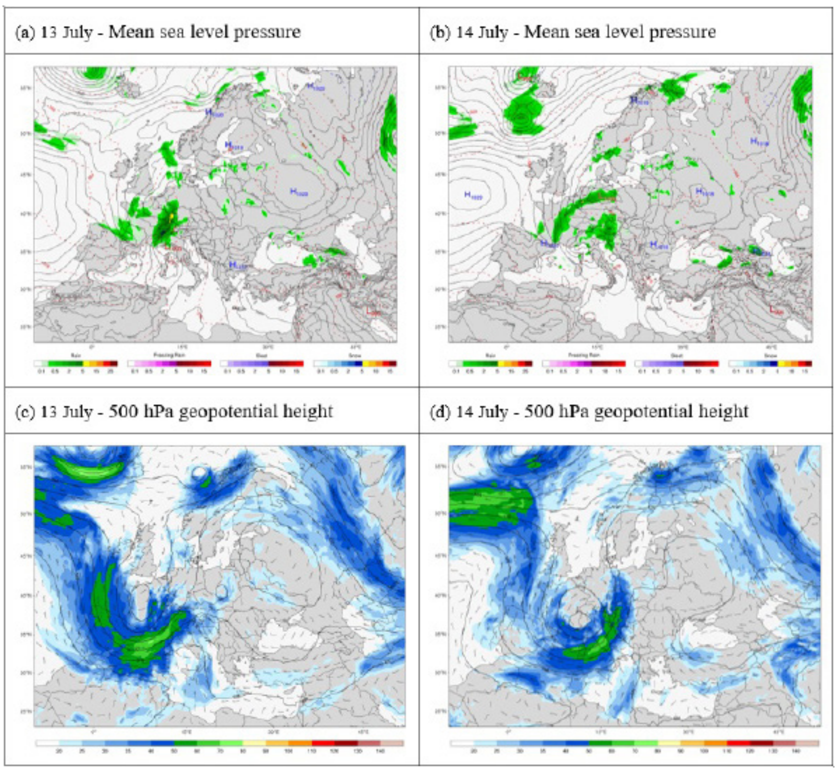

Figure 9.3. Mean sea level pressure (hPa), precipitation (mm/h) and 1000-500hPa thickness (dam) (a) 13 July; (b) 14 July; 500 hPa geopotential height (dam), wind vectors and speed (knots) (c) 13 July; (d) 14 July; (Courtesy of https://climatereanalyzer.org/) (1 knots is equal to 1 m/s.)

Sea surface temperature (SST) is one of the major climate variables due to its key role for climate variability and change.

SSTs play a vital role in extreme rainfall events by increasing or decreasing resulting precipitation amounts (Doğan et al., 2019; Demirtaş, 2016). Some research studies highlighted that the spatial pattern of the Black Sea SST has an increasing tendency (Baltaci, 2021; Mohamed et al., 2022; Sakalli et al., 2018; Meredith et al., 2015). Examining the mean SSTs of the Black Sea for 13-14 July period revealed that the south-eastern region had SSTs of 26-30°C (Figure 9.4.a). These SST values are very close to tropical SSTs (Reale and Atlas, 2001). The SST analysis for the period 13-14 July 2021 showed that an extensive area of seawater being 2–4°C warmer than the July climatological averages (Figure 9.4.b). Warmer-than-mean climatological SSTs over the Black Sea may supply anomalous amounts of sensible and latent heat fluxes, which may lead set the scene for heavy precipitation at the boundary layer. Considering the strong westerly and north-westerly winds of the quasi-stationary surface low and continuous transport of hot and humid air over the flood affected area for subsequent days, SSTs warmer than climate mean may play a key role in producing and maintaining large amounts of hourly and daily precipitations.

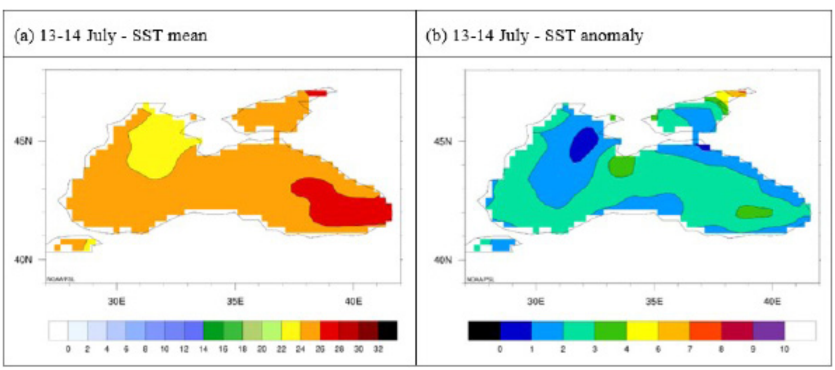

Figure 9.4. 13-14 July (a) Mean sea surface temperature; (b) Sea surface temperature anomaly.

9.3.2. A Mesoscale Overview

On the satellite image of 13 July (Figure 9.5.a), the pronounced north-south oriented cloud bands and as well as zonally placed clouds –which were parallel to the prevailing westerly and north westerly winds (Figure 9.3.c)- were noted over the eastern Black Sea region.

On 14 July, clouds converged towards south and affected north-eastern shore line of Turkey in the eastern Black Sea region (Figure 9.5.b). The continuous advection of warm and moist air from the Black Sea sustained heavy precipitations over Rize and its provinces (Figure 9.1 and Figure 9.2), and also the paces on its west (Giresun and Trabzon).

Heavy precipitation events are usually related with mesoscale convective systems (MCS), which are triggered by the upper level large-scale dynamics and a surface low transporting warm and moist air (Delrieu, et al., 2005; Nuissier, et al., 2008) and maintained by local thermodynamic conditions. MCSs may stay over a place for several hours and pave the way for heavy precipitation.

On 13 July, lightning events indicated existence of MCS over the flood affected region (Figure 9.5.c), which was in line with satellite image of the same day (Figure 9.5.a). On 14 July, lightning activities intensified and continued over the same area and hinted effects of highly active thunderstorm clouds. Intense lightening events usually indicate deep cumuliform type of cloud formations, which has high potential for intense precipitation.

The reflectivity scanning of the Trabzon dual polarized C-Band Doppler radar, which has a volume-scanning of 1-km horizontal resolution and 6-minute interval in a maximum radar range of 250 km, is presented in Figure 9.5.e-f). On 13 July, radar reflectivity based total precipitation estimates were noted particularly over Giresun and Rize at 2200 UTC (Figure 9.5.e).

On 14 July at 2100 UTC, the heavily precipitated area was noticeable over Rize and its provinces (Figure 9.5.f). Strong radar echoes hinted large amounts of accumulated precipitations, which were supported by measurements from the automated weather observing systems of TSMS (Figure 9.1 and Figure 9.2). The long stay of the rain producing convective system paved the way for intense precipitation amounts (Figure 9.2). For examples; Çayeli-Bakır's maximum hourly precipitation was 69 mm, which was about 35% percent of its daily total precipitation. Similarly, Çayeli-TEİAŞ station's hourly maximum precipitation was 64 mm, which was 33% of its daily precipitation.

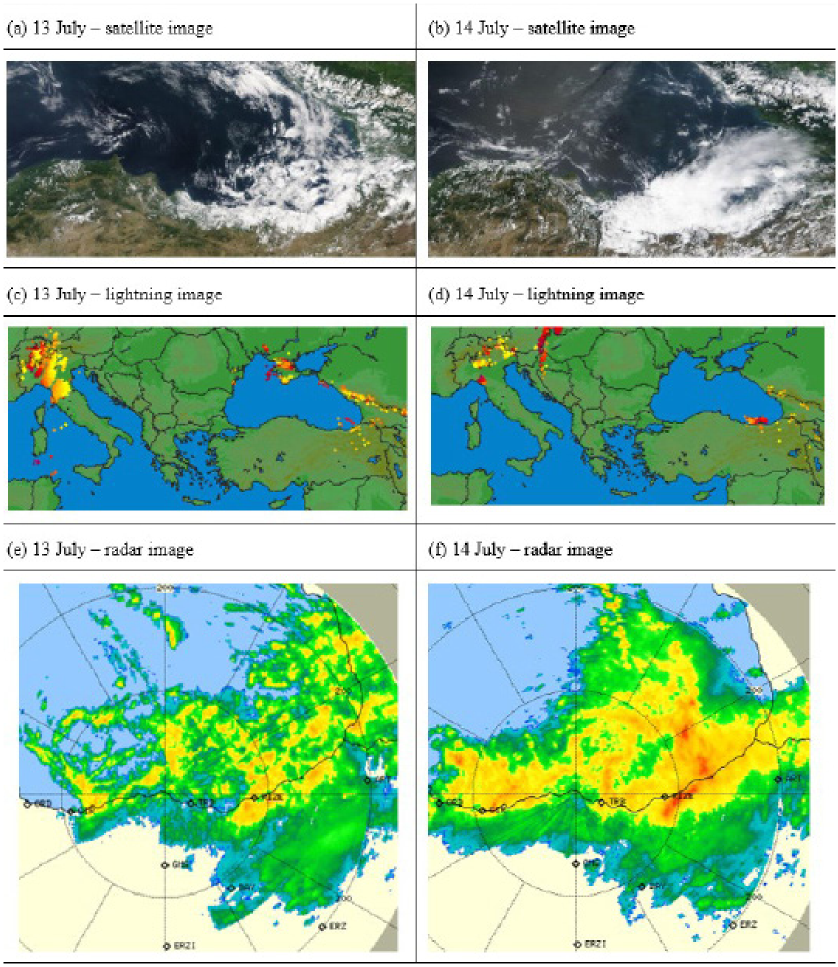

Figure 9.5. Satellite imageries from NASA Terra MODIS 7-2-1 bands with 250 m resolution for: (a) 13 July and (b) 14 July; lightning images for: (c) 13 July; (d) 14 July; TSMS Trabzon weather radar images for: (d) 13 July; (e) 14 July

9.4. CONCLUSIONS

In 13-14 July, the eastern Black Sea region of Turkey experienced severe flash-floods, which led to some casualties and structural damages. Giresun, Trabzon and Rize were affected by heavy precipitation. This study focused on recorded precipitations of Rize which has average precipitation of 158.1 mm for July (Web-3). Analysing the 48-hour total precipitations of Güneysu (245 mm), Çayeli (246 mm) and Rize centre (205 mm) highlighted that they were well above the July climatological average. Examining in detail daily and hourly maximum precipitation amounts of 14 July for Rize showed that hourly maximum precipitation amounts were very high for Güneysu, Çayeli-Bakır and Çayeli-TEİAŞ stations. The observed 24-hour total precipitation was 219 mm in Güneysu station, and its hourly maximum precipitation was 67 mm, which was approximately 31% percent of its daily total precipitation. Similarly, Çayeli-Bakır station recorded 200 mm daily total precipitation, and its maximum hourly precipitation was 69 mm, which covered approximately 35% percent of its daily total precipitation. The total 24-hour precipitation was 192 mm in Çayeli-TEİAŞ station, and hourly maximum precipitation was 64 mm. It indicated that 33% percent of daily precipitation fell in one hour.

Analyses of surface and upper-level weather maps, satellite and weather radar images and lightning data revealed surface and upper level atmospheric conditions that paved the way for the extreme precipitation and resulting devastating flash-flood events. The quasi-stationary surface low and the upper level through were located over the flood affected region and the prevailing strong westerly and north westerly winds transported hot and humid air of the Black Sea towards the land and led to large amounts of precipitation for two successive days. Examining the mean SSTs of the Black Sea for 13-14 July period showed that its south-eastern part had SSTs of 26-30°C which are very close to tropical SSTs. The SST analysis for the period 13-14 July 2021 highlighted that an extensive area of seawater being 2–4°C warmer than the July climatological averages, which might be attributed to the pronounced hourly maximum precipitations. The GFS model's performance in simulating precipitation was good in terms of placing it on flood affected region, but predicted precipitation amounts were very poor, this can be attributed to global model's low horizontal and vertical resolutions and associated generalized model physics. A meso-scale event of this type may be simulated better with a regional numerical weather prediction model which may have finer horizontal and vertical resolutions, and equipped well with high resolution model physics to employ explicit cumulus formation and accompanying large precipitations. Predictability of severe weather events like this one well in advance can be better handled with ensemble forecasting techniques, which contains several sets of initial and boundary conditions to address uncertainty in atmospheric flow and model physics (Demirtaş, 2016).

Acknowledgements

The author thanks to the Turkish State Meteorological Service for the precipitation data and Trabzon weather radar images, the NASA the Earth Observing System Data and Information System and the Worldview Snapshots application (https://wvs.earthdata.nasa.gov), the Climate Reanalyzer of the Climate Change Institute at the University of Maine for providing a platform for visualizing climate and weather datasets (https://climatereanalyzer.org/), Blitzortung for providing lightning data archives (https://www.lightningmaps.org/), and the NOAA PSL for providing OI SST V2 High Resolution Dataset and graphics.

REFERENCES

Baltaci, H. (2021), *Temporal evolution of surface humidity in Turkey: recent trends and the role of sea surface temperatures,* Theoretical and Applied Climatology, 146, 1277-1296.

Baltaci, H., Sen O.L., Kindap T. and Karaca, M. (2011), *Determination of rainfall thresholds for the landslides of Eastern Black Sea Region,* National Geographical Congress with International Participation, 7-10 September 2011, Istanbul, Turkey.

Demirtas, M. (2016), *The October 2011 devastating flash flood event of Antalya: Triggering mechanisms and quantitative precipitation forecasting,* Q. J. R. Meteorol. Society, 142, 2336–2346

Demirtaş, M. (2017), *The large scale environment of the European 2012 high-impact cold wave: prolonged upstream and downstream atmospheric blocking,* Weather, 72(10), 297-301. https://doi:10.1002/wea.302

Doğan, H., Önol, B., Turunçoğlu, U., A., Kahraman (2019), *Heavy Precipitation Sensitivity of Sea Surface Temperature over the Eastern Black Sea Region: Ensemble Simulations of Hopa / Artvin Case,* Proceedings of 9th Atmospheric Sciences Symposium, Istanbul, 23-26 October, 2019, pp. 36–43.

Mohamed, B., İbrahim, O., Nagy, H. (2022), *Sea Surface Temperature Variability and Marine Heatwaves in the Black Sea*, Remote Sens., 14, 2383. https://doi.org/10.3390/rs14102383

Sakalli, A., Başusta, N. (2018), *Sea surface temperature change in the Black Sea under climate change: A simulation of the sea surface temperature up to 2100,* Int. J. Climatol. 2018, 38, 4687–4698.

Meredith, E.P., et al., (2015), *Crucial role of Black Sea warming in amplifying the 2012 Krymsk precipitation extreme,* Nature Geoscience 8:615–620 https://doi.org/10.1038/NGEO2483

Reale, O., and Atlas, R. (2001), *Tropical cyclone-like vortices in the extratropics: Observational evidence and synoptic analysis,* Weather and Forecasting 16: 7–34.

Delrieu, et al., (2005), *The catastrophic flash-flood event of 8–9 September 2002 in the Gard region, France: A first case study for the C´evennes–Vivarais Mediterranean Hydrometeorological Observatory,* J. Hydrometeorol. 6: 34–52.

Nuissier, O., et al., (2008). "A numerical study of three catastrophic precipitating events over southern France. I: Numerical framework and synoptic ingredients", Q. J. R. Meteorol. Soc. 134: 111–130.

Web-1: https://en.wikipedia.org/wiki/2021_European_floods, accessed 15 June 2022

Web-2: https://floodlist.com/asia/turkey-floods-rize-july-2021, accessed 14 July 2022

Web-3:https://www.mgm.gov.tr/veridegerlendirme/il-ve-ilceler-istatistik.aspx?m, accessed 10 June 2022

CHAPTER 10

CMIP6 MULTI-MODEL ENSEMBLE DEVELOPMENT FOR FUTURE OFFSHORE WIND RESOURCES OF TURKEY

İrem Işık ÇETİN[1,2], İsmail YÜCEL[1,3]

[1]Middle East Technical University, Türkiye
Graduate School of Natural and Applied Sciences
Department of Earth System Sciences

[2]Climate Service Center Germany (GERICS),
Helmholtz-Zentrum Hereon, Hamburg, Germany
(current address)

[3]Middle East Technical University, Türkiye
Water Resources Laboratory
Department of Civil Engineering

Abstract

Rapid developments in technology and urgent requirement to reduce CO_2 emissions to combat climate change improves offshore wind energy market. Electricity market in Turkey shows high dependency for import while it shares %10 from onshore wind. On the other hand, Turkey has approximately 70 GW offshore wind energy potential. However, changes in the global atmospheric circulation caused by human-induced global warming result in changes for the inter/intra-annual variability of wind. Therefore, the latest generation and high-equilibrium CMIP6 climate models which are proven to be improved are used in this study to predict future offshore wind resource availability and variability for seas around Turkey. The wind speeds at 100 m, roughly represented as hub height are obtained by using hypsometric equation and shear exponent for each of 13 CMIP6 climate models. Then random forest-based regression (RF) method applied to 13 CMIP6 models are used to obtain multi-model ensemble prediction. In the analyses, historical CMIP6 period (1980-2014) is selected for train period and two different scenarios (SSP2-4.5 and SSP5-8.5) are used for test period (2014-2100). RF results showed higher correlation (> 0.85) than individual models (< 0.63) with reference data (ERA5) for all seasons. SSP2-4.5 scenario wind speeds are slightly higher than SSP5-8.5 at summer months for Marmara and Black Sea. According to RF predictions, wind speeds are expected to increase for near, mid and long period at summer months in the Black Sea (around % 10-20), spring months for Aegean Sea (around% 10) for both scenarios. Mediterranean Sea wind speeds are expected to decrease in the winter months and increase in fall by approximately 10 % for three periods.

Keywords: *Climate change, CMIP6, multi-model ensemble, offshore wind.*

10.1. INTRODUCTION

Increasing CO_2 emissions that lead to climate change during the last decades, government policies have been alerted to take actions in reducing Greenhouse Gas (GHG) emissions. Therefore, wind energy share in the electricity markets is dramatically increased both in the World and in Turkey over the last decades. World has reached 894 GW wind energy installed capacity by the end of 2021. Global offshore wind power capacity has also reached at 57 GW by the end of 2021 (GWEC, 2022). Currently, as of 2021, Turkey's installed onshore wind power capacity is exceeded 10 GW. Besides, Turkey's total installed electricity capacity is approximately 99.5 GW and the share of wind energy is approximately % 10 of total installed capacity (Web-1). It is also estimated that Turkey has approximately 70 GW offshore wind energy potential. Moreover, Turkey had also launched 1.2 GW Offshore Wind Power tender, which is postponed due to the market conditions and lack of on-site measurements (GWEC, 2022). However, there are still no offshore wind measurement in Turkey especially for the wind energy applications. Therefore, global re-analysis data and Earth System Models (ESM) can be a good alternative to determine past and future wind resource conditions.

Wind speed changes due to the climate change are widely investigated in the current literature (Carvalho et al., 2021; Costoya et al., 2021). Moreover, in order to take an advantage of each Global Circulation Model (GCM), multimodel ensemble (MME) techniques are advised (Tebaldi, C., and Knutti, R, 2007). However, multi model ensemble studies are mostly used simple mean ensemble for individual models. These techniques are also used in many studies use climate projections (Akinsanola et al., 2021; McInnes et al., 2011; Tobin et al., 2016). However, machine learning approaches involving ensemble approach of GCM are limited in the literature except some short term wind power forecasting studies (Niu et al., 2018; Vassallo et al., 2020). On the other hand, wind turbine heights are also getting higher with the advances in the technology. Therefore, 100 m hub heights for turbines require extrapolation of 10 m surface wind speeds from ESMs.

Within this study, it is aimed to determine wind speed variability of the recent climate projections from Coupled Model Intercomparison Project-6 (CMIP6)-based ESM models for surrounding seas around Turkey for future offshore wind energy installation possibilities. CMIP6s projections with two different scenarios (SSP 4.5 and SSP 8.5) are evaluated using random forest (multi-model ensemble) prediction method. In order to make the analyses at turbine-heights the pressure level winds taken from 1000 mb are converted to 100 m height using hypsometric equation and power law. The advantage of using random forest-based ensemble method for multiple CMIP6 models is also sought. The possible changes in the offshore wind speeds during entire 21st century is also reported.

10.2. DATA AND METHOD

10.2.1. Study Area

Study area including internal Marmara Sea and three seas around Turkey is shown in Figure 10.1.

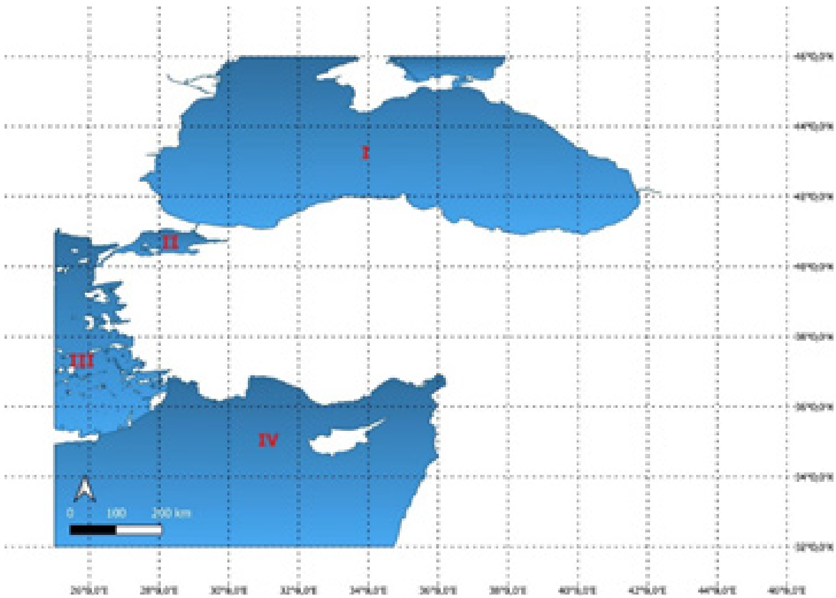

Figure 10.1. Study Area including the seas surrounding Turkey (I: Black Sea, II: Marmara Sea, III: Aegean Sea, IV: Mediterranean Sea) (Flanders Marine Institute, 2018)

10.2.2. Data

13 CMIP6 models (Table 10.1) with monthly time step specific humidity (huss), surface temperature (tas), wind speed, (sfcWind) and pressure (ps), northward (ua) and eastward (va) wind speeds at pressure levels for historical, SPP2-4.5 and SSP5-8.5 scenarios are obtained from Copernicus Climate Change Services (Web-2). Reference data is ERA5 re-analysis data which has been used for many years to determine available wind resources both in the literature and wind energy market. The hourly ERA5 wind speed data at 10 m and 100 m have been obtained from Copernicus Climate Change Services (Web-2) with a 0.25-degree spatial resolution from 1980 to 2020 (Hersbach et al., 2018).

Table 10.1. CMIP6 GCMs used in this study

No	Model Name	Resolution (degree)	Institute	References
GCM1	AWI-CM-1-1-MR	0.9 × 0.9	Alfred Wegener Institute for Polar and Marine Research (Germany)	(Semmler et al., 2018)
GCM 2	CanESM5-CanOE	2.8 × 2.8	Canadian Climate Centre (Canada)	(Swart et al., 2019)
GCM 3	CESM2	1.3x0.9	National Center for Atmospheric Research (USA)	(Danabasoglu, 2019)
GCM 4	CMCC-ESM2	1.3x0.9	Fondazione Centro Euro-Mediterraneo sui Cambiamenti Climatici (Italy)	(Peano et al., 2020)
GCM 5	GFDL-ESM4	1.3x1.0	Geophysical Fluid Dynamics Laboratory (USA)	(Guo et al., 2019)
GCM 6	FIO-ESM-2-0	1.3x0.9	First Institute of Oceanography, State Oceanic Administration (China)	(Song et al., 2019)
GCM 7	INM-CM4-8	2.0x1.5	Russian Institute for Numerical Mathematics Climate Model (Russia)	(Volodin et al., 2019a)
GCM 8	INM-CM5-0	1.5 × 2.0	Russian Institute for Numerical Mathematics Climate Model (Russia)	(Volodin et al., 2019b)
GCM 9	IPSL-CM6A-LR	2.5 × 1.3	Institute Pierre-Simon Laplace (France)	(Boucher et al., 2018)
GCM 10	MIROC6	1.4x1.4	National Institute for Environmental Studies, The University of Tokyo (Japan)	(Tatebe & Watanabe, 2018)
GCM 11	MPI-ESM1-2-LR	1.9x1.9	Max Planck Institute (Germany)	(Wieners et al., 2019)
GCM 12	NorESM2-MM	1.3x0.9	Norwegian Climate Center (Norway)	(Bentsen et al., 2019)
GCM 13	TaiESM1	1.25×0.94	Research Center for Environmental Changes, Academia Sinica (Taiwan)	(Lee & Liang, 2020)

10.3. METHOD

10.3.1. Calculation of the Wind Speeds at 100 m Heights

In order to obtain CMIP6 wind speeds at 100 m, all available models are investigated. In order to calculate the thickness (m) between surface and 1000 mb pressure level, hypsometric equation is used where h is the height between two levels, p_1 is the pressure of the surface level, p_2 is the 1000 mb, g is the gravity, Rd is the ideal gas constant (287 J K^{-1} kg^{-1}) and T_v is the virtual temperature.

$$h = z2 - z1 = \frac{R_d * T_v}{g} * \ln(\frac{p_1}{p_2}) \tag{10.1}$$

Virtual temperature (T_v) is calculated by using specific humidty (q)(kg/kg) and temperature (T)^{0}K at related level.

$$\mathrm{T_V} = (1 + 0.61\mathrm{q}) * \mathrm{Ts} \tag{10.2}$$

For calculating wind speeds at 100 m, power law (eq.3) is used which defines the changes of the wind speed with height.

$$WS_2 \ = \ WS_1 x (\frac{Z_2}{Z_1})^{\alpha} \tag{10.3}$$

where: WS_1 = wind speed (m/s) at height Z_1; WS_2 = wind speed (m/s) at height Z_2; Z_1 = Height 1 (lower height); Z_2 = Height 2 (upper height); α = a is the friction coefficient or Hellmann exponent. In this study shear exponent is assumed constant (0.14). Since it is the general assumption of the shear exponent (1/7) and International Electrotechnical Committee (IEC) also assumes 0.14 for offshore operational conditions (IEC, 2009).

10.3.2. Statistical Error Metrics

In order to understand the relationship between models and observations, classical error metrics, RMSE, Pbias and Pearson Correlation coefficients have been calculated between ERA5 grids and observations. Equation 4 explains the RMSE formula which includes "a" that is an actual value (observation), "f" is a forecasted value; "n" is the number of data. RMSE is widely used for determining errors studies in literature; this is because square values of errors show bigger errors with bigger values. The weight of errors is increased by using RMSE.

$$\boldsymbol{RMSE} = \sqrt{\frac{\boldsymbol{1}}{\boldsymbol{n}} \boldsymbol{x} \sum_{\boldsymbol{i=1}}^{\boldsymbol{n}} (\boldsymbol{a} - \boldsymbol{f})^2} \tag{10.4}$$

Equation 5 shows the calculation of percent bias to understand percentage of differences between models and reference data. PBIAS calculations are made for MME results.

$$\boldsymbol{PBIAS}\ (\%) = \frac{\sum_{i=1}^{n}(f - a)}{\sum_{i=1}^{n}(a)}\ x100 \tag{10.5}$$

Equation 6 defines correlation coefficient for two variables. It is used for determining the linear relationship between two variables. a_i is the actual wind speed in each time step on monthly time interval (i), $\bar{a}$ is the actual avarage wind speed for entire time period or each season for seasonal results, f_i and $\bar{f}$ is same but for forecast.

$$\boldsymbol{r} = \frac{\sum((\boldsymbol{a_i} - \overline{\boldsymbol{a}})\ \boldsymbol{x}\ (\boldsymbol{f_i} - \overline{\boldsymbol{f}})}{\sqrt{\sum\ (\boldsymbol{a_i} - \overline{\boldsymbol{a}})^2\ \boldsymbol{x}\ \sum(\boldsymbol{f_i} - \overline{\boldsymbol{f}})^2}} \tag{10.6}$$

Equation 10.7 shows the Standard Deviation of Error (SDE).

$$\mathbf{SDE}{=}\mathrm{std} \sum_{i=1}^{n} (f{-}a) \tag{10.7}$$

10.3.3. Random Forest Regression Development for Multi-model Ensemble

Random forest (RF) method is used in this study to increase the individual model performances and determine the performance of RF among other multiple linear regression. The method is a machine learning approach to produce multiple regressions with decision tree. Method creates decision trees based on the conditions in the model data. These trees are grown in each step of method and compares results with the reference data. Multiple decision trees in the method tend to reduce uncertainties in the predictions. The method is also successful in the large data sets (G James et al., 2013). Therefore, this method is used in this study with 13 CMIP6 model monthly data from 1980 to 2100. The method has also ability to detect non-linear relationships or composite demeanors in the data (Li et al., 2021). For 100 m wind speed calculations, all grids at each sea are averaged together with the ERA5 data. All calculations are done for historical, SSP2-4.5 and SSP5-8.5 periods. Historical period with ERA5 is chosen as the train period (1980-2014). After training the data, predictions are produced for entire test (projection) period (2014-2100). "*Python Scikit-learn: Machine learning*" packages are used to calculate random forest predictions (*Scikit-Learn: Machine Learning in Python, 2011*). Mean square error (MSE) for each decision tree is calculated for determining the best regression results from 100 decision trees. Equation 8 defines the MSE where f is the forecast a is the observation data.

$$\mathrm{MSE} = \frac{1}{n}\sum_{i=1}^{n}(f-a)^2 \tag{10.8}$$

10.4. RESULTS AND ANALYSIS

10.4.1. Model Performances

The validation of offshore models is assessed by matching the nearest GCM grid points to each ERA5 grid included in the region. After obtaining the nearest grid values for 4 regions, ERA5 wind speeds averaged for each same model grid and then the error metrics are calculated for each model and each sea. Figure 10.2 shows the correlation coefficients (CORR), root mean square error (RMSE), percent bias (PBIAS), and standard deviation error (SDE for all 4 seas and models. Although the other models have relatively high positive correlations, INM-CM4-8 and INM-CM5-0 models have mostly negative correlations and highest negative PBIAS for all seas. The lowest PBIAS values are calculated at Mediterranean Sea for GFDL-ESM4 models. The highest correlations are found for FIO-ESM-2-0 model and CMCC-ESM2 at Black Sea (> 0.63). The lowest and negative PBIAS is also valid for INM-CM4-8 and INM-CM5-0 at Black Sea and Aegean Sea (< -80). The highest negative PBIAS values can be seen for the AWI-CM-MR2 model which has also relatively high correlations at the Black Sea and Aegean Sea. However, all models are nearly underestimated the ERA5 100 m data. Due to the low resolution of the models, Marmara Sea has lower model grids than other regions. Therefore, although model performances are calculated for all models for Marmara Sea, (using closest grid point to ERA5) the region is represented with 9 CMIP6 models in the RF calculations, in contrast to other regions where they are represented with 13 GCM models.

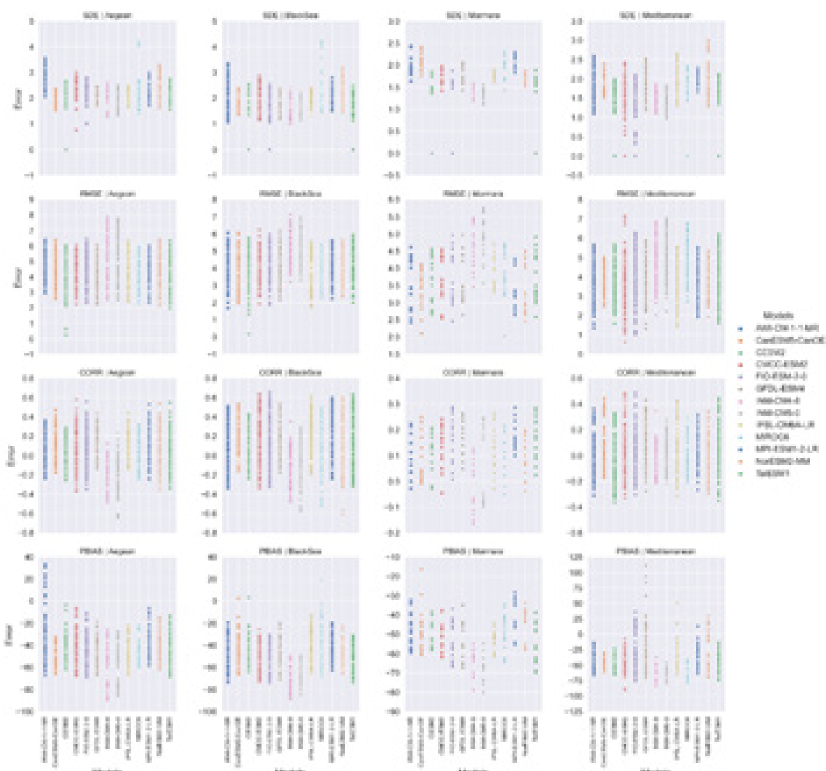

Figure 10.2. Errors between ERA5 and CMIP6 models during the train period (1980-2014) for all model grids at each region (dots represents the grid points errors associated with each model).

10.4.2. Random Forest Results for Future Scenarios

10.4.2.1. Performance Evaluation of RF Results for Train Period

Since the model data and reference data are available for 1980-2014 train period, produced predictions through RF is also evaluated with ERA5 data by using statistical error metrics at each region. GCM means are also compared with ERA5 as well. Figure 10.3 shows the box plots of individual models, produced RF predictions and ERA5 data wind speeds at the train period. Underestimation of ERA5 can be seen from each raw model but such biases are greatly reduced with the RF predictions for all seas.

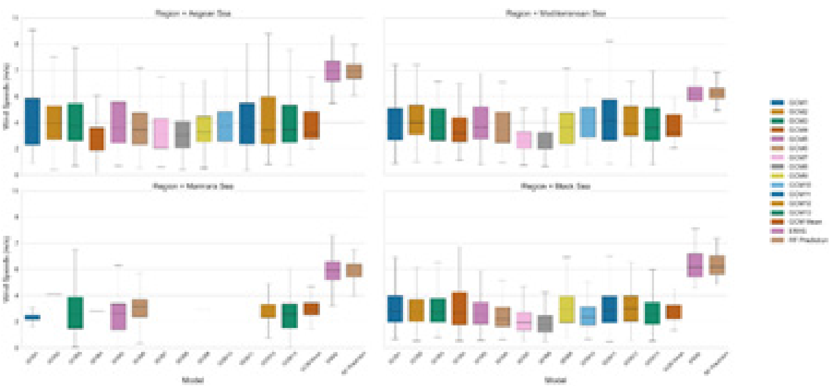

Figure 10.3. Train period wind speeds for individual models, GCM means, ERA5 and RF predictions

Seasonal RF performances during the train period are also examined and given in the Table 10.2. Marmara and Mediterranean Sea have higher RMSE for Summer and Fall seasons respectively. Correlation coefficients are very close to each other, however, Aegean Sea correlations for all seasons are higher than the other regions especially for the fall and spring seasons. The lowest correlations are found for Black Sea at summer season. Moreover, individual model performances were obviously low PBIAS (changes from -75 to 40 % see figure 10.2) when compared to the RF predictions (changes between -2.96 % and 3.78 %).

Table 10.2. Seasonal errors for RF predictions in terms of regions

REGION	SEASON	RMSE-RF	SDE-RF	PBIAS-RF	Corr-RF
Aegean Sea	DJF	0.39	0.36	-1.76	0.98
	JJA	0.33	0.33	-0.46	0.97
	MAM	0.26	0.25	0.89	0.98
	SON	0.35	0.33	1.59	0.97
Black Sea	DJF	0.32	0.30	-1.63	0.93
	JJA	0.28	0.20	3.69	0.85
	MAM	0.32	0.32	-1.00	0.97
	SON	0.27	0.27	-0.64	0.96
Marmara Sea	DJF	0.38	0.33	-2.96	0.96
	JJA	0.40	0.40	0.92	0.95
	MAM	0.31	0.30	1.28	0.96
	SON	0.32	0.32	1.00	0.96
Mediterranean Sea	DJF	0.42	0.39	-2.41	0.97
	JJA	0.17	0.17	-0.35	0.95
	MAM	0.22	0.22	-0.57	0.97
	SON	0.33	0.25	3.78	0.92

Distribution of the predicted wind speeds for train period is illustrated in Figure 10.4. As it can be seen in the figure, Aegean and Black Sea RF prediction results performed better with the ERA5 data. However, Marmara Sea results are worse than any other regions. GCM means for the Marmara and Mediterranean Sea show the negative correlations (-0.04 for Marmara Sea, -0.05 for Mediterranean Sea). This could be explained by the use of simple mean, which is not able to represent the reference data correctly.

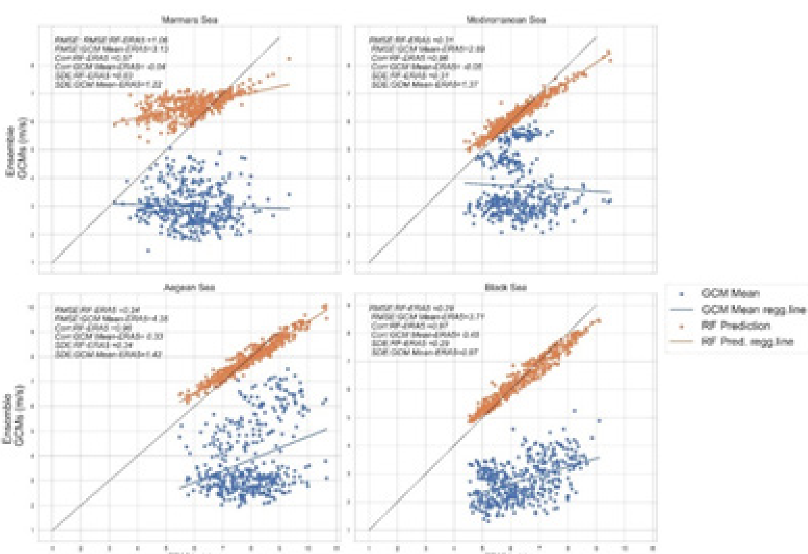

Figure 10.4. Regional scatter plots for RF prediction and GCM means versus ERA5 data

10.4.3. Time Series Analysis and Future Projections

Time series results for each region together with reference data (ERA5) are also produced for SSP2-4.5 and SSP5-8.5 scenarios at each region. As it is illustrated in Figure 10.5, ERA5 is higher than all models and model means, however random forest predictions are closer to ERA5. Aegean Sea has the highest wind speeds. Variability of wind speeds in the region are high as well.

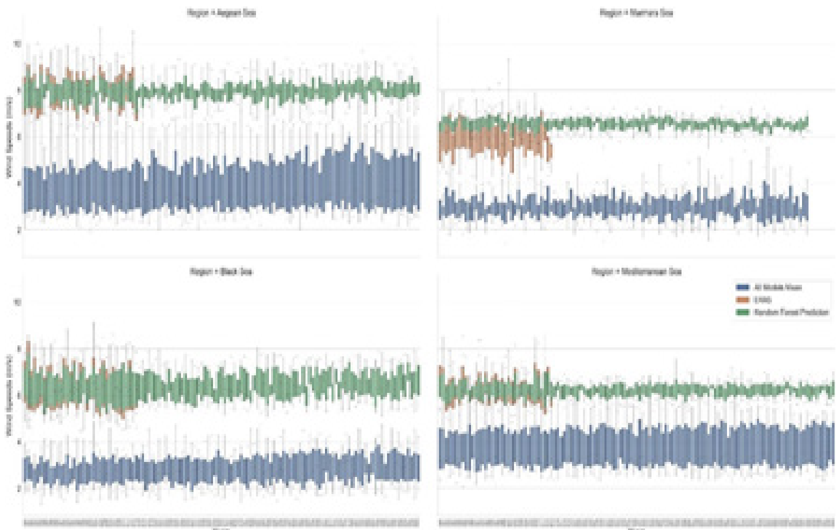

Figure 10.5. RF Predictions for entire period together with ERA5 re-analysis data and GCM means (Each boxplot represents a year which contains 12 months wind speed data)

Since the boxplots were nearly same for two scenarios, SSP2-4.5 are not illustrated in this part. However, detailed differences between scenarios can be seen in figure 10.6. Produced RF predictions for entire test period are also compared with the reference period monthly means to obtain wind speed changes for near term, mid-term, and long-term periods. Wind speeds are expected to increase for three period at summer months in the Black Sea (around % 10-20). Aegean Sea spring months are also expected to higher wind speeds for both scenarios. The difference between SSP5-8.5 and SSP2-4.5 are low, however, it is obvious especially in the Marmara Sea where negative differences occurred in the summer months.

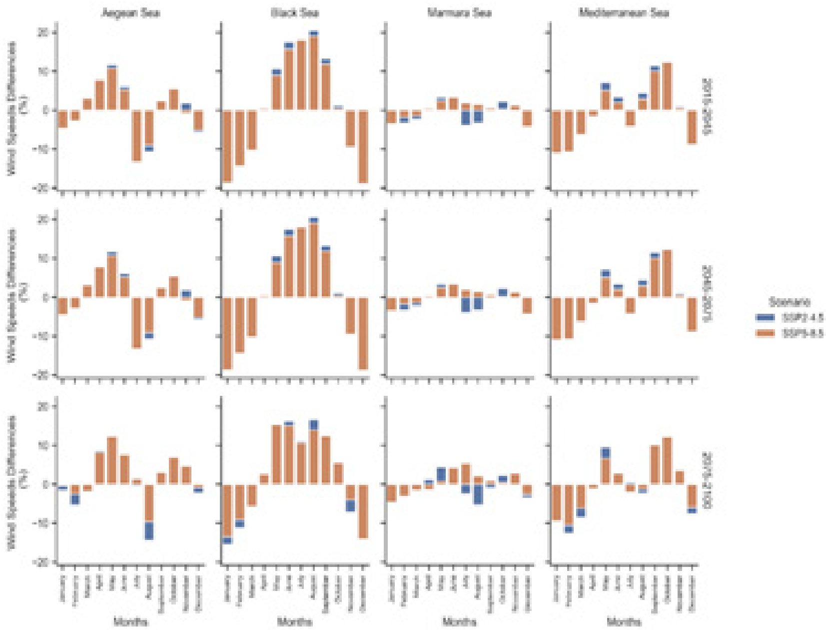

Figure 10.6. Averaged monthly wind speed changes (%) between three future periods and reference period based on ERA5 for two scenarios.

10.5. CONCLUSION

100 m wind speeds are calculated at 100 above the sea level by using pressure level CMIP6 data for surrounding seas around Turkey. Two different climate change scenarios' results for RF prediction are produced and results showed that using individual GCMs cannot represents ERA5 re-analysis data for a region.

CMIP6 models are underestimates the ERA5 data over the study area. Aegean Sea wind speeds change between 7 m/s to 10 m/s for entire study period for ERA5 and RF predictions which promise a good opportunity for offshore wind power installations during the upcoming years. Although Black Sea wind speeds change between 5-8 m/s, the winds in this region are also expected to increase by % 20 in near, mid, and long term especially in summer months. Mediterranean Sea wind speeds are expected to decrease in the winter months and increase in fall by approximately 10 %. Seasonal variability of the wind speed changes is also considered due to the increasing electricity demand for those regions in the summer months. Projected changes in the Marmara Sea are low but the reasons can be varied due to the low number of grids in this region, or it may be reasoned because of the internal sea.

RF prediction results performed better than any GCMs and correlations with the ERA5 data is found high (changes 0.85 to 0.98). Difference between scenarios is also found very small. However, SSP2-4.5 are only higher than the SSP5-8.5 for summer months at Marmara and Black Sea.

However, this study only includes the GCMs with coarse resolution which gives rough estimation about wind climatology. Therefore, further work is needed to establish to increase resolution of the GCMs due to the wind climatology requires higher resolution for better representation of the area.

Conflict of Interests

The authors declare no competing interests. This study is part of Irem Isik Cetin's PhD Thesis which is supervised by Prof.Dr. Ismail Yücel, obtained at the Department of Earth System Science, Middle East Tehnical University.

REFERENCES

Akinsanola, A. A., Ogunjobi, K. O., Abolude, A. T., & Salack, S. (2021). Projected changes in wind speed and wind energy potential over West Africa in CMIP6 models. Environmental Research Letters, 16(4), 44033. https://doi.org/10.1088/1748-9326/abed7a

Bentsen, M., Oliviè, D. J. L., Seland, Ø., Toniazzo, T., Gjermundsen, A., Graff, L. S., Debernard, J. B., Gupta, A. K., He, Y., Kirkevåg, A., Schwinger, J., Tjiputra, J., Aas, K. S., Bethke, I., Fan, Y., Griesfeller, J., Grini, A., Guo, C., Ilicak, M., . . . Schulz, M. (2019). Ncc NorESM2-MM model output prepared for CMIP6 CMIP historical. Advance online publication. https://doi.org/10.22033/ESGF/CMIP6.8040

Boucher, O., Denvil, S., Levavasseur, G., Cozic, A., Caubel, A., Foujols, M.-A., Meurdesoif, Y., Cadule, P., Devilliers, M., Ghattas, J., Lebas, N., Lurton, T., Mellul, L., Musat, I., Mignot, J., & Cheruy, F. (2018). Ipsl IPSL-CM6A-LR model output prepared for CMIP6 CMIP historical. Advance online publication. https://doi.org/10.22033/ESGF/CMIP6.5195

Carvalho, D., Rocha, A., Costoya, X., deCastro, M., & Gómez-Gesteira, M. (2021). Wind energy resource over Europe under CMIP6 future climate projections: What changes from CMIP5 to CMIP6. Renewable and Sustainable Energy Reviews, 151, 111594. https://doi.org/10.1016/j.rser.2021.111594

Costoya, X., deCastro, M., Carvalho, D., Feng, Z., & Gómez-Gesteira, M. (2021). Climate change impacts on the future offshore wind energy resource in China. Renewable Energy, 175, 731–747. https://doi.org/10.1016/j.renene.2021.05.001

Danabasoglu, G. (2019). Ncar CESM2 model output prepared for CMIP6 CMIP historical. Advance online publication. https://doi.org/10.22033/ESGF/CMIP6.7627

Flanders Marine Institute. (2018). IHO Sea Areas, version 3. https://www.marineregions.org/

G James, D Witten, T Hastie, & R Tibshirani. (2013). An introduction to statistical learning. Springer. https://link.springer.com/content/pdf/10.1007/978-1-4614-7138-7.pdf%20http://link.springer.com/10.1007/978-1-4614-7138-7.pdf

Guo, H., John, J. G., Blanton, C., McHugh, C., Nikonov, S., Radhakrishnan, A., Rand, K., Zadeh, N. T., Balaji, V., Durachta, J., Dupuis, C., Menzel, R., Robinson, T., Underwood, S., Vahlenkamp, H., Bushuk, M., Dunne, K. A., Dussin, R., Gauthier, P. P. G.,. . . Zhang, R. (2019). Noaa-GFDL GFDL-CM4 model output historical. Advance online publication. https://doi.org/10.22033/ESGF/CMIP6.8594

Global Wind Report. Küresel Rüzgar Enerjisi Konseyi. (2022).

Hersbach, H., Bell, B., Berrisford, P., Biavati, G., Horányi, A., Muñoz Sabater, J., Nicolas, J., Peubey, C., Radu, R., Rozum, I., Schepers, D., Simmons, A., Soci, C., Dee, D., & Thépaut, J.-N. (2018). ERA5 hourly data on single levels from 1979 to present. Advance online publication. https://doi.org/10.24381/cds.adbb2d47

International Electrotechnical Committee (IEC) (2009). Wind Turbines Part 3: Design Requirements for Offshore Wind Turbines. Geneva, Switzerland. IEC.

Lee, W.-L., & Liang, H.-C. (2020). As-RCEC TaiESM1.0 model output prepared for CMIP6 CMIP historical. Advance online publication. https://doi.org/10.22033/ESGF/CMIP6.9755

Li, T., Jiang, Z., Le Treut, H., Li, L., Zhao, L., & Ge, L. (2021). Machine learning to optimize climate projection over China with multi-model ensemble simulations. Environmental Research Letters, 16(9), 94028. https://doi.org/10.1088/1748-9326/ac1d0c

McInnes, K. L., Erwin, T. A., & Bathols, J. M. (2011). Global Climate Model projected changes in 10 m wind speed and direction due to anthropogenic climate change. Atmospheric Science Letters, 12(4), 325–333. https://doi.org/10.1002/asl.341

Niu, D., Di Pu, & Dai, S. (2018). Ultra-Short-Term Wind-Power Forecasting Based on the Weighted Random Forest Optimized by the Niche Immune Lion Algorithm. Energies, 11(5), 1098. https://doi.org/10.3390/en11051098

Peano, D., Lovato, T., & Materia, S. (2020). Cmcc CMCC-ESM2 model output prepared for CMIP6 LS3MIP. Advance online publication. https://doi.org/10.22033/ESGF/CMIP6.13165

Scikit-learn: Machine learning in Python. (2011). https://www.jmlr.org/papers/volume12/pedregosa11a/pedregosa11a.pdf?source=post_page

Semmler, T., Danilov, S., Rackow, T., Sidorenko, D., Barbi, D., Hegewald, J., Pradhan, H. K., Sein, D., & Wang, Q. and Jung, T. (2018). AWI-CM-1.1-MR model output prepared for CMIP6 ScenarioMIP: links to SSP126, SSP245, SSP370, and SSP585 scenarios. doi: 10.22033/ESGF/CMIP6.376

Song, Z., Qiao, F., Bao, Y., Shu, Q., Song, Y., & Yang, X. (2019). F1o-QLNM FIO-ESM2.0 model output prepared for CMIP6 GMMIP amip-hist. Advance online publication. https://doi.org/10.22033/ESGF/CMIP6.9165

Swart, N. C., Cole, J. N., Kharin, V. V., Lazare, M., Scinocca, J. F., Gillett, N. P., Anstey, J., Arora, V., Christian, J. R., Jiao, Y., Lee, W. G., Majaess, F., Saenko, O. A., Seiler, C., Seinen, C., Shao, A., Solheim, L., Salzen, K. von, Yang, D., . . . Sigmond, M. (2019). Cccma CanESM5-CanOE model output prepared for CMIP6 CMIP. Advance online publication. https://doi.org/10.22033/ESGF/CMIP6.10205

Tatebe, H., & Watanabe, M. (2018). Mıroc MIROC6 model output prepared for CMIP6 CMIP historical. Advance online publication. https://doi.org/10.22033/ESGF/CMIP6.5603

Tebaldi, C., and Knutti, R (2007). The use of the multi-model ensemble in probabilistic climate projections. Philosophical Transactions of the Royal Society a: Mathematical, Physical and Engineering Sciences.

Tobin, I., Jerez, S., Vautard, R., Thais, F., van Meijgaard, E., Prein, A., Déqué, M., Kotlarski, S., Maule, C. F., Nikulin, G., Noël, T., & Teichmann, C. (2016). Climate change impacts on the power generation potential of a European mid-century wind farms scenario. Environmental Research Letters, 11(3), 34013. https://doi.org/10.1088/1748-9326/11/3/034013

Vassallo, D., Krishnamurthy, R., Sherman, T., & Fernando, H. J. S. (2020). Analysis of Random Forest Modeling Strategies for Multi-Step Wind Speed Forecasting. Energies, 13(20), 5488. https://doi.org/10.3390/en13205488

CHAPTER 11

SPATIAL CLUSTERING OF DROUGHT INTENSITY IN TURKEY USING K-MEANS ALGORITHM

Hıdır SERKENDİZ[1], Hasan TATLI[1], Ayşegül KILIÇ[1], Mahmut ÇETİN[2], Ali SUNGUR[3]

[1] Çanakkale Onsekiz Mart University, Türkiye
Faculty of Sciences and Arts
Department of Geography

[2] University of Çukurova, Türkiye
Faculty of Agriculture
Department of Agricultural Structures and Irrigation

[3] Çanakkale Onsekiz Mart University, Türkiye
Soil Science and Plant Nutrition Department

Abstract

One of the most complex natural disasters is drought, which can spread over vast areas and has an impact on socioeconomic, biophysical, and other dimensions. With varied levels of annual water deficit, a sizable area of Turkey has a semi-arid, arid-semi-humid, or semi-humid climate. The climate of Turkey makes it particularly susceptible to drought in this situation. Therefore, it is crucial to carefully examine the peculiarities of the drought that Turkey is currently experiencing. In this context, the Standardized Precipitation and Evaporation Index technique was used in this work to analyze the geographical peculiarities of drought intensity in Turkey. First, the drought intensity was calculated from these numbers using the Run Theory method. The drought intensity was then shown to cluster regionally using the K-Means method. According to the Elbow and Silhouette approaches, the best number of clusters of drought intensity was found to be two and three, respectively. As a result, the first (low value) cluster is located in the western, southern, central, and eastern areas, whereas the second (high value) cluster is found in the western, southern, central, and eastern areas. The distribution pattern of the three-center clustering model is as follows: the first cluster contains Anatolia's west, south, central, and southeast parts; and the second cluster includes Anatolia's northern and northeastern regions.

Keywords: *Drought, SPEI, drought intensity, K-Means, Turkey.*

11.1. INTRODUCTION

Drought is one of the most complicated natural disasters, affecting various variables such as socioeconomic and biophysical and spreading over large territories. Drought, on the other hand, is a natural occurrence with no universal and precise definition (Wilhite 2005). Drought, in general, can be characterized as a shortage of precipitation, usually lasting a season or more, resulting in a lack of water for some activity, community, or environmental sector (UNISDR 2007). Wilhite and Glantz (1985) analyzed over 150 published definitions of drought and classified it into four types: meteorological, hydrological, agricultural, and socioeconomic. Meteorological drought is defined climatologically as a considerable decrease in predicted precipitation during a specific period (Wilhite 2005). The consequences of chronic precipitation shortfall on surface and ground waters, specifically streams, lake levels, and subterranean aquifers, are referred to as hydrological drought (Wilhite 2005; Türkeş et al. 2009; Tatli and Dalfes 2020). Drought in agriculture occurs when a lack of water restricts vegetative development. It happens when a lack of soil moisture creates significant plant stress (Wilhite 2005; Türkeş et al. 2009; Zarafshani et al. 2016). The consequences of meteorological, hydrological, and agricultural droughts on socioeconomic systems (water, grazing, hydroelectric power, and so on) are referred to as socioeconomic drought (Tatli and Dalfes 2020). Furthermore, the repercussions of drought are defined as economic, environmental, and social (Zarafshani et al. 2016). Drought has an economic impact by increasing product prices, water consumption, and credit; a social impact by increasing migration, poverty, low quality of life, and political work; and an environmental impact by increasing pollution, biodiversity damage, groundwater depletion, and soil erosion.

Drought in Turkey, on the other hand, has been researched from numerous perspectives. Türkeş (1990), for example, used the Erinç drought index to analyze the spatial and temporal aspects of drought episodes in Turkey between 1956 and 1987. Türkeş and Tatli (2009) suggested a new SPI approach that takes into consideration the local time averages of precipitation data to investigate the temporal and spatial aspects of drought in Turkey, and they implemented it throughout the country. Türkeş et al. (2009) used the Palmer Drought Severity Index to analyze the drought features of the Konya Section (PDSI). Furthermore, Tatli (2015) employed the SPI approach in conjunction with a new statistical downscaling tool to investigate the potential consequences of climate change on meteorological drought episodes in Turkey. Tatli and Türkeş (2011) used the PDSI and Palmer Hydrological Drought Index to assess drought occurrences in Turkey (PHDI). Models of Empirical Orthogonal Functions of the acquired values are also generated. Tatli (2021), on the other hand, used a novel approach to investigate the drought in Turkey, utilizing the conditional precipitation likelihood related with climate change.

Drought has social as well as natural components, like all natural disasters. However, both the region's vulnerability to drought and its exposure to drought contribute to the drought-related risk for any given location. In other words, it's important to know both the sorts of hazards that can affect a place and the degree of vulnerability to those hazards in order to understand natural catastrophes like drought (Wisner et al. 2004). Therefore, a good place to start when trying to understand drought vulnerability is by looking at the physical properties of drought events, such as intensity, duration, and spatial extent. This viewpoint led the authors of this study to evaluate the intensity and spatial distribution of the drought in Turkey. Using the Standardized Precipitation and Evapotranspiration Index, the 50-year drought between 1970 and 2019 was examined to determine the intensity of the drought (SPEI). Next, the Run Theory approach was used to calculate the intensity of the drought during this time. In order to expose the spatial grouping pattern of drought intensity, the K-Means clustering algorithm was applied.

11.2. DATA AND METHODOLOGY

11.2.1. Data

Monthly temperature (in °C) and total precipitation (in mm/month) data were used in this investigation. These data from 221 meteorological stations dispersed around Turkey are depicted in Figure 11.1 and are based on information from the Turkish State Meteorological Service. ArcGIS Pro software was utilized to create distribution maps, while R programming language was used for data analysis and computation.

Figure 11.1. Weather stations' locations and spatial distribution, as well as the research area's physical geography. Eastern Anatolia Region (EAR), Southeast Anatolia Region (SEAR), Central Anatolia Region (CAR), Black Sea Region (BSR), Marmara Region (MAR), Aegean Region (AR), Mediterranean Region (MEDR), Central Anatolia Region (CAR), and Southeastern Anatolia Region (SEAR).

11.2.2. Standardized Precipitation Evapotranspiration Index

Vicente-Serrano et al. (2010) state that SPEI is calculated using water-deficit (D), which is obtained by deducting potential evapotranspiration from precipitation (PET) as follows:

$$D_i = P_i - PET_i \tag{11.1}$$

where Pi, PETi, and Di stand for precipitation, evapotranspiration, and water deficit during the i-th month, respectively. The first step in the SPEI approach is the estimation of PET. This study utilized one of the many empirical methods for PET, Thornthwaite (1948). The first step in the SPEI approach is the estimation of PET. This study used the Thornthwaite (1948) method, one of the empirical approaches. As stated below (Tatli and Türkeş 2011; Thornthwaite 1948), the PET is acquired.

$$PET = dl\, 16\left(\frac{10T}{I}\right)^{b} \tag{11.2}$$

Where T is the monthly mean temperature (°C), I is the heat index, which is the sum of the 12-month heat index determined as follows, and dl is the latitude dependent correction factor used to calculate day length depending on the latitude angle of the site.

$$I = \sum_{j=}^{12} (\frac{T}{T})^{1.514} \tag{11.3}$$

Following is a computation of the constant b in Equation 2.

$$b = 6.75 \times 10^{-7} \cdot I^3 - 7.71 \times 10^{5} \cdot I^2 + 1.79 \times 10^{-2} \cdot I + 0.49 \tag{11.4}$$

A probability distribution function is fitted to the Di values in the first stage, and drought indices are computed using the inverse standardized normal distribution in the second stage. When the SPI calculation algorithm is utilized, the Gamma function is often fitted to precipitation values. On the other hand, Vicente-Serrano et al. (2010) suggested that the following definition of a log-logistics distribution would suffice.

$$f(x) = \frac{\beta}{a}\left(\frac{x-\gamma}{a}\right)^{\beta-1}\left[1+\left(\frac{x-\gamma}{a}\right)^{-2}\right] \tag{11.5}$$

Where the parameters for scale, shape, and position are represented, respectively, by, and. These log-logistic distribution parameters can be found using the L-moment technique, as seen below by Vicente-Serrano et al. (2010).

$$\beta = \frac{2w_{1-}w_0}{6w_1 - w_0 - 6w_2} \tag{11.6}$$

$$a = \frac{(w_0 - 2w_1)\beta}{\Gamma(1+1/\beta)\Gamma(1-1/\beta)} \tag{11.7}$$

$$\gamma = w_0 - a\Gamma\left(\frac{1+1}{\beta}\right)\Gamma\left(\frac{1-1}{\beta}\right) \tag{11.8}$$

Here, Γ is the Gamma function, and the probability density function, ws, can be calculated as shown below.

$$w_s = \frac{1}{N}\sum_{i=1}^{N}(1-F_i)^5 D_i \tag{11.9}$$

where the term Fi stands for empirical frequency.

$$F = \frac{i-0.35}{N} \tag{11.10}$$

I stand for the growing number of observation intervals, and N stands for the duration of the data. Using the log-logistic distribution, the probability distribution function for the D series is derived as follows.

$$F(x) = \left[1+\left(\frac{a}{x-\gamma}\right)^{\beta}\right]^{-1} \tag{11.11}$$

The SPEI value can be calculated as follows.

$$SPEI = W - \frac{C_0 + C_1W + C_2W^2}{1 + d_1W + d_2W^2 + d_3W^3} \tag{11.12}$$

where W denotes:

$$W = \sqrt{-2In(P)}\ for\ P \leq 0.5 \tag{11.13}$$

P represents the probability of exceeding a certain D value.

If P > 0.5, then $W = \sqrt{-2\ln(1-P)}$, C_0 = 2.5155, C_1 = 0.8028, C_2 = 0.203, d_1 = 1.4327, d_2 = 0.1892, d_3 = 0.0013 are the constants in Equation 12. The classification of SPEI values into drought categories is shown in Table 11.1.

Table 11.1. Standard Precipitation and Evapotranspiration Index values and classes (Tatli, 2015).

SPEI Values	Drought Class
≥ 2	Extremely wet
1.5-1.99	Vert wet
1-1.49	Moderately wet
-0.99-0.99	Near-normal
-1-1.49	Moderately dry
-1.5-1.99	Vert dry
≤ -2.00	Extremely dry

11.3. RUN THEORY

Droughts are defined by the duration, intensity, and frequency with which they occur. The Run Theory method proposed by Yevjevich (1967) used to calculate drought intensity in this study. Drought intensity is frequently predicted using Run Theory (Liu et al. 2021; Mishra et al. 2009; Mishra and Singh 2010; Wu et al. 2019). This method is defined as a part of a time series in which all values are above or below (lower or higher than the threshold) a chosen threshold (this threshold can be any value), also known as a negative or positive condition. As a result, in this study, the drought intensity is calculated as follows (Liu et al. 2021; Wu et al. 2019).

$$I = \frac{\sum_{n=1}^{T} |I_{SPEI} - K|}{T} \tag{11.14}$$

where K is the threshold value, which is *-0.5* in this case that I_{SPEI} is the number of drought values below this threshold, T is the duration of the drought, and I is the intensity of the drought.

11.4. K-MEANS ALGORITHM

Clustering can be used to find groups or clusters in data. Similarly, cluster analysis is the process of identifying meaningful groups of objects in a dataset that share common features. In this way, cluster analysis enables the analysis, identification, and utilization of information hidden in groups (Wu 2012). Cluster analysis has a wide range of applications in many fields, including life science, social science, and earth science (Lee 1981). One of the most common approaches to clustering is to define an objective function over data points and then find a partitioning that provides the best solution to the given objective function. The K-Means algorithm with a center-based objective function is used here, which is one of the oldest and most widely used clustering approaches. The center point (center of weight of the clusters) in this algorithm is set to k, and clusters are created by allocating each data point to the closest center point. The binary distance function used to determine proximity here specifies how different the two data points are from one another (Awasthi and Balcan 2016, p. 68). The most popular way for choosing the distance function, according to Wu (2012), is the Euclidean distance. Euclidean distance was therefore chosen for this study's distance function. According to Bishop (2006), the K-Means algorithm can assign data points to clusters using the following statement.

$$J = \sum_{n=1}^{N} \sum_{k=1}^{K} r_{nk} \| x_n - \mu_k \|^2 \tag{11.15}$$

where μk represents the sum of the squared distances of each data point assigned to the vector (cluster) from the cluster. The aim here is to find the r_{nk} and μk values and thus minimize J. The process here progresses in an iterative procedure involving two sequential steps corresponding to sequential optimization. First, a start value for μk is chosen. Then, in the first step, μk is kept constant and J is minimized relative to r_{nk}. In the second step, r_{nk} is kept constant and J is minimized relative to μk. This two-step optimization is repeated until convergence.

where μk is the sum of the squared distances from the cluster of each data point assigned to the vector (cluster). The goal here is to find the r_{nk} and μk values in order to minimize J. The procedure here is iterative, with two sequential steps that correspond to sequential optimization. First, a starting value for μk is determined. Then, in the first step, μk is maintained constant while J is minimized in relation to r_{nk}. The second step maintains r_{nk} constant while minimizing J relative to k. This two-step optimization process is repeated until convergence is reached.

11.5. RESULTS

The SPEI values in this study were calculated using temperature and precipitation data from 221 weather stations located throughout Turkey. The drought density of the stations was then calculated using the Run Theory approach. Finally, cluster analysis using the K-Means algorithm was performed to reveal the clustering characteristics of drought intensity.

The highest intensity values are generally found in the Aegean Region, Mediterranean Region, south of Central Anatolian Region, southeast of Anatolia Region, and east and west of Eastern Anatolia Region, according to Figure 11.2, which displays the standardized drought intensity values. The two stations with the highest levels of drought intensity are Igdir and Ceylanpinar in particular. On the other side, the north and northeastern regions have the lowest densities. The Akcakoca, Kocaeli, and Zonguldak stations in this area have the lowest density values.

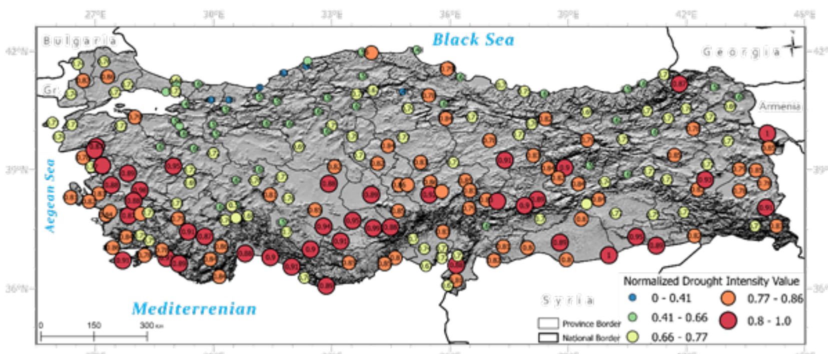

Figure 11.2. Geographical distribution of SPEI data used in the run theory approach to obtain normalized drought intensity values.

The K-Means technique grouped the drought intensity values in Figure 11.2. The number of clusters, or k-value, is known to be the most essential point in the K-Means method. While determining the k value is optional, there are some techniques to determining the ideal k value. The Elbow and Silhouette procedures are used to determine the best k value. Figure 11.3 shows the best k values for the elbow and silhouette. However, due to the size of the research region and the physical geography features, clusters ranging from 2 to 6 were constructed, since 2 or 3 clusters would not give enough representation.

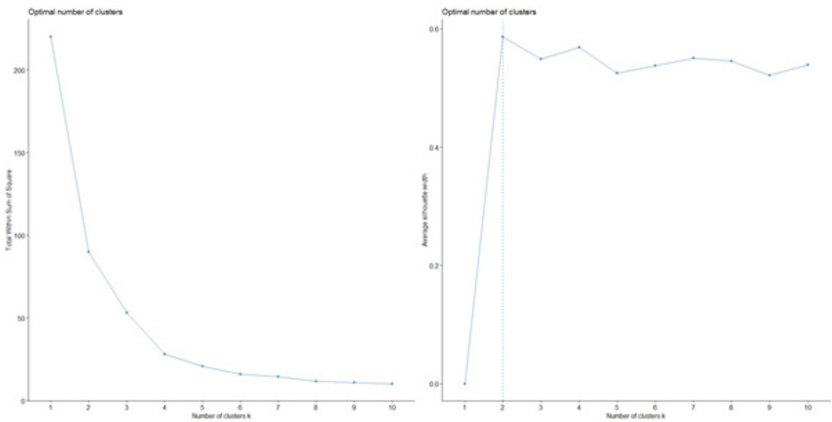

Figure 11.3. Optimal k values using the Elbow (left) and Silhouette (right) techniques. While the Elbow approach indicated the optimal number of clusters to be three, the Silhouette method advised two.

Figure 11.4 depicts the clustering pattern of the stations when the K value is set to 2. As a result, practically all stations, with the exception of those in the north and northeast, are part of the drought cluster. The drought cluster includes almost all stations in the Aegean and Mediterranean Regions where the Mediterranean climate is prominent, particularly in the west of the Marmara Region, Central Anatolia, Southeastern Anatolia, and Eastern Anatolia Regions.

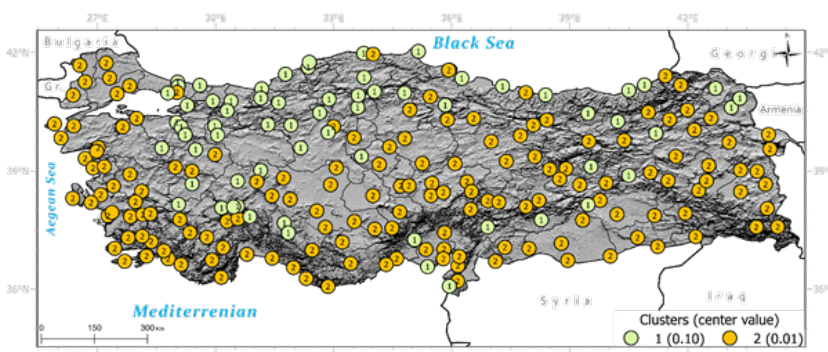

Figure 11.4. Station spatial clustering pattern when the optimum k value is specified as 2.

The geographical grouping pattern of the stations looks like Figure 11.5 when the ideal number of clusters is found to be 3. This clustering model indicates that cluster 1 is the most drought-prone cluster. As a result, this cluster includes the majority of the Aegean, Mediterranean, and Central Anatolian Regions. The cluster (3), which often has a low-density value, contains the Black Sea Region and the east of the Marmara Region. The second cluster, also known as the transition cluster, on the other hand, has a diffuse dispersion pattern. The majority of the stations in this group are located in Eastern Anatolia, the Marmara Region, and the Bay of Iskenderun.

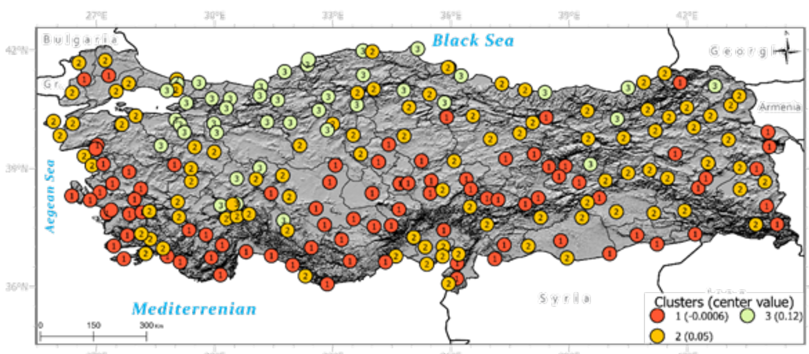

Figure 11.5. Spatial clustering pattern of stations when the optimal k value is specified as 3.

Figure 11.6 depicts the clustering pattern with the optimal k value set to 4. According to this model, the fourth cluster, which is the most droughty, consists mostly of stations in the Aegean, Mediterranean, south of Central Anatolia, Eastern and Southeastern Anatolia, and the Black Sea. Stations in the Northeast Anatolian region, on the other hand, are in the third and first clusters, which are largely low-density. The dispersed pattern is seen in the second cluster, which has the largest density following the fourth cluster. However, it is most concentrated in West Marmara, the southern Aegean Region, Iskenderun Bay, and the east and northeast of Eastern Anatolia.

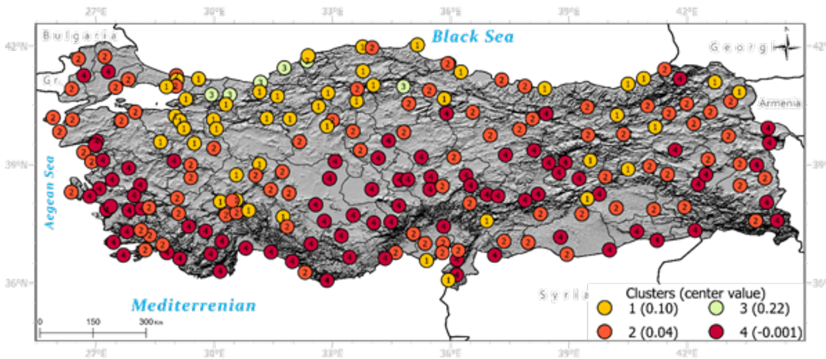

Figure 11.6. Spatial clustering pattern of stations when the optimum k value is specified as 4.

When the number of clusters is set to 5, the clustering pattern of the stations is shown in Figure 11.7. As a result, there are stations with the lowest density values in the Northeast Anatolian region of the third and second clusters. Stations in the Aegean, Marmara, Central, Southeast, and Eastern Anatolia Regions, on the other hand, are located in the 5th and 4th clusters, which have the greatest density value. The first cluster, known as the transition cluster, has a distributed clustering structure, but it is most dense in the east of Marmara Region and Iskenderun Bay.

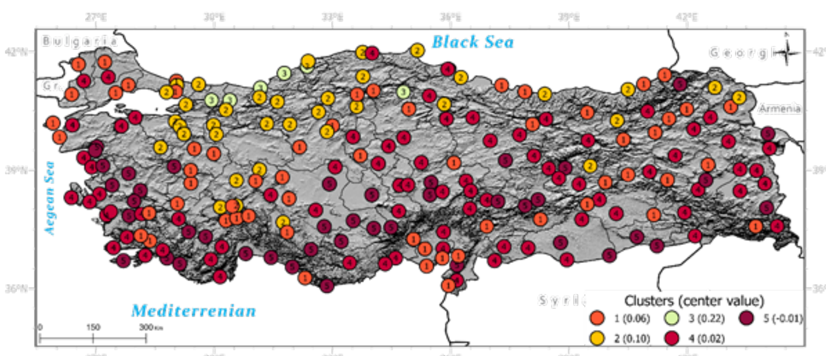

Figure 11.7. Spatial clustering pattern of stations when the optimum k value is specified as 5.

Finally, the clustering model is as shown in Figure 11.8 when the k value is set to 6. The first and sixth clusters reflect the clusters with the highest densities, respectively, according to this model. The Aegean, Mediterranean, Central, Eastern, and Southeastern areas seem to host the most of these clusters. However, as shown in other cluster patterns, the third and fourth-lowest density clusters are clustered in the Northeast Anatolian region. Finally, the second and fifth clusters, which may be referred to as transitional clusters, have a dispersed distribution pattern, although they are mostly found in the regions northeast and east of Eastern Anatolia, the Iskenderun Bay, and the east of the Marmara.

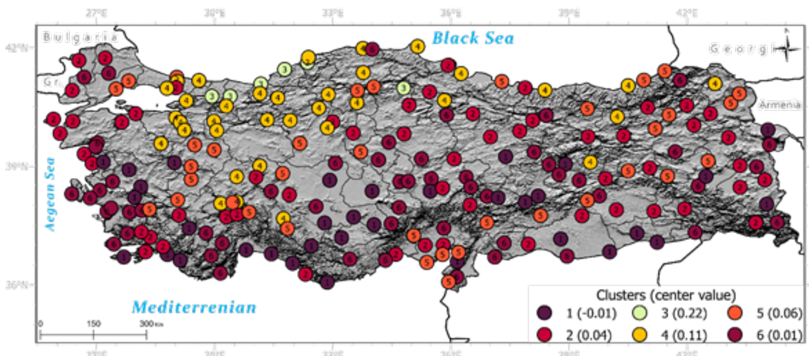

Figure 11.8. Spatial clustering pattern of stations when the optimum k value is defined as 6.

11.6. RESULTS AND DISCUSSION

First, the drought of 221 weather stations located throughout Turkey was analyzed using SPEI. Second, drought intensity is computed using the SPEI values acquired using the Run Theory technique. Finally, the geographical clustering structure of drought intensity was investigated using the K-Means technique.

To determine the optimal number of clusters, the approach proposed by Elbow and Silhouette was utilized. According to the Elbow and Silhouette procedures, the ideal cluster counts are 3 and 2, respectively. In addition to these findings, cluster configurations ranging from 2 to 6 were constructed. According to the findings, as the number of clusters rises, the spatial layout of the cluster becomes increasingly erraticIn the Elbow and Silhouette techniques, 2 and 3 ideal k values may be given based on the climatic and physical geography features of the studied region. It should be noted in this context that both techniques are successful in identifying the optimal number of clusters. In specifically, the cluster-2 approximation divides meteorological stations into two clusters: arid and humid, whereas the cluster-3 approximation divides stations into arid, humid, semi-arid, or semi-humid, respectively. As a result, the geographical clustering model of drought intensity in Turkey may be applicable for two or three groups.

Acknowledgements

This work was financed by the Turkish Scientific and Technological Research Council (TUBITAK) within the scope of 1001, project number 121O384 - Funding Program for Improving Universities' R&D Potential. The authors would like to thank TÜBTAK for their support.

REFERENCES

Awasthi, Pranjal; Balcan, Maria Florina (2016): Foundations for Center-Based Clustering: Worst-Case Approximations and Modern Developments. In Christian M. Hennig, Marina Meila, Fionn Murtagh, Roberto Rocci (Eds.): Handbook of cluster analysis. Boca Raton: CRC Press, Taylor & Francis Group (Chapman & Hall/CRC handbooks of modern statistical methods), pp. 67–100.

Bishop, Christopher M. (2006): Pattern recognition and machine learning. New York: Springer (Information Science and Statistics).

Lee, R. C. T. (1981): Clustering Analysis and Its Applications. In Julius T. Tou (Ed.): Advances in Information Systems Science. Volume 8, 169-291. Berlin: Springer.

Tatli, Hasan (2015): Downscaling standardized precipitation index via model output statistics. In *Atmósfera* 28 (2), pp. 83–98. DOI: 10.1016/S0187-6236(15)30002-3.

Tatli, Hasan (2021): Multivariate-drought indices—case studies with observations and outputs of NCAR CCSM-4 ensemble models. In *Theoretical and Applied Climatology*. DOI: 10.1007/s00704-021-03736-4.

Tatli, Hasan; Dalfes, H. Nüzhet (2020): Long-Time Memory in Drought via Detrended Fluctuation Analysis. In *Water Resources Management* 34 (3), pp. 1199–1212. DOI: 10.1007/s11269-020-02493-9.

Tatli, Hasan; Türkeş, Murat (2011): Empirical Orthogonal Function analysis of the palmer drought indices. In *Agricultural and Forest Meteorology* 151 (7), pp. 981–991. DOI: 10.1016/j.agrformet.2011.03.004.

Thornthwaite, C. W. (1948): An Approach toward a Rational Classification of Climate. In *Geographical Review* 38 (1), pp. 55–94.

Türkeş, Murat (1990): Türkiye'de Kurak Bölgeler ve Önemli Kurak Yıllar. Doktora Tezi. İstanbul Üniversitesi, İstanbul. Deniz Bilimleri ve Coğrafya Enstitüsü.

Türkeş, Murat; Akgündüz, A. Serap; Demirörs, Zerrin (2009): Palmer Kuraklık İndisi'ne Göre İç Anadolu Bölgesi'nin Konya Bölümü'ndeki Kurak Dönemler ve Kuraklık Şiddeti. In *Coğrafi Bilimler Dergisi* 7 (2), pp. 129–144. DOI: 10.1501/Cogbil_0000000102.

Türkeş, Murat; Tatli, Hasan (2009): Use of the standardized precipitation index (SPI) and a modified SPI for shaping the drought probabilities over Turkey. In *International Journal of Climatology* 29, pp. 2270–2282. DOI: 10.1002/joc.1862.

UNISDR (2007): Drought Risk Reduction Framework and Practices: Contributing to the Implementation of the Hyogo Framework for Action. United Nations secretariat of the International Strategy for Disaster Reduction. Geneva, Switzerland.

Vicente-Serrano, Sergio M.; Beguería, Santiago; López-Moreno, Juan I. (2010): A Multiscalar Drought Index Sensitive to Global Warming: The Standardized Precipitation Evapotranspiration Index. In *Journal of Climate* 23 (7), pp. 1696–1718. DOI: 10.1175/2009JCLI2909.1.

Wilhite, Donald A. (Ed.) (2005): Drought and water crises. Science, technology, and management issues / edited by Donald A. Wilhite. Boca Raton: Taylor & Francis.

Wilhite, Donald A.; Glantz, Michael H. (1985): Understanding: the Drought Phenomenon: The Role of Definitions. In *Water International* 10 (3), pp. 1–16.

Wisner, Benjamin; Blaikie, Piers; Cannon, Terry; Davis, Ian (2004): At risk. Natural hazards, people's vulnerability, and disasters. 2nd ed. London, New York: Routledge.

Wu, Junjie (2012): Advances in K-means Clustering. Berlin, Heidelberg: Springer Berlin Heidelberg.

Zarafshani, Kiumars; Sharafi, Lida; Azadi, Hossein; van Passel, Steven (2016): Vulnerability Assessment Models to Drought: Toward a Conceptual Framework. In *Sustainability* 8 (6), pp. 1–21.

CHAPTER 12

ANALYSIS OF RELATIONS BETWEEN SOLAR ACTIVITY, COSMIC RAYS AND EARTH'S CLIMATE USING MACHINE LEARNING TECHNIQUES

Bükem BELEN[1], Uğur Murat LELOĞLU[2], Melahat Bilge DEMİRKÖZ[3]

[1]Middle East Technical University, Türkiye
Institute of Marine Sciences
Department of Oceanography

[2]University of Turkish Aeronautical Association, Türkiye
Faculty of Aeronautics and Astronautics
Department of Astronautical Engineering

[3]Middle East Technical University, Türkiye
Faculty of Science
Department of Physics

Abstract

Earth's climate is part of a complicated system that can be affected by many different parameters, both internal and external. Important external forces on the climate are galactic cosmic rays (GCR) and the Sun. Some research has already been conducted to investigate the relationship between the climate and external forcers such as the GCR and solar activity. However, the relations are quite complicated and buried into almost chaotic meteorological measurements. This paper looks deeper into the interactions between them. The parameters used in the correlation analysis are GCR flux, Sunspot number (SSN), total solar irradiance (TSI), UV irradiance (UVI), and the Oceanic Niño Index (ONI) as the predictor variables; total cloud amount (TCA) and low cloud amount (LCA) as the response variables. The analysis begins with standard statistical techniques and continues with multiple regression methods. Both geographical and temporal patterns have been investigated. Machine learning (ML) methods for non-linear regression, such as random forests will further be implemented and the predictive power of the algorithm will be measured.

Keywords: *Cosmic rays, solar activity, clouds, climate, multiple regression.*

12.1. INTRODUCTION

The consequences of climate change on the earth and humanity is an urgent issue. Earth's climate is directly driven by internal parameters such as ocean currents, volcanic explosions and anthropogenic activity. However, the role of the external forces, such as galactic cosmic rays (GCR) and the Sun, are not yet fully understood.

A positive correlation between cosmic rays and the global total cloud (TC) cover between 1983-1991 was first reported by Svensmark and Friis-Christensen (1997). Extending the ISCCP data up to 1994, and investigating the cloud levels separately, the GCR correlation was found to be restricted only to low level clouds (LLCs) (Marsh & Svensmark, 2000). This correlation was suggested to be caused by the fact that the GCR data acquired from neutron monitors were located on the ground level, representing predominantly the lower regions of the atmosphere (Pallé Bagó & Butler, 2000). Higher concentrations of aerosol formation in the troposphere were also suggested to play a role in more evident association between LLCs and GCRs (Carslaw et al., 2002), (Yu, 2002). The connection between cosmic rays and clouds was provided by the effect of ions on cloud microphysics. The "Ion-Aerosol Clear-Air" can be briefly explained as the GCRs, modulated by the solar activity, generating particle cascades in the atmosphere and leading to ionization. Under the right atmospheric circumstances, this ionization causes an increase in the nucleation of aerosols and leads to the growth of cloud condensation nuclei (CCN), which are the seeds of clouds, influencing cloud properties (Carslaw et al., 2002).

The relationship between GCR ionization and the ISCCP LLC amount was found to be significant in the mid-latitude region (Pallé Bagó et al., 2004). The correlations were also improved by detrending the ISCCP LLC data and using data obtained from regions not affected by higher-level clouds (Usoskin et al., 2004) (Usoskin et al., 2006).

The reported correlations (Svensmark, 1997) became questionable when datasets were extended up to the year 2000 (Laut, 2003; Kristjánsson et al., 2008; Erlykin et al., 2009). The disappearance of strong correlation between LLC and GCR indicated that global temperatures were not affected by changes in the GCR, TSI, or SSN (Ahluwalia, 2014). Other studies found no globally significant correlation between GCR/TSI and clouds (Kristjánsson et al., 2008, Ahluwalia 2013). Investigating the solar-cosmic ray-cloud relations by using datasets from MODIS showed that there was no evidence for a solar-cloud link (Laken et al., 2012). Erlykin et al. (2009) suggested that there was no "causal connection" between GCRs and the LLC cover and that the two parameters were only correlated due to their common dependence on the TSI at the Earth. Previously observed effect of GCRs on climate could just be a result of GCRs being a proxy for solar activity rather than being a separate mechanism (Čalogović & Laken, 2015). GCRs also could not explain the current increase in global temperature, and anthropogenic forcing had to be involved (Tsonis et al., 2015).

There are also difficulties in the analysis of climate parameters. The internal climate forcings, such as volcanic activity or the El Nino Southern Oscillation (ENSO), can have similar periods of variation as solar activity, making it difficult to distinguish between the internal and external forcings on climate (Marsh & Svensmark, 2003; Voiculescu et al., 2007). The ISCCP cloud data is also not that reliable in long-term analyses (Laken et al., 2012). Therefore, there is no compelling and consistent evidence to prove the cosmic ray and cloud relationship.

As no definite statement regarding the cosmic rays-clouds-climate interactions can be made, further research is required on this controversial relationship. The present study aimed to investigate the effect the GCRs and the solar activity on Earth's climate and to define the temporal and geographic patterns by examining the existing complex data using machine learning methods. Machine learning (ML) will be used for the first time to investigate the non-linear effects of the external parameters on climate, while previous studies used standard statistical methods such as linear correlation analysis on similar datasets.

Also, different data sources of climate parameters such as the TC amount and LLC amount were investigated. The period of the datasets is extended up to 2017, and multiple regression models are used as the primary investigation methods.

12.2. DATA AND METHODS

12.2.1. Data Used

Cosmic ray flux data was obtained from the Oulu Cosmic Ray Station (ONM) operated by the Sodankyla Geophysical Observatory (Usoskin et al., 2001). Three different parameters have been used as solar activity proxies. The SSN data has been taken from the World Data Center SILSO, Royal Observatory of Belgium, Brussels (SILSO, 1984-2017). The TSI and UVI data have been taken from the NOAA Climate Data Record created with the Naval Research Laboratory model for solar spectral and total solar irradiance (Coddington et al., 2021).

Oceanic Niño Index (ONI) has been used as the indice for ENSO events in this analysis (NOAA, 2021). Monthly averages between the years 1984 to 2017 have been used. The cloud data is from the International Satellite Cloud Climatology Project (ISCCP), H-Series (Young et al., 2018).

12.2.2. Methodology

The parameters used in this analysis are separated as predictors and predictands. The predictors, that is, the GCR flux, SSN, TSI, UVI, and ONI, are independent variables used to predict the outcomes, while the TC and LLC are the predictands. First, the obtained raw data is explored, and all datasets are pre-processed using a 12-month moving average to remove seasonal effects. Additionally, the ISCCP data is detrended because there is a clear decreasing trend seen in the dataset, and this trend is claimed to be artificial (Usoskin et al. 2004, Laken et al. 2012, Singh et al. 2020).

The analysis started by trying to obtain the same results as previous studies investigating the linear correlation between GCRs and clouds (Svensmark et al. 1997, Usoskin et al. 2004) and then extending those studies to the present. The analysis continued with regression analysis using multiple linear regression models.

R^2 values were calculated, and cross-validation methods were used to evaluate the performance of models. Hold-out validation of 25% was used, meaning that 25% of the data has been used to test the ML models while 75% of the data has been used to train them. Holding out a certain percentage of the data can be done in two ways; first, data points can be randomly selected and held out from the dataset. Second, the data can be held out as a continuous block of data points. Such methods are investigated and compared. Random hold-out method works well for ML models, yet the results are suspicious. When the data points are randomly selected from the entire dataset, and the data is periodic throughout the 33 years, it is not that difficult for the algorithm to predict the trends in the held-out data points. Two successive points, which are almost identical due to the large auto-correlation functions of the predictors, may end up in the test and training sets, respectively. This is not very different from having the same points in both sets. Thus, it is crucial to hold out continuous parts of the dataset to test and check the model's performance then. Particularly, if the last part of the data is held out, we can test how well the past data can predict the future. Hence, in this analysis the final 25% of the dataset is held out and tested in the ML models.

Also, both in the linear correlation and multiple regression steps, the predictand datasets are either used as global/regional averages or as pixelwise global data. The pixelwise analysis creates a different regression model for each pixel, and the results are shown as global maps. Meanwhile, there are four different latitude zones used as global or regional averages in the analysis: 90°N - 90°S (Global), 70°N - 60°S (Region I), 25°N - 25°S (Region II), and (70° - 25°)N & (25° - 60°)S (Region III). The regions are similar to previous regional analyses ((Usoskin et al., 2004) and (Voiculescu et al., 2006)).

12.3. RESULTS

12.3.1. Reanalysis of Previous Studies

The linear correlation coefficient between GCR flux and cloud amount was calculated for three different periods; 1984-1994 (analysis period of Marsh & Svensmark, 2000), 1984-2000 (analysis period of Usoskin et al. 2004), and 1984-2017, which is the entire period of the analysis in this paper.

The ISCCP LLC was found to be highly correlated with GCRs from 1984 to 1994, and consistent with previous report (Marsh & Svensmark, 2000), the Pearson correlation coefficient (*R*) was significantly high (> 0.8) both globally and for the average cloud amounts in all regions. The ISCCP TC amount did not have a similar high correlation for all regions in the same period. Only region IV was highly correlated. However, when we expanded the analysis time period even by six years, there is a significant drop in the correlation coefficient. LLC amount was still significantly correlated in most regions, just as Usoskin et al. (2004), but the TC amount was not.

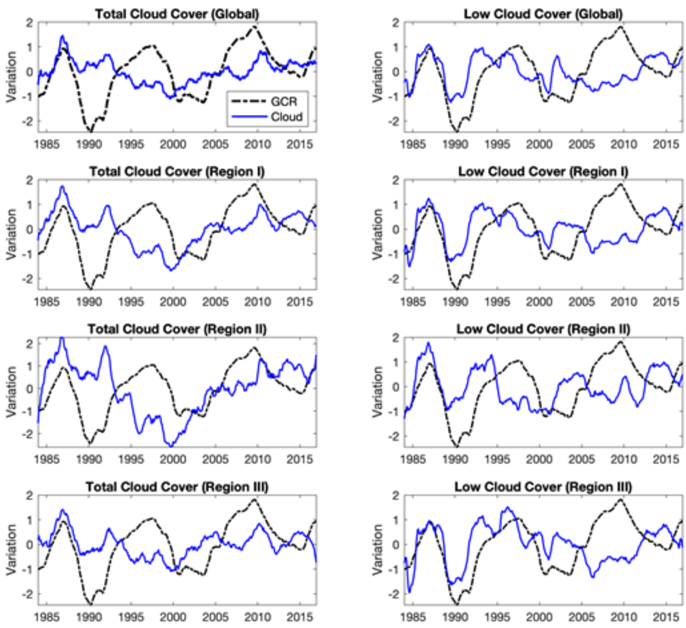

Figure 12.1. Time series of the normalized GCR flux in comparison to normalized ISCCP cloud products for; a) ISCCP TC averaged globally, b) ISCCP TC averaged over Region I, c) ISCCP TC averaged over Region II, d) ISCCP TC averaged over Region III, e) ISCCP LLC averaged globally, f) ISCCP LLC averaged over Region I, g) ISCCP LLC averaged over Region II, h) ISCCP LLC averaged over the Region III.

When the time period was expanded even further until 2017, the R values remarkably decreased for all regions of the ISCCP TC and Region II of the ISCCP LC. Plotting the full period of cloud data against the GCR flux showed the temporal differences clearly in Figure 12.1. From 1984 to almost 1994, the GCR flux and the LLC were highly correlated in all regions. For the TC, there was a correlation in most regions from 1984 to around 1990. However, the correlation was lost entirely after ~1990.

12.3.2. Pixelwise Linear Correlation Results

The results of the pixelwise analysis of the linear correlation between each cloud dataset and the GCR is presented in Figure 12.2. For each pixel, an independent *R* is calculated between the time signals.

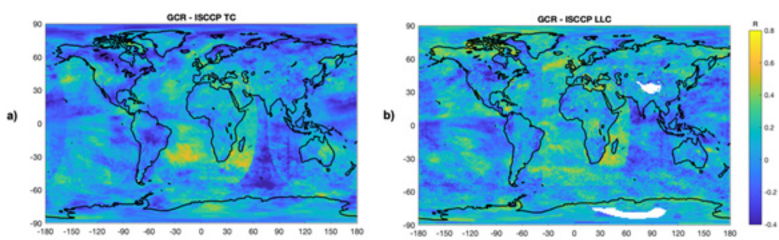

Figure 12.2. Maps of *R* between the GCR flux and the cloud products from 1984 to 2017. a) Using ISCCP TC, b) Using ISCCP LLC.

First of all, the satellite footprints mentioned in Laken et al. (2012), can be seen in the maps using ISCCP data, especially over the Indian Ocean and slightly over the Pacific Ocean. There is also missing data in the ISCCP LLC dataset, seen as blank over Asia and Antarctica in Figure 12.2.b. The regions with a high positive correlation, such as the southern mid-latitudes over the Atlantic, Pacific, and Indian Oceans, can be seen in the ISCCP TC and ISCCP LLC maps. Similarly, the regions with negative correlations are parallel in both maps.

12.3.3. Multiple Regression Models

The previous sections investigated the linear correlations between only two variables at a time. However, studying the variables together in a model is crucial to investigate the common predictive value of all the predictors and the interactions between them. This section shows the results of the linear multiple regression models.

Figure 12.3 shows maps using the linear regression model with the predictors and predictands. Negative pixels are shown as zero in these maps in order to see the positive pixels better. Such negative pixels are the pixels where the linear model is a poor fit.

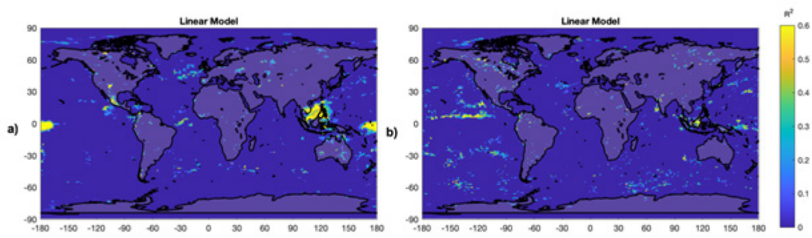

Figure 12.3. R^2 map of the linear regression models where predictands are a) ISCCP TC, b) ISCCP LLC.

The majority of pixels have a negative R^2 value in Figure 12.3, meaning that the performance of the linear models is very poor for these sets of predictors and predictands. However, there are similarities in the regions with strong positive pixels. These regions are mainly in the equatorial and tropics regions in the Pacific Ocean. Some narrower strong R^2 areas can also be seen in the mid-latitudes in both hemispheres.

12.4. DISCUSSION

The seemingly high correlations observed between certain variables for specific time periods and regions that cannot be observed for others can be interpreted differently. Firstly, they can be totally accidental. Secondly, there might be other parameters that change over time and space, and when they are not considered, we can observe the correlations only during certain times or at certain places. It is also possible that the relations are not linear, and we can only observe them when they are more or less linear under certain conditions. The noise might not be independent either. These results show that it is tough to interpret the cosmic ray-cloud relationship based on regionally or globally averaged datasets, and it would be better to analyze the globe pixel by pixel to explore subtler correlations and to reveal location-dependent correlations that may disappear when averaged out over the globe or regions.

Reanalysis of previous studies with a strong linear correlation between LLC and GCR flux showed that *R* values weakened as the study period extended and disappeared completely after ~2003. This shows that a long period is vital for such analyses and using a short time frame may cause a spurious correlation. Consistent with previous reports, pixelwise correlation analysis for 1984-2017 revealed a strong positive correlation between GCR-cloud in the mid-latitude oceans. It is observed that the linear correlation between GCR and cloud products vary from each other in different regions. Hence, taking global or regional averages lead to low *R* values.

According to the results of comparing different hold-out validation methods for the ML models, random hold-out validation worked well for all ML models, yet it was thought to create artificially high R^2 values. A hold-out validation method uses past data to predict future data in a time-dependent dataset by holding out the final parts of a dataset. As this validation method uses predictive power, the values obtained are less likely to be coincidental.

The TC cover has stronger R^2 pixels in the ML model maps. Again, this could be because of the reported (Voiculescu et al., 2007) false ENSO index-high cloud cover correlation, as the most visibly strong pixels, are in the tropical Pacific Ocean. Another reason for these visible areas along the equator could be due to SO4 and NaCl masses observed in the Equatorial Pacific regions. The global maps of these masses are given in Mann et al. (2012), and the areas with high concentration are parallel to the high positive R^2 pixels in the regression model maps of this study. The study by Mann et al. evaluates a global aerosol microphysics module and generates maps using these molecules. Both the sulfate and the sea-salt maps display similar patterns in the Pacific. The shapes for sulfate masses are also shown in Hommel et al. (2011); and for sea-salt masses, they are shown in the research by Wang et al. (2017). However, the stated relations are beyond the scope of this study and could be part of future research.

12.5. CONCLUSION

The present study investigated the relationships between external forces on Earth's climate and the meteorological parameters by employing ML techniques for the first time. Different geographical regions and temporal periods were evaluated. The parameters used in the analysis were GCR flux, SSN, TSI, UVI and ONI as the predictor variables; TC amount and LLC amount as the response variables. All monthly averaged datasets were pre-processed, smoothed, and analyzed for the years 1984-2017. After standard statistical techniques were applied, multiple linear regression models were used.

12.6. FUTURE WORK AND SUGGESTIONS

The GCR-climate connection will be investigated further by looking at non-linear relationships using random forests. Interrelations between the parameters was the main focus of this study, and the reasons for the relationships have not been investigated. Based on the results of the present study, further research should focus on the regions found with high R^2 values in the Indian Ocean and Pacific Ocean mid-latitudes. The parameters sulfate and sea-salt masses could be added to the analysis to see how the relations change. Using the predictors as gridded datasets instead of globally averaged data would help to understand relationships for each pixel further. Such changes could be, for example, to calculate and use cosmic ray-induced ionization in the atmosphere at certain altitudes, for each pixel, instead of the neutron monitor count rates as the GCR data.

Acknowledgements

Bilge Demirkoz thanks the Turkish Academy of Sciences (TÜBA) for financial support during the preparation of this paper.

REFERENCES

Ahluwalia, H. S. (2013). No direct correlation between galactic cosmic rays and Earth surface temperature. Advances in Space Research, 52(12), 2119–2121.

Ahluwalia, H. S. (2014). Galactic cosmic rays, total solar irradiance, sunspots, Earth surface air temperature:

Correlations. Indian Journal of Radio & Space Physics, 43, 141–150.

Čalogović, J., & Laken, B. A. (2015). Reflections on the late Cosmoclimatology. Central European Astrophysical Bulletin, 39, 145–160.

Carslaw, K. S., Harrison, R. G., & Kirkby, J. (2002). Cosmic rays, clouds, and climate. Science, 298(5599), 1732–1737.

Coddington, O., Lean, J. L., Lindholm, D., Pilewskie, P., Snow, M., & (2015), N.C. NOAA Climate Data Record (CDR) of Solar Spectral Irradiance (SSI), NRLSSI Version 2. Doi:10.7289/V51J97P6

Coddington, O., Lean, J. L., Lindholm, D., Pilewskie, P., Snow, M., & (2015), N.C. NOAA Climate Data Record (CDR) of Total Solar Irradiance (TSI), NRLTSI Version 2. doi:10.7289/V55B00C1

Erlykin, A. D., Gyalai, G., Kudela, K., Sloan, T., & Wolfendale, A. W. (2009). On the correlation between cosmic ray intensity and cloud cover. Journal of Atmospheric and Solar-Terrestrial Physics, 71(17-18), 1794–1806.

Erlykin, A. D., Sloan, T., & Wolfendale, A. W. (2009). Solar activity and the mean global temperature. Environmental Research Letters, 4, 014006.

Hastie, T., Tibshirani, R., & Friedman, J. H. (2009). The elements of statistical learning: data mining, inference, and prediction (Vol. 2). New York: Springer.

Hommel, R., Timmreck, C., & Graf, H. (2011). The global middle-atmosphere aerosol model MAECHAM5-SAM2: comparison with satellite and in-situ observations. Geoscientific Model Development, 4(3), 809-834.

James, G., Witten, D., Hastie, T., & Tibshirani, R. (2013). An Introduction to Statistical Learning. Springer.

Kristjansson, J. E., Stjern, C. W., Stordal, F., Fjaeraa, A. M., Myhre, G., & Jonasson, K. (2008). Cosmic rays, cloud condensation nuclei and clouds–a reassessment using MODIS data. Atmospheric Chemistry and Physics, 8, 7373–7387.

Laken, B. A., Pall Bag , E., & Miyahara, H. (2012). A Decade of the Moderate Resolution Imaging Spectroradiometer: Is a Solar–Cloud Link Detectable? Journal of Climate, 25, 4430–4440.

Laken, B. A., Pall Bag , E., Čalogović, J., & Dunne, E. M. (2012). A cosmic ray-climate link and cloud observations. Journal of Space Weather and Space Climate, 2, A18.

Laut, P. (2003). Solar activity and terrestrial climate: an analysis of some purported correlations. Journal of Atmospheric and Solar-Terrestrial Physics, 65, 801–812.

Mann, G. W., Carslaw, K. S., Ridley, D. A., Spracklen, D. V., & others. (2012). Intercomparison of modal and sectional aerosol microphysics representations within the same 3-D global chemical transport model. Atmospheric Chemistry and Physics, 12, 4449–4476.

Marsh, N., & Svensmark, H. (2000). Cosmic rays, clouds, and climate. Space Science Reviews, 94, 215–230.

Marsh, N., & Svensmark, H. (2003). Galactic cosmic ray and El Nino–Southern Oscillation trends in International Satellite Cloud Climatology Project D2 low-cloud properties. Journal of Geophysical Research: Atmospheres, 108(D6), 1 - 11.

MATLAB. (2020). 9.9.0.1495850 (R2020b). Natick, Massachusetts: The MathWorks Inc.

NOAA. (2021, January 17). Historical El Nino / La Nina Episodes. Retrieved from National Weather Service, Climate Prediction Center: https://origin.cpc.ncep.noaa.gov/products/analysis_monitoring/ensostuff/ONI_v5.php

Palle Bago, E., & Butler, C. J. (2000). The influence of cosmic rays on terrestrial clouds and global warming. Astronomy & Geophysics, 41, 4–18.

Palle Bago, E., Butler, C. J., & O'Brien, K. (2004). The possible connection between ionization in the atmosphere by cosmic rays and low level clouds. Journal of Atmospheric and Solar-Terrestrial Physics, 66, 1779–1790.

SILSO, W. D. (1984-2017). The International Sunspot Number. International Sunspot Number Monthly Bulletin and online catalogue. Retrieved from http://www.sidc.be/silso/

Singh, A. K., & Bhargawa, A. (2020). Delineation of possible influence of solar variability and galactic cosmic rays on terrestrial climate parameters. Advances in Space Research, 65, 1831–1842.

Svensmark, H., & Friis-Christensen, E. (1997). Variation of cosmic ray flux and global cloud coverage, a missing link in solar-climate relationships. Journal of Atmospheric and Solar Terrestrial Physics, 59, 1225-1232.

Tsonis, A. A., Deyle, E. R., May, R. M., Sugihara, G., Swanson, K., Verbeten, J. D., & Wang, G. (2015). Dynamical evidence for causality between galactic cosmic rays and interannual variation in global temperature. Proceedings of the National Academy of Sciences, 112, 3253–3256.

Usoskin, I. G. (2021). Cosmic Ray Station of the University of Oulu. Retrieved January 17, 2021, from The University of Oulu, Sodankyla Geophysical Observatory: http://cosmicrays.oulu.fi/

Usoskin, I. G., Marsh, N., Kovaltsov, G. A., Mursula, K., & Gladysheva, O. G. (2004). Latitudinal dependence of low cloud amount on cosmic ray induced ionization. Geophysical Research Letters, 31(16).

Usoskin, I. G., Voiculescu, M., Kovaltsov, G. A., & Mursula, K. (2006). Correlation between clouds at different altitudes and solar activity: Fact or Artifact? Journal of Atmospheric and Solar-Terrestrial Physics, 68, 2164–2172.

Usoskin, I. G., Mursula, K., Kangas, J., & Gvozdevsky, B. (2001). Online database of cosmic ray intensities. International Cosmic Ray Conference, 9, pp. 3842–3842.

Voiculescu, M., Usoskin, I. G., & Mursula, K. (2006). Different response of clouds to solar input. Geophysical Research Letters, 33.

Voiculescu, M., Usoskin, I. G., & Mursula, K. (2007). Effect of ENSO and volcanic events on the Sun–cloud link. Advances in Space Research, 40, 1140–1145.

Wang, H., Wang, X., Yang, X., Li, W., Xue, L., Wang, T., & others. (2017). Mixed chloride aerosols and their atmospheric implications: a review. Aerosol and Air Quality Research, 17(4), 878-887.

Young, A. H., Knapp, K. R., Inamdar, A., Hankins, W., & Rossow, W. B. (2018). The International Satellite Cloud Climatology Project H-Series climate data record product. Earth Syst. Sci. Data,10, 583–593. doi:10.7289/V5QZ281S

Yu, F. (2002). Altitude variations of cosmic ray induced production of aerosols: Implications for global cloudiness and climate. Journal of Geophysical Research: Space Physics, 107, SIA–8.

CHAPTER 13

EVALUATION OF HISTORICAL CMIP6 BASED CONVECTION-PERMITTING CLIMATE SIMULATION OVER THE BLACK SEA REGION

Mehmet Barış KELEBEK, Barış ÖNOL

Istanbul Technical University, Türkiye
Faculty of Aeronautics and Astronautics
Department of Meteorological Engineering

Abstract

The human influence on climate change is at a remarkable rate compared to the pre-industrial era, and this influence is projected to lead to an increase in climatic extremes in the future. In this context, high-resolution climate information is of great importance in developing regional adaptation and mitigation strategies against the possible impacts of climate change. In this study, we performed a high-resolution climate simulation at the convection-permitting scale over the Black Sea Region for the period of 2005-2014 using the WRF model, and this is the first time a regional climate model was run using the Coupled Model Intercomparison Project Phase 6 (CMIP6) outputs as the boundary conditions over the interested region. Comparison of the simulation outputs with high-resolution observational and reanalysis data showed that the model captures spatial distribution of the seasonal precipitation amount satisfactorily, despite a positive bias in winter months, especially over the mountainous regions. In terms of temperature, we found that model has a general positive bias in all seasons except for spring for maximum temperatures and for minimum temperatures in all seasons. These biases of the model can partly be explained due to observational uncertainties, especially over the mountainous areas of the domain.

Keywords: *Regional climate modelling, convection-permitting modelling, the Black Sea Region.*

13.1. INTRODUCTION

The anthropogenic forcing on global climate change is at a remarkable level compared to the pre-industrial era. According to the Sixth Assessment Report of the Intergovernmental Panel on Climate Change (IPCC AR6), in the 2011-2020 period, the global surface temperature increased by 1.09°C compared to the 1850-1900 period (Arias et al., 2021). Moreover, the projections show that climatic extremes will increase due to anthropogenic forcing in the future (Seneviratne et al., 2012; Seneviratne et al., 2021). Therefore, future projections of the Earth's climate play a critical role in developing adaptation and mitigation strategies. However, although climate change is a global problem, its societal and environmental impacts are not the same for every region because regional climate change and changes in the extremes are the results of global forcing along with small-scale processes and local feedbacks (Dobles-Reyes et al., 2021; Seneviratne et al., 2021). In this context, regional climate models (RCMs) (Dickinson et al., 1989; Giorgi and Bates, 1989) have been introduced to produce more detailed and physically more reliable regional climate information compared to the global coupled climate model (GCM) outputs (Feser et al., 2011; Prein et al., 2013; Rummukainen, 2016; Giorgi, 2019; Gutowski et al., 2020). Their higher horizontal resolution, most of which are on the order of 10 km, allows them to better capture small-scale and extreme weather events by enabling a better representation of complex topography and surface characteristics over mountainous and coastal areas (Feser et al., 2011; Rummukainen, 2016; Giorgi, 2019). Nevertheless, unresolved sub-grid scale thermodynamic and dynamic processes are still parametrized at these resolutions (Kendon et al., 2017), which makes the performance of the RCMs questionable. Particularly, convective parametrizations are the primary source of errors and uncertainties in climate simulations (Hohenegger et al., 2008; Kendon et al., 2014; Fosser et al., 2015; Prein et al., 2015; Lucas-Picher et al., 2021). Recently, RCMs are run at grid spacings less than 4 km with increasing computational power (Prein et al., 2020). At these resolutions, RCMs resolve topography and land-surface processes at a scale that allows the explicit representation of deep convection without a convective parametrization scheme (Hohenegger et al., 2008; Kendon et al., 2012Fosser et al., 2015). These models are called convection-permitting models (CPMs) and, compared to the low-resolution RCMs, represent precipitation characteristics more realistically (Hohenegger et al., 2008; Kendon et al., 2012; Prein et al., 2013; Ban et al., 2014; Fosser et al., 2015; Brisson et al., 2016; Stocchi et al., 2022). Given the benefits of the CPMs, we performed a convection-permitting climate simulation to downscale the last generation CMIP6 MPI-ESM1.2-HR (Gutjahr et al., 2019) earth system model outputs by using the WRF model at 3 km horizontal resolution over the Black Sea region, where complex topographical features and strong air-sea interactions intensify destructive heavy precipitation. We evaluated model performance in representing the precipitation and temperature using the high-resolution gridded observational and reanalyses data between 2005-2014. This is the first study that uses a convection-permitting climate model based on CMIP6 (Eyring et al., 2016) protocols over a broad part of Turkey and the Black Sea Region to advance the previous climate change studies over the region of interest (e.g., Önol and Semazzi, 2009; Önol and Unal, 2012; Önol et al., 2014).

13.2. METHOD AND DATA

In the study, we ran WRF (Version 3.9.1) model (Skamarock et al., 2008) at 3 km horizontal resolution and 50 vertical levels over the Black Sea Region and a broad part of the Anatolian Peninsula (Figure 13.1) between 1 September 2004 – 1 January 2015. We performed the simulation using 100 km horizontal resolution boundary conditions at 6-hour intervals from the last generation CMIP6 MPI-ESM1.2-HR earth system model (referred to as MPI-ESM-HR). The first four months of the simulation are left as spin-up time and are not included in the analyses. Most importantly, we switched off the deep and shallow cumulus parametrization schemes to let the model solve the convection explicitly. Other model parametrization schemes are summarized in Table 13.1.

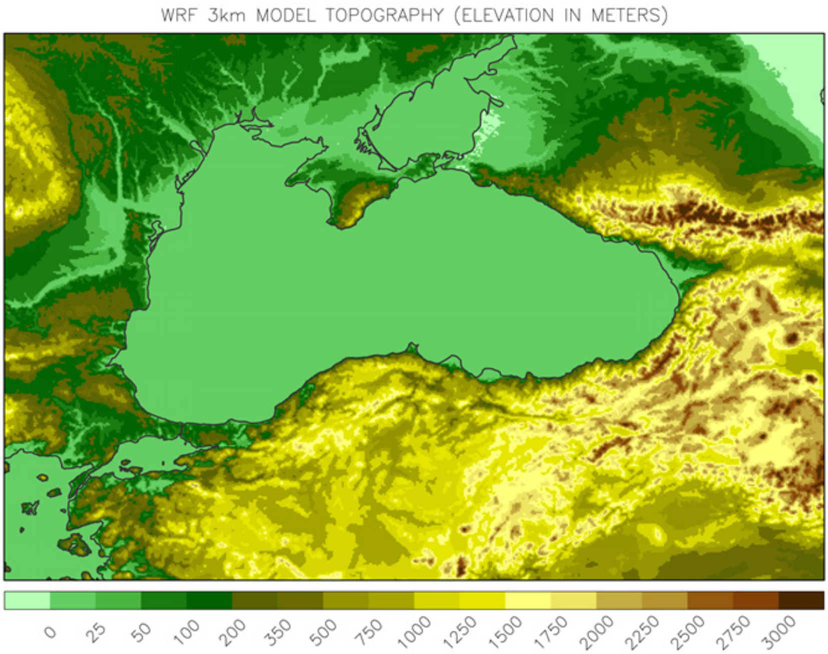

Figure 13.1. WRF model topography at 3 km horizontal resolution.

To evaluate the model performance, we compared simulation outputs (hereafter called WRFCP) with high-resolution gridded observational and reanalysis datasets (referred to as reference datasets). For the precipitation, we used CHIRPS (0.05deg horizontal resolution) (Funk et al., 2015) and MSWEP (0.1deg horizontal resolution) (Beck et al., 2019), and for the temperature, TerraClimate (referred to as TERRACLIMATE) (~4 km horizontal resolution) (Abatzoglou et al., 2018) gridded observational data. Both for precipitation and temperature, we also used the ERA5-Land reanalyses at 0.1deg horizontal resolution (Sabater, 2019) (referred to as ERA5LAND). For the analyses, absolute values such as seasonal total precipitation are represented on the original grids of the data. To calculate the model bias, we interpolated WRFCP to the resolution of the target data using bicubic interpolation for grid point compatibility.

Table 13.1. Model parametrization options and schemes.

Parametrization Option	Parametrization Scheme
Microphysics	Thompson (Thompson et al., 2008)
Shortwave and Longwave Radiation	RRTMG (Iacono et al., 2008)
Planetary Boundary Layer	YSU (Hong et al., 2006)
Surface Layer	Monin-Obukhov (Jiménez et al., 2012)
Land-surface Model	Noah LSM (Ek et al., 2003)

13.3. RESULTS

The annual total precipitation climatology of MPI-ESM-HR, WRFCP, and the reference data are given in Figure 13.2. In terms of the spatial distribution of the total precipitation amount, WRFCP agrees with reference datasets. However, the model has a positive bias over the Western and Eastern Black Sea Regions and mountainous areas such as the Caucasus. Therefore, to investigate the model performance in different seasons, we showed the seasonal total precipitation climatologies in Figure 13.3. WRFCP captures spatial distribution of the precipitation amount satisfactorily in all seasons, except for the winter, over most of the domain. We calculated root mean square error (RMSE) between WRFCP-CHIRPS, WRFCP-MSWEP, and WRFCP-ERA5LAND over the domain and found that the highest (around 165 mm) and the lowest (around 67 mm) errors occur in the winter and autumn months, respectively (Table 13.2).

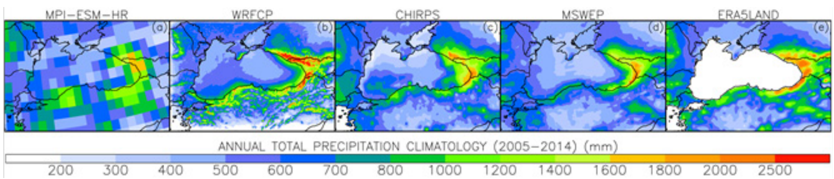

Figure 13.2. Annual mean total precipitation of MPI-ESM-HR (a), WRFCP (b), CHIRPS and MSWEP observations (c, d), and ERA5LAND reanalysis (e).

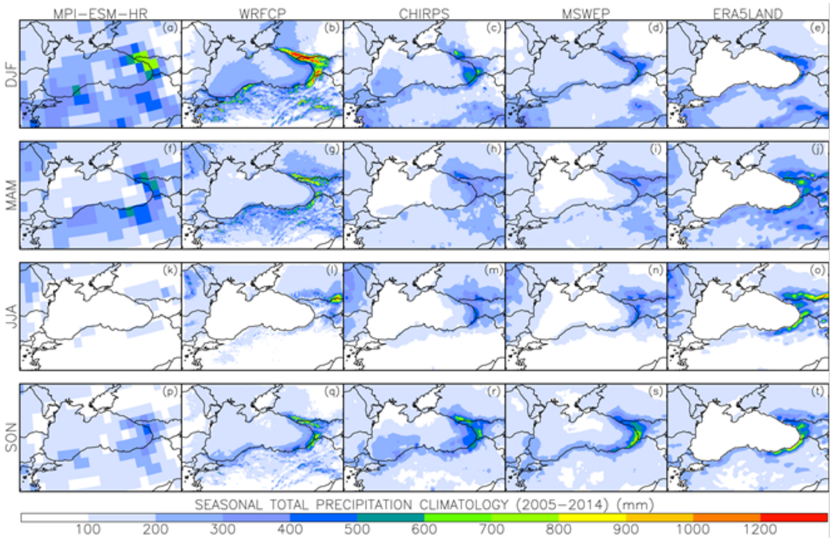

Figure 13.3. Seasonal mean total precipitation in winter (a–e), spring (f–j), summer (k–o), and autumn (p–t).

Table 13.2. Seasonal total precipitation RMSE of WRFCP with respect to reference datasets.

Seasonal RMSE (mm)	DJF	MAM	JJA	SON
WRFCP-CHIPRS	164.77	101.93	80.47	68.01
WRFCP-MSWEP	167.91	100.81	72.47	67.65
WRFCP-ERA5LAND	156.83	92.62	101.45	78.3

Additionally, we calculated the seasonal total precipitation bias of WRFCP at each grid point to reveal the region in which and how much the model most differs from the reference datasets (Figure 13.4). The highest difference occurs in the winter months over the mountainous areas of the Anatolian Peninsula and the Eastern Black Sea Region. Model bias is around 500 mm over the mountains and, in particular, reaches up to 1500 mm over the Caucasus. Part of this bias can be related to the higher model resolution that resolves complex topography better than the low-resolution gridded datasets and also can be due to the low-density station network at higher elevations, which increases the observational uncertainty over the interested areas (Önol and Semazzi, 2009; Önol, 2012). Besides, we found that, in the winter months, MPI-ESM-HR produces more precipitation by 400 mm over the Western Black Sea Region, parts of Eastern Anatolia, and the Caucasus Mountains. These indicate that the WRFCP bias over these regions is a direct consequence of the driving boundary conditions on the regional climate simulation. A similar issue occurs in the summer months when MPI-ESM-HR produces less precipitation over the Eastern Black Sea region compared to the reference datasets. During these months, WRFCP has a negative bias of around 300 mm compared to CHIRPS and MSWEP observations and 500 mm compared to ERA5LAND reanalysis over this region. In the spring months, the difference is lower compared to the winter and summer months, which becomes a maximum of about 800 mm over the Caucasus and does not become more than 500 mm in other regions. In addition, in spring, WRFCP has a lower bias for ERA5LAND compared to CHIRPS and MSWEP in magnitude over the Black Sea coast of Turkey. These bias differences in summer and spring due to different datasets also highlight the inconsistencies among the reference data and indicates the importance and requirement of observations in mountainous regions for model evaluations. In the autumn, there is no significant total precipitation difference between WRFCP and the reference datasets.

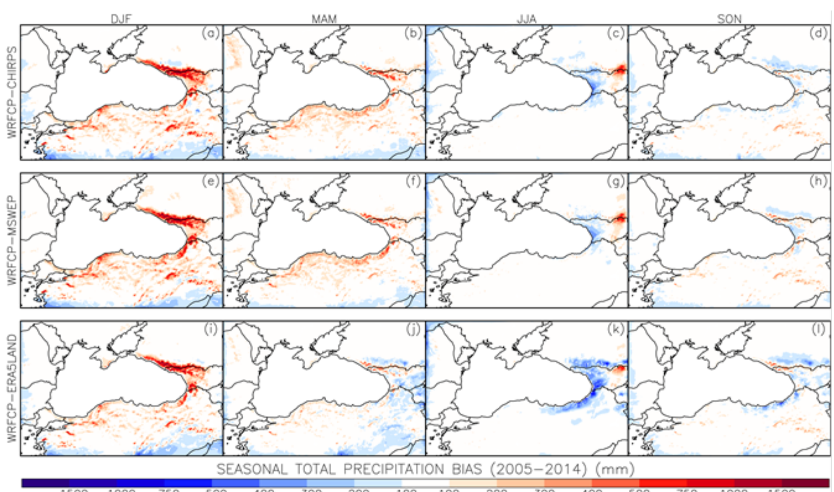

Figure 13.4. WRFCP seasonal total precipitation bias with respect to CHIRPS (a–d), MSWEP (e–h), and ERA5LAND (i–l).

Biases of seasonal climatologies of daily maximum temperatures are given in Figure 13.5. The choice of observational or reanalysis data for temperature bias calculations resulted in differences. In terms of maximum temperature, WRFCP has negative biases of around 2°C and 4°C in winter and spring, respectively, compared to TERRACLIMATE over the Anatolian Peninsula and the Caucasus. In comparison to ERA5LAND, WRFCP bias becomes positive over most of this area and is around 3°C. Similarly, in the autumn, the model has a positive bias around 3°C compared to ERA5LAND. This bias reduces to 1°C for TERRACLIMATE and even becomes negative over Eastern Anatolia. Most significantly, in the summer, while WRFCP has a negative bias of about 3°C compared to TERRACLIMATE over the mountains of the Eastern Black Sea Region of Turkey, there is no significant difference between WRFCP and ERA5LAND over the same region. These differences may be related to the different production methods of the reference data. TERRACLIMATE uses observational data to produce high-resolution temperature information (Abatzoglou et al., 2018), while the ERA5LAND is a reanalysis based on a dynamic model (Sabater, 2019). The representation of clouds in the models affects and decreases the near-surface air temperature. TERRACLIMATE does not include cloud information, and observational deficiencies in data-sparse regions can lead to errors in the production of this data which employs simple bilinear interpolation (Abatzoglou et al., 2018) and no other physical corrections such as lapse-rate correction. Therefore, the different biases of WRFCP between TERRACLIMATE and ERA5LAND can be explained by cloud dynamics which affect the surface radiation budget. These results indicate the advantages of high-resolution WRFCP that aids the detailed representation of climatic variables over complex topography.

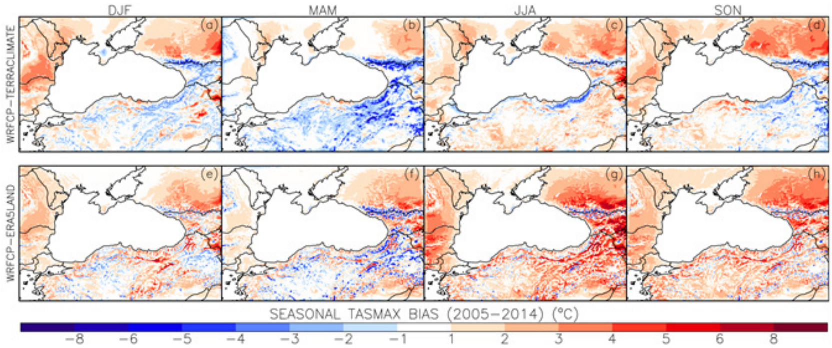

Figure 13.5. WRFCP seasonal mean daily maximum temperature bias with respect to TERRACLIMATE (a–d) and ERA5LAND (e–h).

Figure 13.6 shows the biases of seasonal climatologies of daily minimum temperatures. Compared to both TERRACLIMATE and ERA5LAND, in winter, WRFCP has a positive bias of about 2°C and 4°C, respectively. In spring, the model has a negative bias of around 3°C over Eastern Anatolia, comparing both data. The positive bias over other regions is around 2°C. The highest difference between WRFCP and the reference datasets is in the summer months. In summer, WRFCP has a positive bias reaching up to 5°C across the Anatolian Peninsula. The model also exhibits significant positive bias in the autumn months which is around 4°C over the study area.

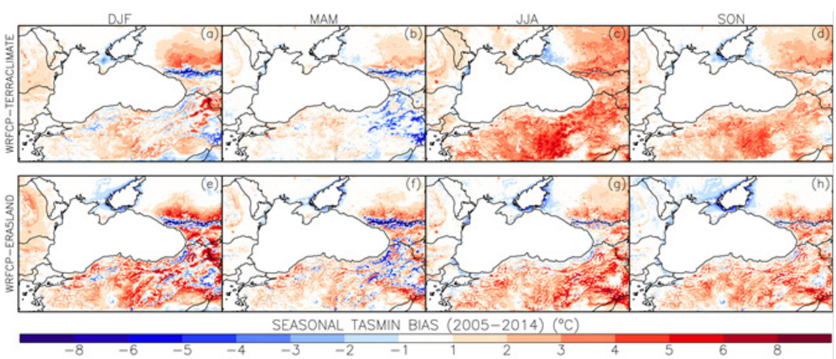

Figure 13.6. WRFCP seasonal mean daily minimum temperature bias with respect to TERRACLIMATE (a–d) and ERA5LAND (e–h).

13.4. CONCLUSION

In this study, we performed a convection-permitting climate simulation at 3 km horizontal resolution using the WRF model over the Black Sea Region between 2005-2014. We downscaled the last generation CMIP6 MPI-ESM-HR earth system model outputs and compared simulation results with high-resolution gridded observational and reanalysis datasets. The result indicates that the WRF model produces more seasonal total precipitation compared to reference data, especially in winter months and over mountainous regions. Part of this bias can be related to the observational uncertainty due to the low-density observation network at higher elevations of the study area. For maximum temperature, WRFCP has a general positive bias in winter, summer, and autumn and a negative bias in spring. Compared with the different reference data, the WRFCP biases exhibit regional differences, which can be related to data production techniques and deficient observations over the mountains. For the minimum temperatures, WRFCP has a positive bias in all seasons over most of the domain.

This study highlighted the performance of a convection-permitting climate model over the complex topography of the Black Sea Region. This promising study can be extended to perform high-resolution climate simulations using the CMIP6 shared socioeconomic pathways for future greenhouse gas emissions to develop suitable regional climate change adaptation and mitigation strategies.

Acknowledgements

The numerical calculations reported in this paper were fully performed at TUBITAK ULAKBIM, High Performance and Grid Computing Center (TRUBA resources).

REFERENCES

Abatzoglou, J. T., Dobrowski, S. Z., Parks, S. A., & Hegewisch, K. C. (2018), *TerraClimate, a high-resolution global dataset of monthly climate and climatic water balance from 1958–2015*. Scientific Data, 5(1), 170191. https://doi.org/10.1038/sdata.2017.191

Arias, P.A., N. Bellouin, E. Coppola, R.G. Jones, G. Krinner, J. Marotzke, V. Naik, M.D. Palmer, G.-K. Plattner, J. Rogelj, M. Rojas, J. Sillmann, T. Storelvmo, P.W. Thorne, B. Trewin, K. Achuta Rao, B. Adhikary, R.P. Allan, K. Armour, G. Bala, R. Barimalala, S. Berger, J.G. Canadell, C. Cassou, A. Cherchi, W. Collins, W.D. Collins, S.L. Connors, S. Corti, F. Cruz, F.J. Dentener, C. Dereczynski, A. Di Luca, A. Diongue Niang, F.J. Doblas-Reyes, A. Dosio, H. Douville, F. Engelbrecht, V. Eyring, E. Fischer, P. Forster, B. Fox-Kemper, J.S. Fuglestvedt, J.C. Fyfe, N.P. Gillett, L. Goldfarb, I. Gorodetskaya, J.M. Gutierrez, R. Hamdi, E. Hawkins, H.T. Hewitt, P. Hope, A.S. Islam, C. Jones, D.S. Kaufman, R.E. Kopp, Y. Kosaka, J. Kossin, S. Krakovska, J.-Y. Lee, J. Li, T. Mauritsen, T.K. Maycock, M. Meinshausen, S.-K. Min, P.M.S. Monteiro, T. Ngo-Duc, F. Otto, I. Pinto, A. Pirani, K. Raghavan, R. Ranasinghe, A.C. Ruane, L. Ruiz, J.-B. Sallée, B.H. Samset, S. Sathyendranath, S.I. Seneviratne, A.A. Sörensson, S. Szopa, I. Takayabu, A.-M. Tréguier, B. van den Hurk, R. Vautard, K. von Schuckmann, S. Zaehle, X. Zhang, and K. Zickfeld, 2021: Technical Summary. In Climate Change (2021), The Physical Science Basis. Contribution of Working Group I to the Sixth Assessment Report of the Intergovernmental Panel on Climate Change [Masson-Delmotte, V., P. Zhai, A. Pirani, S.L. Connors, C. Péan, S. Berger, N. Caud, Y. Chen, L. Goldfarb, M.I. Gomis, M. Huang, K. Leitzell, E. Lonnoy, J.B.R. Matthews, T.K. Maycock, T. Waterfield, O. Yelekçi, R. Yu, and B. Zhou (eds.)]. Cambridge University Press, Cambridge, United Kingdom and New York, NY, USA, pp. 33−144.

Ban, N., Schmidli, J., & Schär, C. (2014), *Evaluation of the convection-resolving regional climate modeling approach in decade-long simulations*. Journal of Geophysical Research: Atmospheres, 119(13), 7889–7907. https://doi.org/10.1002/2014JD021478

Beck, H. E., Wood, E. F., Pan, M., Fisher, C. K., Miralles, D. G., van Dijk, A. I. J. M., McVicar, T. R., & Adler, R. F. (2019), *MSWEP V2 Global 3-Hourly 0.1° Precipitation: Methodology and Quantitative Assessment*. Bulletin of the American Meteorological Society, 100(3), 473–500. https://doi.org/10.1175/BAMS-D-17-0138.1

Brisson, E., Van Weverberg, K., Demuzere, M., Devis, A., Saeed, S., Stengel, M., & van Lipzig, N. P. M. (2016), *How well can a convection-permitting climate model reproduce decadal statistics of precipitation, temperature and cloud characteristics?* Climate Dynamics, 47(9–10), 3043–3061. https://doi.org/10.1007/s00382-016-3012-z

Dickinson, RobertE., Errico, RonaldM., Giorgi, F., & Bates, GaryT. (1989), *A regional climate model for the western United States*. Climatic Change, 15(3). https://doi.org/10.1007/BF00240465

Doblas-Reyes, F.J., A.A. Sörensson, M. Almazroui, A. Dosio, W.J. Gutowski, R. Haarsma, R. Hamdi, B. Hewitson, W.-T. Kwon, B.L. Lamptey, D. Maraun, T.S. Stephenson, I. Takayabu, L. Terray, A. Turner, and Z. Zuo, (2021), Linking Global to Regional Climate Change. In Climate Change 2021: The Physical Science Basis. Contribution of Working Group I to the Sixth Assessment Report of the Intergovernmental Panel on Climate Change [Masson-Delmotte, V., P. Zhai, A. Pirani, S.L. Connors, C. Péan, S. Berger, N. Caud, Y. Chen, L. Goldfarb, M.I. Gomis, M. Huang, K. Leitzell, E. Lonnoy, J.B.R. Matthews, T.K. Maycock, T. Waterfield, O. Yelekçi, R. Yu, and B. Zhou (eds.)]. Cambridge University Press, Cambridge, United Kingdom and New York, NY, USA, pp. 1363–1512.

Ek, M. B., Mitchell, K. E., Lin, Y., Rogers, E., Grunmann, P., Koren, V., Gayno, G., & Tarpley, J. D. (2003), *Implementation of Noah land surface model advances in the National Centers for Environmental Prediction operational mesoscale Eta model*. Journal of Geophysical Research: Atmospheres, 108(D22), 2002JD003296. https://doi.org/10.1029/2002JD003296

Eyring, V., Bony, S., Meehl, G. A., Senior, C. A., Stevens, B., Stouffer, R. J., & Taylor, K. E. (2016), *Overview of the Coupled Model Intercomparison Project Phase 6 (CMIP6) experimental design and organization*. Geoscientific Model Development, 9(5), 1937–1958. https://doi.org/10.5194/gmd-9-1937-201

Feser, F., Rockel, B., von Storch, H., Winterfeldt, J., & Zahn, M. (2011), *Regional Climate Models Add Value to Global Model Data: A Review and Selected Examples*. Bulletin of the American Meteorological Society, 92(9), 1181–1192. https://doi.org/10.1175/2011BAMS3061.1

Fosser, G., Khodayar, S., & Berg, P. (2015), *Benefit of convection permitting climate model simulations in the representation of convective precipitation*. Climate Dynamics, 44(1–2), 45–60. https://doi.org/10.1007/s00382-014-2242-1

Funk, C., Peterson, P., Landsfeld, M., Pedreros, D., Verdin, J., Shukla, S., Husak, G., Rowland, J., Harrison, L., Hoell, A., & Michaelsen, J. (2015), *The climate hazards infrared precipitation with stations—A new environmental record for monitoring extremes*. Scientific Data, 2(1), 150066. https:/doi.org/10.1038/sdata.2015.66

Giorgi, F. (2019), *Thirty Years of Regional Climate Modeling: Where Are We and Where Are We Going next?* Journal of Geophysical Research: Atmospheres, 2018JD030094. https://doi.org/10.1029/2018JD030094

Giorgi, F., & Bates, G. T. (1989), *The Climatological Skill of a Regional Model over Complex Terrain*. Monthly Weather Review, 117(11), 2325–2347. https://doi.org/10.1175/1520-0493(1989)117<2325:TCSOAR>2.0.CO;2

Gutjahr, O., Putrasahan, D., Lohmann, K., Jungclaus, J. H., von Storch, J.-S., Brüggemann, N., Haak, H., & Stössel, A. (2019), *Max Planck Institute Earth System Model (MPI-ESM1.2) for the High-Resolution Model Intercomparison Project (HighResMIP).* Geoscientific Model Development, 12(7), 3241–3281. https://doi.org/10.5194/gmd-12-3241-2019

Gutowski, W. J., Ullrich, P. A., Hall, A., Leung, L. R., O'Brien, T. A., Patricola, C. M., Arritt, R. W., Bukovsky, M. S., Calvin, K. V., Feng, Z., Jones, A. D., Kooperman, G. J., Monier, E., Pritchard, M. S., Pryor, S. C., Qian, Y., Rhoades, A. M., Roberts, A. F., Sakaguchi, K., ... Zarzycki, C. (2020), *The Ongoing Need for High-Resolution Regional Climate Models: Process Understanding and Stakeholder Information*. Bulletin of the American Meteorological Society, 101(5), E664–E683. https://doi.org/10.1175/BAMS-D-19-0113.1

Hohenegger, C., Brockhaus, P., & Schär, C. (2008). *Towards climate simulations at cloud-resolving scales*. Meteorologische Zeitschrift, 17(4), 383–394. https://doi.org/10.1127/0941-2948/2008/0303

Hong, S.-Y., Noh, Y., & Dudhia, J. (2006), *A New Vertical Diffusion Package with an Explicit Treatment of Entrainment Processes*. Monthly Weather Review, 134(9), 2318–2341. https://doi.org/10.1175/MWR3199.1

Iacono, M. J., Delamere, J. S., Mlawer, E. J., Shephard, M. W., Clough, S. A., & Collins, W. D. (2008), *Radiative forcing by long-lived greenhouse gases: Calculations with the AER radiative transfer models*. Journal of Geophysical Research, 113(D13), D13103. https://doi.org/10.1029/2008JD009944

Jiménez, P. A., Dudhia, J., González-Rouco, J. F., Navarro, J., Montávez, J. P., & García-Bustamante, E. (2012), *A Revised Scheme for the WRF Surface Layer Formulation*. Monthly Weather Review, 140(3), 898–918. https://doi.org/10.1175/MWR-D-11-00056.1

Kendon, E. J., Ban, N., Roberts, N. M., Fowler, H. J., Roberts, M. J., Chan, S. C., Evans, J. P., Fosser, G., & Wilkinson, J. M. (2017), *Do Convection-Permitting Regional Climate Models Improve Projections of Future Precipitation Change?* Bulletin of the American Meteorological Society, 98(1), 79–93. https://doi.org/10.1175/BAMS-D-15-0004.1

Kendon, E. J., Roberts, N. M., Fowler, H. J., Roberts, M. J., Chan, S. C., & Senior, C. A. (2014). *Heavier summer downpours with climate change revealed by weather forecast resolution model*. Nature Climate Change, 4(7), 570–576. https://doi.org/10.1038/nclimate2258

Kendon, E. J., Roberts, N. M., Senior, C. A., & Roberts, M. J. (2012), *Realism of Rainfall in a Very High-Resolution Regional Climate Model.* Journal of Climate, 25(17), 5791–5806. https://doi.org/10.1175/JCLI-D-11-00562.1

Lucas-Picher, P., Argüeso, D., Brisson, E., Tramblay, Y., Berg, P., Lemonsu, A., Kotlarski, S., & Caillaud, C. (2021), *Convection-permitting modeling with regional climate models: Latest developments and next steps.* WIREs Climate Change, 12(6). https://doi.org/10.1002/wcc.731

Muñoz Sabater, J., (2019), E*RA5-Land hourly data from 1981 to present*. Copernicus Climate Change Service (C3S) Climate Data Store (CDS).

Önol, B., & Semazzi, F. H. M. (2009), *Regionalization of Climate Change Simulations over the Eastern Mediterranean*. Journal of Climate, 22(8), 1944–1961. https://doi.org/10.1175/2008JCLI1807.1

Önol B. (2012), *Understanding the coastal effects on climate by using high resolution regional climate simulation*. Clim Res 52: 159–174

Önol, B., & Unal, Y. S. (2012), *Assessment of climate change simulations over climate zones of Turkey*. Regional Environmental Change. https://doi.org/10.1007/s10113-012-0335-0

Önol, B., Bozkurt, D., Turuncoglu, U. U., Sen, O. L., & Dalfes, H. N. (2014), *Evaluation of the twenty-first century RCM simulations driven by multiple GCMs over the Eastern Mediterranean–Black Sea region.* Climate Dynamics, 42(7–8), 1949–1965. https://doi.org/10.1007/s00382-013-1966-7

Prein, A. F., Gobiet, A., Suklitsch, M., Truhetz, H., Awan, N. K., Keuler, K., & Georgievski, G. (2013), *Added value of convection permitting seasonal simulations.* Climate Dynamics, 41(9–10), 2655–2677. https://doi.org/10.1007/s00382-013-1744-6

Prein, A. F., Langhans, W., Fosser, G., Ferrone, A., Ban, N., Goergen, K., Keller, M., Tölle, M., Gutjahr, O., Feser, F., Brisson, E., Kollet, S., Schmidli, J., Lipzig, N. P. M., & Leung, R. (2015), *A review on regional convection-permitting climate modeling: Demonstrations, prospects, and challenges.* Reviews of Geophysics, 53(2), 323–361. https://doi.org/10.1002/2014RG000475

Prein, A. F., Liu, C., Ikeda, K., Bullock, R., Rasmussen, R. M., Holland, G. J., & Clark, M. (2020), *Simulating North American mesoscale convective systems with a convection-permitting climate model.* Climate Dynamics, 55(1–2), 95–110. https://doi.org/10.1007/s00382-017-3993-2

Rummukainen, M. (2016), *Added value in regional climate modeling.* WIREs Climate Change, 7(1), 145–159. https://doi.org/10.1002/wcc.378

Seneviratne, S. I., Nicholls, N., Easterling, D., Goodess, C. M., Kanae, S., Kossin, J., Luo, Y., Marengo, J., McInnes, K., Rahimi, M., Reichstein, M., Sorteberg, A., Vera, C., Zhang, X., Rusticucci, M., Semenov, V., Alexander, L. V., Allen, S., Benito, G., … Zwiers, F. W. (2012), Changes in Climate Extremes and their Impacts on the Natural Physical Environment. In C. B. Field, V. Barros, T. F. Stocker, & Q. Dahe (Eds.), *Managing the Risks of Extreme Events and Disasters to Advance Climate Change Adaptation* (1st ed., pp. 109–230). Cambridge University Press. https://doi.org/10.1017/CBO9781139177245.006

Seneviratne, S.I., X. Zhang, M. Adnan, W. Badi, C. Dereczynski, A. Di Luca, S. Ghosh, I. Iskandar, J. Kossin, S. Lewis, F. Otto, I. Pinto, M. Satoh, S.M. Vicente-Serrano, M. Wehner, and B. Zhou, 2021: Weather and Climate Extreme Events in a Changing Climate. In Climate Change (2021), The Physical Science Basis. Contribution of Working Group I to the Sixth Assessment Report of the Intergovernmental Panel on Climate Change [Masson-Delmotte, V., P. Zhai, A. Pirani, S.L. Connors, C. Péan, S. Berger, N. Caud, Y. Chen, L. Goldfarb, M.I. Gomis, M. Huang, K. Leitzell, E. Lonnoy, J.B.R. Matthews, T.K. Maycock, T. Waterfield, O. Yelekçi, R. Yu, and B. Zhou (eds.)]. Cambridge University Press, Cambridge, United Kingdom and New York, NY, USA, pp. 1513–1766.

Skamarock WC, Klemp JB, Dudhia J, Gill DO, Barker DM, Duda MG, Huang XY, Wang W, Powers JG (2008), *A description of the advanced research WRF version 3*. National Centre of Atmospheric Research: Boulder. CO, USA

Stocchi, P., Pichelli, E., Torres Alavez, J. A., Coppola, E., Giuliani, G., & Giorgi, F. (2022), *Non-Hydrostatic Regcm4 (Regcm4-NH): Evaluation of Precipitation Statistics at the Convection-Permitting Scale over Different Domains*. Atmosphere, 13(6), 861. https://doi.org/10.3390/atmos13060861

Thompson, G., Field, P. R., Rasmussen, R. M., & Hall, W. D. (2008), *Explicit Forecasts of Winter Precipitation Using an Improved Bulk Microphysics Scheme. Part II: Implementation of a New Snow Parameterization*. Monthly Weather Review, 136(12), 5095–5115. https://doi.org/10.1175/2008MWR2387.1

CHAPTER 14

GREENHOUSE GAS EMISSIONS IN ISTANBUL: A COMPARATIVE ANALYSIS OF PRODUCTION AND CONSUMPTION BASED ACCOUNTING PERSPECTIVE

Nizamettin MANGIR, Ülkü ALVER ŞAHİN

Istanbul University-Cerrahpasa, Türkiye
Engineering Faculty
Environmental Engineering Department

Abstract

Cities, a part, and the victims of the climate change problem, strive to reduce their greenhouse gas (GHG) emissions around the world. The GHG emission inventory serves as the foundation for climate change mitigation strategies and measures in cities. Although most cities focus on production-based accounting (PBA), there are a growing number of cities using consumption-based accounting (CBA) to address their GHG emissions and formulate reduction strategies. In this study, we analyze and compare PBA and CBA GHG emissions accounts for Istanbul. The GPC Basic methodology and Environmentally-Extended Input–Output Modeling (EEIO) are used to calculate Istanbul's PBA and CBA emissions, respectively. The Eora26 database, which is a simplified version of the Eora database adapted to 26 economic sectors, is performed in EEIO model. We find that Istanbul's PBA emissions of 47 MtCO2e and 3.23 tCO2e per capita is 2.58 times lower than the CBA emissions of 121.5 MtCO2e and 8.29 tCO2e per capita. The results stress out the importance of CBA when designing city-level GHG mitigation policies, as significant part of emissions may occur outside the city boundaries. This paper illustrates how local governments can combine both perspectives for a more holistic climate policy. Carbon neutrality in cities should be achieved by demonstrating net zero GHG emissions not only in PBA and but also in CBA.

Keywords: *GHG inventory, Istanbul, Consumption-based, Production-based, Cities.*

14.1. INTRODUCTION

Climate change is one of the major challenges facing the world. Scientific evidence indicates that the climate crisis is 'unequivocally' human driven and continues at an unprecedented rate (IPCC, 2021). According to the recently released report by the Intergovernmental Panel on Climate Change (IPCC), human-induced climate change is already affecting many weather and climate extremes in every region across the globe, including cities (IPCC, 2021). Over half of the world's population (55 %) live in urban areas and that figure is expected to grow to 68% by 2050 (UN, 2020). Although cities occupy only 3% of the global surface area, they consume 60-80% of the world's energy and generate as much as 70% of human-induced GHG emissions (UN, 2020). If all indirect GHG emissions associated with products consumed by urban residents are included, this share would be more than 80% of global GHG emissions (Hoornweg et al., 2011). Therefore, cities are both the trigger and the victim of a changing climate, obliging them also to become part of the solution. Fortunately, cities have significant institutional and technical capacity to do so (C40, 2021a).

Currently, thousands of cities are preparing climate change action plans, committing ambitious reduction targets, creating innovative policies, becoming members of international city initiatives and trying to raise social awareness on climate crisis. Over 11000 actors representing more than 13000 actions are reported to the United Nations Framework Convention on Climate Change (UNFCCC) Global Climate Action Portal just by the cities and regions as of October 2021 (UNFCCC, 2021). Furthermore, a growing number of cities are making pledges to get to net-zero emissions. As of December 2020, 73 states and regions and 55 cities with a population above 500000 have already pledged to reach net zero (Black et al., 2021). This figure may grow depending on the "city" definition. According to another study, 823 cities and 101 regions that a total of 846 million people call home have net-zero targets (DDE&NCI, 2020). Race to Zero, a global campaign led by the COP26 Presidency and High-Level Climate Champions for Climate Action rallies leadership and support from all actors, including cities (UNFCCC, 2019). Under this umbrella campaign, C40 Cities Climate Leadership Group (C40), the Global Covenant of Mayors for Climate & Energy (GCoM), Local Governments for Sustainability (ICLEI), United Cities and Local Governments (UCLG), the Carbon Disclosure Project (CDP), the World Wide Fund for Nature (WWF), and the World Resources Institute (WRI) have come together and launched the Cities Race to Zero effort with the goal of recruiting 1000 cities to campaign (C40, 2021b). During the COP26, C40 announced that more than 1000 cities and local governments have joined the Cities Race to Zero campaign (C40, 2021c).

These initiatives and programs aim to promote city-level action. The road from targets to actual reductions should be well planned with the help of a climate change action plan (CCAP). A complete GHG emissions inventory is the first step for developing a CCAP and integrating it into city-level policymaking (Arioli et al., 2020). An urban GHG emissions inventory identifies the main sources of emissions in a base year and within a specific boundary and serves as a necessary foundation for the city's climate policy and emission reduction targets (C40, 2019).

City inventories are usually based on international GHG standards for comparability and compatibility (Arioli et al., 2020; Ohshita et al., 2015). Over the past two decades, several international organizations, such as the WRI, ICLEI, C40, the United Nations Environment Program (UNEP), the United States Environmental Protection Agency (US EPA), the British Standards Institution (BSI) have been active in establishing methodologies for accounting urban GHG emissions (Kennedy et al., 2011). Available GHG emission accounting approaches can be roughly categorized into PBA and CBA methods (C40, 2018; Ramaswami et al., 2011). In addition, hybrid approaches are also used as a combination of these approaches in order to better determine the drivers of GHG emissions (Arioli et al., 2020; Chavez and Ramaswami, 2011; Lin et al., 2015; Ramaswami et al., 2008; Tukker et al., 2020).

The PBA, also called as territorial emission accounting framework (Pichler et al., 2017), is employed by the UNFCCC and follows the guidelines of the IPCC (Lenk et al., 2021). The PBA approach attributes the responsibility of GHG emissions from the production of energy, goods and services to the producer and captures only those emissions that occur within the city boundary (Munksgaard and Pedersen, 2001). In contrast, the CBA captures direct and lifecycle GHG emissions of goods and services and allocates them to the final consumers instead of the original producers of those emissions (C40, 2018). Conceptually, a city CBA emissions can be defined as the city PBA emissions; minus the emissions from the production of goods and services exported to outside the city; plus emissions from the production of goods and services produced outside the city but imported for its residents' demand (Andrade et al., 2018).

The CBA has both advantages and disadvantages. Key benefits of the CBA include expanded emissions coverage, options for mitigation, its consideration of carbon leakage and encouragement of cleaner production practices (Afionis et al. 2017; Peters, 2008; Peters and Hertwich 2008; Steininger et al. 2014). However, the CBA also has some disadvantages. These include its complicated nature and calculations, increased uncertainty, and political feasibility (Fan et al., 2016; Franzen and Mader, 2018; Jakob and Marschinski, 2013; Liu, 2015; Peters, 2008). Even so, CBA can help better understand the trends and patterns in emission levels to develop new mitigation policies (Afionis et al., 2017; Karakaya et al., 2019; Liu, 2015; OECD, 2019).

The Global Protocol for Community-Scale Greenhouse Gas Emission Inventories (GPC) and the PAS 2070 Specification for the Assessment of Greenhouse Gas Emissions of a City (PAS 2070) are the most advanced and recent standards to date (Wiedmann et al., 2016). The GPC, jointly developed by WRI, ICLEI, and C40 (C40, 2014) follows the PBA approach and is one of the most popular methodologies employed by cities to account for their emissions (Chen et al., 2019). This standard has been adopted by many initiatives and platforms including the Global Covenant of Mayors for Climate and Energy, the Carbon Disclosure Project (CDP) reporting platform, ISO 37120 Sustainable Development of Communities Indicators for City Services and Quality of Life, and C40's data platform (Balouktsi, 2020). Istanbul Metropolitan Municipality (IMM), a member city of the C40, also develops its GHG reports using the GPC methodology (IMM, 2018a). The CBA approach was systematically introduced to city accounting protocols for the first time by PAS 2070 (Chen et al., 2019). It has two separate yet complementary methodologies. The first one, the PAS 2070 Direct plus Supply Chain (PAS 2070-DPSC) captures the direct emissions plus indirect emissions associated with the largest supply chains serving the cities. The second one, PAS 2070 Consumption-Based (PAS 2070-CB) captures the direct and life cycle emissions for all goods and services consumed by the city's residents and allocates the emissions to the final consumers rather than to the original producers (BSI, 2013). However PAS 2070 cannot be considered as an universal standard or as a widely accepted protocol (Balouktsi, 2020; Lombardi et al., 2017).

CBA emissions can also be calculated with the EEIO model as recommended by PAS 2070 (BSI, 2013; Mi et al., 2019; Tukker et al., 2020). EEIO is a simple and robust method that can be used to assess environmental impacts associated with economic consumption (Kitzes, 2013). C40 (2018) states that applying a top-down methodology like an EEIO analysis is the only practical way to calculate city CBA GHG emissions. Thanks to improved computational tools and a wider availability of economic and environmental accounts, EEIO models enabled the development of multiregional input-output (MRIO) databases containing data for hundreds of countries (Malik et al., 2018). Among these databases, the most known and used are EXIOBASE (Stadler et al. 2018), GTAP (Aguiar et al., 2019), WIOD (Dietzenbacher et al., 2013), OECD ICIO (OECD, 2016), and Eora (Lenzen et al., 2013). Recently presented reviews on the CBA literature revealed that there is a considerable attention at the city level, following the development of those MRIO databases (Afionis et al., 2017; Chen et al., 2019; Heinonen et al., 2020; Ottelin et al., 2019).

Most of the city-level GHG inventories focused on PBA (Andrade et al., 2018; Chen et al., 2019; Harris et al., 2020). However, there is an increasing interest in the use of CBA as well (C40, 2018; Chen et al. 2019; Dahal and Niemelä 2017; Harris et al. 2020; Sudmant et al. 2018). Recently, several studies have been published that calculate and compare urban carbon emissions with both the PBA and CBA approaches. Some examples to these are a study for thirteen Chinese cities (Mi et al., 2016), Beijing (Shao et al., 2016), Bristol UK (Millward-Hopkins et al., 2017), Berlin, Delhi NCT, Mexico City, and New York metropolitan area (Pichler et al., 2017), the urban centers in China, the UK and the US (Sudmant et al., 2018), Brussels Capital Region (Athanassiadis et al., 2018), 79 C40 Cities (C40, 2018), Madrid and London (Andrade et al. 2018), Hebei Province of China (Mi et al., 2019), four megacities in China (Chen et al., 2020), Vienna (Schmid, 2020), British Columbia (Macedo et al., 2021), and Bogota (Gilles et al., 2021). There is even a study that compared them at the urban district level (Lenk et al., 2021).

In the last 10 years, many cities in Turkey, pioneered by Istanbul and other metropolitan cities have developed their GHG inventories with the PBA approach (Uyanık, 2021). For Istanbul, like the other Turkish cities, studies on CBA analysis or a PBA-CBA comparison are quite limited. One of these papers by Moran et al. (2018) estimated the consumption carbon footprints in 13000 cities, including Istanbul, pursuing the downscaling approach just for CO2 and for the year 2013. Harris et al. (2020) compared the PBA and CBA in ten European cities including Istanbul. They calculated emissions using the EXIOBASE MRIO for a base year (2010) and two divergent future scenarios for 2050 (Harris et al., 2020). C40 (2018) investigated the CBA GHG emissions from 79 cities including Istanbul, to better understand the ability of cities and to compare the two approaches. C40 study is performed for the year 2011 using the GTAP MRIO and PAS 2070 methodology. The results of C40 study, however, are presented only regional without city names (C40, 2018; Wiedmann et al., 2020). For these mentioned papers, the study years are all earlier than 2015 and the database used are different. Furthermore, none of them provides a PBA-CBA comparison for Istanbul. This study is a continuation and enhancement of our earlier study which we estimated Turkey's GHG emissions with the PBA and CBA approaches (Mangır and Şahin, 2022), and also attempts to advance earlier studies by analyzing Istanbul's emissions as a case study with both PBA and CBA perspectives. The Eora MRIO will be applied to account for the CBA emissions. The results aim to help cities in general, and Istanbul in particular, revisit and adjust their GHG emission reduction strategies.

14.2. MATERIAL AND METHODS

Istanbul counts as one of the megacities with a population of more than 15 million residents, currently. It is Turkey's economic, social and cultural hub and an intersection point thanks to its strategic location between Asia and Europe. Studies show that climate change already has some effects on Istanbul, as is the case in many other locations in the world. It was observed that Istanbul's annual average temperature has already rose by 0.94°C over 1912-2016 due to anthropogenic climate change (Şahin et al., 2019; Toros et al., 2017). A detailed study on how Istanbul will be affected by climate change and its consequences has been discussed in the first Istanbul Climate Change Action Plan (ICCAP) prepared by the Istanbul Metropolitan Municipality (IMM) in 2018 (IMM, 2018b). According to the report, the change in temperature and precipitation patterns, drought and increased sea levels are the emerging issues for Istanbul and its surroundings. Moreover, extreme climatic events are expected to increase in their frequency and severity. In the first ICCAP, Istanbul had a target of GHG emission reduction by 33% until 2030 compared to the business-as-usual scenario. The IMM has recently revised the ICCAP in November 2021 and ambitiously pledged to achieve the carbon neutral target by 2050.

In this study, the two approaches were used to assess PBA and CBA GHG emissions. In general, the methodological steps (flowchart) to account and compare of Istanbul's PBA and CBA GHG emissions are shown in Figure 14.1. This paper presents a portion of findings from a larger PhD thesis investigating the accounting approaches based on the PBA and the CBA in Istanbul case (Mangir, 2021).

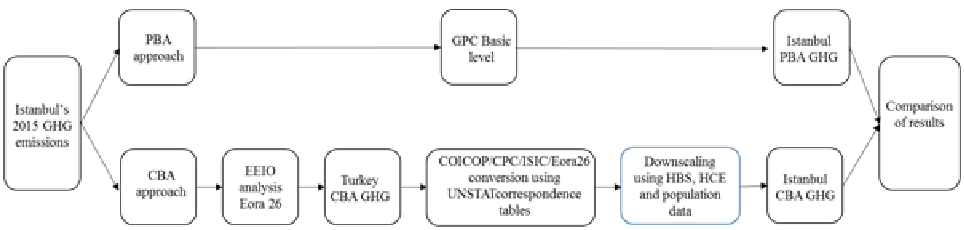

Figure 14.1. The flowchart of methodology to calculate the GHG emissions in both approaches.

14.2.1. Production-based Accounting

The GPC methodology is used to account for PBA emissions. Data related to Istanbul's GHG emissions for 2015 are obtained from the reports prepared by the IMM within the scope of ICCAP (IMM 2018a). The GPC methodology defines three scopes for urban GHG emissions calculation based on where they occur (C40, 2014):

- *Scope 1* includes the direct emissions from sources (stationary energy, transportation, waste, Industrial Processes and Product Use (IPPU), and Agriculture, Forestry and Other Land Use (AFOLU) physically located within the city boundary.

- *Scope 2* covers the indirect emissions that occur as a consequence of consumption of grid-supplied electricity, heat, steam and/or cooling within the city's boundary.

- *Scope 3* includes all other indirect emissions outside the city's boundary as a result of activities that take place within the city boundary.

It gives cities two reporting levels. The Basic level includes scope 1 and scope 2 emissions from stationary energy and transportation, as well as scope 1 and scope 3 emissions from waste. The Basic+ level covers the Basic categories plus emissions from IPPU, AFOLU, and transboundary transportation (C40, 2014). The GPC Basic level is used to report Istanbul's 2015 GHG emissions (IMM, 2018a).

The boundary of the inventory comprises the geopolitical border of the Istanbul metropolitan area, where IMM and Istanbul Province have equivalent jurisdictions. Basic reporting requirements were met. Activity data was collected by IMM from credible and primary sources such as the annual reports of the official agencies. The report includes the three GHGs covered by the Kyoto Protocol: carbon dioxide (CO_2); methane (CH_4); and nitrous oxide (N_2O). Other GHGs are not included in the scope of the inventory due to a lack of traceability of these gases in Turkey and consequently the amount consumed in Istanbul is unknown.

14.2.2. Consumption-based Accounting

EEIO analysis is used to account for CBA emissions. EEIO analysis is based on the input-output (IO) analysis, first developed by Wassily Leontief (Leontief, 1936) and used to assess the economic linkages between different economic sectors or industries (Miller and Blair, 2009). The EEIO method can be briefly described as follows and can be found in our previous study (Mangır and Şahin, 2022).

In a general IO framework, the intermediate inputs from each product sector to the other sectors plus the final demand consumed in the economy equals the total output of the economy. In the MRIO model, the vector of total outputs of all countries X can be expressed as the sum of intermediate inputs matrix Z and the final demand vector Y. Matrix A is known as the 'technical coefficients matrix' developed by dividing the inputs to each product by the final output of the product. Matrix notations below are taken from Miller and Blair (Miller and Blair, 2009).

$$Z = \left[\begin{pmatrix} Z11 & \cdots & Z1n \\ \vdots & \ddots & \vdots \\ Zn1 & \cdots & Znn \end{pmatrix}\right] \qquad A = \left[\begin{pmatrix} \frac{Z11}{X1} & \cdots & \frac{Z1n}{Xn} \\ \vdots & \ddots & \vdots \\ \frac{Zn1}{X1} & \cdots & Znn/Xn) \end{pmatrix}\right]$$

$$Y = \begin{bmatrix} Y1 \\ \vdots \\ Yn \end{bmatrix} \qquad X = \begin{bmatrix} X1 \\ \vdots \\ Xn \end{bmatrix}$$

Depending on the relationship between Z, A, Y, and X, the whole economic system can be formulated in Equation 14.1-3:

$$X = AX + Y \tag{14.1}$$

Equation (14.1) can be rearranged as in Equation (14.2).

$$X = (I - A)^{-1}\, Y = LY \tag{14.2}$$

Here I is the identity matrix and the matrix $L = (I - A)\text{-}1$ is called Leontief inverse matrix, which captures both direct and indirect inputs in monetary values.

The total GHG emissions vector from each product sector in CO_2eq unit can be obtained from national and international reports. By dividing this vector by the economic total output vector X, the vector of the direct GHG emissions intensity, q, in tCO_2eq/\$ unit can be calculated. To calculate the total CBA emissions, the MRIO table was multiplied with the direct GHG emissions intensity, q, as expressed in Equation 14.3.

$$C = qLY \tag{14.3}$$

In this study, the Eora26 database, a simplified version of the Eora database harmonized to 26 sectors, is preferred thanks to its publicly available large amount of data set covering 189 countries, including Turkey (Lenzen et al. 2013; Lenzen et al., 2012). Eora provides the MRIO in basic prices, recommended for use for EEIO analysis (EORA, 2015).

Compiling MRIOs is a time and cost intensive process involving exhaustive amount of data (Lenzen et al., 2014). These challenges limit the availability and accuracy of MRIOs at the city scale (Wiedmann et al., 2020; Zheng et al., 2019). High-resolution

MRIO data is currently only available at the national level but not at the city level for Istanbul. For that reason, firstly, CBA GHG emissions of Turkey are calculated using the Eora26 database for the year 2015 and the results have been published (Mangır and Şahin, 2022). Subsequently, Turkey's CBA GHG emissions in Eora 26 categories are converted to the United Nation's Classification the Household Budget Survey (HBS) data conducted by Turkish Statistical Institute (TurkStat) for this study. Whilst the Eora 26 is based on the International Standard Industrial Classification of All Economic Activities (ISIC) Rev.3 classification system, the COICOP has been used by TurkStat to classify the consumption expenditures of households since 2015. The HBS microdata includes a total of 303 different categories of goods and services at 5-digit-level of COICOP (v.2011) and 15.552 households in 2015 (TurkStat, 2020). In order to use these two data sets together, we matched the COICOP product categories with the Eora26 product classification. However, there is no standard concordance matrix for directly converting the HBS data to ISIC Rev.3 classification system. Therefore, as a first step, the HBS data in the COICOP (v.2011) system is matched with the United Nations Central Product Classification (CPC) system. In the next step, the CPC is mapped to ISIC Rev.3 and then to the Eora26 product classification (Lenzen et al., 2013). United Nations Statistic Division (UNSD) correspondence tables are used for these mappings (UNSD, 2019). Finally, Turkey's CBA GHG emissions are downscaled to the city level for Istanbul. The HBS, the regional Household Consumption Expenditures (HCE), and the population data are used for downscaling. There are six components of final demand in Eora26: Household Final Consumption (HFC), Non-Profit Institutions Serving Households (NPISH), Government Final Consumption (GFC), Gross Fixed Capital Formation (GFCF), Changes in Inventories (CI), and Acquisitions Less Disposals of Valuables (ALDV). The regional Household Consumption Expenditures (HCE) data are provided by TurkStat at Istanbul level (TurkStat, 2016a). The share of Istanbul is rearranged using the HBS and Eora26 data and used for downscaling of HFC emissions. The share of other components of final demand is not available at Istanbul level and is allocated to Istanbul according to population.

14.3. RESULTS AND DISCUSSIONS

14.3.1. Production-Based Accounting

The results given in this section are taken from Istanbul's GHG emission report for the year 2015 (IMM, 2018a). Istanbul's

PBA GHG emissions for 2015 following GPC Basic amounts to 47.3 Mt CO2e and 3.23 tCO2e per capita. Results show that 61% and 39% of emissions originate from Scope 1 and Scope 2 emissions, respectively.

Table 14.1 shows the breakdown by PBA GHG emissions source. The stationary units make up over half of the total carbon footprint, accounting for 66% of emissions. Mobile units also make significant contributions to the carbon footprint, accounting for 28% of the total. Emissions from waste make up a minor proportion of the total PBA GHG emissions. Whilst the residential buildings category has the highest share (48%) in stationary unit's category, on-road transportation makes up almost all emissions from mobile units.

Table 14.1. Istanbul 2015 PBA GHG emissions - Breakdown by GHG source (IMM, 2018a)

Source Category	**GHG Emission (tCO_2e)**	**% Contribution of source category**	**% Contribution of total GHG emission**
Stationary Units			
Residential Buildings	15.108.426	48	31,9
Commercial/ Institutional Facilities	9.435.656	30	19,9
Manufacturing Industries and Construction	6.829.063	22	14,4
Mobile Units			
On-Road Transportation	13.081.381	98	27,6
Railways	149.475	1	0,3
Water-Borne Navigation	111.799	1	0,2
Waste			
Solid Waste Disposal	1.855.211	71	3,9
Biological Treatment of Waste	17.496	1	0
Incineration and Open Burning	4.391	0	0
Wastewater Treatment and Discharge	747.827	28	1,6
Total	47.340.725		

As shown in Table 14.1, stationery and mobile units contribute to about 94% of the city emissions. Although useful, an in-depth analysis into the breakdown of major emission source categories as shown in Table 14.2 provides much more insight into these sub-categories. The consumption of electricity and other fuels as carbon-intensive sectors that contribute more than 5% to the total carbon footprint are shown in Table 14.2. Diesel consumption in on-road transportation champions the highest emissions by 23%, followed by electricity consumed in commercial/institutional facilities by 17% and natural gas consumed in residential buildings by 16%.

Table 14.2. Istanbul 2015 PBA GHG emissions - Carbon hotspots (IMM, 2018a)

Scope	GHG Emission Sources	Fuel/ Emission	Footprint (tCO_2e)	%
1	On-Road Transportation	Diesel	10.670.516	23
2	Commercial/ Institutional Facilities	Electricity	7.939.816	17
1	Residential Buildings	Natural Gas	7.680.593	16
2	Residential Buildings	Electricity	6.652.673	14
2	Industrial Energy Use	Electricity	3.508.344	7
1	Industrial Energy Use	Natural Gas	2.481.486	5

14.3.2. Consumption-Based Accounting

As stated previously, to account the CBA GHG emissions of Istanbul, Turkey's emissions were calculated as a first step. According to the Eora26-based MRIO analysis, Turkey's CBA GHG emissions for 2015 have been reported as 545.9 MtCO2e by Mangır and Şahin (2022). After downscaling, Istanbul's CBA GHG emissions amount was found as 121.5 MtCO2e. Emissions arising from just household consumption in Istanbul are 82.9 MtCO2e and represent 68% of the total final demand CBA emissions.

Figure 14.2 shows Istanbul's GHG emissions calculated using the CBA approach at the Eora26 sector level. The dominant contributors are found to be the Financial Intermediation and Business Activities (10.1%), Transport (8.9%), Food & Beverages (8.5%), Education, Health and Other Services (8.0%), and Construction (7.9%).

The total and per capita CBA GHG emissions of Istanbul in COICOP categories are given in Table 14.3. While the per capita

CBA emission is 8.29 tCO2e, the per capita emission arising only from household expenditures is 5.65 tCO2e.

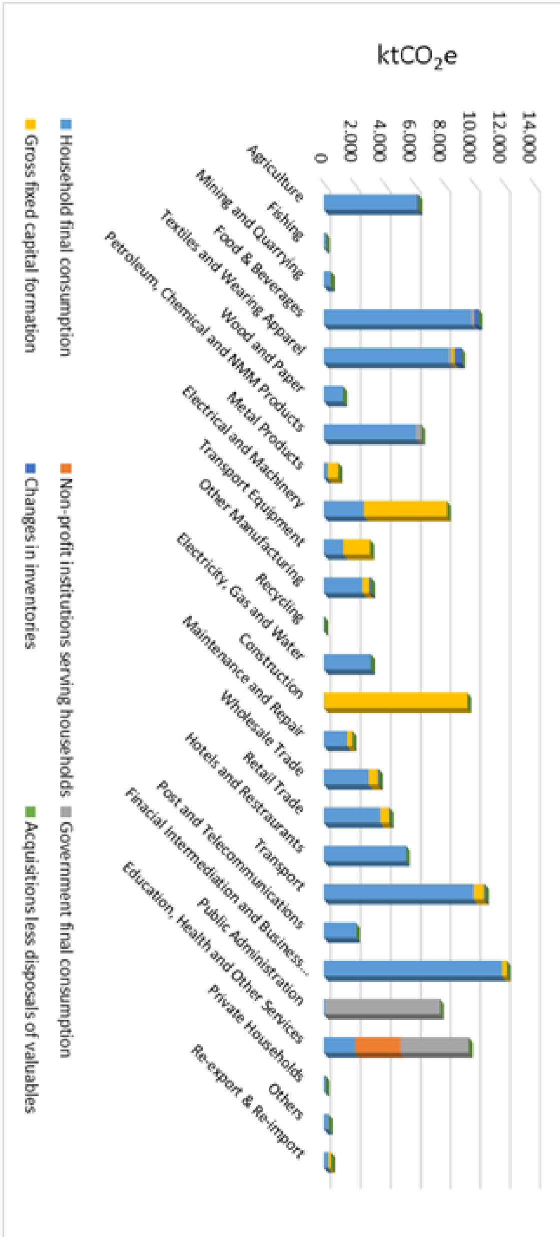

Figure 14.2. Distribution of Istanbul CBA GHG emissions by Eora26 sectors.

Table 14.3. Distribution of the total and per capita CBA GHG emissions by COICOP categories in Istanbul.

COICOP Categories	Emissions $ktCO_2e$	*Per capita* tCO_2e
Food and non-alcoholic drinks	16.744	*1,14*
Alcoholic drinks and tobacco	3.458	*0,24*
Clothing and footwear	4.302	*0,29*
Housing, fuel and power	21.584	*1,47*
Household goods and services	5.087	*0,35*
Health	1.658	*0,11*
Transport	14.064	*0,96*
Communication	3.022	*0,21*
Recreation and culture	2.379	*0,16*
Education	1.797	*0,12*
Restaurants and hotels	5.264	*0,36*
Miscellaneous goods and services	3.527	*0,24*
Sub Total	82.885	*5,65*
Government	20.952	*1,43*
Capital	13.425	*0,92*
Other	4.261	*0,29*
Total	121.524	*8,29*

Figure 14.3 shows the relative contributions of COICOP categories to the total CBA emissions in Istanbul. The 5 key sectors within COICOP categories, Housing, fuel and power, Government, Food and non-alcoholic drinks, and Transport and Capital account for approximately 71% of total CBA emissions in Istanbul.

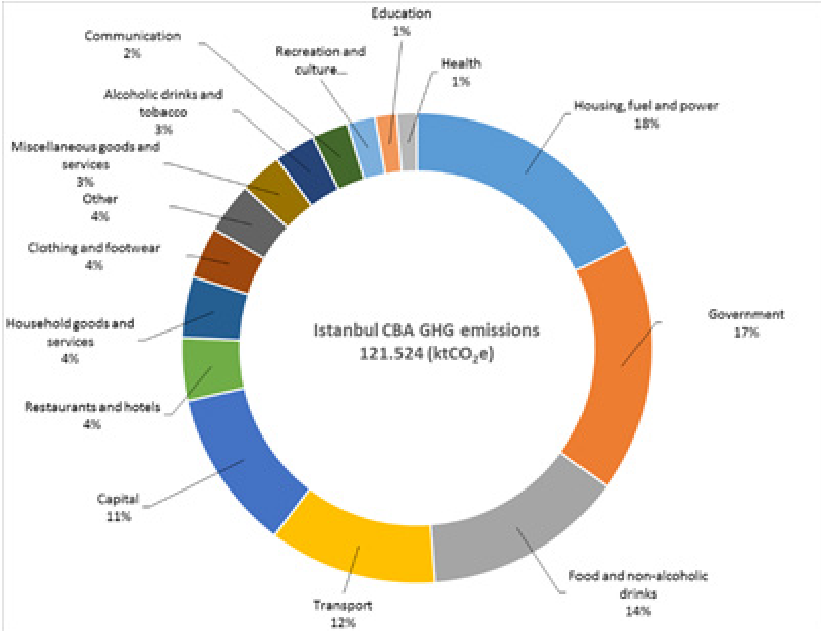

Figure 14.3. Contribution of the COICOP sectors to Istanbul's CBA GHG emissions for the year 2015

While Turkey's total GHG emission in 2015 was calculated as 475.1 Mt CO2e and 6.07 tCO2e per capita by TurkStat (2017) with the PBA approach, these values were found to be 47.3 MtCO2e and 3.23 tCO2e per capita for Istanbul, respectively. Istanbul's per capita PBA GHG emissions are almost two times lower than the national per capita emissions. Accordingly, approximately 10% of Turkey's GHG emissions occur in Istanbul, although economic activities in Istanbul constitute over 30% of Turkey's annual Gross Domestic Product (GDP) (TurkStat, 2019). Istanbul's population of 14.7 million constituted around 19% of Turkey's population for the year 2015 (TurkStat, 2016b). According to Turkstat (2016c) data, 18% of Turkey's road motor vehicles are registered in Istanbul. This shows that Istanbul has a smaller PBA GHG emission compared to the Turkish average. Considering these rates, assuming that the carbon footprint of Istanbul for the same year is 20% of the national carbon footprint, the expected emissions would amount to almost double. The difference between Istanbul's and national per capita emissions can be explained by emission sources and gases included or excluded in inventories, relocating the industries outside the city, relatively, dense public transport system, effective waste management, smaller houses, and central heating systems in Istanbul. Per capita basis emissions reflect not only an individual's lifestyle preferences, but also nature of infrastructure and economy in a geographic area. Emissions per capita in cities are usually lower than their national inventories, especially in OECD countries. For example, per capita GHG emission was 6.1 tCO2e in New York City while 19 tCO2e in the whole USA in 2015 (NY, 2017). In contrast per capita GHG emissions of China's industrial-dense cities can be as high as three times the national average (Hoornweg et al., 2020).

There are some studies in the literature for estimating the sectoral GHG emissions using the different methods in Istanbul such as from transport (Güzel and Alp, 2020), from municipal solid waste collection (Korkut et al., 2018), from residential buildings (Dino and Akgül, 2019), from electric taxis (Onat et al., 2017) and from metal industry (Altay et al., 2011). Guzel and Alp (2020) estimated the effect of different transportation management scenarios on the GHG emission reduction and the results represent that the total GHG reduction is 1.1% for electric rail transportation, 11% for electric and hybrid cars and 39% for limited CO2 emission scenarios in 2050. Korkut et al. (2018) found that the total GHG of municipal solid waste collection in Istanbul for the year of 2015 is 46,4 ktCO2e, which is accounting low level into total. As seen in Table 14.2 residential electricity is 14% of total fuel GHG emission and Dino and Akgül (2019) stated that overheating due to the climate change impact will have a strong effect on cooling energy use. Onat et al. (2017) state that the GHG emission reduction potential of electric taxis is lower than expected compared to conventional taxis which are powered by liquefied petroleum gas. Overall, these results indicate that the authorities may focus on the stationary electricity and transport to achieve the net zero goals in 2050 in Istanbul.

C40 cities regularly update their GHG inventories, using GPC, and disclose them through the CDP and C40's platform. The per capita PBA GHG emissions of Istanbul and some other selected cities using the GPC Basic level are shown in Figure 14.4. The average per capita emission of C40 cities at GPC Basic level is given as 5.26 tCO2e in C40's data platform (GPC, 2020). Istanbul has lower per capita emissions than the C40 average.

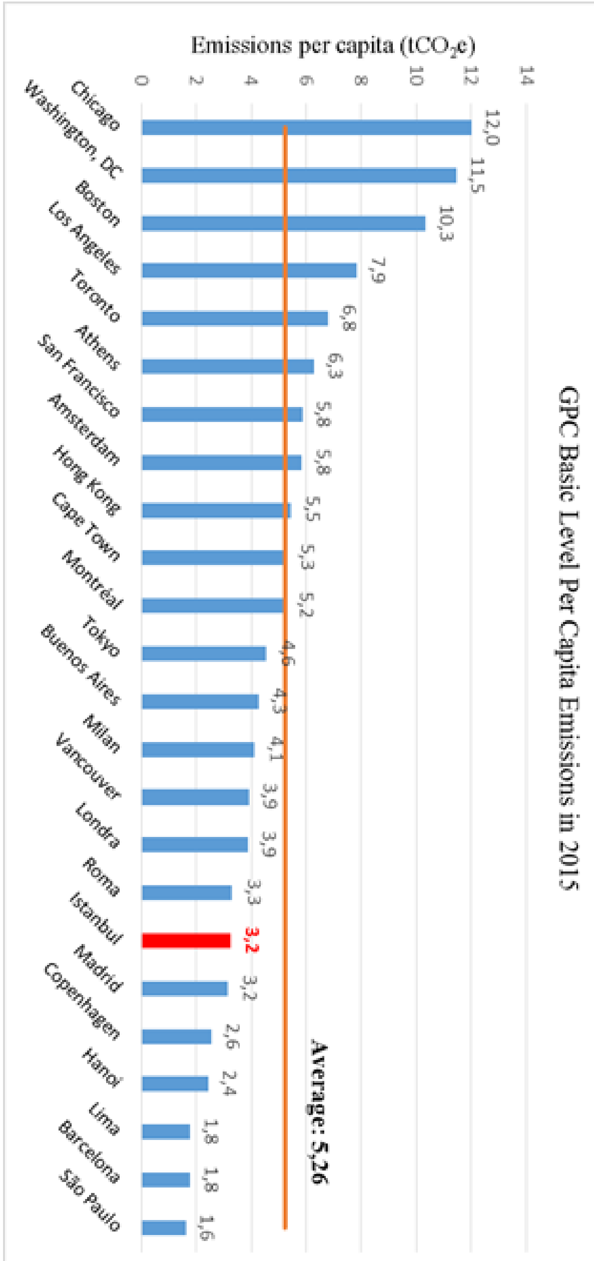

Figure 14.4. Comparison of C40 Cities' per capita emissions (GPC, 2020)

Istanbul's CBA GHG emissions for 2015 are calculated as 121.5 MtCO2e in total and 8.29 tCO2e per capita. C40 (2018) states that the average per capita CBA GHG emissions of its member cities is 10.7 tCO2e. Similar to the PBA case, Istanbul's per capita emissions in CBA are lower than the C40 average. In our study, emissions from capital investments by the private sector and government, and other expenditures account for approximately 32% of total CBA GHG emissions. In the study conducted by C40, these emissions constitute 30% of the CBA GHG emissions of all C40 cities together (Wiedmann et al. 2020).

According to our analysis, Istanbul's CBA emissions make up around 22.3% of Turkey's CBA emissions. Figure 14.5 shows per capita emissions for Turkey and Istanbul for the year 2015, split into COCIOP categories. According to the TurkStat (2016a) data; 25.3% of total consumption expenditure was made by households in Istanbul for the year 2015.

Istanbul's CBA emissions are approximately 2.6 times higher than the PBA emissions for the year 2015. This finding indicates that a significant part of the goods and services consumed in Istanbul are procured from outside the country or the city through trade and do create emissions where they are produced. Therefore, for 2015, Istanbul is a net importer of GHG emissions, or in other words, a consumer city. Considering the global average per capita GHG emissions as 6.7 tCO2e in 2015 (Crippa et al., 2019), Istanbul has higher CBA emissions and less PBA emissions than the global average. Usually, urban measures for reducing GHG emissions are defined in the light of PBA-based inventories and focus on technological options such as renewable energy and energy efficiency. This is also the case in Istanbul. As a matter of fact, Istanbul's mitigation actions and strategies in its previous and revised ICCAP mainly reflect this PBA approach for different sectors such as transportation, infrastructure, building, waste, water management, industry and energy. Although the revised ICCAP includes some demand-side measures such as enhancing the public transportation, increasing daily trips made on foot and bike, improving waste management, and enhancing renewable energy, and energy efficiency, individuals' consumption behaviors are largely ignored. The way of reducing CBA emissions is to decrease both absolute consumption levels and the emission intensity of those consumption activities. The housing and rent, food and beverages, and transportation are the main contributing sectors to Istanbul's CBA emissions, and they are also the sectors with the highest reduction potential. In order to reduce CBA emissions in these carbon-intensive sectors in Istanbul, we recommend that the following measures be taken, mainly by consumers directly or with the guidance of consumers. The list of recommended measures is shown in Table 14.4. The mentioned measures will also have additional benefits, such as more comfortable homes, less traffic congestion, new job opportunities and, accordingly, less air pollution, healthier cities, and economic benefits.

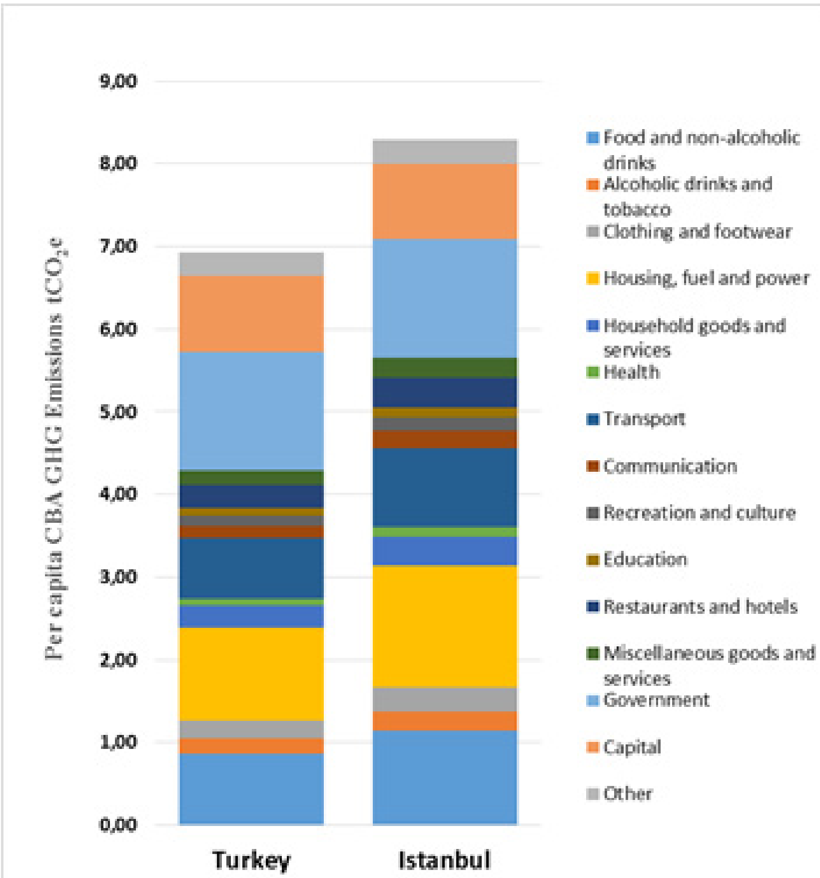

Figure 14.5. Per capita emissions for Turkey and Istanbul for the year 2015.

Table 14.4. List of recommended measures to reduce CBA GHG emissions.

Category	Measures
Housing, Renting, Buildings and Infrastructure	Turn the urban transformation into an advantage in Istanbul, preferring long-lasting, recyclable, and local materials in new buildings
	Prefer energy efficient products and materials
	Retrofit older buildings for functional and energy performance
	Use low-carbon cement in construction and infrastructure projects
	Recycle the building components generated in urban transformation
	Choose smaller homes and buildings
Food and beverages	Strengthen local and urban agriculture
	Shorten the distances in the supply chain and to create a sustainable food strategy
	Shift consumption from high-GHG to low-GHG foods and beverages
	Reduce and recycle or convert food waste
Private Transportation	Prefer walking, cycling or public transportation instead of individual driving
	Reduce personal or business air travel or prefer low-GHG transportation vehicles
	Use technological opportunities to reduce the need for travel as much as possible at events such as meeting, lecture and seminar
Good, Product and Services	Shift consumption from individually owned goods to shared goods
	Extend the longevity of the products with the care and maintenance
	Prefer low-GHG and more durable products or services
	Purchase local products as much as possible instead of imported products
	Obtain goods and clothing as needed

14.4. CONCLUSION

This study aims to compare the PBA and CBA GHG emissions of Istanbul. We used the GPC methodology to account PBA emissions and the EEIO model and household consumption data to account CBA emissions. According to the results of the two approaches, Istanbul's CBA emissions are 2.6 times higher than the PBA and Istanbul has higher CBA and less PBA emissions than the global average. While emissions are decreasing within the borders of Istanbul, the city's high demand for products and services due to its sheer size may lead to more emissions globally. Therefore, the consumption-based policy measures should be kept in mind in Istanbul to essentially become a real carbon neutral city in 2050.

Compared to city-level PBA categories (buildings, transport, industry, waste, agriculture, etc.), the CBA categories reflect the consumption of households such as food, housing, clothing, and goods. CBA helps consumers to identify the GHG emission reduction potential of their consumption choices. This may help individuals to substitute, postpone or even completely refrain from high-GHG products and services. Furthermore, this can also encourage cleaner production practices. Eventually, it is still the suppliers who will need to reduce emissions. PBA and CBA can be seen on the two sides of the same coin. As the world moves towards a carbon-neutral future, cities can combine PBA and CBA in city-scale GHG accounting. This would enable city decision-makers to address a more holistic carbon emission reduction strategy.

This study has some limitations. Firstly, GPC Basic reporting level is used instead of GPC +, which covers more emission sources, due to data availability in PBA. Secondly, the EEIO model used in CBA is limited by its design, including the lack of city-scale input-output tables, trade and emission data uncertainty, aggregation, allocation, and data balancing. Finally, this study covers only the year 2015 and does not provide a larger period to observe the trends and drivers in GHG emissions, which can be more helpful in developing policies and actions. In future research, the GPC+ in PBA and the Full Eora and other database models in CBA can be employed for more robust results. Furthermore, demographics can be discussed, as CBA is affected by consumption behaviors of various age and income groups within the country and the city.

Acknowledgements

Many thanks to the Istanbul Metropolitan Municipality (IMM) for supporting the data of Istanbul.

Author Contribution

Nizamettin MANGIR: Conceptualization, Methodology, Calculation, Data curation, Writing Original draft preparation, Visualization, Investigation. Ülkü Alver Şahin: Supervision, Writing- Reviewing and Editing. All the authors read and approved the final manuscript.

Declarations Competing Interests

The authors declare no competing interests.

Data Availability

Data is available from the authors.

REFERENCES

Afionis, S., Sakai, M., Scott K., Barrett, J., Gouldson, A. (2017). Consumption-based carbon accounting: does it have a future?: Consumption-based carbon accounting. Wiley Interdiscip. Rev. Clim. Change. 8, e438. https://doi.org/10.1002/wcc.438

Aguiar, A., Chepeliev, M., Corong, E., Mcdougall, R. (2019). The GTAP Data Base: Version 10. J. Glob. Econ. Anal. 4, 27.

Andrade, J.C.S., Dameno, A., Pérez, J., de Andrés Almeida, J.M., Lumbreras, J. (2018). Implementing city-level carbon accounting: A comparison between Madrid and London. J. Clean. Prod. 172, 795–804. https://doi.org/10.1016/j.jclepro.2017.10.163

Altay, M.C., Sivri, S., Onat, B., Şahin, U., Zorağa, M., Altay, H.F. (2011). Recycle of metals for end-of-life vehicles (ELVs) and relation to Kyoto protocol, Ren. and Sus. Energy Rev., 15, 5,2447-2451, https://doi.org/10.1016/j.rser.2011.02.017.

Arioli, M.S., D'Agosto, M., de A, Amaral, F.G., Cybis, H.B.B. (2020). The evolution of city-scale GHG emissions inventory methods: A systematic review. Environ. Impact Assess. Rev. 80, 106316. https://doi.org/10.1016/j.eiar.2019.106316

Athanassiadis, A., Christis, M., Bouillard, P., Vercalsteren, A., Crawford, R.H., Khan, A.Z. (2018). Comparing a territorial-based and a consumption-based approach to assess the local and global environmental performance of cities. J. Clean. Prod. 173, 112–123. https://doi.org/10.1016/j.jclepro.2016.10.068

Balouktsi, M. (2020). Carbon metrics for cities: production and consumption implications for policies. Build. Cities 1, 233–259. https://doi.org/10.5334/bc.33

Black, R., Cullen, K., Fay, B., Hale, T., Lang, J., Mahmood, S., Smith, S. (2021). Taking Stock: A global assessment of net zero targets. Energy & Climate Intelligence Unit and Oxford Net Zero.

BSI (British Standards Institute). 2013. PAS 2070:2013 specification for the assessment of greenhouse gas emissions of a city—Direct plus supply chain and consumption-based methodologies. L ondon: The British Standards Institution. [WWW Document]. URL https://shop.bsigroup.com/upload/PASs/Free-Download/PAS-2070-2013.pdf (accessed 6.7.21).

C40. (2021a). Why Cities? [WWW Document]. URL https://www.c40.org/why_cities (accessed 8.18.21).

C40. (2021b). Cities Race to Zero [WWW Document]. URL https://www.c40knowledgehub.org/s/cities-race-to-zero?language=en_US (accessed 7.7.21).

C40. (2021c). Press Release, November 2, 2021 [WWW Document]. C40 Cities. URL https://www.c40.org/news/cop-26-cities-race-to-zero/ (accessed 12.10.21).

C40. (2019). Defining Carbon Neutrality for Cities and Managing Residual Emissions – Cities' Perspective and Guidance. NYC Mayor's Office of Sustainability C40 Cities Climate Leadership Group [WWW Document]. URL https://c40-production-images.s3.amazonaws.com/researches/images/76_Carbon_neutrality_guidance_for_cities_20190422.original.pdf (accessed 10.5.21).

C40. (2018). Consumption-based GHG Emissions of C40 Cities [WWW Document]. URL https://www.c40.org/researches/consumption-based-emissions (accessed 4.18.18).

C40 (2014). Global Protocol for Community-Scale Greenhouse Gas Emission Inventories, WRI, C40, ICLEI [WWW

Document]. URL https://ghgprotocol.org/sites/default/files/standards_supporting/GPC_Executive_Summary_1.pdf (accessed 6.30.20).

Chavez, A., Ramaswami, A. (2011). Progress toward low carbon cities: approaches for transboundary GHG emissions' footprinting. Carbon Manag. 2, 471–482. https://doi.org/10.4155/cmt.11.38

Chen, G., Shan, Y., Hu, Y., Tong, K., Wiedmann, T., Ramaswami, A., Guan, D., Shi, L., Wang, Y. (2019). Review on City-Level Carbon Accounting. Environ. Sci. Technol. 53, 5545–5558. https://doi.org/10.1021/acs.est.8b07071

Chen, S., Long, H., Chen, B., Feng, K., Hubacek, K. (2020). Urban carbon footprints across scale: Important considerations for choosing system boundaries. Appl. Energy 259, 114201. https://doi.org/10.1016/j.apenergy.2019.114201

Crippa, M., Oreggioni, G., Muntean, M., Schaaf, E., Lo Vullo, E., Solazzo, E., Monforti, F., Oliver, J., Vignati, E. (2019). Fossil CO2 and GHG emissions of all world countries - 2019 Report, EUR 29849 EN, Publications Office of the European Union, Luxembourg,. https://doi.org/10.2760/687800

Dahal, K., Niemelä, J. (2017). Cities' Greenhouse Gas Accounting Methods: A Study of Helsinki, Stockholm, and Copenhagen. Climate 5, 31. https://doi.org/10.3390/cli5020031

DDE&NCI. (2020). Data-Driven EnviroLab & NewClimate Institute. (2020). Accelerating Net Zero: Exploring Cities, Regions, and Companies' Pledges to Decarbonise. Research report prepared by the team of: Angel Hsu, Zhi Yi Yeo, Amy Weinfurter, Yin Xi Tan, Ian French, Vasu Namdeo, Odele Tan, Sowmya Raghavan, Elwin Lim, and Ajay Nair (Data-Driven EnviroLab) and Thomas Day, Silke Mooldijk, Niklas Höhne, and Takeshi Kuramochi (NewClimate Institute).

Dietzenbacher, E., Los, B., Stehrer, R., Timmer, M., de Vries, G. (2013). THE CONSTRUCTION OF WORLD INPUT–OUTPUT TABLES IN THE WIOD PROJECT. Econ. Syst. Res. 25, 71–98. https://doi.org/10.1080/09535314.2012.761180

Dino, I.G., Akgül, C.M. (2019). Impact of climate change on the existing residential building stock in Turkey: An analysis on energy use, greenhouse gas emissions and occupant comfort. Renew. Energy 141, 828–846. https://doi.org/10.1016/j.renene.2019.03.150

EORA. (2015). Eora Global MRIO [WWW Document]. URL https://worldmrio.com/ (accessed 3.25.19).

Fan, J.L., Hou, Y.B., Wang, Q., Wang, C., Wei, Y.M. (2016). Exploring the characteristics of production-based and consumption-based carbon emissions of major economies: A multiple-dimension comparison. Appl. Energy 184, 790–799. https://doi.org/10.1016/j.apenergy.2016.06.076

Franzen, A., Mader, S. (2018). Consumption-based versus production-based accounting of CO2 emissions: Is there evidence for carbon leakage? Environ. Sci. Policy 84, 34–40. https://doi.org/10.1016/j.envsci.2018.02.009

Gilles, E., Ortiz, M., Cadarso, M.Á., Monsalve, F., Jiang, X. (2021). Opportunities for city carbon footprint reductions through imports source shifting: The case of Bogota. Resour. Conserv. Recycl. 172, 105684. https://doi.org/10.1016/j.resconrec.2021.105684

GPC. (2020). GHG Interactive Dashboard Data. London, UK: C40 Cities Climate Leadership Group [WWW Document]. URL https://www.c40knowledgehub.org/s/article/C40-cities-greenhouse-gas-emissions-interactive-dashboard?language=en_US (accessed 6.5.21).

Güzel, T.D., Alp, K. (2020). Modeling of greenhouse gas emissions from the transportation sector in Istanbul by 2050. Atmospheric Pollut. Res. 11, 2190–2201. https://doi.org/10.1016/j.apr.2020.08.034

Harris, S., Weinzettel, J., Bigano, A., Källmén, A. (2020). Low carbon cities in 2050? GHG emissions of European cities using production-based and consumption-based emission accounting methods. J. Clean. Prod. 248, 119206. https://doi.org/10.1016/j.jclepro.2019.119206

Heinonen, J., Ottelin, J., Ala-Mantila, S., Wiedmann, T., Clarke, J., Junnila, S. (2020). Spatial consumption-based carbon footprint assessments - A review of recent developments in the field. J. Clean. Prod. 256, 120335. https://doi.org/10.1016/j.jclepro.2020.120335

Hoornweg, D., Sugar, L., Gomez, C.L.T. (2020). Cities and Greenhouse Gas Emissions: Moving Forward. Urbanisation 5, 43–62. https://doi.org/10.1177/2455747120923557

Hoornweg, D., Sugar, L., Trejos, Gómez, C.L. (2011). Cities and greenhouse gas emissions: moving forward. Environ. Urban. 23, 207–227. https://doi.org/10.1177/0956247810392270

IMM. (2018a). Istanbul Metropolitan Municipality GHG Emision Inventory 2015 https://www.iklim.istanbul/raporlar/.

IMM. (2018b). Istanbul Climate Change Action Plan Summary Report 2018 https://www.iklim.istanbul/raporlar/.

IPCC. (2021). Summary for Policymakers. In: Climate Change 2021: The Physical Science Basis. Contribution of Working Group I to the Sixth Assessment Report of the Intergovernmental Panel on Climate Change [Masson-Delmotte, V., P. Zhai, A. Pirani, S. L. Connors, C. Péan, S. Berger, N. Caud, Y. Chen, L. Goldfarb, M. I. Gomis, M. Huang, K. Leitzell, E. Lonnoy, J. B. R. Matthews, T. K. Maycock, T. Waterfield, O. Yelekçi, R. Yu and B. Zhou (eds.)]. Cambridge University Press. In Press.

Jakob, M., Marschinski, R. (2013). Interpreting trade-related CO2 emission transfers. Nat. Clim. Change 3, 19–23. https://doi.org/10.1038/nclimate1630

Karakaya, E., Yılmaz, B., Alataş, S. (2019). How production-based and consumption-based emissions accounting systems change climate policy analysis: the case of CO2 convergence. Environ. Sci. Pollut. Res. 26, 16682–16694. https://doi.org/10.1007/s11356-019-05007-2

Kennedy, C.A., Ramaswami, A., Carney, S., Dhakal, S. (2011). Greenhouse Gas Emission Baselines for Global Cities and Metropolitan Regions, in: Cities and Climate Change: Responding to an Urgent Agenda. The World Bank, pp. 15–54. https://doi.org/10.1596/9780821384930_CH02

Kitzes, J. (2013). An Introduction to Environmentally-Extended Input-Output Analysis. Resources 2, 489–503. https://doi.org/10.3390/resources2040489

Korkut, N.E., Yaman, C., Küçükağa, Y., Jaunich, M.K., Demir, İ. (2018). Greenhouse gas contribution of municipal solid waste collection: A case study in the city of Istanbul, Turkey. Waste Manag. Res. J. Sustain. Circ. Econ. 36, 131–139. https://doi.org/10.1177/0734242X17744656

Lenk, C., Arendt, R., Bach, V., Finkbeiner, M. (2021). Territorial-Based vs. Consumption-Based Carbon Footprint of an Urban District—A Case Study of Berlin-Wedding. Sustainability 13, 7262. https://doi.org/10.3390/su13137262

Lenzen, M., Geschke, A., Wiedmann, T., Lane, J., Anderson, N., Baynes, T., Boland, J., Daniels, P., Dey, C., Fry, J., Hadjikakou, M., Kenway, S., Malik, A., Moran, D., Murray, J., Nettleton, S., Poruschi, L., Reynolds, C., Rowley, H., Ugon, J., Webb, D., West, J. (2014). Compiling and using input–output frameworks through collaborative virtual laboratories. Sci. Total Environ. 485–486, 241–251. https://doi.org/10.1016/j.scitotenv.2014.03.062

Lenzen, M., Kanemoto, K., Moran, D., Geschke, A. (2012). Mapping the Structure of the World Economy. Environ. Sci. Technol. 46, 8374–8381. https://doi.org/10.1021/es300171x

Lenzen, M., Moran, D., Kanemoto, K., Geschke, A. (2013). Building EORA: A Global Multi-Region Input–Output Database at High Country and Sector Resolution. Econ. Syst. Res. 25, 20–49. https://doi.org/10.1080/09535314.2013.769938

Leontief, W.W. (1936). Quantitative Input and Output Relations in the Economic Systems of the United States. Rev. Econ. Stat. 18, 105. https://doi.org/10.2307/1927837

Lin, J., Hu, Y., Cui, S., Kang, J., Ramaswami, A. (2015). Tracking urban carbon footprints from production and consumption perspectives. Environ. Res. Lett. 10, 054001. https://doi.org/10.1088/1748-9326/10/5/054001

Liu, L. (2015). A critical examination of the consumption-based accounting approach: has the blaming of consumers gone too far?: Has the blaming of consumers gone too far? Wiley Interdiscip. Rev. Clim. Change 6, 1–8. https://doi.org/10.1002/wcc.325

Lombardi, M., Laiola, E., Tricase, C., Rana, R. (2017). Assessing the urban carbon footprint: An overview. Environ. Impact Assess. Rev. 66, 43–52. https://doi.org/10.1016/j.eiar.2017.06.005

Macedo, F.D.R., Boucher, J.L., Ramonde, G.M.P., Herrera, O.E., Mérida, W. (2021). Greenhouse gas emissions in British Columbia: Production versus consumption accounting from 2010 to 2015. Sustain. Prod. Consum. 28, 1600–1621. https://doi.org/10.1016/j.spc.2021.08.021

Malik, A., McBain, D., Wiedmann, T.O., Lenzen, M., Murray, J. (2018). Advancements in Input-Output Models and Indicators for Consumption-Based Accounting: MRIO Models for Consumption-Based Accounting. J. Ind. Ecol. https://doi.org/10.1111/jiec.12771

Mangir, N. (2021). Development of A Methodology for Establishment of Greenhouse Gases Emission Inventory in Metropolis: Istanbul Case. Ph.D. Thesis. Istanbul University-Cerrahpasa Institute of Graduate Studies Department of Environmental Engineering.

Mangır, N., Şahin, Ü.A. (2022). An environmentally extended global multi-regional input–output analysis of consumption-based and embodied import-based carbon emissions of Turkey. Environ. Sci. Pollut. Res. https://doi.org/10.1007/s11356-022-19290-z

Mi, Z., Zhang, Y., Guan, D., Shan, Y., Liu, Z., Cong, R., Yuan, X.C., Wei, Y.M. (2016). Consumption-based emission accounting for Chinese cities. Appl. Energy 184, 1073–1081. https://doi.org/10.1016/j.apenergy.2016.06.094

Mi, Z., Zheng, J., Meng, J., Zheng, H., Li, X., Coffman, D., Woltjer, J., Wang, S., Guan, D. (2019). Carbon emissions of cities from a consumption-based perspective. Appl. Energy 235, 509–518. https://doi.org/10.1016/j.apenergy.2018.10.137

Miller, R.E., Blair, P.D. (2009). Input–Output Analysis: Foundations and Extensions, Second Edition 784.

Millward-Hopkins J, Gouldson A, Scott K, Barrett J, Sudmant A (2017) Uncovering blind spots in urban carbon management: the role of consumption-based carbon accounting in Bristol, UK. Reg. Environ. Change 17, 1467–1478. https://doi.org/10.1007/s10113-017-1112-x

Moran, D., Kanemoto, K., Jiborn, M., Wood, R., Többen, J., Seto, K.C. (2018). Carbon footprints of 13 000 cities. Environ. Res. Lett. 13, 064041. https://doi.org/10.1088/1748-9326/aac72a

Munksgaard, J., Pedersen, K.A. (2001). CO2 accounts for open economies: producer or consumer responsibility? Energy Policy 29, 327–334. https://doi.org/10.1016/S0301-4215(00)00120-8

NY. (2017). Inventory of New York City Greenhouse Gas Emissions in 2015 City of New York Inventory of New York City's Greenhouse Gas Emissions, April 2017, by Cventure LLC, Cathy Pasion, Christianah Oyenuga, and Kate Gouin, Mayor's Office of Sustainability, New York, 2017.

OECD. (2019). Exploring changes in world production and trade: Insights from the 2018 update of OECD's ICIO/TIVA database (OECD Science, Technology and Industry Working Papers No. 2019/04), OECD Science, Technology and Industry Working Papers. https://doi.org/10.1787/6f9a10dc-en

OECD. (2016). Estimating CO2 Emissions Embodied in Final Demand and Trade Using the OECD ICIO 2015: Methodology and Results (OECD Science, Technology and Industry Working Papers No. 2016/05). https://doi.org/10.1787/5jlrcm216xkl-en

Ohshita, S., Zhou, N., Price, L., Fridley, D., Khanna, N., Hong, L., Lu, H., Fino-Chen, C., He, G. (2015). Low Carbon Development for Cities: Methods and Measures, in: Yan, J. (Ed.), Handbook of Clean Energy Systems. John Wiley & Sons, Ltd, Chichester, UK, pp. 1–23. https://doi.org/10.1002/9781118991978.hces107

Onat, N.C., Kucukvar, M., Toufani, P., Haider, M.A. (2017). Carbon Footprint Analysis of Electric Taxis in Istanbul 11.

Ottelin, J., Ala-Mantila, S., Heinonen, J., Wiedmann, T., Clarke, J., Junnila, S. (2019). What can we learn from consumption-based carbon footprints at different spatial scales? Review of policy implications. Environ. Res. Lett. 14, 093001. https://doi.org/10.1088/1748-9326/ab2212

Peters, G.P. (2008). From production-based to consumption-based national emission inventories. Ecol. Econ. 65, 13–23. https://doi.org/10.1016/j.ecolecon.2007.10.014

Peters, G.P., Hertwich, E.G. (2008). Post-Kyoto greenhouse gas inventories: production versus consumption. Clim. Change 86, 51–66. https://doi.org/10.1007/s10584-007-9280-1

Pichler, P.P., Zwickel, T., Chavez, A., Kretschmer, T., Seddon, J., Weisz, H. (2017). Reducing Urban Greenhouse Gas Footprints. Sci. Rep. 7, 14659. https://doi.org/10.1038/s41598-017-15303-x

Ramaswami, A., Chavez, A., Ewing-Thiel, J., Reeve, K.E. (2011). Two Approaches to Greenhouse Gas Emissions Foot-Printing at the City Scale. Environ. Sci. Technol. 45, 4205–4206. https://doi.org/10.1021/es201166n

Ramaswami, A., Hillman, T., Janson, B., Reiner, M., Thomas, G. (2008). A Demand-Centered, Hybrid Life-Cycle Methodology for City-Scale Greenhouse Gas Inventories. Environ. Sci. Technol. 42, 6455–6461. https://doi.org/10.1021/es702992q

Şahin, Ü.A., Onat, B., Ayvaz, C. (2019). Climate Change and Greenhouse Gases in Turkey, in: Balkaya, N., Guneysu, S. (Eds.), Recycling and Reuse Approaches for Better Sustainability, Environmental Science and Engineering. Springer International Publishing, Cham, pp. 201–214. https://doi.org/10.1007/978-3-319-95888-0_17

Schmid, F. (2020). Vienna's GHG emissions from a production vs. consumption-based accounting perspective - A comparative analysis. Social Ecology Working Paper 183 Vienna, March 2020.

Shao, L., Chen, B., Gan, L. (2016). Production-based and Consumption-based Carbon Emissions of Beijing: Trend and Features. Energy Procedia 104, 171–176. https://doi.org/10.1016/j.egypro.2016.12.030

Stadler, K., Wood, R., Bulavskaya, T., Södersten, C.J., Simas, M., Schmidt, S., Usubiaga, A., Acosta-Fernández, J., Kuenen, J., Bruckner, M., Giljum, S., Lutter, S., Merciai, S., Schmidt, J.H., Theurl, M.C., Plutzar, C., Kastner, T., Eisenmenger, N., Erb, K.H., de Koning, A., Tukker, A. (2018). EXIOBASE 3: Developing a Time Series of Detailed Environmentally Extended Multi-Regional Input-Output Tables: EXIOBASE 3. J. Ind. Ecol. 22, 502–515. https://doi.org/10.1111/jiec.12715

Steininger, K., Lininger, C., Droege, S., Roser, D., Tomlinson, L., Meyer, L. (2014). Justice and cost effectiveness of consumption-based versus production-based approaches in the case of unilateral climate policies. Glob. Environ. Change 24, 75–87. https://doi.org/10.1016/j.gloenvcha.2013.10.005

Sudmant, A., Gouldson, A., Millward-Hopkins, J., Scott, K., Barrett, J. (2018). Producer cities and consumer cities: Using production- and consumption-based carbon accounts to guide climate action in China, the UK, and the US. J. Clean. Prod. 176, 654–662. https://doi.org/10.1016/j.jclepro.2017.12.139

Toros, H., Abbasnia, M., Sagdic, M., Tayanç, M. (2017). Long-Term Variations of Temperature and Precipitation in the Megacity of Istanbul for the Development of Adaptation Strategies to Climate Change. Adv. Meteorol. 2017, 1–14. https://doi.org/10.1155/2017/6519856

Tukker, A., Pollitt, H., Henkemans, M. (2020). Consumption-based carbon accounting: sense and sensibility. Clim. Policy 20, S1–S13. https://doi.org/10.1080/14693062.2020.1728208

TurkStat. (2020). Turkish Statistical Institute. Household Budget Survey Micro Data, 2015.

TurkStat. (2019). Turkish Statistical Institute (TurkStat). Gross Domestic Product by Provinces, 2015-2017 [WWW Document]. URL https://data.tuik.gov.tr/Bulten/Index?p=Il-Bazinda-Gayrisafi-Yurt-Ici-Hasila-2015-2017-30888 (accessed 5.5.22).

TurkStat. (2017). Turkish Statistical Institute (TurkStat). Greenhouse Gas Emissions Statistics, 1990-2015. [WWW Document]. URL https://data.tuik.gov.tr/Bulten/Index?p=Sera-Gazi-Emisyon-Istatistikleri-1990-2015-24588 (accessed 5.5.22).

TurkStat. (2016a). Turkish Statistical Institute (TurkStat). Household Consumption Expenditures, 2015 [WWW Document]. URL https://data.tuik.gov.tr/Bulten/Index?p=Household-Consumption-Expenditures-2015-21580 (accessed 5.5.22).

TurkStat. (2016b). Turkish Statistical Institute (TurkStat). The Results of Address Based Population Registration System, 2015 [WWW Document]. URL https://data.tuik.gov.tr/Bulten/Index?p=The-Results-of-Address-Based-Population-Registration-System-2015-21507 (accessed 5.6.22).

TurkStat. (2016c). Turkish Statistical Institute (TurkStat). Road Motor Vehicles, December 2015 [WWW Document]. URL https://data.tuik.gov.tr/Bulten/Index?p=Motorlu-Kara-Tasitlari-Aralik-2015-21600 (accessed 5.5.22).

UN (2020). World Cities Report 2020: The Value of Sustainable Urbanization. United Nations Human Settlements Programme (UN-Habitat). https://unhabitat.org/sites/default/files/documents/2019-09/strategic_plan_2020-2023.pdf.

UNFCCC. (2021). GCAP UNFCCC [WWW Document]. URL https://climateaction.unfccc.int/ (accessed 9.29.21).

UNFCCC. (2019). Race To Zero Campaign | UNFCCC [WWW Document]. URL https://unfccc.int/climate-action/race-to-zero-campaign#eq-3 (accessed 7.7.21).

UNSD. (2019). UNSD [WWW Document]. Classif. Econ. Stat. URL https://unstats.un.org/unsd/classifications/Econ#Correspondences (accessed 5.27.20).

Uyanık, S. (2021). The Role of Local Governments in Accounting Climate Change and Carbon Management: Recent Developments in Turkey, in: Aksoy, T., Hacioglu, U. (Eds.), Auditing Ecosystem and Strategic Accounting in the Digital Era: Global Approaches and New Opportunities.

Springer International Publishing, Cham, pp. 25–58. https://doi.org/10.1007/978-3-030-72628-7_2

Wiedmann, T., Chen, G., Owen, A., Lenzen, M., Doust, M., Barrett, J., Steele, K. (2020). Three-scope carbon emission inventories of global cities. J. Ind. Ecol. jiec.13063. https://doi.org/10.1111/jiec.13063

Wiedmann, T.O., Chen, G., Barrett, J. (2016). The Concept of City Carbon Maps: A Case Study of Melbourne, Australia: The Concept of City Carbon Maps. J. Ind. Ecol. 20, 676–691. https://doi.org/10.1111/jiec.12346

Zheng, H., Meng, J., Mi, Z., Song, M., Shan, Y., Ou, J., Guan, D. (2019). Linking city-level input–output table to urban energy footprint: Construction framework and application. J. Ind. Ecol. 23, 781–795. https://doi.org/10.1111/jiec.12835